

GEOLOGICA ULTRAIECTINA

Mededelingen van de  
Faculteit Geowetenschappen  
Universiteit Utrecht

No. 268

**Dynamic recrystallization and grain growth  
in olivine rocks**

Arthur Kellermann Slotemaker

Cover:

Qualitative and quantitative evolution of microstructure during grain growth

The research described in this thesis was carried out under the program “Earth materials, properties and processes” of the Vening Meinesz Research School of Geodynamics (VMSG). The project was funded by the Netherlands Organisation for Scientific Research (NWO), grant 811.31.001. The author acknowledges financial support from the Netherlands Research Centre for Integrated Solid Earth Science (ISES) in the wind up stage of the project. The research was carried out at:

Experimental Rock Deformation (HPT) laboratory  
Faculty of Geosciences, Department of Earth Sciences  
Utrecht university  
Budapestlaan 4  
3584 CD Utrecht  
The Netherlands

[www.geo.uu.nl](http://www.geo.uu.nl)

ISBN: 90-5744-132-2

# **Dynamic recrystallization and grain growth in olivine rocks**

## **Dynamische rekristallisatie en korrelgroei in olivijn gesteente**

(met een samenvatting in het Nederlands)

Proefschrift

ter verkrijging van de graad van doctor aan de Universiteit  
Utrecht op gezag van de rector magnificus, prof.dr. W.H.  
Gispen, ingevolge het besluit van het college voor promoties in  
het openbaar te verdedigen op dinsdag 10 oktober 2006 des  
middags te 12.45 uur

door

**Arthur Kellermann Slotemaker**

geboren op 29 maart 1977, te Heeswijk-Dinther

Promotor: Prof. Dr. C.J. Spiers

Co-promotor: Dr. J.H.P. de Bresser



*'Nothing shocks me. I'm a scientist.'*

- Harrison Ford, as Indiana Jones -

*'Things should be made as simple as possible, but not any simpler.'*

- Albert Einstein -

Aan mijn ouders,  
en in liefdevolle  
herinnering aan  
mijn broer Vincent

Members of the dissertation committee:

Prof. Dr. G. Dresen  
GeoforschungsZentrum Potsdam, Germany

Dr. M.R. Drury  
Utrecht University, The Netherlands

Prof. Dr. D.J. Prior  
University of Liverpool, United Kingdom

Prof. Dr. J.L. Urai  
RWTH Aachen University, Germany

Prof. Dr. S.H. White  
Utrecht University, The Netherlands

# Table of contents

<b>Summary</b> .....	9
<b>Chapter 1: Introduction</b> .....	11
1.1 General scope and motivation.....	11
1.2 Previous work on the rheology of olivine .....	12
1.3 Transient flow behavior in relation to microstructural evolution .....	20
1.4 Aims and thesis structure.....	25
<b>Chapter 2: Effect of dynamic recrystallization on grain size distribution and flow stress during deformation to large strain: A microphysical model</b>	27
2.1 Introduction.....	27
2.2 Model development.....	33
2.3 Numerical implementation.....	47
2.4 Application to olivine.....	48
2.5 Conclusions.....	62
Appendix .....	64
<b>Chapter 3: Deformation induced grain growth in forsterite aggregates</b> .....	69
3.1 Introduction.....	69
3.2 Experimental method.....	71
3.3 Results.....	73
3.4 Discussion.....	82
3.5 Conclusions.....	88
<b>Chapter 4: On the role of grain topology in dynamic grain growth – 2D microstructural modeling</b> .....	91
4.1 Introduction.....	91
4.2 Method.....	97
4.3 Results.....	101
4.4 Discussion.....	110
4.5 Conclusions.....	116

<b>Chapter 5: Flow behaviour and microstructural evolution of Fe-bearing synthetic forsterite-enstatite aggregates</b> .....	119
5.1 Introduction.....	119
5.2 Experimental Method.....	124
5.3 Results.....	127
5.4 Discussion.....	149
5.5 Conclusions.....	164
<b>Chapter 6: Conclusions and suggestions for further research</b> .....	165
6.1 General conclusions.....	165
6.2 Suggestions for further research.....	167
<b>References</b> .....	171
<b>Papers and abstracts</b> .....	180
<b>Samenvatting (summary in Dutch)</b> .....	181
<b>Korte samenvatting voor de leek</b> .....	184
<b>Dankwoord</b> .....	185
<b>Curriculum Vitae</b> .....	187

## Summary

The dynamics of the outer Earth are for a large part controlled by the solid state flow behavior (rheology) of the materials constituting the Earth's upper mantle, in particular olivine. A mechanism based description of the rheology of olivine is essential for numerical modeling of geodynamic processes in the upper mantle and for the interpretation of the rheological significance of mantle deformation structures exposed at the Earth surface. In the past decades, mantle flow has been investigated using single and composite flow laws that describe grain size insensitive (GSI) dislocation creep and/or grain size sensitive (GSS) diffusion creep of olivine. In general, flow laws for GSI or GSS creep have been calibrated on the basis of axial compression experiments to relatively low natural strains, typically  $\epsilon < 0.2$ . In recent years, however, it has become apparent that such low-strain calibrations of flow laws do not represent true steady state flow, as the microstructure continues to evolve and has not yet reached a stable configuration at these low strains. Indeed, few recent high strain experiments on olivine show that significant weakening or hardening may occur well beyond a natural strain of  $\epsilon = 0.2$ . In addition, it has become apparent that a description of the rheology of materials should take into account that rocks exhibit a distributed grain size, rather than that a single mean value is representative for the material.

Various recrystallization processes govern microstructural evolution during large strain transient deformation. These include grain scale processes such as grain boundary migration and new grain formation or "nucleation". Various theoretical and phenomenological models have already been proposed to explain the existence of a relationship between flow stress and dynamically recrystallized grain size (distribution), but only few attempts have been made to fully include the evolution of the microstructure up to steady state. Moreover, little experimental work has been done to date regarding this issue, notably on microstructural evolution in the GSS creep regime. Accordingly, the incorporation into models of the effect of microstructural evolution on the rheology of olivine rocks, and on mantle flow, remains an aspect of innovation.

The broad aim of this thesis is to present an improved description of the solid-state flow behavior of Earth materials in general and olivine in particular, incorporating effects of microstructural evolution up to high strain. This aim has been reached both through new lab experiments on polycrystalline olivine under conditions poorly covered in previous experiments, and through a theoretical treatment and numerical modeling of microstructural evolution during deformation.

In Chapter 1, a brief review is given regarding the rheology of olivine, and problems are outlined concerning the description of olivine rheology using the presently available low-strain flow laws. It is shown that the effect of grain growth and dynamic recrystallization has not yet been adequately addressed for fine-grained materials; data on high strain wet GSS creep of olivine are scarce and in general no satisfactory microphysical model exists that links the effects of grain growth and dynamic recrystallization to transient and steady rheology. A framework is thus established for the present study.

In Chapter 2 a model for dynamic recrystallization is developed through obtaining relations that describe a) the rate of new grain "nucleation" due to dislocation creep and associated subgrain rotation and b) the rate of growth/shrinkage of grains, assuming materials with a distributed grains radius,  $r$ . By combining the results for nucleation and growth as a function of  $r$ , the evolution of the entire grain size distribution is determined as a function of time. The complexity of the problem demands a numerical solution. A simple finite difference approach is used and applied to olivine deforming at laboratory conditions, in order to obtain a first insight into the evolution of grain size distribution and flow stress in this material. The new model shows that the evolution of grain size distribution during

dynamic recrystallization can be highly complex and corroborates that analysis of a single mean grain size when addressing dynamic recrystallization and grain growth is probably inadequate to obtain a meaningful description of large strain transient and steady state flow.

Chapter 3 describes the results of static heat treatment experiments and axial compression tests on wet fine-grained ( $\sim 1 \mu\text{m}$ ) synthetic forsterite aggregates containing  $\sim 0.5$  wt% water and 10 vol% enstatite. Samples were axially compressed to strains of 15, 30 and 45% axial shortening, under conditions where GSS creep and surface energy driven grain growth dominate. Confining pressure and temperature employed were 600 MPa and  $950^\circ\text{C}$ , respectively. Grain growth at static conditions was found to be minor due to grain boundary pinning caused by second phases. Deformation experiments showed continuous hardening with strain. When straining was temporally interrupted for short time intervals, no difference in flow stress was observed before and after the interruption. The observed stress vs. strain rate behavior suggests that deformation took place by a grain size sensitive process. Deformed samples showed an increase in grain size with strain up to values twice the starting value. We relate the observed increase in flow stress with strain to the grain coarsening, which must be deformation induced. A dynamic grain growth model involving an increase in cellular defect fraction (i.e., fraction of non-hexagonal grains) seems best applicable to the grain growth observed.

Chapter 4 further tests the hypothesis that deformation-induced topological changes may explain the dynamic grain growth observed in Chapter 3. The 2D-microstructural modeling package ELLE was used to perform a set of numerical simulations that combined surface energy driven grain boundary migration with simple geometric homogeneous or GSS straining of grain aggregates with distributed grain sizes. The simulations showed extra grain neighbor switching, an increase in defect fraction and enhanced grain growth compared to static (normal) grain growth. An increase in defect fraction was also found in a selected set of natural calcite mylonites that, with increasing temperature, show an increase in grain size and contribution of GSS creep. Analysis of the defect fraction thus appears to be a good microstructural tool to establish whether or not a material has experienced normal static (defect fraction  $\sim 0.7$ ) or dynamic grain growth (defect fraction  $\sim 0.8$ ).

Chapter 5 deals with a similar experimental investigation as presented in Chapter 3, using fine-grained ( $\sim 1 \mu\text{m}$ ) synthetic olivine material, now incorporating a small amount of Fe, i.e.  $\text{fo}_{90}$ . By comparison of the results with previous data on  $\text{fo}_{100}$ , the addition of iron allows to study the effect of Fe on 1) the flow behaviour during GSS creep, and 2) the microstructural evolution during high strain GSS flow. The samples contained  $\sim 0.3$  wt% water and 5 vol% enstatite. Experiments were carried out at temperatures ranging  $850$ - $1000^\circ\text{C}$  and a confining pressure of 600 MPa. Compared to the data for wet  $\text{fo}_{100}$  at similar conditions, adding Fe to wet synthetic olivine was found to have no significant effect on its rheology. Regarding the microstructural evolution, an extra component of grain growth was observed during deformation, causing the material to continuously harden with increasing strain. The analysis shows that this enhanced grain growth can be related to a change in fraction of non-hexagonal grains, similar to what was concluded for  $\text{fo}_{100}$ . The calculated dynamic grain growth rate corresponds well to available data on metals and ceramics. Fitting the experimental results to theoretical models for dynamic grain growth resulted in constraints on model parameters that can be used to build in dynamic grain growth of olivine in geodynamic models.

Finally Chapter 6 summarizes the main conclusions of the study and gives recommendations for future research on dynamic recrystallization and grain growth in olivine rocks.

# Chapter 1

## Introduction

### 1.1 General scope and motivation

The dynamics of the outer Earth are for a large part controlled by the solid state flow behavior (rheology) of the materials constituting the Earth's upper mantle. A mechanism-based description of the rheology of such materials, which can be reliably extrapolated to the relevant time scales, is essential for numerical modeling of geodynamic processes in the upper mantle, and for the interpretation of the rheological significance of mantle deformation structures exposed at the Earth surface.

In order to obtain such a micophysical description, numerous experimental studies have been carried out on olivine materials, resulting in variety of constitutive equations for both grain size sensitive (diffusion) creep and grain size insensitive (dislocation) creep (e.g., Chopra and Paterson, 1981; 1984; Karato et al., 1986; Hirth and Kohlstedt, 1995a; 1995b; McDonnell et al., 1999; 2000). These rate equations have been derived almost exclusively from axial compression experiments employing shortening strains of typically 10-20%. It has long been believed that steady state creep is achieved at these strains and that the steady state flow equations obtained should be appropriate for describing mantle rheology (Bird and Piper, 1980; Houseman and England, 1986; Govers and Wortel, 1995; Wang et al., 2005).

However, recent experimental studies on a variety of rocks and rock analogues, using techniques allowing strains well over 20%, have demonstrated that substantial weakening may occur before true steady state mechanical behavior is approached (e.g., Pieri et al., 1998; Rutter, 1999; Bystricky et al., 1999; Paterson and Olgaard, 2000; Zhang et al., 2000; Barnhoorn et al., 2005). This weakening is believed to be related to an evolution towards a steady state microstructure. In particular, modification of grain size distribution by dynamic recrystallization and grain growth is believed to strongly influence the mechanical behavior (see White, 1976; Atkinson, 1988; De Bresser et al., 1998). It follows that a mechanism-based description of flow behavior suitable for modelling mantle flow must include both large strain transient behavior and true steady state behavior, by incorporating microstructural evolution effects up to high strain. No such description is currently available for olivine.

The broad aim of this study is to develop an improved description of the solid-state flow behavior of Earth materials in general and olivine in particular, incorporating effects of microstructural evolution up to high strain. This study consists of four components: 1) A general theoretical treatment will focus on how processes of deformation and microstructural evolution, including recrystallization and grain growth, can be combined in the framework of a single micophysical model. Then results of new deformation experiments on 2) Fe-free  $f_{0100}$ , and 3) Fe-bearing  $f_{090}$  polycrystalline olivine will be presented, performed under conditions poorly covered by previous experimental investigations, i.e. involving high strains and using small grain sizes at which grain size sensitive creep dominates. Particular attention is paid to the question of whether pure forsterite ( $f_{0100}$ ) and Fe-bearing olivine ( $f_{090}$ ) behave differently under similar conditions, and the mechanistic implications. 4) 2-D microstructural modeling is used to study the deformation-enhanced grain growth found in the experiments.

## 1.2 Previous work on the rheology of olivine

### 1.2.1 Olivine in geodynamic processes

Mantle flow forms one of the main processes of interest in the field of geodynamics, since it is thought to control most of the past and present tectonic movements in the outer Earth. In the Earth's mantle, pressure-temperature conditions vary laterally and especially vertically (Van den Berg et al., 1993; 1995), and directly or indirectly related to this, water content, microstructural character and rock composition may show significant variation. It is thus anticipated that mantle rheology can be variable and strongly heterogeneous. This places high demands on the quality of constitutive descriptions of mantle rheology if meaningful models of mantle flow are to be constructed.

Both abrupt and gradual transitions of various kind have been identified in the shallow and deeper upper mantle at characteristic depths (or depth intervals) by geophysical techniques involving measurement of seismic wave velocity of surface and body waves (Forsyth, 1975; Yoshii et al., 1976; Gaherty and Jordan, 1995), seismic attenuation, electric conductivity (Shankland et al., 1981; Mareschal et al., 1995; Leibecker et al., 2002) and seismic reflections (Flack et al., 1990; Reston, 1990; Keen et al., 1991; Meier and Eisbacher, 1991). The precise meaning of the various transitions observed forms a continuous matter of debate within the geo-scientific community, but in broad terms, chemical/compositional and rheological/microstructural parameters appear the main controlling factor (Ringwood, 1991; Karato, 2003). Many of the observed transitions are characteristic for a specific depth interval or a typical tectonic setting. For example, the low seismic velocity zone detected beneath oceans at ~50–150 km depth (Forsyth, 1975; Yoshii et al., 1976; Shankland et al., 1981; Gaherty and Jordan, 1995), is a transition zone possibly related to a weaker rheology. This may also hold for the strong seismic reflectors below the Mohorovicic discontinuity within present day (e.g. North Sea Basin and Rhine graben) and ancient (e.g. Atlantic passive margin) extensional lithospheric domains (Flack et al., 1990; Reston, 1990; Keen et al., 1991; Meier and Eisbacher, 1991). It has often been speculated that these reflectors may be shear zones that have large and sharp rheological contrasts with their surroundings. In support of this, structural geological investigations made on a scale smaller than that of geophysical studies, i.e. on exposed bodies of mantle rock (e.g., Vissers et al., 1995; Jaroslow et al., 1996; Newman et al., 1999; Handy and Stünitz, 2002), have shown that narrow zones (ranging from the km to hand specimen scale) with characteristics different from the host rock are common in olivine rocks. The interpretation of such zones as mylonites, i.e. zones of localized shear deformation, is of major relevance for our understanding of the role of the upper mantle in processes such as continental rifting and break-up (Malkin and Shemenda, 1991; Ziegler and Cloetingh, 2004).

However, the above observations must be regarded as 'snap shots' and interpreting them in terms of evolution is rarely straightforward. This is where laboratory work on olivine becomes of importance, providing information on strength and strength evolution as a function of time and strain. Various deformation mechanisms have been found to operate in olivine material during laboratory experiments at high pressure and temperature, and it is usually assumed that these are also the mechanisms that control mantle flow. Experimentally calibrated flow laws for the various deformation mechanisms operative in olivine have therefore been used in (numerical) models addressing the dynamics of specific tectonic settings (Rutter and Brodie, 1988; Govers and Wortel, 1993; 1995; Leloup et al., 1999; Frederiksen and Braun, 2001; Yamasaki, 2004). In addition to the mechanisms governing ongoing flow of mantle material, several processes can modify the microstructure during



deformation (Drury and Urai, 1990). In turn, evolving microstructure may progressively change the rheology of the material, particularly at relatively high strains.

Laboratory results on the rheology of olivine have had a profound impact on studies of large scale mantle (asthenospheric) convection. In particular, the notion that both GSS diffusion (i.e. Newtonian) creep and GSI dislocation (i.e. non-Newtonian) creep mechanisms may be of importance in olivine has triggered a range of numerical modeling studies of mantle convection using composite temperature-dependent Newtonian and non-Newtonian rheologies (Van den Berg et al., 1993; 1995; Van den Berg and Yuen 1995; Zhong et al., 2000; Tackley, 2000; Moresi et al., 2002; Hall and Parmentier, 2003; Van Hunen et al., 2005). The results demonstrate that transitions in dominant creep mechanism may occur over time, e.g. during gradual cooling of the Earth, and that zones of localized flow can exist in both upwelling and downwelling limbs of convection cells. Not included extensively in modeling efforts so far is any impact of dynamic changes in microstructure over time.

## 1.2.2 Laboratory results at low strain

*Deformation mechanisms.* As already indicated, most data on the rheology of olivine and other rocks has been obtained in experiments reaching compressive strains of 10-20%. From such work a first order division with respect to solid state flow behavior of Earth materials and in particular olivine is that of grain size sensitive (GSS) diffusion creep versus grain size insensitive (GSI) dislocation creep (Karato et al., 1986; Hirth and Kohlstedt, 1995a; 1995b; Mei and Kohlstedt, 2000a; 2000b). At the elementary level, GSS diffusion creep is governed by the motion of point defects (vacancies) and GSI dislocation creep by motion of line defects (dislocations). Either of these deformation mechanism can be dominant in olivine in the mantle, depending on specific temperature, pressure, grain size and strain rate/stress conditions. Grain boundary sliding (GBS), or granular flow (Drury, 2005), is often regarded as a third basic deformation mechanism, with intergranular strain accommodation by diffusion and dislocation creep (Ashby and Verrall, 1973; Hynes and Doremus, 1996; McDonnell et al., 1999; Casey and Williams, 2000). It is the grain sliding that produces strain in case of GBS, but it is usually the accommodation mechanism, (e.g. diffusion) that controls the rate of straining, so that GBS is frequently included under the general header of GSS creep.

Though grain size is perhaps the most important parameter determining the overall rheology of olivine at given pressure temperature conditions, several other factors are also of importance, such as the presence of H<sub>2</sub>O or melt and the chemical activity of oxygen, even if present in only very minor amounts. Considering low-strain experiments, the presence of water and/or melt has been found to cause a significant reduction in flow strength (Hirth and Kohlstedt, 1995a; 1995b; Karato et al. 1986). In addition, creep rate has been found to increase with oxygen fugacity, which also constrains the chemical stability of Fe-bearing olivine (Ricoult and Kohlstedt, 1985; Karato et al., 1986).

Drury (2005) recently presented state-of-the-art deformation mechanism maps ('rheological regime maps') for dry and wet olivine (fig. 1a-b after Drury, 2005; his fig.'s 2b and 3a), based on the experimental work of Chopra and Paterson (1981), Karato et al. (1986) and Hirth and Kohlstedt (2003). Included is a separate field describing grain size dependent dislocation creep of olivine ('GSS power law creep', after Hirth and Kohlstedt, 2003). In this regime, GBS is accommodated by [a]-slip controlled dislocation motion. This particular type of creep appears to be restricted to nominally dry olivine rocks, since Hirth and Kohlstedt (2003) report no effect of grain size on dislocation creep near the transition to GSS diffusion creep under wet conditions. However, Drury (2005) suggests that GSS power law creep could

also occur in wet olivine, under laboratory conditions, but that more experimental data are needed.

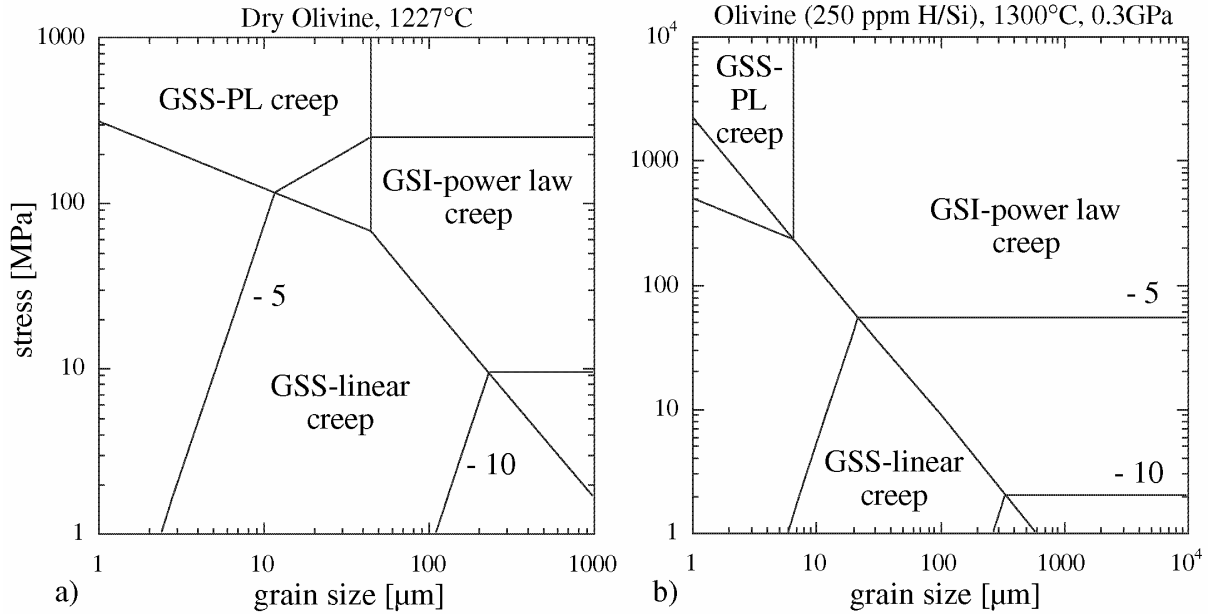


**Figure 1.** Deformation mechanism maps for a) dry and b) wet polycrystalline olivine after Drury 2005, his figures 2b and 3a, respectively.

Role of dynamic recrystallization. Recrystallization mechanisms can operate during deformation and can strongly rework the grain microstructure. Generally speaking, in minerals two basic processes of syn-deformational or dynamic recrystallization can be distinguished, i.e. grain boundary migration (GBM) driven by grain scale differences in stored free energy, and new grain boundary formation (Drury and Urai, 1990; Humphreys and Hatherly, 1996). GBM is defined as motion of a grain boundary *through* the material (not *with* the material), the latter can occur by progressive rotation of subgrains with more or less stationary boundaries (Garofalo et al., 1961; Poirier and Nicolas, 1975) or by migration of a subgrain boundary through an area of cumulative lattice rotation (Urai et al., 1986; Drury and Urai, 1990). Experimental work on a wide range of materials, including rocks, metals and ceramics, has demonstrated that the mean dynamically recrystallized grain size  $\bar{D}$  can be related to the flow stress  $\sigma$  by a relation of the type:

$$\bar{D} = \frac{K_D}{\sigma^p} \quad (1)$$

where  $K_D$ ,  $p$  are material- and mechanism specific constants (Takeuchi and Argon, 1976; Twiss, 1977; De Bresser et al., 2001). Several theoretical models exist that may explain the character of this  $\bar{D}$ - $\sigma$  relationship (Twiss, 1977; Derby and Ashby, 1987; Shimizu, 1998). For olivine polycrystals, recrystallized grain size data as a function of flow stress have been gathered by Mercier et al. (1977), Post (1977), Ross et al. (1980) and Van der Wal et al. (1993), with values for  $p$  ranging 0.8-1.3. All measurements were done in deformed samples having reached relatively low strains (less than 20% shortening). Recrystallization in these samples was generally incomplete, and no obvious change in rheology could be observed. However, plotting equation (1) for olivine on standard deformation mechanism maps (fig. 2, after Drury, 2005, his fig. 4) shows that the trend implied by equation (1) seems to transect

the boundary between the GSI and GSS creep regimes. On the basis of this, it has been suggested that grain size reduction by dynamic recrystallization can bring about a switch in deformation mechanism, from GSI to GSS creep (e.g., Rutter and Brodie, 1988; Furlong, 1993; Karato and Wu, 1993a; Vissers et al., 1995). A switch to GSS creep at constant strain rate could hence result in significant rheological weakening (see fig. 2). The fact that such weakening has not been observed in the low strain experiments on olivine is generally attributed to incomplete grain size reduction in these samples.

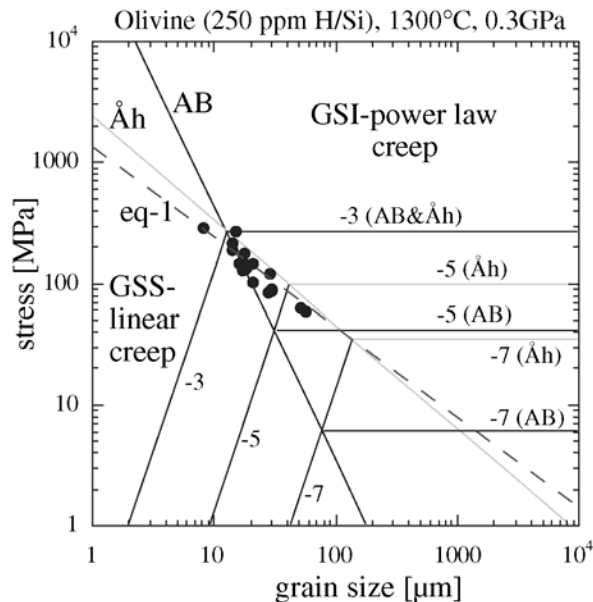


**Figure 2.** Deformation mechanism map for wet polycrystalline olivine after Drury 2005, his figure 4. Strain rate contours for two GSI flows laws based on experiments on Anita Bay and Åheim dunite samples. In combination with the GSS flow law these two different GSI flow laws lead to mechanism boundaries with different slopes. Data from van der Wal (1993) on recrystallized grain size vs stress and a fit to this data (dashed line; equation 1) are shown.

The location of the measured recrystallized grain size data in the deformation map of fig. 2, as apposed to a best fit of the form of (1), shows that the data fall in the boundary between the two creep regimes rather than crosscutting it. De Bresser et al. (1998; 2001) used this observation to put forward the hypothesis that dynamic recrystallization of a deforming material may lead to a balance between grain size reduction and grain growth processes set up in the neighborhood of the boundary between the GSI and GSS creep fields. According to this hypothesis initially coarse (olivine) materials will start deforming in the GSI creep field, but grain size reduction by dynamic recrystallization will produce sufficiently small grains to deform by GSS mechanisms. These new grains will subsequently grow until dislocation mechanisms become significant again. As a consequence, major rheological weakening would not be expected.

Role of grain growth. Static (normal) grain growth in olivine aggregates has been studied in detail by a number of authors, e.g., Karato (1989), Nermond et al. (1993) and Nichols and Mackwell (1991). These investigations showed that surface energy driven grain growth in olivine can be very fast  $T > 1000^\circ\text{C}$ , that the presence of water can enhance grain growth, and that pores or secondary phases are important in inhibiting grain growth. Thus grain size evolution in olivine aggregates can vary substantially depending on composition and microstructure. The occurrence of such effects during deformation will accordingly complicate the rheological behavior of olivine. For example, Karato (1989) pointed out that dynamic recrystallization may well reduce the grain size such that GSS mechanisms become important, resulting in weakening, but that the potentially fast grain growth kinetics of olivine might subsequently result in hardening. Cyclic softening-hardening may then be expected, though this was not observed in low strain experiments. In contrast, low strain deformation

studies of olivine materials with small starting grain sizes generally demonstrated grain growth simultaneously with a monotonic increase in flow stress (e.g., Karato et al., 1986; Hirth and Kohlstedt, 1995a, Mei and Kohlstedt, 2000a). Estimates of the grain size at a particular moment during a deformation test were made by application of a static grain growth law (Karato, 1986). This approach assumes that deformation does not enhance grain growth and limited support for this assumption was provided by a single, squeeze-hold squeeze experiment by Karato et al. (1986), which showed hardening during the hold period. Clearly, grain growth affects the rheology of olivine, but a direct impact of deformation on the grain growth process, of the type seen in some ceramics (Seidensticker and Mayo, 1998a&b), has not yet been explored in detail.

### 1.2.3 Laboratory results at high strain

At high strain, recrystallization and grain growth processes are expected to more strongly influence microstructure than at low strain. However, flow laws formulated on the basis of the low strain experimental results do not include the effects of microstructural modification. Hence, deformation experiments to high strain are required to get a better grip on the impact of microstructural evolution, and much laboratory work has been focused on this in recent years. With respect to olivine, the high strain saw-cut shear and torsion shear studies of Zhang & Karato (1995), Zhang et al. (2000), and Bystricky et al. (2000) are of particular importance.

Zhang & Karato (1995) and Zhang et al. (2000) report moderately high strain experiments (shear strains  $\gamma$  up to  $\sim 2$ ) on olivine material in simple shear geometry, applying a saw-cut double shear experimental technique. Starting material was a dense olivine polycrystal with an average grain size of  $\sim 35 \mu\text{m}$ , obtained by hot isostatic pressing (HIP) of olivine powder made by grinding San Carlos single crystals. Zhang and coworkers found a strong effect of dynamic recrystallization on the development of the lattice preferred orientation (LPO) of the material and on the mechanical behavior. Deformation tests at a temperature of  $1200^\circ\text{C}$  and a pressure of 300 MPa showed continuous strain-hardening up to shear strains of  $\gamma \sim 1.2$ , while tests at higher temperature ( $1300^\circ\text{C}$ ), up to  $\gamma \sim 1.8$ , showed moderate weakening (less than 25%) after a stress maximum at shear strains of  $\sim 0.6$ . LPO analysis suggested that multiple slip texture hardening (see also Wenk et al., 1991) and only limited dynamic recrystallization occurred at the lower temperature, while the softening observed at the higher temperature and larger strains could be related to significant dynamic recrystallization and strong modification of the LPO. With increasing shear strain, LPO patterns evolved from girdles oriented oblique to the shear plane to more symmetric patterns. Zhang et al. (2000) and Lee et al. (2002) suggested that grain size reduction due to dynamic recrystallization promoted local GSS diffusion creep and GBS in the tests. The observation of a weak LPO and abundant four-grain junctions in the fine-grained recrystallized parts of the moderately strained and recrystallized bulk material at  $1200^\circ\text{C}$  formed the basis for this suggestion. At higher strain, temperature ( $1300^\circ\text{C}$ ) and degree of recrystallization, a more substantial contribution of GSS creep to the overall straining was proposed to relax the strain compatibility problem for dislocation creep such that dominant ‘single-slip’ is allowed and a strong single-slip LPO is formed. This LPO is characterized by [100] maxima parallel to the shear direction, [010] normal to the shear plane and [001] within the shear plane and perpendicular to the shear direction.

Bystricky et al. (2000) performed high shear strain (up to  $\gamma = 5$ ) torsion experiments at a pressure of 300 MPa  $1200^\circ\text{C}$  i.e. at temperature similar to the lower temperature tests of Zhang et al. (2000). The starting material was an aggregate with an average grain size of  $\sim 20$

$\mu\text{m}$ , hot-pressed from San Carlos olivine powder. Bystricky et al. observed 15 to 20 % weakening after a peak stress at  $\gamma = 0.5$  before steady state behaviour was approached at  $\gamma \sim 5$ . Contemporaneously with this weakening, an almost completely recrystallized, fine-grained ( $\sim 3 \mu\text{m}$ ) recrystallized microstructure developed (at  $\gamma = 5$ ) with a strong LPO. Apart from being much stronger and more symmetric with respect to the shear plane (even at low strain), the LPO's closely resemble the results of Zhang et al. (2000). Because of the strong LPO, Bystricky et al. (2000) conclude that deformation dominantly took place by dislocation creep and that no evidence exists for a full switch in deformation mechanism (cf. section 1.2.2). However, this does not exclude the possibility that there was at least some contribution of GSS creep to the overall straining, resulting from the substantial grain size reduction by dynamic recrystallization and causing the observed modest weakening. This is in line with the suggestions of Zhang et al. (2000).

The above deformation experiments on olivine samples of relatively large starting grain size ( $\geq 20 \mu\text{m}$ ) to high natural strains ( $\epsilon \approx 2.0$ ) has demonstrated that low strain ( $\epsilon \approx 0.2$ ) mechanical data are not sufficient to establish flow laws that accurately describe steady state behavior. The reason for this is that the microstructure (grain size, LPO, etc.) continues to evolve up to high (shear) strains and that its modification directly affects the strength of the material, causing on-going weakening. Surprisingly, however, the amount of weakening is not as large as would be expected if a starting material with large grain size initially deforms by GSI dislocation mechanisms, but switches to GSS creep as the small recrystallized grain size progressively develops. One way of reasoning then is that starting from GSI creep, the material evolves to a state in which creep occurs by composite GSI-GSS mechanisms. To our knowledge, all high strain investigations focused on evolution of flow stress and microstructure in olivine polycrystalline material starting in the GSI creep field. In order to understand the hybrid steady state behavior a quantitative understanding is required of the end member transient behaviour (see also Handy, 1994), and data are needed regarding microstructural evolution of (olivine) materials starting to deform in the GSS creep field, that is at relative small grain sizes, generally  $\ll 20 \mu\text{m}$ .

#### 1.2.4 Evidence for composite creep of olivine

When the low-strain flow laws calibrated in the laboratory are extrapolated to upper mantle conditions, i.e. applying a realistic geotherm, pressure profile, water-melt distribution and rate of deformation, a prominent outcome is the prediction of a severe weakening around the lithosphere-asthenosphere transition (Karato and Wu, 1993b; Hirth and Kohlstedt, 2003; Karato, 2003). Pronounced strain accumulation and decoupling at this transition are accordingly expected. Given that the laboratory-identified GSI and GSS mechanisms apply, rheology at the lithosphere-asthenosphere boundary appears best described by a composite flow law, while dislocation mechanisms become dominant going deeper into the asthenosphere.

Ter Heege et al. (2004) have recently shown, following previous work by Raj and Gosh (1981), Freeman and Ferguson (1986) and Wang (1994), that the characteristics of the full grain size distribution are of importance when dealing with composite GSS+GSI flow, and that using a single mean value as representative of the grain size is an oversimplification of the rheological behavior. In the same rock, small grains in the distribution might deform by GSS mechanisms while large grains at the same time deform by GSI creep (note: GSI and GSS creep operate as independent, parallel concurrent processes - Poirier, 1985). Taking the distribution as lognormal (after Michibayashi, 1993; Newman et al., 1999; Dijkstra, 2001) and using median grain size and standard deviation as microstructural descriptors, Ter Heege

et al. (2004) showed that for a realistic grain size ( $d = 100 \mu\text{m}$ ) and range of standard deviations (0 - 1.2), the strain rate for olivine at  $1000^\circ\text{C}$  can change at least one order of magnitude with increasing width of the distribution. The calculations clearly demonstrate the need for further work on (a) the character and evolution of grain size distributions of olivine, notably towards higher strains where dynamic recrystallisation and grain growth are important, and (b) the application of the results in any evaluation of the rheological behavior of those parts of the mantle where both GSI and GSS are of importance.

The deformation maps for dry/wet olivine presented in fig. 1 include a field of grain size dependent dislocation creep. This GSS power law regime can be regarded as a transitional regime between GSI dislocation creep and GSS diffusion creep (Hirth and Kohlstedt, 1995b; Drury and Fitz Gerald, 1998; Jin et al., 1998; Hirth and Kohlstedt, 2003). In other words, the regime is an example of composite GSS+GSI flow, though the character of the end-members is not fully clear. Two different interpretations of this intermediate regime have been proposed (see Jin et al., 1998; Hirth and Kohlstedt, 2003): (i) the flow is dominantly governed by diffusion creep, but minor contribution of dislocation creep in the vicinity of the boundary with this mechanism cause an LPO to be formed, (ii) the flow behavior is controlled by dislocation mechanisms, even in the finer grains, but that different slip systems, with different strengths, control the deformation of the finer and coarser grains.

The former of these two interpretations relies on the fact that the olivine rock shows a distributed grain size rather than a single size (cf. Ter Heege et al., 2004). The larger grains deforming by GSI creep than would develop the LPO. However, the observations tell that also the finer fractions of the grain size distribution show a strong LPO. Possibly, the small new grains have inherited the LPO during recrystallization of the original parents. It may take higher strains than realized in the present experimental record to be able to observe a randomizing effect of GSS creep mechanisms on relict LPO (White et al., 1980; Van Swygenhoven and Derlet, 2001; Ford et al. 2002; Kim et al., 2005). Moving to the second interpretation, the idea is that when a material deforms by GSI dislocation glide using multiple slip systems, the 'hardest' operative slip-system controls the flow stress (Hirth and Kohlstedt, 2003). If the grain size is reduced (by dynamic recrystallization) and the boundary with GSS diffusion creep field is approached, less activity is needed on (hard) slip systems as more strain can be accommodated by GSS mechanisms (i.e., diffusion and/or GBS). Hirth and Kohlstedt (2003) suggest that the boundaries of the intermediate rheological regime are given by the easiest ([a] direction) and the hardest ([c] direction) slip systems for the relatively finer and coarser grain sizes, respectively. Thus it appears that easy vs. hard slip systems alone are not sufficient to explain the behaviour of olivine in the transition regime from GSI to GSS creep, but that diffusion and/or GBS need to be considered.

### 1.2.5 The effect of Iron on the rheology of olivine

Iron plays an important role in governing the point defect chemistry in olivine and according to several workers (Mei and Kohlstedt, 2000a; Ji et al., 2001) iron therefore strongly influences solid state diffusion and kinetic properties of olivine during deformation. In general, different charge neutrality conditions are evaluated for Fe-bearing and Fe-free olivine material (Kröger and Vink, 1956; Smyth and Stocker, 1975; Nakamura and Schmalzried 1984; Ricoult and Kohlstedt; 1985; Mei and Kohlstedt, 2000a). These charge neutrality conditions form constraints on the sensitivity of specific point defects to the thermodynamic environment (e.g. oxygen fugacity, chemical activities etc.). Through combination of theoretical predictions and experimental calibration of diffusion sensitivity to e.g. oxygen fugacity, the rate-controlling point defect in a diffusion controlled process can be

assessed. Ricoult and Kohlstedt (1985) evaluated the rate-limiting step for dislocation climb creep in Fe-free forsterite  $fo_{100}$  and Fe-bearing natural olivine  $fo_{90}$  single crystals applying the above procedure and surprisingly found oxygen self-diffusion to be rate-controlling for both materials, despite the difference in the charge neutrality condition. For both nominally dry and wet grain boundary diffusion creep in  $fo_{90}$  material, Hirth and Kohlstedt (1995a) and Mei and Kohlstedt (2000a) conclude that diffusion of silicon is rate-limiting, with charge neutrality conditions controlled by Fe (and H) related defects. No such evaluation exists for wet or dry grain boundary diffusion in Fe-free  $fo_{100}$ . It can not be excluded that for this material Si is rate limiting as well, despite charge neutrality cannot be controlled by Fe-related defects. Deformation experiments in the GSS creep field on both  $fo_{100}$  and  $fo_{90}$  material at otherwise similar conditions will give an unambiguous insight on the effect of iron.

Hitchings et al. (1989) studied the effect on rheology of adding finely dispersed iron and magnetite to Fe-bearing olivine-pyroxene aggregates, fabricated by hot-pressing natural crushed San Carlos olivine. Deformation was governed by dislocation creep. Hitchings et al. found a strong weakening effect for magnetite addition, but none if iron was added. However, the amount of weakening caused by magnetite was substantially greater than expected for the relatively small changes in Fe content (i.e. from  $FO_{90}$  to  $FO_{85}$ ). Here much less weakening was anticipated from the known strength- and melting point difference between pure forsterite and pure fayalite. Combined with the lack of any significant change in strength when Fe was added, the authors concluded the weakening observed for addition of magnetite could best be attributed to a strong increase in oxygen fugacity, rather than to an increase in Fe content.

In contrast to the systematic investigations of the effect of Fe on GSI dislocation creep of olivine (Ricoult and Kohlstedt, 1985; Hitchings et al., 1989), similar studies have not yet been performed for GSS diffusion creep. Some insight, though, comes from the work of Mei and Kohlstedt (2000a) on wet diffusion creep of  $fo_{90}$  olivine. They compared their own data on Fe-bearing aggregates synthesized by hot-pressing natural crushed San Carlos olivine ( $FO_{90}$ ) with the data on synthetic, sol-gel prepared Fe-free forsterite ( $FO_{100}$ ) from McDonnell et al. (1999). Both studies concerned deformation of 'wet' specimens, known to be weaker than their dry counterparts. Normalizing all data to a temperature of 1300°C, the  $FO_{100}$  material appears substantially stronger than  $FO_{90}$ , which was attributed by Mei and Kohlstedt (2000a) to the difference in Fe content. They used two arguments to come to this conclusion. First, Mei and Kohlstedt argue that the weakening effect of adding water will be less pronounced for  $FO_{100}$  because of the fact that the solubility of H is a half to one order of magnitude less than for  $FO_{90}$  (see Zhao et al., 2004). Second, they refer to the fact that  $Fe^{3+}$  is a major point defect in  $fo_{90}$ , hence point defect chemistry between the  $fo_{90}$  and  $fo_{100}$  must be different and, as a result, so must their diffusive properties. Despite these important points put forward by Mei and Kohlstedt, their comparison with data of McDonnell et al. (1999) has some shortcomings. First data were collected at a lower temperature range by McDonnell et al. (1999) than applied by Mei and Kohlstedt (2000a), i.e. 850-1000°C and 1200-1300°C, respectively. Further, the flow laws calibrated for the two materials are considerably different, illustrated by the strong difference in stress-exponent, i.e.  $n = 1$  for  $FO_{90}$  and  $n = 2.14$  for  $FO_{100}$ . Comparison of  $FO_{90}$  and  $FO_{100}$  thus requires extrapolation outside the experimental range for one of the materials, introducing uncertainty.

Here, we would like to put forward another intrinsic material property that might play a role. Compared to sol-gel fabricated  $FO_{100}$ , synthetic olivine aggregates fabricated by hot-pressing crushed natural Fe-bearing olivine can contain a relatively high level of segregated impurities at grain boundaries (de Kloe et al., 2000; 2002; Hiraga et al., 2004). Ricoult and Kohlstedt (1985) detected the following impurities in natural San Carlos olivine single crystals by wet chemical analysis: 0.1-0.3% Ni, 0.03-0.1% Mn and less than 0.01% Al, Co,

Cr and V. Previously, Kirby and Wegner (1978) performed a wet chemical analysis on San Carlos single crystal olivine and found its composition is approximately  $\text{Fo}_{88}$  with 0.3 mole%  $\text{Ni}_2\text{SiO}_4$  and 0.07%  $\text{MnSiO}_4$ . A subsequent spectrographic analysis of the same crystal revealed trace amounts of Al, Ca, Ti, Co, Cr, B, V, Sc, Zr, Be, and Ag in descending order of concentration. The total weight percentage of these impurities is less than approximately 0.1%. In contrast, McDonnell et al. (2002) found concentrations of Fe, Al, Ca, Na, K, Co, Ni, Mo, Y, and Zr in their  $\text{Fo}_{100}$  ceramic were all below the detection limits of the analysis techniques used, which are  $\sim 0.02$  wt% for electron probe microanalysis and  $\sim 10$  ppm for inductively coupled plasma atomic emission spectroscopy.

Another way to gain insight into which point defect mechanism governs diffusion kinetics is to compare activation energies obtained from deformation and electrical conductivity studies. Farver et al. (1994) suggest electrical conduction in fine-grained forsterite is governed by  $\text{Mg}^{2+}$  diffusion through grain boundaries. On the basis of measurements of electrical conductivity of dry synthetic forsterite aggregates as produced by McDonnell et al. (2002), Ten Grotenhuis et al. (2004) determined a value for the activation energy  $Q \sim 320$  kJ/mol that agrees well with the value for  $Q = 350$  J/mol for magnesium grain boundary diffusion found by Farver et al. (1994). Importantly, this value for magnesium also agrees with apparent activation energies found for GSS creep in deformation experiments on forsterite by McDonnell et al. (1999) and on Fe-bearing olivine by Hirth and Kohlstedt (1995a).

From the above, it appears that in spite of differences in point defect chemistry between (dry/wet)  $\text{Fo}_{90}$  and  $\text{Fo}_{100}$ , similarities might exist in the type of defect controlling flow and the related activation energies. However, definite conclusions cannot yet be drawn, since data are lacking on olivine materials that differ in Fe content (i.e.,  $\text{Fo}_{90}$  and  $\text{Fo}_{100}$ ), but are similar in all other respect (impurity content, grain size, etc.)

### 1.3 Transient flow behavior in relation to microstructural evolution

The brief overview of previous work on the rheology of olivine above shows that there are still many questions to be answered within the broad framework of studies on upper/lower mantle dynamics. In particular, progressive changes in microstructure during deformation to high strain and the question of whether these result in rheological hardening or weakening are topics of importance. The current section gives additional background on the processes of recrystallization and grain growth, how they may cause strain weakening or hardening and present models that try to incorporate these effects in a description of microstructural evolution and transient flow behaviour.

#### 1.3.1 Recrystallization and grain growth

Decrease in four types of energy are believed to drive recrystallization: dislocation stored energy, grain boundary surface energy, chemical free energy and grain scale elastic strain energy (Urai et al., 1986). All four types can drive migration of existing boundaries, whereas only the first and the last, which both involve elastic distortional energy, are primarily thought to activate formation of new grain boundaries out of subgrains.

The classical view of recrystallization involves formation (“nucleation”) and growth of new grains at the expense of deformed older grains (Derby and Ashby, 1987; Drury and Urai,



1990). Operation of this type of recrystallization during deformation is commonly referred to as ‘dynamic recrystallization’. Dynamic recrystallization initiates during GSI dislocation creep when a critical strain is reached (Ding and Guo, 2001) and dislocation density has increased sufficiently to force dislocations to reorganize to form strain free, low dislocation density nuclei. Nucleation can result from both new grain boundary formation by progressive subgrain formation (Hobbs, 1968; Poirier and Nicolas, 1975; Schmid, et al., 1980) and grain boundary bulging (Derby and Ashby, 1987; Derby, 1990; Hirth and Tullis, 1992). Following nucleation, dynamic recrystallization involves growth of the nuclei. This grain growth is dominantly driven by dislocation stored energy reduction; i.e. the boundary of a strain-free nucleus migrates outward overgrowing the surrounding higher dislocation density grains. It has long been recognized that the combination of continuous nucleation and subsequent growth during dynamic recrystallization results in a dynamic balance between the two and a related stable grain size (De Bresser et al., 1998; 2001; Gueydan et al., 2001 ; Hirth and Kohlstedt, 2003). The recrystallized grain size is roughly inversely proportional to the flow stress (eq. 1). For a grain size distribution starting deformation in the GSI creep field dynamic recrystallization dominantly leads to grain size reduction and results in a smaller mean recrystallized grain size (for olivine: Van der Wal et al., 1993).

During GSS diffusion creep, dislocation activity is absent or minor, and the dislocation density will not reach a critical level to initiate nucleation of new grains or to set grain boundaries into motion. Rather, surface energy driven GBM will be the important ‘recrystallization’ process during GSS diffusion creep, which may lead to significant net grain growth. Unlike nucleation and nucleus growth during or after deformation by GSI mechanisms, surface energy driven grain growth does not necessarily need contemporaneous or previous deformation to be activated. It is in principle a static process, but can operate during dynamic conditions as long as an aggregate is sufficiently fine-grained, such that it contains enough (grain boundary) surface energy to drive GBM. Also note for any kind of GBM to occur, grain boundaries must not be pinned by a second phase or pores.

Clearly, the microstructure of a material with a grain size distribution that prompts deformation to occur by combined GSI+GSS mechanisms (section 1.2.4) is likely to be affected by conventional dynamic recrystallization as well as surface energy driven grain growth. In order to obtain a mechanism based description of flow behavior of materials, undergoing such microstructural change, quantitative understanding of the contribution of dynamic recrystallization and syn-deformational grain growth is needed. It will be difficult to directly obtain such understanding from experiments on materials deforming by composite mechanisms. Rather, a theoretical/model approach should be followed, or attempts must be made to focus on end-member behavior, i.e. grain growth during creep far into the GSS regime.

### 1.3.2 Strain weakening and hardening

In general, weakening or hardening can be induced under natural conditions by (i) a change in rock composition, which includes the formation of new minerals, a change in H<sub>2</sub>O and/or melt content (Hirth and Kohlstedt, 1996; 2003), and, in the particular case of olivine, a change in Fe-content (Ricoult and Kohlstedt, 1985; Hitchings et al., 1989; Mei and Kohlstedt, 2000a), (ii) a change in temperature with time or depth (e.g., Karato and Wu, 1993b), and (iii) a whole range of deformation-related processes that affect straining, including the development of easy slip LPO, a modification of the dislocation substructure (e.g., recovery), shear heating and grain size reduction or growth through dynamic

recrystallization, and/or grain growth (White et al., 1980; Hobbs et al., 1986 ; Karato and Wu, 1993; Jin et al., 1998; Holyoke and Tullis, 2006).

In section 1.2.2, the widely accepted idea was brought forward that strain weakening in crustal and mantle rocks can occur as a result of a switch in deformation mechanism from GSI to GSS creep, caused by a reduction in grain size by dynamic recrystallization. A change in deformation mechanism through grain size reduction will always evolve through a phase of composite rheological behavior, which becomes obvious if a grain size distribution is accounted for (Freeman and Ferguson, 1986; Wang, 1994; Ter Heege et al, 2004; see also Herwegh et al, 2005). However, there is little or no direct experimental data supporting the possibility that dynamic recrystallization can continue far into the GSS creep field (Twiss, 1977; Karato et al., 1986; Brodie and Rutter, 2000; Ter Heege et al.; 2002; 2005), producing major weakening (Rutter and Brodie, 1988; Karato and Wu, 1993b). An absence of dynamic recrystallization in the GSS creep field is also consistent with available theoretical models that explain the development of a stable recrystallized grain size as a function of stress (cf. eq. 1; Twiss, 1977; Derby and Ashby, 1987; Derby, 1990; Shimizu, 1998, see review in De Bresser et al., 2001). The models all include dislocation stored energy as the main driving force for grain size reduction and growth. Evolution to a recrystallized grain size thus needs to start from an originally coarse grained rock at least for a large part deforming by GSI dislocation creep. In contrast, the hypothesis put forward by De Bresser et al. (1998; 2001) includes grain surface energy as a potential driving force for grain growth. As a consequence, also evolution (i.e. grain growth) to a recrystallized grain size starting from an initially fine-grained material is included in the model, in contrast to the models of Derby/Ashby and Shimizu. Eventually, microstructure modification during deformation can be expected to evolve to a steady state balance between grain growth and grain size reduction in the neighborhood of the GSI-GSS transition. De Bresser et al., (2001) have formulated this ‘boundary hypothesis’ in the form of a grain size - stress relationship by equating conventional rate equations for GSS and GSI-creep, expressing the grain microstructure by a single mean grain size. Ter Heege (2002) modified the boundary equation to account for the (lognormal) distribution of grain size. Notwithstanding the very useful idea behind the boundary hypothesis, a detailed microphysical basis is as yet still lacking.

### 1.3.3 Microstructural evolution models to date

As mentioned before, the presently available flow-laws for olivine, calibrated in the laboratory at relative low strains, lack incorporation of effects of microstructural evolution towards a steady state recrystallized grain size. Nevertheless, several attempts have been made to quantitatively simulate these effects, using available flow laws and assumed phenomenological descriptions of grain size evolution, i.e. equations for grain size reduction (including a stress – recrystallized grain size relation of the type of eq. 1.1) and grain growth (Kameyama et al., 1997; Braun et al., 1999; Montesi and Zuber, 2002; Hall and Parmentier, 2003; Montesi and Hirth, 2003). An evolutionary law describing the change in grain size due to dynamic recrystallization,  $\dot{d}_{\text{dyn-rex}}$ , can be written (after Montesi and Hirth, 2003):

$$\dot{d}_{\text{dyn-rex}} = -\dot{\epsilon} \cdot d / \epsilon_c \quad (2)$$

where  $\dot{\epsilon}$  is the strain rate,  $d$  is the (recrystallized) grain size and  $\epsilon_c$  is the critical strain at which dynamic recrystallization is assumed to cease (Kameyama et al., 1997). Note, however, no microphysical basis exists for this relation. For static grain growth due to surface

energy driven GBM, the following relation is usually applied (e.g., Covey-Crump 1997; Evans et al., 2001)

$$d^m - d_0^m = Kt \quad (3)$$

where  $t$  is the elapsed time,  $d_0$  is the initial grain size at  $t = 0$ ,  $K$  is a growth rate constant and  $m$  is a power-law constant depending on the process controlling grain growth. Equation (3) can be rewritten into:

$$\dot{d}_{\text{gg}} = m^{-1} d^{1-m} K \quad (4)$$

where  $\dot{d}_{\text{gg}}$  is the rate of static grain growth. Furthermore,  $K$  in (3) and (4) is a thermally activated rate constant of the form:

$$K = k_0 \exp\left(-\frac{H}{RT}\right) \quad (5)$$

where  $k_0$  is a reference growth rate constant,  $H$  is the activation enthalpy for grain growth,  $T$  is the absolute temperature and  $R$  is the gas constant. By combining relations (2) and (4) or variants thereof, the evolution of grain size can be simulated in the manner attempted by Kameyama et al., 1997, Braun et al., 1999, Hall and Parmentier, 2003 and Montesi and Hirth, 2003. The essential aim in all cases was to somehow build in the constraint that (the combination of) the rates of change in grain size evolve towards a steady state recrystallized grain size at constant stress. Montesi and Hirth (2003) restricted relation (2) to grain sizes for which the ratio of dislocation to diffusion accommodated strain rate is above some critical value  $R_c$  and likewise restricted relation (4) to grain sizes for which this ratio is below  $R_c$  (the 'field boundary' evolution law). As an alternative, they restricted the operation of grain refinement by dynamic recrystallization (2) to grain sizes larger than the piezometric grain size (1) and the operation of static grain growth (4) to smaller grain sizes (the 'modified field boundary' evolution law). The above two approaches may be criticized on the fact that in reality dynamic recrystallization and static grain growth are continuous processes that do not cease activity when the 'stable' recrystallized grain size is reached. Also, the question can be asked if taking a static grain growth law (3) is applicable if dealing with a dynamic (deformation) situation. In fact, simultaneous operation of grain size reduction and growth is thought to evolve the microstructure to a dynamically stable grain size where both processes balance each other (De Bresser et al., 1998; 2001). Such an approach by Hall and Parmentier (2003) led to a single 'continuous recrystallization' evolution law (see Montesi and Hirth, 2003) by simply summing relation (2) and (4):

$$\dot{d}_{\text{gg}} + \dot{d}_{\text{dyn-rex}} = 0 \quad (6)$$

Another approach followed to come to a steady state recrystallized grain size is the application of so-called 'grain size relaxation' evolution laws by Kameyama et al. (1997), Braun et al. (1999) and Montesi and Zuber (2002). In these laws, the rate of grain size change due to dynamic recrystallization is somewhat different from its form in eq. (2). Instead, the change in grain size is proportional to the difference between the grain size at a given moment and the piezometric grain size,  $D$  (cf. eq. 1), rather than simply using only the grain size, c.f. (2). A modified form of relation (2) is then given by:

$$\dot{d}_{\text{dyn-rex}} = -\dot{\varepsilon}(d - D)/\varepsilon_c \quad (7)$$

In the form of eq. (7), the rate of grain size change simply reduces to zero when  $D$  is reached. Note that relation (7) also allows a positive grain size change rate (i.e. grain growth) for grain sizes smaller than  $D$ , while (2) only allows grain size reduction. Kameyama et al. (1997) and Braun et al. (1999) apply the total strain rate in (7), including composite GSS+GSI creep, while Montesi and Zuber (2002) use only the strain rate accommodated by GSI dislocation creep, reasoning that dynamic recrystallization requires only dislocation activity to be operative (see section 1.3.2). On the other hand, Montesi and Zuber (2002) do not include a surface energy driven grain growth term in their analysis, while Kameyama et al. (1997) and Braun et al. (1999) do. Braun and coworkers artificially restrict grain growth to be dominant only in the diffusion creep regime. In fact, the approaches of Kameyama et al. (1997) and Braun et al. (1999) are also continuous, similar to Hall and Parmentier (2003), but include a build-in assurance that the rate of change of the dynamic recrystallization grain size decreases when  $D$  is approached.

One of the main goals of the various modeling studies referred to above was to evaluate the range of conditions for which weakening and localization by a mechanism switch (GSI to GSS) could occur in the upper mantle, and to predict the subsequent evolution and stability of such localization phenomena. Interesting results have been produced. Kameyama et al. (1997) found that progressive localization in mantle shear zones, that is, the stability of shear zones, is restricted to medium temperatures (around 1000K / 727°C ) and stresses (~100 MPa) and low  $k_0$  (cf. eq. 1.5). At higher T and/or larger stresses, shear zones become unstable, though the magnitude of the grain growth kinetics is critical in determining stability. Braun et al. (1999) found that localization is more likely to take place during cooling than at constant temperature. Further, they concluded that to initiate localization in the first place, the rheology of olivine needs to be nonlinearly related to grain size (i.e., if  $\dot{\varepsilon} \propto d^{-m}$ , the grain size exponent  $m > 1$ ). Hall and Parmentier (2003) investigated how localization involving grain size evolution can lead to convective instabilities; i.e. in mantle regions where convective stresses are initially low, grain size evolution can lead to high viscosity contrasts that change the convective pattern and form isolated domains.

Though important conclusions resulted from these various numerical modeling studies that attempted to include grain size evolution, we note the following problems with the approach adopted:

- a) Dynamic grain size reduction and grain growth have been introduced into the models in an entirely phenomenological way, without establishing a mechanism-based relationship between microstructural evolution, active creep mechanisms and rheology.
- b) A characteristic strain constant had to be introduced into the models for the system to approach a stable microstructure via dynamic recrystallization ( $\varepsilon_c$  in eqs. 2 and 7). This strain is not linked to the mechanical behavior, that is, the (low strain) steady state flow laws applied. Taking it as a constant does not consider how far away the initial deformation conditions and mean grain size reside from the steady state configuration.
- c) The modeling assumed single values for grain size, whereas real rock materials invariably show distributed grain size.

## **1.4 Aims and thesis structure**

In the above, several questions have been put forward that need answers in order to obtain an improved description of the solid state flow behavior of olivine. The aims of this thesis (and the chapters involved) can now be specified as follows:

- 1) To develop a microphysical model that describes large strain transient as well as steady state mechanical behavior and microstructural evolution of olivine rocks, including a composite rheology, distributed grain size and the various processes involved in dynamic recrystallization and grain growth (chapter 2).
- 2) To experimentally determine the characteristics of the microstructural evolution of fine-grained olivine material (both  $fo_{90}$  and  $fo_{100}$ ) that starts deforming in the GSS creep regime, in particular focusing on the role of syn-deformational (dynamic) grain growth in comparison to static grain growth under similar pressure-temperature conditions (chapter 3, and 5).
- 3) To use 2D-microstructural modeling (ELLE) for assessment of the hypothesis that enhanced grain switching and increase in cellular defect fraction may explain enhanced grain growth during deformation (chapter 4).
- 4) To investigate the effect of Fe on the GSS (GBS) deformation behavior of wet olivine material, and on the grain microstructure evolution (i.e. dynamic grain growth) in this creep regime (chapter 5).



## Chapter 2

# Effect of dynamic recrystallization on grain size distribution and flow stress during deformation to large strain: A microphysical model

**Abstract.** Dynamic recrystallization involves a number of different processes. These include: new grain nucleation and grain boundary migration (GBM) driven by gradients in various forms of free energy, but also the operation of grain size sensitive (GSS) diffusion creep and grain size insensitive (GSI) dislocation creep. Experimental data on a number of minerals infer the existence of a simple relation between steady state dynamic recrystallized grain size ( $\bar{D}$ ) and flow stress ( $\sigma$ ). Several theoretical models have been put forward to provide a solid physical basis for extrapolation of a  $\bar{D}$ - $\sigma$  to natural conditions. Recently, grain size distribution (GSD), composite rheology and transient evolution have been recognized as important elements in a polycrystalline material undergoing dynamic recrystallization. These elements are not yet fully incorporated in any existing model. Here a new model for dynamic recrystallization is developed that describes transient evolution of a polycrystalline material with distributed grain size towards a dynamic recrystallized steady state including all processes involved. The basic equations used to derive expressions for nucleation rate and effective GBM rate for grains of a radius  $r$ , are obtained from consideration of the microphysical mechanisms operating. However the complexity of the problem demands a numerical implementation. First application of the model using olivine material parameters shows that evolution of grain size distribution can be highly complex involving multimodal stages and a strong attraction for the evolution to reach steady state at the inverse relation between subgrain size and flow stress. Relative high natural strains ( $\varepsilon \gg 0.1$ ) are needed before a true steady state is reached.

## 2.1 Introduction

Numerous studies of experimentally deformed olivine (Mercier et al., 1977; Post, 1977; Ross et al., 1980; Karato et al., 1980; Van der Wal et al., 1993) and other materials (NaCl: Guillopé and Poirier, 1979; Ter Heege et al., 2005; Calcite: Schmid et al., 1980; Rutter, 1995; Quartz: Stipp and Tullis, 2003; Metals and alloys: Takeuchi and Argon, 1976; Drury et al., 1985) have demonstrated the existence of a systematic relationship between the mean dynamically recrystallized grain size ( $\bar{D}$ ) and the steady state flow stress ( $\sigma$ ). It is generally found that  $\bar{D}$  decreases with increasing  $\sigma$  according to an empirical relation of the form:

$$\bar{D} = \frac{K_D}{\sigma^p} \quad (1)$$

where  $K_D$  and  $p$  are material- and recrystallization mechanism dependent constants, with  $p$  typically taking values of 0.7-1.4. Such  $\bar{D}$ - $\sigma$  relations have attracted much attention in the geological literature (e.g., Twiss, 1977; White, 1979; Hirth et al., 2001) because of their potential for estimating paleo-stresses from the microstructure of naturally deformed rocks (Nicolas et al., 1971; Mercier et al., 1977; Nicolas, 1978; Avé Lallement, 1985; Hacker et al., 1990; Busch and Van der Pluijm, 1995; Jaroslow et al., 1996; Dijkstra et al., 2002; Stipp et al., 2002).

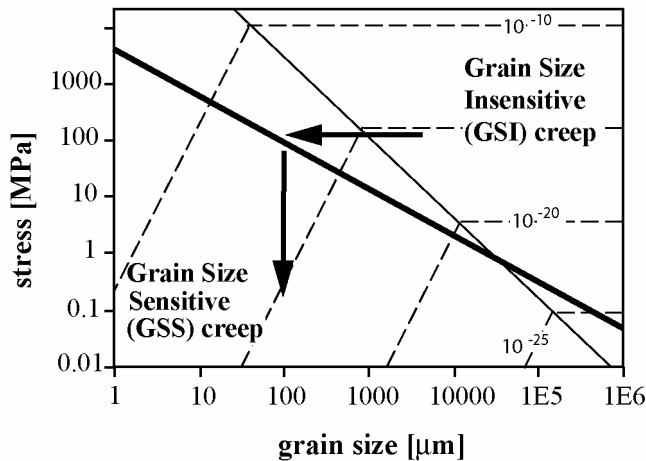


**Figure 2.1.** Empirical stress versus recrystallized grain size relation (heavy line) for olivine extrapolated into a deformation mechanism map drawn for a temperature of 600°C. Based on data from Rutter and Brodie (1988). Strain rate contours in  $s^{-1}$ . The arrows illustrate the notion of rheological weakening resulting from a switch in deformation mechanism associated with grain size reduction by dynamic recrystallization, at constant strain rate. Figure after De Bresser et al. (2001).

In addition,  $\bar{D}$ - $\sigma$  relationships for geological materials have frequently been extrapolated into deformation mechanism maps, for example for olivine (Karato et al., 1986; Rutter and Brodie, 1988; Handy, 1989; Drury, 2005), to evaluate the mechanical effect of recrystallization. At relatively large grain sizes and low stresses, relation (1) for olivine plots in the grain size insensitive (GSI) dislocation creep field, while towards lower grain sizes and higher stresses, it crosses the boundary in to the grain size sensitive (GSS) diffusion creep field (see fig. 2.1, after De Bresser et al., 2001, and Rutter and Brodie, 1988). This has been taken to imply that rocks in the Earth's crust and mantle initially deforming by GSI creep, may switch to GSS creep if dynamic recrystallization results in sufficient grain size reduction, this producing a significant drop in stress at constant strain rate (fig. 2.1). This has been suggested by many authors as a key mechanism for strain weakening and localization of deformation in shear zones (White et al., 1980; Schmid, 1982; Karato et al., 1986; Drury et al., 1991; Karato and Wu, 1993; Rutter and Brodie, 1988; Furlong, 1993; Vissers et al., 1995). Together with grain growth laws, equation (1) has accordingly been widely applied in numerical modeling studies performed to investigate the conditions under which weakening due to a switch in mechanism from GSI to GSS creep might lead to strain localization and shear zone formation particularly in the upper mantle (Govers and Wortel, 1995; Kameyama et al., 1997; Braun et al., 1999; Montesi and Zuber, 2002; Hall and Parmentier, 2003; Montesi and Hirth, 2003).

In an attempt to underpin equation (1), several theoretical models have been proposed (Twiss, 1977; Derby and Ashby, 1987; Shimizu, 1998). The well-known model of Twiss (1977) is based on an equilibrium thermodynamic approach which assumes that a unique recrystallized grain size exists at which the total strain energy of dislocations ordered in a grain boundary is equal to the stored energy of the dislocations in the enclosed volume. The models of Derby and Ashby (1987) and Shimizu (1998) more correctly address the dynamic balance between grain size reduction, through new grain nucleation at mean rate  $\dot{N}$ , and grain growth at mean rate  $\dot{R}$ . At steady state, the recrystallized grain size is then expressed using an Avrami-type model (Kim et al., 2003; Riedel and Karato, 1996; Shimizu, 1998; 1999), describing competition between nucleation and grain growth. This yields:

$$\bar{D} = \left( \frac{\dot{R}}{\dot{N}} \right)^z \quad (2)$$



where  $z = 1/4$  (Shimizu, 1998) or  $1/3$  (Derby and Ashby, 1987, Derby, 1990). To obtain  $\bar{D}(\sigma)$ , Derby and Ashby (1987) and Shimizu (1998) subsequently expressed  $\dot{N}$  and  $\dot{R}$  as functions of  $\sigma$ , resulting in relationships of the type of (1) with specific constraints on  $K_D$  and  $p$ . Of particular importance is the result that  $K_D$  in the models of Derby/Ashby and Shimizu is not a true constant, but is weakly temperature dependent. De Bresser et al. (1998; 2001) predicted a similar result by advancing the hypothesis that dynamic recrystallization results in a balance between grain size reduction and grain growth processes set up in the vicinity of the boundary between the GSI and GSS creep fields. In this conceptual model, initially coarse materials start deforming in the GSI creep field, but grain size reduction by nucleation from subgrains produces sufficiently small grains to deform by GSS mechanisms. These new grains subsequently grow until dislocation mechanisms become significant again.

The application of empirical  $\bar{D}-\sigma$  relationships like (1) to natural rocks, numerical modeling focusing on the role of grain size reduction in strain weakening and localization, and the attempts to obtain a theoretical underpinning of (1) have all produced important insights into the effect of dynamic recrystallization on the rheological behavior of Earth materials such as olivine. However, there are several problems with the various approaches adopted.

First, for meaningful extrapolation of empirical  $\bar{D}-\sigma$  relations (1) to natural conditions a solid microphysical basis for (1) is crucial. Existing theoretical models either apply equilibrium thermodynamics to a non-equilibrium process (see Poirier, 1985, and Derby, 1990, discussing the model of Twiss, 1977), or assume that the stress controlling  $\dot{N}$  and  $\dot{R}$  in (2) is determined solely by GSI dislocation creep, ignoring a possible contribution by GSS mechanisms (Derby/Ashby and Shimizu models). De Bresser et al. (1998; 2001) include GSI as well as GSS creep, but their hypothesis lacks solid underpinning in terms of the microphysical processes relevant during dynamic recrystallization.

Second, few microstructural data exist on the transient evolution of a grain size distribution towards a recrystallized steady state, and a theoretical model describing such evolution and its effect on flow strength is lacking. It is therefore unclear whether calibrated versions of (1) represent a true steady state or apply only to a limited range in strain. Microstructural evolution is expected to be dominated by grain size reduction through nucleation from subgrains in the dislocation creep field, and by grain growth under the action of surface energy in the diffusion creep field. Hence a general evolution of the grain size towards the mechanism boundary will tend to occur depending on the deformation conditions (De Bresser et al., 2001; Kameyama et al., 1997; and Braun et al., 1999). It is unclear, however, whether this type of evolution can be described by simply combining equation (1) with grain growth laws for materials such as olivine, as frequently done in attempts to model localization and flow phenomena in the mantle (Kameyama et al., 1997; Braun et al., 1999; Montesi and Zuber, 2002; and Hall and Parmentier, 2003).

Third,  $\bar{D}$  in relation (1) is an average grain size characterizing the recrystallized part of a rock aggregate. However real materials are characterized by a grain size distribution (GSD), as shown schematically in fig. 2.2. Several studies have shown that the shape of the GSD (mean/median, width, skewness, etc.) can significantly affect the rheological behavior and microstructural evolution of a deforming material, since fine grains will tend to deform by GSS creep and coarse grains by GSI creep (Raj and Ghosh, 1981; Freeman and Ferguson, 1986; Wang, 1994; Ter Heege et al, 2004). The measurement of a single average  $\bar{D}$  in experimentally and naturally deformed materials, thus, might not be an adequate description of the microstructure for a unique correlation with the flow stress. Moreover, if grain boundary migration is inhibited due to the presence of a second phase, grain growth cannot

freely counterbalance grain size reduction and the pinned grain size distribution and mean will more likely reflect the second phase distribution than the steady state stress.

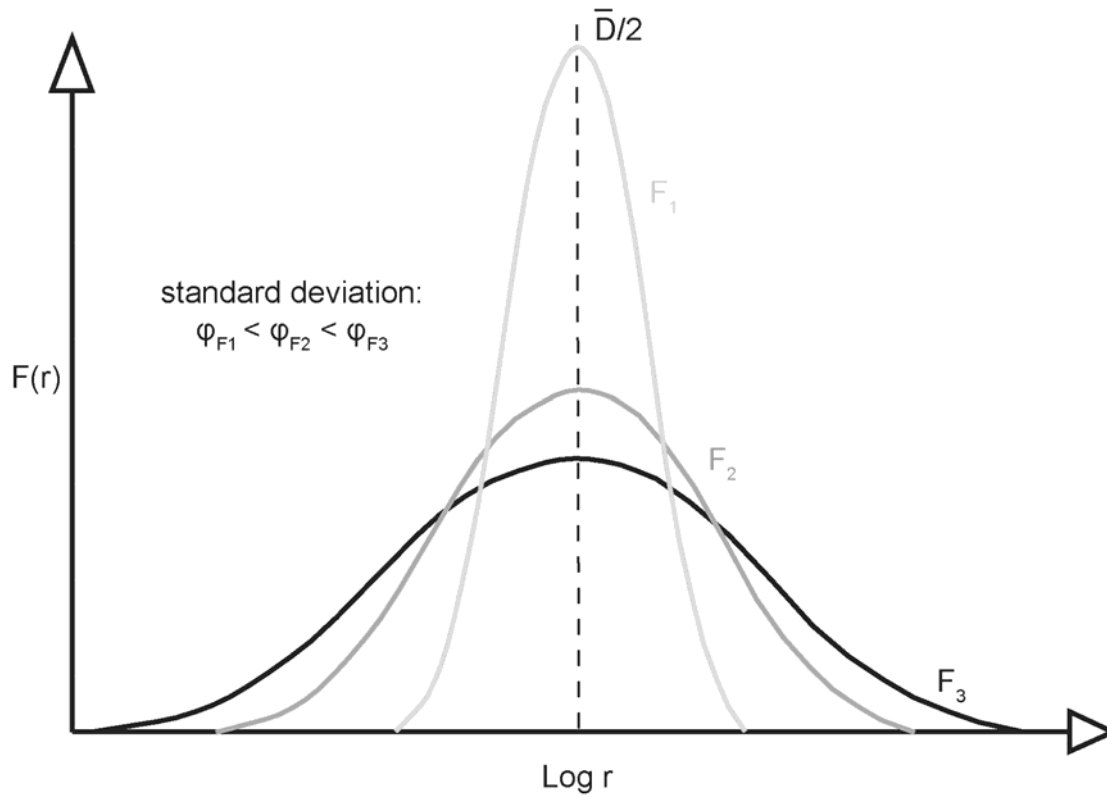


**Figure 2.2.** Recrystallized grain size distributions, showing varying standard deviations at constant mean recrystallized grain diameter,  $\bar{D}$ ;  $r$  is the grain radius and  $F(r)$  is the number density function.

The aim of the present study is to develop a microphysically based model that provides a description of the large strain transient evolution of both GSD and flow stress towards a recrystallized steady state, as a result of dynamic competition between nucleation by progressive subgrain rotation and GBM driven by free energy differences across grain boundaries. We treat the problem by assuming that a polycrystalline material with distributed grain size deforms at a uniform strain rate by both GSI dislocation creep and GSS diffusion creep mechanisms. Relations are derived describing a) the rate of new grain “nucleation” due to dislocation creep and associated subgrain rotation occurring in grains of radius  $r$ , and b) the rate of growth/shrinkage of grains of radius  $r$ . Central to obtaining the latter is an equivalent medium approach in which grains of a given size are assumed to be surrounded by a matrix characterized by the average flow stress and free energy. By combining the results for nucleation and growth as a function of  $r$ , the evolution of the entire GSD is determined as a function of time. The evolution of the bulk stress with time is determined by volume averaging the contribution by each grain size. The basic equations used are obtained from a consideration of the microphysical mechanisms operating. However, the complexity of the problem demands a numerical solution. We used a simple finite difference approach and applied it to olivine deformed under lab conditions in order to obtain a first insight into the evolution of GSD and flow stress in this highly relevant Earth material.

Table 2.1 List of symbols used with description and S.I. units

symbol*	description/expression, units
$\bar{D}$	mean recrystallized grain size (diameter), m
$\sigma$	flow stress, MPa
$K_D$	material specific constant in $\sigma$ - $\bar{D}$ relation, m MPa <sup>-m1</sup>
$p$	mechanism specific stress-exponent in $\sigma$ - $\bar{D}$ relation
$\dot{\epsilon}^{diff}$	strain rate governed by diffusion creep, s <sup>-1</sup>
$A(T)$	$T$ -dependent rate-parameter in diffusion creep law, m <sup>m</sup> MPa <sup>-1</sup> s <sup>-1</sup>
$r$	grain radius, m
$m$	grain size exponent in diffusion creep law
$B(T)$	$T$ -dependent rate-parameter in dislocation creep law, MPa <sup>-n</sup> s <sup>-1</sup>
$n$	stress exponent in dislocation creep law
$\dot{\epsilon}^{disl}$	strain rate governed by dislocation creep, s <sup>-1</sup>
$z$	exponent in Avrami-type relation
$\dot{N}$	new grain nucleation rate, s <sup>-1</sup>
$\dot{R}$	grain growth rate, m s <sup>-1</sup>
$\delta r$	discrete grain radius class interval, m
$F(r)$	number density function, m <sup>-1</sup>
$N(r)$	cumulative grain radius distribution function,
$t$	time, s
$N_t$	total number of grains in a distribution
$r_{max}$	maximum grain radius present in a distribution, m
$A(r)$	probability density function
$\sigma_o$	bulk stress for the whole aggregate, MPa
$\dot{\epsilon}_o$	bulk strain rate for the whole aggregate, s <sup>-1</sup>
$\sigma_i$	local stresses for individual grains within the aggregate, MPa
$\dot{\epsilon}_i$	local strain rates for individual grains within the aggregate, s <sup>-1</sup>
$\dot{F}(r, t)$	time-derivative of $F(r)$ , m <sup>-1</sup> s <sup>-1</sup>
$\dot{\epsilon}$	either $\dot{\epsilon}_i$ or $\dot{\epsilon}_o$ , since $\dot{\epsilon}_i = \dot{\epsilon}_o = \dot{\epsilon}$ is assumed, s <sup>-1</sup>
$G(\sigma_i)$	mathematical function used in applying Newton's method to find $\sigma_i$
$dv_f$	volume fraction of grain size interval $dr$
$k_v$	shape factor in the calculation of grain volume
$V_t$	total volume of the grain size distribution
$V_{initial}$	initial total volume of the grain size distribution
$\dot{N}_v$	new grain nucleation rate per volume, m <sup>-3</sup> s <sup>-1</sup>
$N_v$	number of potential nuclei (or subgrains) per volume, m <sup>-3</sup>
$t_c$	the critical time for nucleation to occur, s
$d$	subgrain diameter, m
$K^*$	constant in subgrain size stress relation
$b$	magnitude of the Burgers' vector, m
$\mu$	shear modulus, MPa
$K$	product of $K^* b \mu$ , m MPa
$\theta_c$	critical misorientation angle for nucleation, rad
$\rho$	free dislocation density, m <sup>-2</sup>
$v_d$	velocity of free dislocations, m s <sup>-1</sup>
$J_d$	flux of free dislocations into subgrain walls, m <sup>-1</sup> s <sup>-1</sup>
$J_{dex}$	excess flux of free dislocation into subgrain walls, increasing misorientation, m <sup>-1</sup> s <sup>-1</sup>
$f$	excess fraction of free dislocations
$\theta$	subgrain boundary misorientation, rad
$s$	mean dislocation spacing in a subgrain wall, m
$\dot{\theta}$	misorientation rate of subgrains, rad s <sup>-1</sup>
$\dot{N}_g$	new grain nucleation rate in a single grain, s <sup>-1</sup>
$V_m$	grain mantle volume

## Chapter 2

$\Delta \Phi$	driving force for grain boundary migration, $\text{J m}^{-3}$
$\gamma_{gb}$	specific grain boundary energy, $\text{J m}^{-2}$
$r_{av}$	arithmetic mean grain radius, m
$\gamma_{sg}$	specific subgrain boundary energy, $\text{J m}^{-2}$
$k_a$	shape factor in calculation of grain boundary area
$w$	specific dislocation line energy, $\text{J m}^{-1}$
$\alpha$	dimensionless constant in relation between $w$ , $\mu$ and $b$
$\beta$	dimensionless constant in relation between $\rho$ , $\mu$ and $\sigma$
$E$	Youngs modulus, MPa
$\dot{r}_+$	migration rate of a grain boundary surface, $\text{m s}^{-1}$
$M(T)$	grain boundary mobility, $(\text{m/s}) \cdot (\text{m}^2/\text{N})$
$v(r)$	effective grain growth rate of an individual grain, $\text{m s}^{-1}$
$\dot{r}_-$	individual grain shrinkage rate due to nucleation of new grains, $\text{m s}^{-1}$
$\dot{V}$	rate of change of a grains' volume, $\text{m}^3 \text{s}^{-1}$
$N_i$	Number of grains in a specific grain size interval $r_i$
$N_{LB}$	The number of grains transferred at the <i>lower bound</i> of the interval $dr$ in time $\delta t$
$N_{UB}$	The number of grains transferred at the <i>upper bound</i> of the interval $dr$ in time $\delta t$
$N_{nucl}$	The number of grains introduced into the interval $dr$ due to nucleation in time $\delta t$
$\delta r_p$	discrete grain radius class interval of parent grains producing subgrains of radius $r$ , m
$\delta N_p$	number of parent grains in $\delta r_p$
$\dot{N}_p$	nucleation rate in a parent grain size interval $\delta r_p$ , $\text{s}^{-1}$
$(\dot{N}_g)_p$	new grain nucleation rate in parent grain of radius $r_p$ , $\text{s}^{-1}$
$\sigma_p$	stress in the parent grain(s), MPa
$T_1$	First term in expression for time-derivative of $F(r,t)$ related to $v$
$T_2$	First term in expression for time-derivative of $F(r,t)$ related to $\dot{N}_p$
$\sigma_a$	applied stress, MPa
$\Delta$	dissipation due to internal processes of a system, $\text{J m}^{-3}$
$\Phi$	Helmholtz free energy of a system, $\text{J m}^{-3}$
$\dot{\Delta}$	dissipation rate due to internal processes of a system, $\text{J m}^{-3} \text{s}^{-1}$
$\dot{\Phi}$	rate of change of Helmholtz free energy of a system, $\text{J m}^{-3} \text{s}^{-1}$
$\epsilon_o$	bulk strain
$\tau$	shear stress, MPa
$M_o$	pre-exponential constant in mobility equation, $(\text{m/s}) \cdot (\text{m}^2/\text{N})$
$Q_M$	activation energy in mobility equation, kJ/mol
$Q_{gg}$	activation energy in grain growth law, kJ/mol
$k_o$	pre-exponential constant in grain growth law, $\mu\text{m}^2 \text{s}^{-1}$
$C_{HILL}$	constant (after Hillert, 1965) in grain growth law
$d_g$	arithmetic mean grain diameter, $\mu\text{m}$
$r_v$	antilog of average volume-weighted log grain radius, $\mu\text{m}$
$A_o$	pre-exponential constant in diffusion creep law, $\text{m}^m \text{MPa}^{-1} \text{s}^{-1}$
$B_o$	pre-exponential constant in dislocation creep law, $\text{MPa}^{-n} \text{s}^{-1}$
$Q_A$	activation energy in diffusion creep law, kJ/mol
$Q_B$	activation energy in dislocation creep law, kJ/mol
$\mu_o$	shear modulus at 300 K
$T_m$	forsterite ( $\text{fo}_{100}$ ) melting temperature

\* -  $\Delta \Phi$  subscripts: *gg-*, *sg-*, *disl-*, and *el-* refer to respectively grain boundary surface energy, subgrain stored energy, dislocation stored energy and elastic energy driven grain boundary migration.

- *d* subscripts: *o* and *i* refer to subgrain diameters outside and inside a grain of radius  $r_i$ , respectively.

-  $\dot{V}$  subscripts: + and - refer to grain-volume change due to GBM or grain volume 'eroded' away due to new grain nucleation.

-  $\Delta$  and  $\Phi$  subscripts: *g* and *gb* refer to intragranular (bulk) and grain boundary dissipation or free energy, respectively.

## 2.2 Model development

The present model addresses the evolution of grain size distribution and flow stress with time in a polycrystalline material undergoing dynamic recrystallization during plastic deformation at constant strain rate. All symbols used are defined in Table 2.1.

### 2.2.1 Starting point and principal assumptions

Construction of the microphysical model starts with defining the initial microstructure of the material considered and identifying the physical processes operating in the system. The model considers a polycrystalline aggregate, with an evolving grain size distribution (GSD) represented by a continuous distribution of grain radii  $r$ . At any moment in time, we assume that this GSD can be described by a number density function  $F(r, t) \mid_t = F(r) = \partial N(r) / \partial r$  or by the cumulative grain radius distribution function  $N(r)$  given by:

$$N(r) = \int_0^r F(r) dr \quad (3)$$

The total number of grains in the distribution,  $N_t$ , is given by  $N_t = \int_0^\infty F(r) dr$ , or  $N_t = \int_0^{r_{max}} F(r) dr$  when  $r_{max}$  is the maximum grain size present in a finite sample (see fig. 2.3a). In terms of a conventional probability density function  $A(r)$ , the GSD is given by  $F(r) = N_t A(r)$ . The starting GSD can be of any form, but in practice is assumed to be lognormal and is specified using the conventional mean and standard deviation parameters. Fig. 2.3b shows a schematic 2-D representation of a GSD, described by  $F(r)$  and  $N(r)$ . This illustrates the distinction made in our model between the bulk stress and strain rate for the whole aggregate ( $\sigma_o$  and  $\dot{\epsilon}_o$ , respectively) and the local stresses and strain rates within individual grains in the aggregate ( $\sigma_i$  and  $\dot{\epsilon}_i$ , respectively).

Within the material thus defined, we consider the operation of two independent, parallel deformation mechanisms, i.e. steady state diffusion creep and GSI dislocation (recovery) creep. Diffusion creep is described by the relation:

$$\dot{\epsilon}^{diff} = \frac{A(T)}{r^m} \sigma \quad (4)$$

where  $A(T)$  is a temperature dependent rate-parameter,  $r$  represents the grain radius and  $m$  is a grain size exponent. Dislocation creep is described by the power law relation:

$$\dot{\epsilon}^{disl} = B(T) \sigma^n \quad (5)$$

where  $B(T)$  is a temperature dependent rate-parameter and  $n$  is the stress exponent.

With respect to recrystallization, the following processes are taken into account: a) nucleation by subgrain rotation, and b) GBM driven by grain boundary surface energy and/or grain scale gradients in subgrain stored energy, free dislocation stored energy or elastic stored energy.

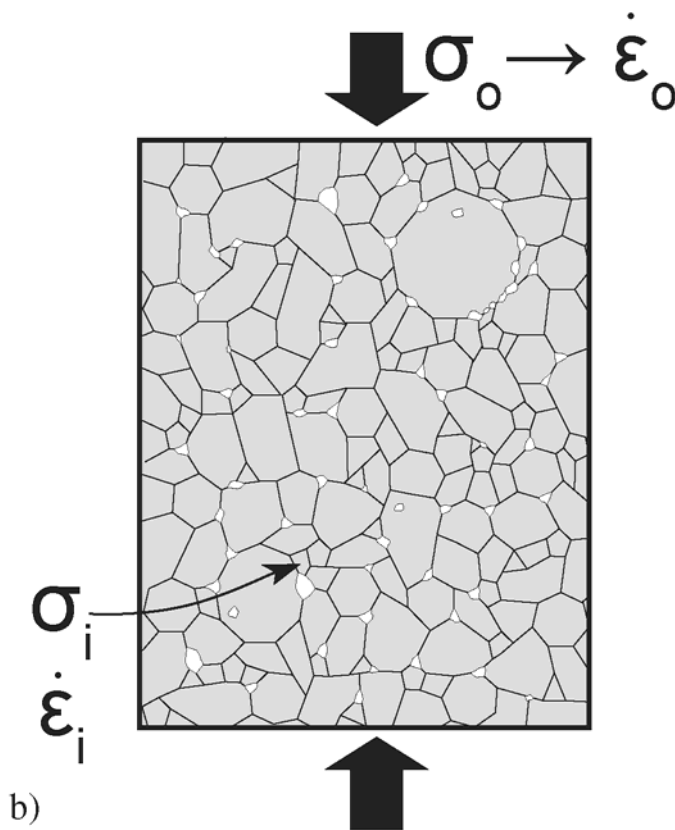
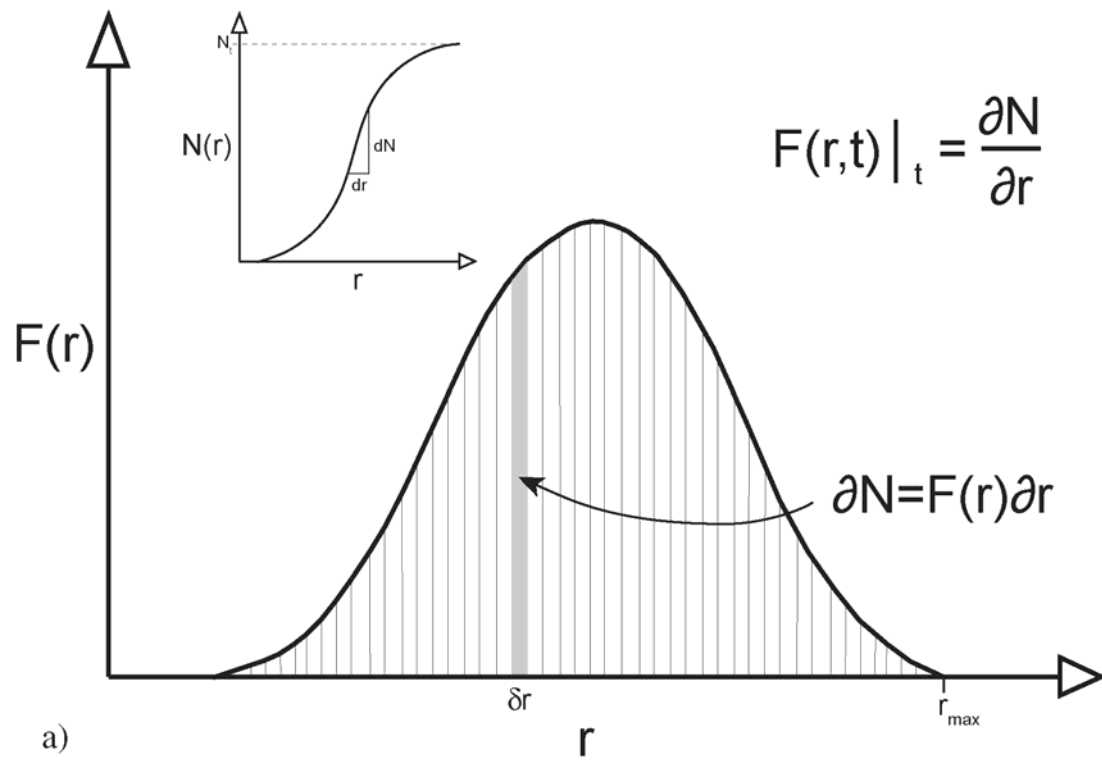


**Figure 2.3.** Model geometry; a) A discrete grain radius distribution  $F(r)$  is considered. Number of grains  $\partial N$  in a particular grain size interval  $\delta r$  is given by  $F(r) \delta r$ . b) Schematic 2-dimensional representation of the model. The model distinguishes between bulk stress and strain rate ( $\sigma_0$  and  $\dot{\epsilon}_0$ , respectively) for the whole sample and local stresses and strain rates ( $\sigma_i$  and  $\dot{\epsilon}_i$ , respectively) experienced by individual grains. Recrystallized grains are white.

In addition, we make the following principal assumptions:

- i) The rheological behaviour of every individual grain size in the distribution  $F(r)$  obeys the steady state flow laws (4)-(5), which implies that the stress varies within the aggregate between grains of different size,
- ii) The bulk behaviour is the volume average of the aggregate,
- iii) The energy jump driving GBM in grains of a given size  $r$  can be approximated by taking the difference between local (grain size specific) and average (bulk material) energy levels, and
- iv) The applied strain rate is homogeneous and constant throughout the aggregate, i.e.  $\dot{\epsilon}_i = \dot{\epsilon}_o$  (see fig. 2.3b).

We justify our use of steady state flow laws under assumption (i) as follows. In the present model, we are concerned with the effects of dynamic recrystallization on microstructural evolution and flow stress over the large strains typically needed to reach a steady state recrystallized grain size, i.e. natural strains in the range 0.5 to 4 (Karato et al., 1980; Pieri et al., 2001; Ter Heege et al., 2002; and Barnhoorn et al., 2004). However, the strains needed to attain steady state flow by dislocation or diffusion creep mechanisms, disregarding dynamic recrystallization, are much smaller, i.e.  $< 0.1$  (McDonnell et al., 1999; Ter Heege et al., 2002). Thus the intergranular flow stress within individual grains can be reasonably approximated by (4) and (5).

To achieve the stated aim of developing a truly dynamic model for dynamic recrystallization, we must now determine how the grain size distribution, described by the number density function  $F(r, t)$ , and the bulk flow stress,  $\sigma_o$ , evolve with time and strain, at a given constant strain rate  $\dot{\epsilon}_o = \dot{\epsilon}_i$ . In the following, we proceed by first obtaining expressions for  $\sigma_i$  and  $\sigma_o$ . We then go on to derive expressions for a) the nucleation rate, b) the absolute grain boundary migration rate and c) the effective grain growth rate. The last is determined by the net result of internal nucleation rate and absolute grain boundary migration rate at any instant within an individual grain of radius  $r$ . The nucleation rate and effective grain growth rate are then used to derive an expression for the change with time of the number density function, i.e. for  $\dot{F}(r, t)$ .

## 2.2.2 Intragranular and bulk stress

### Obtaining $\sigma_i$ as a function of $r$

Having assumed constant homogenous strain rate throughout the whole aggregate and parallel operation of diffusion and dislocation creep in all grains, the strain rate within in each grain,  $\dot{\epsilon}_i = \dot{\epsilon}_o = \dot{\epsilon}$ , is given by the sum of the respective strain rates, so that:

$$\dot{\epsilon} = \frac{A(T)}{r_i^m} \sigma_i + B(T) \sigma_i^n \quad (6)$$

$$\text{or} \quad \frac{A(T)}{r_i^m} \sigma_i + B(T) \sigma_i^n - \dot{\epsilon} = 0 \quad (7)$$

If we now put  $G(\sigma_i)$  equal to the left-hand side of (7), then finding the root of  $G(\sigma_i) = 0$  will give us  $\sigma_i$ . For general values of  $n > 3$ , however, this equation cannot be solved analytically.

In our numerical implementation of the model we therefore obtain the solution for  $\sigma_i$  through application of Newton's method.

#### Obtaining the bulk stress $\sigma_o$ at time $t$

Following Ter Heege et al. (2004) in their analysis of the composite flow behaviour of an aggregate with distributed grain size, we assume that  $\sigma_o$  is equal to the volume-weighted average of  $\sigma_i$  for all grain radii. The stress contribution,  $d\sigma_o$ , of the grain radius interval  $dr$  to the bulk stress is thus given by:

$$d\sigma_o = \sigma_i(r) dv_f \quad (8)$$

where  $dv_f$  is the volume fraction of grains in the grain size interval  $dr$ , and the total bulk stress  $\sigma_o$  in the whole aggregate is given:

$$\sigma_o = \frac{k_v}{V_t} \int_0^{\infty} \sigma_i(r) \cdot F(r) \cdot r^3 dr \quad (9)$$

Here  $k_v$  is a shape factor equal to  $4\pi/3$  assuming spherical grains (grain volume =  $k_v r^3$ ), and  $V_t$  is the total grain aggregate volume. During deformation,  $V_t$  remains constant and is thus equal to the initial total volume  $V_{initial}$ , so that:

$$V_t = \int_0^{\infty} dV = k_v \int_0^{\infty} F(r) \cdot r^3 dr = \text{constant} = V_{initial} \quad (10)$$

### 2.2.3 Nucleation rate in grains of size $r$

Following Shimizu (1998), the nucleation rate, i.e. the number of new grain nucleation events occurring per volume of a given grain in unit time,  $\dot{N}_v$ , can be approximated as:

$$\dot{N}_v = \frac{N_v}{t_c} \quad (11)$$

where  $N_v$  is the number of potential nuclei that can form in the grain by subgrain rotation per unit volume and  $t_c$  is the critical time for subgrains to rotate to the point that new, high angle grain boundaries form – i.e. the time for pervasive nucleation.

#### Grain volume nucleation

Assuming homogeneous nucleation from subgrains throughout the volume of a given grain,  $N_v$  can be described as the reciprocal of the subgrain volume. Approximating the subgrains and nuclei as spherical in shape thus yields:

$$N_v = \frac{1}{k_v (d/2)^3} = \frac{8}{k_v d^3} \quad (12)$$

where  $d$  is the subgrain diameter. Now, it is well established from experiments that subgrain diameter is inversely related to flow stress in a wide range of materials undergoing



deformation by dislocation creep (Takeuchi and Argon, 1976; Twiss, 1977; Ross et al., 1980; Karato et al. 1980; Raj and Pharr, 1986; Carter et al., 1982). Takeuchi and Argon (1976) expressed this relationship between subgrain size (diameter) and stress in the form:

$$d = \frac{K^* b \mu}{\sigma} = \frac{K}{\sigma} \quad (13)$$

where  $K^*$  is a constant of order 10-100,  $b$  is the magnitude of the Burgers' vector of principle dislocations,  $\mu$  is the shear modulus of the material and the constant  $K$  substitutes for the product  $K^* b \mu$ . Substitution of (13) into (12) now gives:

$$N_v = \frac{8\sigma^3}{k_v K^3} \quad (14)$$

An expression for  $t_c$  must now be derived. Since we assume subgrain rotation to be the nucleation mechanism,  $t_c$  can be thought of as the time taken to reach a critical misorientation angle  $\theta_c$  at which a subgrain boundary becomes a high angle boundary. Using Orowan's equation, the strain rate within a grain due to dislocation creep can be described:

$$\dot{\varepsilon}^{disl} = \rho \cdot b \cdot v_d \quad (15)$$

where  $\rho$  is the mobile dislocation density and  $v_d$  is the mean velocity of these free dislocations. Assuming a dislocation creep process in which subgrain walls are both the principle glide barriers and are the main annihilation sites for dislocations of opposite sign (Burton 1972, Blum 1982), then the strain rate component accommodated by dislocation creep is associated with a flux,  $J_d$ , of free dislocations into subgrain walls (or subgrain boundaries). Following Edward et al. (1982), this flux of free dislocations (i.e. total free dislocation length) entering the unit area of subgrain boundary per unit time, is given:

$$J_d = \rho \cdot v_d \quad (16)$$

A large proportion of the free dislocations annihilate when entering the subgrain boundary, through climb towards dislocations of opposite sign that enter the boundary from the other side. However, a small 'excess' fraction  $f$  of geometrically necessary dislocations of one sign will generally enter the boundary, thus contributing to ongoing misorientation of the subgrain boundary. The excess flux of dislocations entering an individual sub-boundary  $J_{dex}$  can hence be described by:

$$J_{dex} = f \cdot \rho \cdot v_d \quad (17)$$

where  $f$  is assumed constant (Edward et al., 1982). Combining this with relation (5) for dislocation creep and Orowan's equation (15) gives:

$$J_{dex} = f \cdot \frac{B(T)\sigma^n}{b} \quad (18)$$

which now describes the line length of dislocations accumulating per unit area of subgrain wall per second. From the relation for sub-boundary misorientation  $\theta = b \cdot s^{-1}$ , where  $s$  is the

mean dislocation spacing (e.g. Hull and Bacon 1984), it is seen that  $\dot{\theta} = b \cdot d(s^{-1})/dt$ . In the present case, the rate of change of  $s^{-1}$ , i.e.  $d(s^{-1})/dt$  is exactly equal to  $J_{dex}$ , so we may write  $\dot{\theta} = b \cdot J_{dex}$ . At the same time the misorientation rate  $\dot{\theta}$  can be approximated (Shimizu 1998) using:

$$\dot{\theta} = \frac{\theta_c}{t_c} \quad (19)$$

where  $\theta_c$  is the critical misorientation at which a subboundary becomes a high angle grain boundary. We thus obtain the relation:

$$J_{dex} = \frac{\dot{\theta}}{b} = \frac{\theta_c}{t_c \cdot b} \quad (20)$$

which on combining with (18) gives:

$$t_c = \frac{\theta_c}{f \cdot B(T) \cdot \sigma^n} \quad (21)$$

Putting the above relations for  $N_v$  (eq. 14) and  $t_c$  into relation (11) now gives:

$$\dot{N}_v = \frac{8fB(T)\sigma^{n+3}}{K^3\theta_c k_v} \quad (22)$$

Finally, we can derive an expression for the volume nucleation rate in a grain of size  $r$ ,  $\dot{N}_g$ , by multiplying  $\dot{N}_v$  by the grain volume, yielding:

$$\dot{N}_g = \frac{8fB(T)\sigma^{n+3}}{K^3\theta_c k_v} \cdot k_v r^3 = \left[ \frac{8f}{K^3\theta_c} \right] \cdot B(T) \cdot \sigma^{n+3} \cdot r^3 \quad (23)$$

### Grain boundary nucleation

If nucleation by subgrain rotation only occurs adjacent to grain boundaries,  $\dot{N}_g$  must be obtained slightly differently (see also Shimizu 1998). Considering a single grain, the volume in which potential nuclei form reduces to the grain mantle volume adjacent to the grain boundary. A given grain with radius  $r$  will have a grain mantle volume,  $V_m$ , given approximately by the difference between the grain volume minus the volume of a sphere with radius  $(r - d)$ . Recalling that  $d$  is the internal subgrain diameter, and  $k_v$  is a shape factor ( $\sim 4/3\pi$ ), we thus have:

$$V_m = k_v r^3 - k_v (r - d)^3 \quad (24)$$

The number of subgrains forming per grain,  $N_g$ , is then given by the ratio of the grain mantle volume to the subgrain volume:

$$N_g = \frac{k_v r^3 - k_v (r-d)^3}{k_v (d/2)^3} = \frac{8 \cdot (d^3 + 3r^2 - 3rd^2)}{d^3} \quad (25)$$

As for the case of grain volume nucleation, we finally arrive at an expression for the grain boundary nucleation rate in a grain of size  $r$  through division of (25) by  $t_c$  as given by (21). Substituting for  $d$  using (13), then gives:

$$\dot{N}_g = \frac{N_g}{t_c} = \left[ \frac{24f}{K^2 \theta_c} \right] \cdot B(T) \cdot \sigma^{n+2} \cdot \left[ r^2 - \frac{K}{\sigma} r \right] \quad (26)$$

#### Constraints on nucleation rates

The above expressions for  $\dot{N}_g$  apply for grains that are larger than the internally growing subgrains. i.e. when  $2r > d$ . When  $2r \leq d$  subgrains will not form and  $\dot{N}_g = 0$ . This point is addressed in detail in Appendix A.

### 2.2.4 Grain boundary migration rate in grains of size $r$

#### Driving forces for GBM

We consider GBM to be driven by several driving forces. Within a grain aggregate, the grain boundary surface energy causes a significant driving force,  $\Delta\Phi_{gg}$ , for GBM leading to net grain growth, usually referred to normal grain growth under static conditions (e.g. Burke and Turnbull, 1952; Evans et al., 2001). Further driving forces are caused by grain-to-grain jumps or gradients in the free energy of the solid phase. In line with the assumptions stated earlier, we approximate these jumps for individual grains by assuming that the surrounding grains are on average characterized by the bulk sample stress,  $\sigma_o$ , the corresponding bulk free energy and the mean grain size. The free energy differences considered as driving forces for GBM are the subgrain-stored energy,  $\Delta\Phi_{sg}$ , the free dislocation stored energy,  $\Delta\Phi_{disl}$ , and the elastic stored energy,  $\Delta\Phi_{el}$ . All driving forces have units of  $J/m^3$  here. The total driving force for GBM of an individual grain is then given by the sum of the individual driving forces mentioned above, such that:

$$\Delta\Phi_t = \Delta\Phi_{gg} + \Delta\Phi_{sg} + \Delta\Phi_{disl} + \Delta\Phi_{el} \quad (27)$$

Note that it depends on state of the grain relative to the average bulk environment, whether the total driving force is positive or negative, thus causing net growth or shrinkage. Note also that  $\Delta\Phi_t$  can in principle be dominated by any of the terms in (27).

We follow the formulation of Hillert (1965) for describing the driving force for surface energy driven GBM, so that:

$$\Delta\Phi_{gg} = \gamma_{gb} \left( \frac{1}{r_{av}} - \frac{1}{r} \right) \quad (28)$$

where  $r_{av}$  is the arithmetic mean grain radius and  $\gamma_{gb}$  is the specific grain boundary energy in  $J/m^2$ . This formulation means that grains bigger than the average grain size ( $r > r_{av}$ ) grow, while grains smaller than the average grain size ( $r < r_{av}$ ) shrink. The driving force related to

jumps in subgrain-stored energy is given by the difference between the energy outside,  $o$ , and inside,  $i$ , a specific grain. Hence we obtain for the subgrain related driving force:

$$\Delta\Phi_{sg} = \left[ \frac{k_a \gamma_{sg}}{k_v d_o} \right] - \left[ \frac{k_a \gamma_{sg}}{k_v d_i} \right] \quad (29)$$

where  $\gamma_{sg}$  is the average specific energy of subgrain walls/boundaries [ $\text{J}/\text{m}^2$ ],  $k_a$  is a geometric area factor equal to  $4\pi$  for spherical subgrains and  $d_i$  is the subgrain diameter inside a grain of radius  $r$ . Using the relation of Takeuchi and Argon (1976) (13) to substitute for the subgrain sizes  $d_o$  and  $d_i$ , relation (29) can hence be rewritten as:

$$\Delta\Phi_{sg} = \frac{3\gamma_{sg}}{K} [\sigma_o - \sigma_i] \quad (30)$$

where it is assumed that the subgrains can be approximated as having a spherical shape, and that the average subgrain diameter outside a grain of radius  $r_i$  can be approximated using the bulk stress,  $\sigma_o$ , in relation (13). Moving on to the driving force for GBM due to a jump in mobile dislocation stored energy this is proportional to the product of the specific line energy of the dislocations,  $w$ , and the difference in mobile dislocation density across the grain boundary,  $\Delta\rho$ . It is accordingly approximated by the relation:

$$\Delta\Phi_{disl} = w \cdot \Delta\rho = \frac{\alpha \cdot \beta}{\mu} [\sigma_o^2 - \sigma_i^2] \quad (31)$$

where  $w = \alpha\mu b^2$ ,  $\Delta\rho = (\beta/\mu^2 b^2) \cdot (\sigma_o^2 - \sigma_i^2)$  and  $\alpha$  and  $\beta$  are constants (Hull and Bacon, 1984; Hirth and Lothe, 1982; Humphries and Hatherly, 1996). Lastly, assuming axially symmetric loading of the bulk sample, the driving force related to a difference in elastic stored energy outside and inside an individual grain is given by a relation quite similar to (31):

$$\Delta\Phi_{el} = \frac{1}{2E} [\sigma_o^2 - \sigma_i^2] \quad (32)$$

where  $E$  is the mean Young's modulus for the polycrystalline material.

#### Migration rate and effective migration rate

It is well established that at any instant the migration rate of a grain boundary,  $\dot{r}_+$ , is proportional to the product of a mobility term  $M(T)$  and the driving force  $\Delta\Phi$ . Hence, here we can describe  $\dot{r}_+$  as:

$$\dot{r}_+ = M(T) \cdot \Delta\Phi_t \quad (33)$$

Note that  $\dot{r}_+$  can be positive or negative, depending on the total driving force, causing either net grain growth or shrinkage, respectively. However, in a grain within which new grains are nucleating by the assumed mechanism of subgrain rotation, the effective migration rate must also account for the "erosion" of the host or parent grain by the nucleation process. Considering an individual grain, the effective grain growth rate,  $v$ , resulting from combined effects of the GBM and new grain nucleation is therefore given as:

$$v = \dot{r}_+ - \dot{r}_- \quad (34)$$

where  $\dot{r}_-$  is the grain shrinkage rate due to nucleation of new grains. To evaluate  $v$ , consider the rate of change of grain volume,  $\dot{Y}$ , given by the difference between  $\dot{Y}_+$ , i.e. the rate of volume change due to true GBM, and  $\dot{Y}_-$ , i.e. the volume eroded away due to nucleation at the rate  $\dot{N}_g$ . This can be expressed as

$$\dot{Y} = \dot{Y}_+ - \dot{Y}_- \approx k_a r^2 \cdot v = 3k_v r^2 \cdot v \quad (35)$$

where

$$\dot{Y}_+ = k_a r^2 \dot{r}_+ = 3k_v r^2 \dot{r}_+ = 3k_v r^2 \cdot M(T) \cdot \Delta\Phi_t \quad (36)$$

and

$$\dot{Y}_- = \dot{N}_g \cdot k_v \left( \frac{d}{2} \right)^3 = \dot{N}_g \cdot k_v \frac{K^3}{8\sigma_i^3} \quad (37)$$

Hence according to (35)

$$v = M(T) \cdot \Delta\Phi_t - \frac{\dot{N}_g K^3}{24r^2 \sigma_i^3} \quad (38)$$

Relation (38) applies to both expressions for  $\dot{N}_g$ , considering grain volume nucleation (23), or grain boundary nucleation (26).

### 2.2.5 Determining $\dot{F}(r,t)$

With the above expression for the effective grain growth rate,  $v$  (38), and the nucleation rate per grain,  $\dot{N}_g$ , we are able to derive an expression for the rate of change of the number density function  $F(r,t)$ , i.e. for  $\dot{F}(r,t)$ . With reference to fig. 2.3a, consider a given grain size interval  $\delta r$  at a given instant. The number of grains in this interval is

$$N_i = \delta N = F(r) \cdot \delta r \quad (39)$$

The number of grains entering the interval in a time increment  $\delta t$  at the lower bound of the interval  $\delta r$ , due to growth at the effective velocity  $v$ , is given by

$$N_{LB} = F(r) \cdot v(r) \cdot \delta t = J(r) \cdot \delta t = J \delta t \quad (40)$$

where  $J(r) = J$  simply substitutes for  $F(r) \cdot v(r)$ . The number of grains leaving the interval in a time increment  $\delta t$  at the upper bound of the interval  $\delta r$ , due to growth at effective velocity  $v$ , is given by

$$N_{UB} = F(r + \delta r) \cdot v(r + \delta r) \cdot \delta t = J(r + \delta r) \cdot \delta t = (J + \delta J) \cdot \delta t \quad (41)$$

Turning to the effects of new grain nucleation, the number of grains of radius  $r$  introduced into the interval  $\delta r$  due to nucleation from subgrains of size  $d = 2r$  developed within the parent grains (radius  $r_p$ ), in time  $\delta t$  is expressed as

$$N_{nucl} = \dot{N}_p(r) \delta t = \left( \dot{N}_g \right)_p \delta N_p \delta t \quad (42)$$

where  $\dot{N}_p(r)$  is the nucleation rate (number per sec) in the parent grain size interval  $\delta r_p$ ,  $\left( \dot{N}_g \right)_p$  is the nucleation rate per parent grain and  $\delta N_p$  is the number of parent grains in  $\delta r_p$  ( $\neq \delta r$ ). We can now write for the total change in the number of grains in the interval  $\delta r$  in time  $\delta t$ :

$$\delta N = N_{LB} - N_{UB} + N_{nucl} \quad (43)$$

which on substituting for  $N_{LB}$ ,  $N_{UB}$  and  $N_{nucl}$  using (40)-(42) gives:

$$\delta N = J \delta t - (J \delta t + \delta J \delta t) + \dot{N}_p \delta t = -\delta J \delta t + \dot{N}_p \delta t \quad (44)$$

The change in number density of grains in the interval  $\delta r$  in time  $\delta t$  is hence:

$$\frac{\delta N}{\delta r} = \delta F = -\frac{\delta J}{\delta r} \delta t + \frac{\dot{N}_p}{\delta r} \delta t \quad (45)$$

which leads to the result:

$$\frac{\delta F}{\delta t} = -\frac{\delta J}{\delta r} + \frac{\left( \dot{N}_g \right)_p}{\delta r} \delta N_p \quad (46)$$

In the limit that  $\delta t$  and  $\delta r$  approach zero, this yields:

$$\frac{\partial F}{\partial t} = \dot{F}(r, t) = -\frac{\partial J}{\partial r} + \left( \dot{N}_g \right)_p \cdot \frac{\partial N_p}{\partial r} \quad (47)$$

and hence

$$\dot{F}(r, t) = -\frac{\partial(Fv)}{\partial r} + \left( \dot{N}_g \right)_p \cdot \frac{\partial N_p}{\partial r} \quad (48)$$

In equation (48), let the first term on the right hand side be  $T_1$  and the second be  $T_2$ . Using the product-rule  $T_1$  can be written as:

$$T_1 = -\left[ \frac{F \partial v}{\partial r} + \frac{v \partial F}{\partial r} \right] \quad (49)$$

Note that this term is equivalent to the continuity equation derived by Hillert (1965) in his analysis of normal grain growth, but accounts for grain erosion as well as GBM through the appearance of  $v$  instead of  $\dot{r}_+$ . The term  $T_2 = (\dot{N}_g)_p \cdot \partial N_p / \partial r$  represents the rate of appearance of new grains of size  $r$  due to nucleation in the corresponding parent grains.

### Evaluating $T_2$ for volume nucleation in parent grains

#### (1) Obtaining $(\dot{N}_g)_p$

First, it is crucial to note that  $\delta r_p$  is not equal to  $\delta r$ . Let stress in the parent grains of radius  $r_p$  be  $\sigma_p$ . Then, assuming volume nucleation (23), we can write the number of nucleation events per parent grain per second,  $(\dot{N}_g)_p$ , as:

$$(\dot{N}_g)_p = \left[ \frac{8f}{K^3 \theta_c} \right] \cdot B(T) \cdot \sigma_p^{n+3} \cdot r_p^3 \quad (50)$$

New grains of size  $r$  originate from subgrains of diameter  $d = 2r$  in the parent grains. Using the Takeuchi and Argon subgrain versus stress relation (13), this implies that the stress in the parent grains is:

$$\sigma_p = \frac{K}{2r} \quad (51)$$

Substituting  $\sigma_p$  and  $r_p$  into our assumed composite flow law (6) gives:

$$\dot{\epsilon} = \frac{A(T)}{r_p^m} \sigma_p + B(T) \sigma_p^n \quad (52)$$

and in turn using the right-hand side of (51) to eliminate for  $\sigma_p$ , now allows us to derive the following expression for  $r_p$  as a function of  $r$ :

$$r_p = \left[ \frac{(2r)^{n-1} \cdot A(T) \cdot K}{(2r)^n \cdot \dot{\epsilon} - B(T) \cdot K^n} \right]^{1/m} \quad (53)$$

Similarly we can write  $(\dot{N}_g)_p$  as a function of  $r$  through substitution of the right-hand sides of (51) and (53) into relation (50). This gives:

$$(\dot{N}_g)_p = \left[ \frac{8f}{K^3 \theta_c} \right] \cdot \frac{B(T) \cdot K^{n+3}}{(2r)^{n+3}} \cdot \left[ \frac{(2r)^{n-1} \cdot A(T) \cdot K}{(2r)^n \cdot \dot{\epsilon} - B(T) \cdot K^n} \right]^{3/m} \quad (54)$$

#### (2) Obtaining $\frac{\partial N_p}{\partial r}$

Recalling that  $\delta N_p$  is the number of parent grains in the parent radius interval  $\delta r_p$ , from the definition of  $F$  ( $F|_t = \delta N / \delta r$ ) we can write:

$$\delta N_p = F(r_p) \cdot \delta r_p \quad (55)$$

It follows that

$$\frac{\delta N_p}{\delta r} = F(r_p) \cdot \frac{\delta r_p}{\delta r} \quad (56)$$

and in the limit  $\delta r, \delta r_p \rightarrow 0$  at  $t$  is constant, that

$$\frac{\partial N_p}{\partial r} = F(r_p) \cdot \frac{\partial r_p}{\partial r} \quad (57)$$

Combing the relation  $T_2 = (\dot{N}_g)_p \cdot \partial N_p / \partial r$  with (54) and (57) now results in the following expression for  $T_2$  when volume nucleation is responsible for new grain production:

$$T_2 = \left[ \frac{8f}{K^3 \theta_c} \right] \cdot \frac{B(T) \cdot K^{n+3}}{(2r)^{n+3}} \cdot \left[ \frac{(2r)^{n-1} \cdot A(T) \cdot K}{(2r)^n \cdot \dot{\epsilon} - B(T) \cdot K^n} \right]^{3/m} \cdot F(r_p) \cdot \frac{\partial r_p}{\partial r} \quad (58)$$

Here, the change in parent grain size with changing ‘daughter’ grain size, i.e.  $\partial r_p / \partial r$ , remains to be evaluated. Using relation (53), we can rewrite  $r_p$  as:

$$r_p = \left[ \frac{ar^{n-1}}{br^n - c} \right]^{1/m} = [x]^{1/m} \quad (59)$$

where  $a = 2^{n-1} \cdot A(T) \cdot K$ ,  $b = 2^n \cdot \dot{\epsilon}$ ,  $c = B(T) \cdot K^n$ , and  $x = (ar^{n-1}) / (br^n - c)$

Now, using

$$\frac{\partial r_p}{\partial r} = \frac{\partial r_p}{\partial x} \cdot \frac{\partial x}{\partial r} \quad (60)$$

we obtain

$$\frac{\partial r_p}{\partial r} = \frac{1}{m} \left[ \frac{br^n - c}{ar^{n-1}} \right]^{\frac{m-1}{m}} \cdot \left[ \frac{ar^{n-2} [c(1-n) - br^n]}{(br^n - c)^2} \right] \quad (61)$$

By combining this with relations (48), (49) and (58) we now have arrived at a full description of  $\dot{F}(r, t)$  for the case of grain volume nucleation.

### Evaluating $T_2$ for grain boundary nucleation in parent grains



In this case, recalling relation (26) for the rate of grain boundary nucleation events  $\dot{N}_g$  in an individual grain of radius  $r$ , we can write the nucleation rate per parent grain,  $(\dot{N}_g)_p$ , as:

$$(\dot{N}_g)_p = \left[ \frac{24f}{K^2\theta_c} \right] \cdot B(T) \cdot \sigma_p^{n+2} \cdot \left[ r_p^2 - \frac{K}{\sigma_p} r_p \right] \quad (62)$$

Using relations (51) and (53), for  $\sigma_p$  and  $r_p$  now gives:

$$(\dot{N}_g)_p = \left[ \frac{24f}{K^2\theta_c} \right] \cdot \frac{B(T) \cdot K^{n+2}}{(2r)^{n+2}} \cdot \left\langle \left[ \frac{(2r)^{n-1} \cdot A(T) \cdot K}{(2r)^n \cdot \dot{\epsilon} - B(T) \cdot K^n} \right]^{2/m} - 2r \cdot \left[ \frac{(2r)^{n-1} \cdot A(T) \cdot K}{(2r)^n \cdot \dot{\epsilon} - B(T) \cdot K^n} \right]^{1/m} \right\rangle \quad (63)$$

Which provides the first factor in the term  $T_2$  for grain boundary nucleation. The remaining factor  $\partial N_p / \partial r = F(r_p) \partial r_p / \partial r$  is as for volume nucleation. Hence combining relations (48), (57) and (63),  $T_2$  for grain boundary nucleation becomes:

$$T_2 = \left[ \frac{24f}{K^2\theta_c} \right] \cdot \frac{B(T) \cdot K^{n+2}}{(2r)^{n+2}} \cdot \left\langle \left[ \frac{(2r)^{n-1} \cdot A(T) \cdot K}{(2r)^n \cdot \dot{\epsilon} - B(T) \cdot K^n} \right]^{2/m} - 2r \cdot \left[ \frac{(2r)^{n-1} \cdot A(T) \cdot K}{(2r)^n \cdot \dot{\epsilon} - B(T) \cdot K^n} \right]^{1/m} \right\rangle \cdot F(r_p) \cdot \frac{\partial r_p}{\partial r} \quad (64)$$

where  $\partial r_p / \partial r$ , is given by (61). Combining relations (48), (49), (61) and (64) accordingly results in a full description of  $\dot{F}(r, t)$  for the case of grain boundary nucleation.

### Constraints on new grain production rate

Several extra constraints apply to nucleation rates in parent grains. As mentioned previously, formation of subgrains, hence new grains that are larger than their parent grains, is not possible, so that  $(\dot{N}_g)_p = 0$  under these conditions. Similarly it is impossible to form new grains that are smaller than the subgrains produced in the largest (parent) grains present in the aggregate ( $r_p \rightarrow \infty$ ). These constraints are addressed in detail in Appendix A.

### 2.2.6 Calculation of $F(r)$ and $\sigma_0$ as a function of time

Assuming that  $F(r)$  is continuous, we now have the necessary expressions for  $\sigma_0$  and  $\dot{F}(r, t)$ , given by relations (12) and (48) respectively, to evaluate the variation of  $\sigma_0$  and  $F(r)$  with time. The number density distribution  $F(r, t)$  can be found through integration of its derivative:

$$F(r, t) = \int_0^t \dot{F}(r, t) dt \quad (65)$$

However, since both  $\dot{F}(r, t)$  and  $F(r, t)$  are complex functions of time, an analytical solution for  $F(r, t)$  is not feasible and (65) must be solved numerically.

### 2.2.7 Mass and energy conservation

The present model addresses the evolution of grain size distribution in a polycrystalline solid to which no mass or volume is added or subtracted during deformation. However, the model so far does not intrinsically include this constraint, and the effective growth process will in general lead to changes in grain size that do not conserve mass. Hillert (1965) faced an identical problem in his analysis of normal grain growth and pointed out that the evolution of the grain size distribution due to surface energy reduction must be subject to additional constraints on growth geometry and topology, and hence velocity, to conserve mass. For the relatively simple case of normal grain growth, Hillert used similarity arguments to formulate exact constraints on grain size distribution evolution that satisfied mass conservation. For our more general case, such an approach does not seem possible. Therefore we apply the simplest possible correction to  $\dot{r}_+$  for each grain size to ensure that mass is conserved. This involves adjusting  $\dot{r}_+$  so that the rate of change of volume of all grains is modified in inverse proportion to the uncorrected volume change rate ( $\dot{V}/V_t$ ) for the bulk material. For normal grain growth this approach yields results that are closely similar to Hillert's predictions.

Turning now to energy conservation, our analysis so far has allowed us to determine the evolution of the bulk flow stress,  $\sigma_0$ , as a function of time and strain, at the imposed strain rate  $\dot{\epsilon}_0$ . We have tacitly assumed that the applied stress,  $\sigma_a$ , equals the bulk stress,  $\sigma_0$ . However, this neglects the work that must be done by the applied stress to bring about changes in microstructural state during deformation, and so will not be strictly correct (except at true mechanical AND microstructural steady state). To obtain a general expression for the applied stress,  $\sigma_a$ , valid for large strain flow involving microstructural evolution, we must consider the combined energy and entropy balance for a deforming system at constant mass. This exercise has been performed for a deforming porous medium by Lehner (1990). Applying Lehner's result, and removing the terms related to porosity change yields the following expression:

$$\sigma_a \dot{\epsilon}_0 = \dot{\Phi} + \dot{\Delta} \quad (66)$$

where  $\dot{\Phi}$  is the rate of change of Helmholtz free energy and  $\dot{\Delta}$  is the energy dissipation rate due to internal irreversible processes. This equation is simply a statement of the fact that under conditions of constant temperature and mass, the mechanical work done in deforming a system ( $\sigma_a \dot{\epsilon}_0$ ) is partly stored in the form of free energy ( $\dot{\Phi}$ ), reflecting microstructural changes, and partly dissipated as heat ( $\dot{\Delta}$ ) through the operation of microscale deformation processes. Now for a deforming polycrystalline solid,  $\dot{\Phi}$  can be written as:

$$\dot{\Phi} = \dot{\Phi}_g + \dot{\Phi}_{gb} \quad (67)$$

where  $\dot{\Phi}_g$  is the rate of change of free energy due to changes in free energy of the intragranular solid phase, and  $\dot{\Phi}_{gb}$  is the rate of change of free energy due to changes in grain boundary configuration. Similarly  $\dot{\Delta}$  can be expressed as:

$$\dot{\Delta} = \dot{\Delta}_g + \dot{\Delta}_{gb} \quad (68)$$

where  $\dot{\Delta}_g$  and  $\dot{\Delta}_{gb}$  are the dissipation rates due to irreversible processes in the solid grain volume and the grain boundaries, respectively. Hence, the energy/entropy balance for a deforming dense polycrystal fully written out, gives:

$$\sigma_a \dot{\varepsilon}_o = \dot{\Phi}_g + \dot{\Phi}_{gb} + \dot{\Delta}_g + \dot{\Delta}_{gb} \quad (69)$$

or

$$\sigma_a = \frac{d\Phi_g}{d\varepsilon_o} + \frac{d\Phi_{gb}}{d\varepsilon_o} + \frac{d\Delta_g}{d\varepsilon_o} + \frac{d\Delta_{gb}}{d\varepsilon_o} \quad (70)$$

Terms 1, 2 and 4 on the right hand side of (69) and (70) are not yet incorporated in the model for evaluating  $\sigma_a$ . However, the magnitude of these terms is small and term 3 which accounts for the dissipation due to straining  $d\Delta_g/d\varepsilon_o (= \sigma_o)$  overwhelmingly dominates the value of  $\sigma_a$  compared to the other terms. In other words, our tacit assumption that  $\sigma_a = \sigma_o$  is a good approximation for the present stage of model development.

## 2.3 Numerical implementation

We have derived equations that describe the bulk stress as well as the local state of stress in grains of any size  $r$ , in a polycrystalline material with distributed grain size, during deformation controlled by combined dislocation GSI and diffusion GSS creep. Homogeneous strain rate is assumed and the bulk stress is taken as the volume average of the grain scale stress states. In addition, we have formulated equations describing the new grain nucleation rate within, and effective grain growth rate (i.e. net shrinkage or net growth) of, grains of a particular radius. Further, we have derived a ‘‘continuity equation’’ that describes the change in GSD in terms of the time derivative of the number density function  $F$ . However, the number density function, its derivative, and indeed the entire system of equations obtained, are complex functions that cannot be solved analytically. We have therefore implemented a numerical approach in order to solve for the change in GSD and flow stress as a function of time.

Our numerical implementation consists of a FORTRAN 77 programme (UTREX) embodying a series of finite difference algorithms. Material parameters (creep law parameters, microscale parameters etc.) are input in the form of a dedicated file for specific temperature conditions. To describe the GSD we consider a discrete grain size distribution with a finite total number of grains  $N_t$  (initially set at  $10^6$ ), distributed in grain radius intervals of fixed width. A lognormal grain size distribution is used as input at  $t = 0$ . The initial lognormal mean radius, standard deviation, grain radius range and number of grain radius

intervals can be set as desired when initializing a given run. Typically, 1000 grain radius intervals are chosen in discretizing the grain size distribution.

For a given material, given initial GSD and constant temperature and strain rate conditions, the program first evaluates the sample volume, and then computes the following time-independent quantities per grain size interval:

- The intragranular stress,  $\sigma_i$ , calculated from equation (7) using Newton's method.
- The nucleation rate per grain,  $\dot{N}_g$ , from (23) and (26).
- The parent grain radius interval  $r_p$  from (53) accounting for constraints in Appendix A.
- The nucleation rate per parent grains  $(\dot{N}_g)_p$  from (54).
- The change in parent grain size with changing daughter grain size,  $\partial r_p / \partial r$ , from (61).

A time/strain loop is subsequently initiated, whereby the following quantities are computed per grain size interval in each time step:

- Total nucleation rate, i.e.  $\dot{N}_g$  times the number of grains in the grain size interval.
- Driving force for grain boundary migration,  $\Delta\Phi_i$ , from equation (27)-(32)
- Migration and effective migration rates, i.e.  $\dot{r}_+$  and  $v$ , respectively from (33) and (38).

The rate of change of the number density function  $F(r,t)$  per grain size interval is obtained from equation (48) and (57) by numerically determining the terms  $d(Fv)/dr$  and  $F(r_p)$  using finite difference approximations. The evolution of  $F$  per timestep ( $j$ ) is obtained by numerically integrating equation (65), i.e. by evaluating the expression:

$$F = F_0 + \sum_j \dot{F}_j \Delta t \quad (71)$$

for each grain radius interval. The evolution of the bulk stress  $\sigma_0$  per time step is obtained by numerically evaluating equation (9), i.e. by performing the summation:

$$\sigma_0 = \frac{k_v}{V_t} \sum_i \sigma_i F_i r_i^3 \quad (72)$$

across the entire GSD.

## 2.4 Application to olivine

We will now explore the effects of individual and combined recrystallization processes with or without deformation, focusing on polycrystalline olivine. First the chosen GSD's and material-dependent parameters for olivine are clarified. Then we discuss the predicted evolution of GSD and mean grain size during surface energy driven grain growth. Comparison of this modeled grain growth with experimental grain growth data for olivine (Karato, 1989) allow us to benchmark the model's grain boundary migration kinetics. Finally, simulation of dynamic recrystallization is examined and implications are discussed, focusing on grain boundary nucleation by subgrain rotation and grain boundary migration driven by gradients in both grain boundary surface energy and subgrain energy. Note that in these preliminary recrystallization tests we have chosen not to include grain volume nucleation or GBM driven by gradients in free dislocation or elastic energy. The model as it is set up allows one to explore numerous combinations of processes and driving forces. However, the main objective of the few recrystallization tests reported here, is to get a first impression of

the models' behaviour at a selected set of conditions for which experimental observations/data exist.

### 2.4.1 Choice of initial GSD and input parameters

In case of static grain growth tests a single starting mean radius was used of 10  $\mu\text{m}$ . In order to start deformation in either the GSS or the GSI creep field, the value for the starting mean radius was varied in the range 1.5 to 150  $\mu\text{m}$ , in case of dynamic recrystallization tests. For all tests simulating static grain growth and most tests simulating dynamic recrystallization the initial standard deviation and grain radius range were kept constant at 0.3 and 0 to 250  $\mu\text{m}$ , respectively. Here, the dynamic recrystallization tests at the minimum (1.5  $\mu\text{m}$ ) and maximum (150  $\mu\text{m}$ ) starting mean radius form an exception, since for these tests the range in grain radii was 0 to 180 and 0 to 500  $\mu\text{m}$ , respectively. Size/volume of the initial GSD's was chosen close to the scale of material samples used in deformation experiments. For example, an initial GSD for a dynamic recrystallization test, where we used a log normal distribution with mean radius of 75.0  $\mu\text{m}$  this results in a discrete GSD with a total sample volume  $V_i$  of about 2.6  $\text{cm}^3$ .

Table 2.2 Input parameters

parameter	value-(range)/equation	units	reference(s)
<sup>1)</sup> $T$	1273 - 1573	K	
$R$	0.008314	kJ/molK	
$A(T)$	$A(T) = (1/2^m) A_o \exp(-Q_A/RT)$	$\text{m}^m/\text{MPa s}$	
$A_o$	$1.50 \cdot 10^{-12}$	$\text{m}^m/\text{MPa s}$	Karato et al. (1986)
$Q_A$	250	kJ/mol	Karato et al. (1986)
$m$	3		Karato et al. (1986)
$B(T)$	$B(T) = B_o \exp(-Q_B/RT)$	$1/\text{MPa}^n\text{s}$	
$B_o$	9550	$1/\text{MPa}^n\text{s}$	Chopra & Paterson (1981)
$Q_B$	444	kJ/mol	Chopra & Paterson (1981)
$n$	3.4		Chopra & Paterson (1981)
$\mu(T)$	$\mu_o - 0.35\mu_o (T-300/T_m)$	MPa	Frost & Ashby (1982)
$\mu_o$	81300	MPa	Frost & Ashby (1982)
$T_m$	2140	K	Frost & Ashby (1982)
$K$	0.001012	MPa m	data Karato (1980)
$f$	0.08		
$\theta_c$	0.22 (mean of range 0.17-0.26)	rad	Poirier & Nicolas (1975)
$M(T)$	$M(T) = M_o \exp(-Q_M/RT)$	$(\text{m/s}) \cdot (\text{m}^2/\text{N})$	
$M_o$	$1.14 \cdot 10^{-8}$	$(\text{m/s}) \cdot (\text{m}^2/\text{N})$	data Karato et al. (1989)
$Q_M$	160	kJ/mol	Karato et al. (1989)
$\gamma_{gb}$	1.40	$\text{J/m}^2$	Duyster & Stockhert (2001)
$\gamma_{gb}$	0.59	$\text{J/m}^2$	Duyster & Stockhert (2001)

<sup>1)</sup> See table 2.1 for explanation symbols

The material-parameter values used for olivine are listed in Table 2.2. Note that several parameters are temperature-dependent. As some parameters are poorly constrained, the values applied here are explained below.

Only a few experimental calibrations of subgrain size versus stress relation (cf. eq. 13) have been reported for olivine (Karato et al., 1980; Mercier et al., 1977; Ross et al., 1980). Both Karato et al. (1980) and Ross et al. (1980) found a non-linear relation between subgrain size and the reciprocal flow stress, i.e. a stress exponent of  $\sim 0.65$ . The present model, however, assumes an inverse linear relation, following the classical normalized relation of Takeuchi and Argon (1976). To obtain the best value for  $K$  in (13) based on olivine data, we performed a linear fit ( $R^2 = 0.81$ ) to the data of Karato et al. (1980). This resulted in the value for  $K$  quoted in Table 2.2.

To our knowledge no data have been published on the fraction of excess mobile dislocations  $f$  accumulating in a subgrain wall. However, with reference to eq. (16) - (18) and assuming that the dislocation densities across a subgrain wall are equal,  $f$  can be approximated in terms of the fractional difference in dislocation velocities  $v_d$  on either side of the wall. Furthermore, since  $\dot{\epsilon} = B\tau^n = \rho b v_d$  for deformation on a simple slip system under shear stress  $\tau$  (cf. equations 5 and 15), we can write  $v_d = (B/\rho b)\tau^n$  so that:

$$f \approx \frac{\tau_1^n - \tau_2^n}{\tau_1^n} \quad (73)$$

where the subscripts 1 and 2 refer to each side of a subgrain wall. Using the Schmid-factor to estimate the maximum difference in shear stresses for an average misorientation of  $\theta_c/2 \sim 0.11$  rad (Table 2.2) we get a value of  $\sim 0.08$  for  $f$ . For the first exploratory recrystallization tests reported here, we fixed  $f$  at this value (see Table 2.2), which to a first order appears appropriate.

The value of the grain boundary mobility parameter for olivine  $M = M_o \exp(-Q_m/RT)$ , may span several orders of magnitude at a given temperature, depending on water content, melt content and whether or not confining pressure is applied (Evans et al., 2001). We consider  $M$  values only for wet conditions and elevated temperatures ( $T > 1000^\circ\text{C}$ ) and confining pressures ( $P > 300$  MPa). Karato (1989) obtained a value for  $M$  at  $1300^\circ\text{C}$  from the grain growth behaviour. The activation energy  $Q_M$  roughly equals the activation energy for normal grain growth  $Q_{gg}$ , i.e. 160 kJ/mol determined by Karato (1989). Following the approach of Karato (1989) we used the following (corrected) relation with the constant  $k_o$  in the grain growth law to obtain a value for the pre-exponential term  $M_o$ :

$$M_o = \frac{k_o}{2 \cdot C_{HIL} \cdot \gamma_{gb}} \quad (74)$$

where  $C_{HIL}$  is a constant of value 0.5 (Hillert, 1965). Using the value for  $\gamma_{gb}$  calibrated by Duyster and Stöckhert (2001), we obtain  $M_o = 1.14 \cdot 10^{-8}$  [ $\text{m}^3/\text{Ns}$ ]. Evans et al. (2001) reevaluated the grain growth data of Karato (1989) and found for  $M_o$  and  $Q_M$  values of  $4.2 \cdot 10^{-8}$  (m/s)/(J/m<sup>3</sup>) and 189 kJ/mol, respectively. Using these values for  $M_o$  and  $Q_M$ , results in about a factor 3 lower mobilities compared to Karato (1989) for temperatures in the range 1000 to 1200°C. For the small number of model-tests reported here we fixed  $M_o$  and  $Q_M$  to the values quoted in Table 2.2.

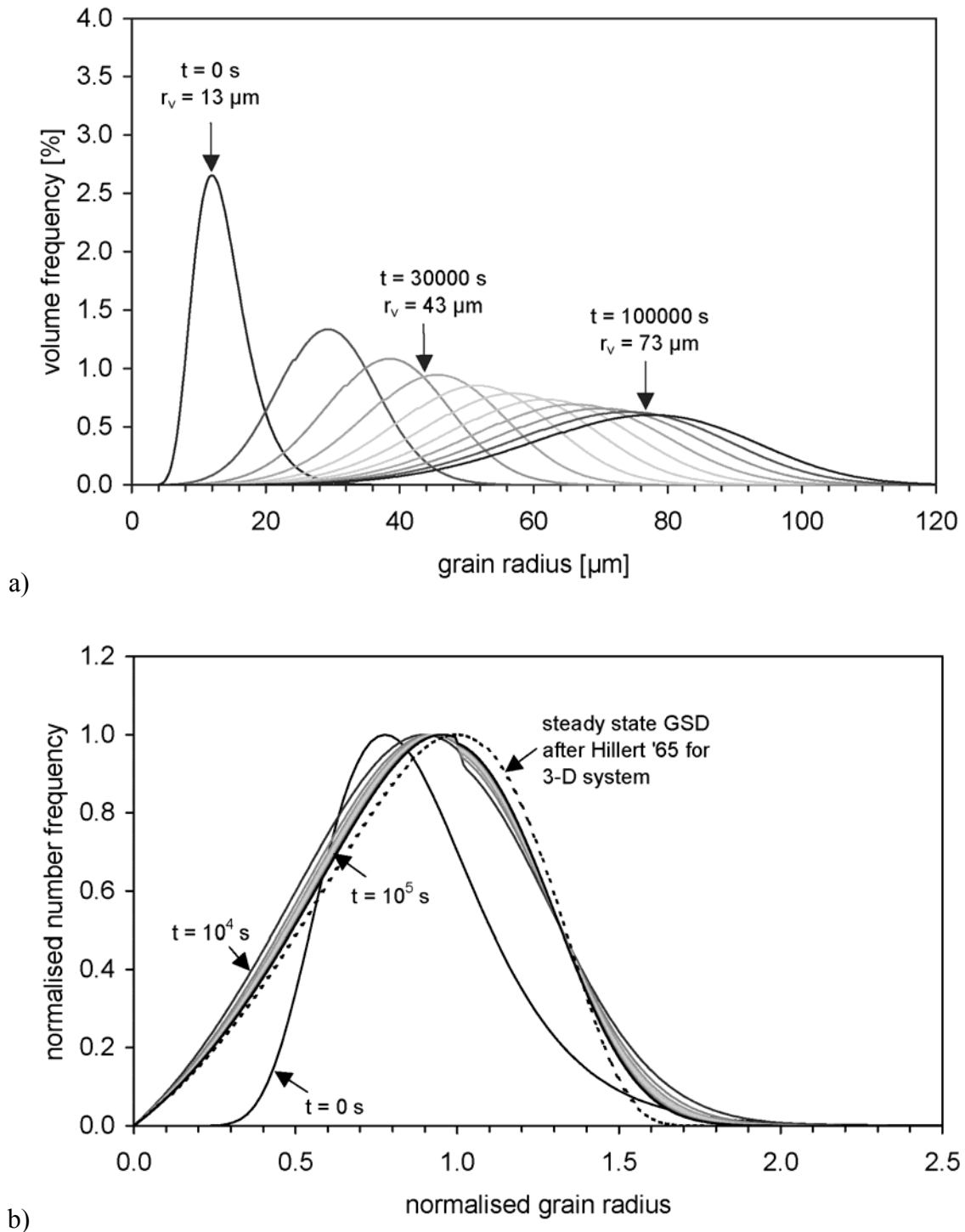


**Figure 2.4.** a) Evolution of grain radius distribution and volume-weighted log grain radius ( $r_v$ ) with time b) Evolution of normalized grain radius distributions. Distribution lines are shown at intervals of  $10^4$  s. With increasing time distribution maxima shift from left to right and gradual change color from black to light-gray, and back to black in the final timestep. Within  $10^4$  s the distribution rapidly evolves to a nearly time invariant shape, which is in good agreement with the steady state shape predicted by Hillert (1965). The small kinks in the curves in both a) and b) are a modeling artifact, i.e. a numerical precision problem, which we were unable to solve at present

## 2.4.2 Benchmarking against lab data on static grain growth

Grain growth tests were performed at temperatures of 1000 up to 1300°C (with  $T$ -steps of 100°C) and for a duration of  $10^5$  s. Fig. 2.4 shows the observed evolution with time for  $T = 1300$  °C. Note that the grain radius distributions are presented as continuous lines but are in fact discreet distributions with a fixed grain radius interval of 0.25  $\mu\text{m}$ . While  $r_v$  (i.e. the antilog of the average volume-weighted log grain radius) increases with time, the distribution widens in terms of absolute grain radii and decreases in maximum frequency value (fig. 2.4a). In order to compare the distributions predicted with the steady state distribution for a 3-dimensional system as derived by Hillert (1965), we plot the normalized number frequency versus normalized grain radius in fig. 2.4b. Here the number frequency is normalized using the maximum number frequency in the distribution and the grain radius is normalized using the arithmetic mean value multiplied by a factor 9/8 (for a 3-D system, after Hillert, 1965). In the first  $10^4$  s of a grain growth test, the distribution rapidly changes from an initially log-normal shape to a shape close to the steady state shape predicted by Hillert (1965). In the following time steps up to  $t = 10^5$  s, the distribution slowly further approaches the ideal steady state shape. It follows that the correction to  $\dot{r}_+$  applied in order to conserve mass produces a similar time-invariant distribution shape as found by Hillert (1965).

Plots of arithmetic mean grain size (i.e. diameter,  $d_g$ ) versus time are shown in fig. 2.5. The resulting grain size vs. time data were non-linearly fitted to a grain size-time relation of the form:

$$d_g^m - d_{g0}^m = k_0 \exp\left(\frac{Q_{gg}}{RT}\right) \cdot t \quad (75)$$

The non-linear fit produces the following values for the parameters in (75);  $k_0 = 5.2 \pm 1.6 \cdot 10^4$  [ $\mu\text{m}^2/\text{s}$ ],  $m = 2.1 \pm 0.0$ ,  $Q_{gg} = 163 \pm 2$  kJ/mol. Table 2.3 compares these values to the values calibrated by Karato (1989) for normal grain growth of olivine. We conclude that the model produces quite closely a square grain growth law, anticipated by Hillert (1965) and presumed by Karato (1989). The calibrated activation energy for grain growth in this study is close to identical to the value obtained by Karato (1989). However, this similarity is inevitable since we used Karato's activation energy value (160 kJ/mol) as input for the temperature dependence of the applied mobility term (see Table 2.2). The rate constant  $k_0$  obtained from the model tests is about a factor of 3 higher compared to the value calibrated by Karato (1989).

In fig. 2.5 we include, for comparison, grain size-time isotherms calculated directly from the grain growth parameters of Karato (1989) given in Table 2.3. At similar time and temperature the grain size predicted by our model is about a factor of 1.2 greater than the grain size predicted by Karato (1989). Thus for the conditions tested the model produces grain growth kinetics that are in good agreement with experimental data and differences are within the order of uncertainty caused by parameters like the mobility (see previous section).



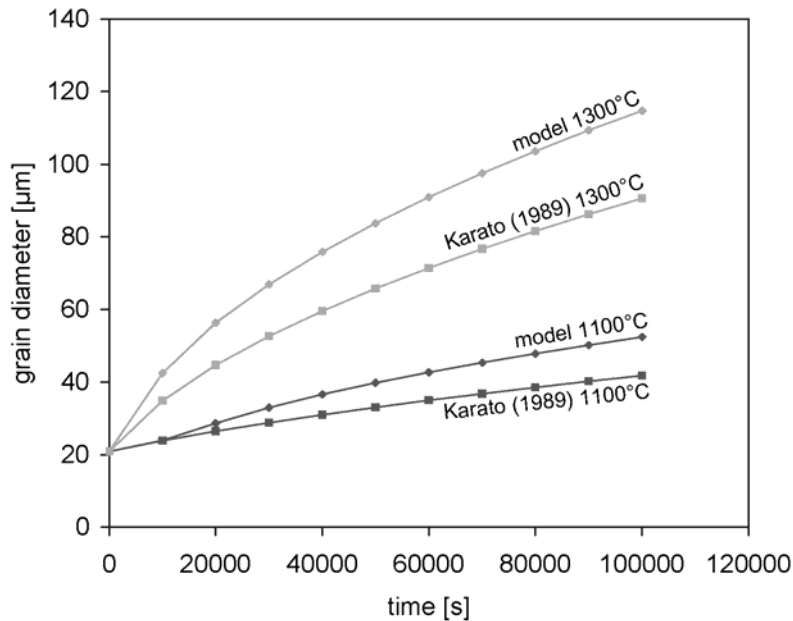


**Figure 2.5.** Plots of arithmetic mean grain diameter versus time for static grain growth predicted by the model and compared with grain growth predictions according to the grain growth law calibrated experimentally by Karato et al. (1989).

### 2.4.3 Results for dynamic recrystallization

#### Evolution of grain size distribution

A set of recrystallization tests was performed at strain rates of  $10^{-7}$ ,  $10^{-5}$ , and  $10^{-3} \text{ s}^{-1}$  and a temperature of  $1250^\circ\text{C}$ . Starting grain size distributions were chosen such that the evolution in stress and grain size either starts in the GSS or in the GSI creep field. Model tests at these conditions allow a first comparison to the available experimental recrystallized grain size-stress data for olivine. As mentioned above, progressive subgrain rotation facilitates new grain nucleation and gradients in both grain boundary surface energy and subgrain energy provide a combined driving force for GBM.

*Deformation starting in the GSS creep field.* In fig. 2.6 the evolution of the grain size distribution with time and strain is shown for a test at  $10^{-5} \text{ s}^{-1}$  and an initial  $r_v$  of  $6.6 \mu\text{m}$ , i.e. starting in the GSS creep field. From  $t = 0$  to  $1000 \text{ s}$ , the evolution is clearly dominated by grain growth. This grain growth must be governed by a dominant surface energy driving force, since the complete distribution is smaller than the maximum subgrain size and hence subgrains cannot yet develop. At  $t = 1000 \text{ s}$  the larger grain radii in the distribution reached the subgrain size-stress relation (i.e. where the grain radius equals the subgrain radius it would produce). The maximum grain radius does not continue to grow beyond the subgrain size-stress relation. With continuing grain growth in the finer grained parts of the distribution, more and more grains start to pile up in the 2 grain radii intervals just above and below the maximum subgrain size. This continues until the complete distribution has migrated into these two grain radius intervals. At this stage steady state is reached. Grain radii larger than the grain size at the subgrain-stress relation are allowed to form subgrains and thus experience a negative subgrain energy driving force for GBM. Therefore grains do not continue to grow, because there is an immediate drop in migration rate for grain radii above the subgrain-stress relation.

*Deformation starting in the GSI creep field.* Fig. 2.7 illustrates multiple phases in the complex evolution of a GSD starting deformation in the GSI creep field. Despite this complex evolution, a recrystallized grain size is reached at the subgrain size-stress relation similar to an evolution starting in the GSS creep field. In the following the various phases are described in more detail.

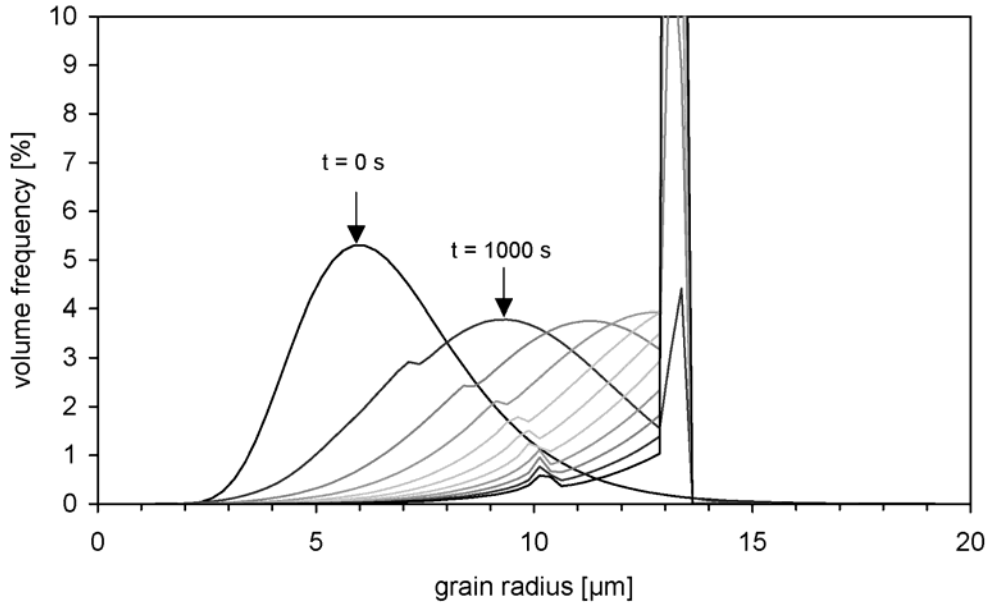


**Figure 2.6.** Evolution of grain radius distribution with time (and strain) during a recrystallization test at a strain rate of  $10^{-5} \text{ s}^{-1}$  and with an initial starting lognormal distribution in the GSS diffusion creep field. The persistent small bump in the fine-grained part of the distribution is the same modeling artifact mentioned in fig. 2.4. The volume frequency percentages at grain radii  $\sim 14 \mu\text{m}$  are cut off in this plot, but have values up to  $\sim 70\%$ . Colors of distribution-lines follows the same sequence as described for fig. 2.4.

In fig. 2.7a the evolution of the grain size distribution with natural strain up to  $\varepsilon = 0.5$  is shown for a test at  $10^{-5} \text{ s}^{-1}$  and an initial volume-weighted log grain radius of  $98 \mu\text{m}$ , i.e. starting in the GSI creep field. Nucleation of new grains in the range  $7.6$  to  $13.0$  (i.e. the maximum subgrain radius)  $\mu\text{m}$  causes a rapid drop in arithmetic mean grain radius in the interval  $\varepsilon = 0 - 0.05$ . In turn, a rapid upward shift occurs for the effective migration rate  $v$  in the range  $0$  to  $\sim 90 \mu\text{m}$  (fig. 2.8a). Nucleation rate is maximum for the smallest possible subgrains causing the formation of a peak (A) at the very fine grain size of  $\sim 7 \mu\text{m}$ . Peak A continues to persist up to a strain of  $\sim 1.2$ , since  $v$  is close to  $0$  due to a negative surface energy driving force being balanced by a positive subgrain energy driving force. Thus for grain radii at  $\sim 7 \mu\text{m}$ , nucleation rate dominates over growth rate (or shrinkage rate). For nucleated and grown grains larger than  $7 \mu\text{m}$ , growth dominates over nucleation, causing these grains initially to pile up at radii just over the maximum subgrain radius (peak B, fig. 2.7a). For grain radii larger than the maximum subgrain radius there is again a drop in  $v$  (note similar to the GSS test above) but  $v$  remains positive (fig. 2.8a). This causes the peak B to grow in size and to migrate its center slowly to higher grain radii up to a strain of  $\sim 0.3$ . Meanwhile, the arithmetic mean grain size slowly increases as well causing the full distribution in  $v$  to slowly shift downwards again. At strains  $> 0.3$  peak B starts to migrate back towards smaller grain radii because of the overall decreasing  $v$ . The remaining part of the original distribution is labeled as peak C in the coarsest grain radii range ( $40$ – $200 \mu\text{m}$ ). The grains around peak C experience significant recrystallization, i.e. produce the new grains that end up in peaks A and B. The distribution at C thus reduces in size and migrates towards smaller grain radii. The evolution discussed so far continues in a similar way as strain progresses until a significant change occurs from  $1.2$  to  $1.5$  natural strain and a negative  $v$  at peak A starts to dominate over the nucleation rate (fig. 2.7b and 2.8b). At a natural strain of  $\sim 1.5$ , peak A is reduced in size. This causes a significant change in the distribution of  $v$  for the grain radii larger than the maximum subgrain radius (i.e.  $> 13 \mu\text{m}$ ). Peak C ‘suddenly’

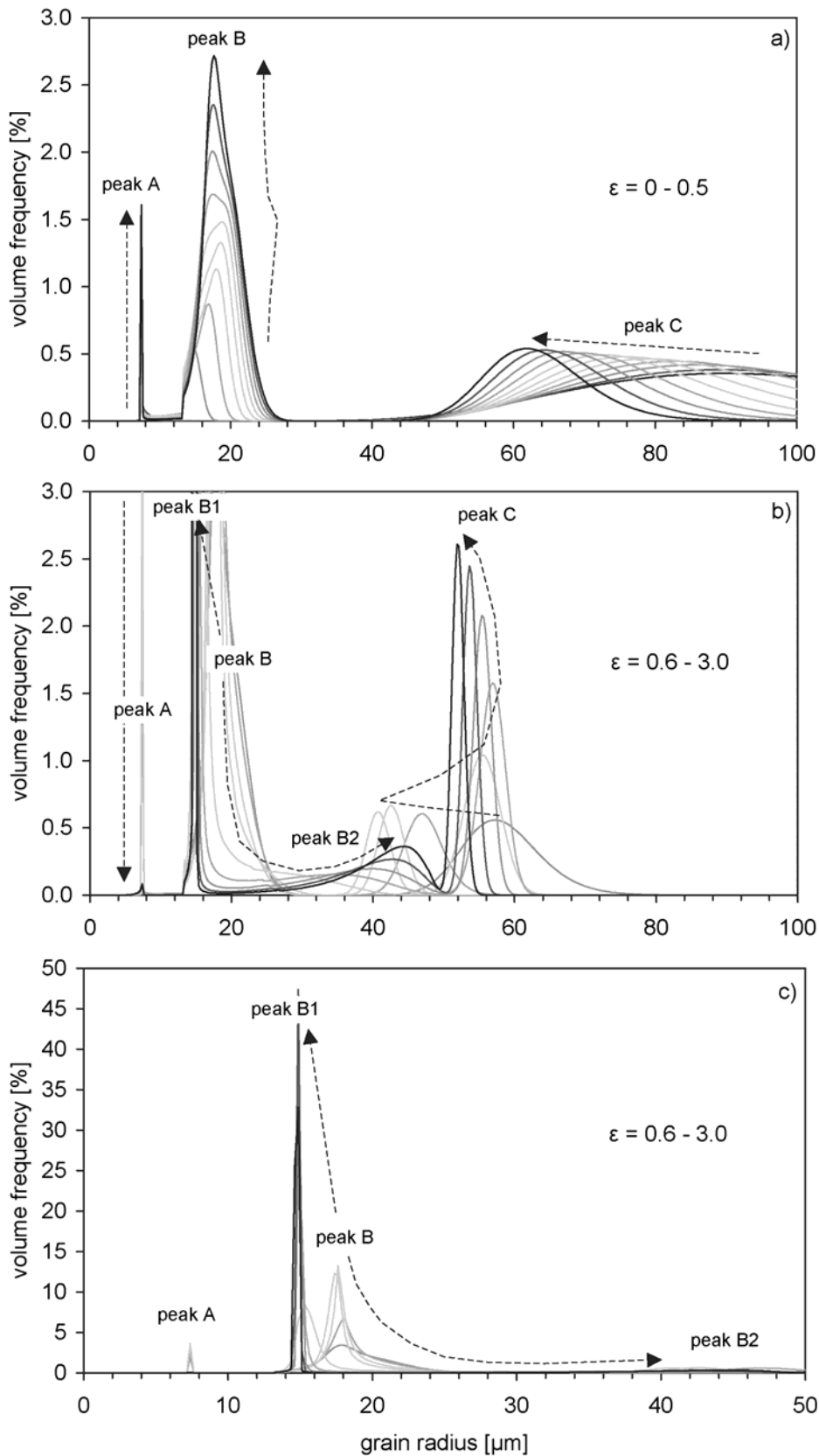


**Figure 2.7.** a) Evolution of grain radius distribution up to a natural strain of 0.5 for a recrystallization test at a strain rate of  $10^{-5} s^{-1}$  and with an initial starting lognormal distribution in the GSI dislocation creep field. The dashed arrows indicate the direction in which the various distribution peaks (A, B and C) migrate with progressive strain. b) Evolution of grain radius distribution in natural strain interval 0.6 to 3.0 c) Same evolution and strain interval as for b) but different x- and y-axis scales.

experiences a positive  $v$  again causing it to migrate towards higher grain radii. Meanwhile peak B with its center at  $\sim 18 \mu\text{m}$  at  $\epsilon = 1.2$ , starts to split up at  $\epsilon = 1.5$  since  $v$  suddenly changes sign at about  $\sim 20 \mu\text{m}$  (i.e.  $v < 0$  for  $r < 20 \mu\text{m}$  and  $v > 0$  for  $r > 20 \mu\text{m}$ ). This causes the formation of peak B1, which migrates towards the (smaller) maximum subgrain size and formation of a significant smaller peak B2, which migrates towards peak C (See also fig. 2.7b and 2.7c). For natural strains  $> 1.5$  peak B2 and C are ‘trapped’ in a grain radius range where  $v$  is positive. Thus ‘trapped’ grains tend to grow up to the range-maximum. At a strain of 1.5 the range-maximum is at  $210 \mu\text{m}$ , but rapidly decreases down to a value around  $50 \mu\text{m}$  for strains  $\geq 2.1$ . At a strain of 3.0 peak B2 and C start to merge at the range maximum, i.e. at  $\sim 50 \mu\text{m}$ . Further evolution progresses at very slow  $\dot{F}(r,t)$ , since the merged peak B2C only reduces in volume due to relative slow nucleation of new grains, which finally end up in peak B1. It is only at a strain of about 22 that peak B2C is fully recrystallized into peak B1 and steady state is reached.

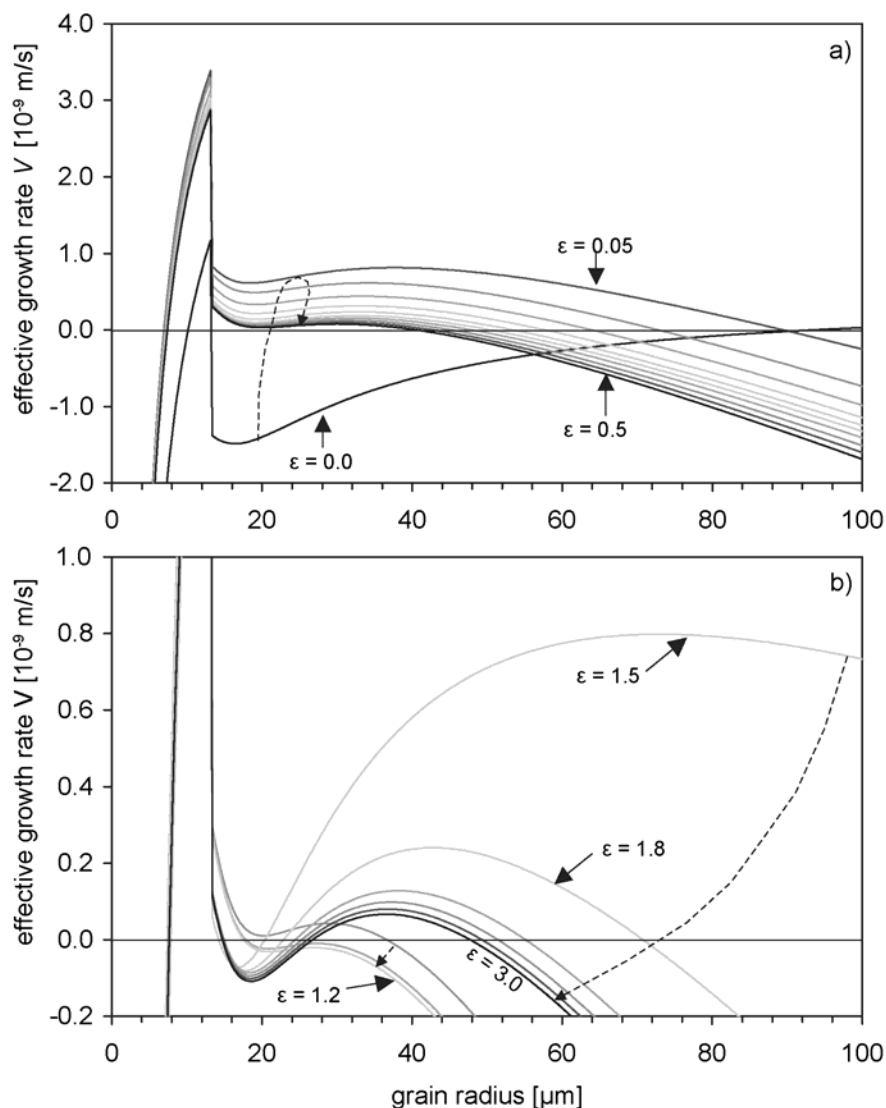


**Figure 2.8.** a) Evolution of effective growth rate  $v$ -distribution up to 0.5 natural strain ( $\epsilon$ ). The dashed arrows indicate schematically the rapid rise and subsequent slow decrease of  $v(r)$  for  $r$  between 0 and  $\sim 90 \mu\text{m}$ . b) Evolution of effective growth rate  $v$ -distribution between 0.6 and 3.0 natural strain. Note the sudden rapid rise in  $v(r)$  between 1.2 and 1.5 natural strain.

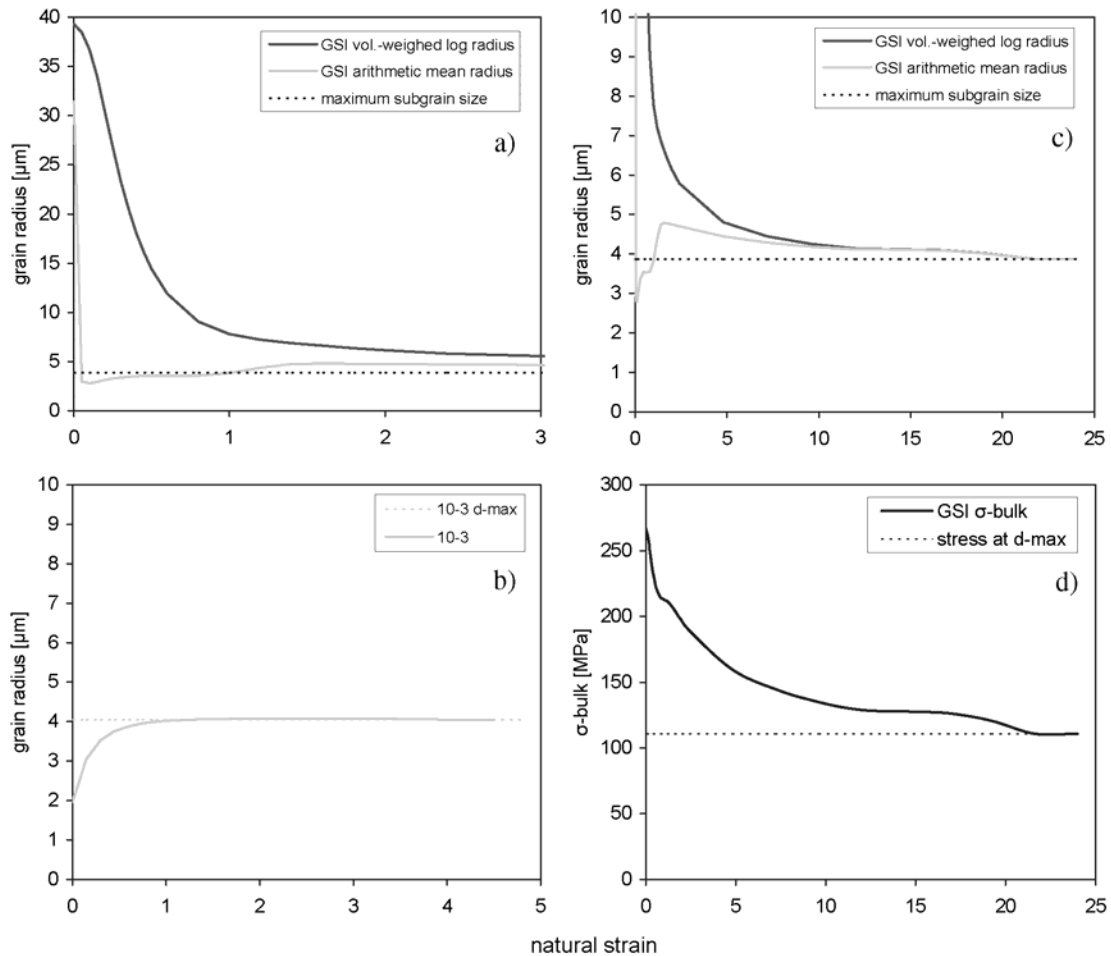
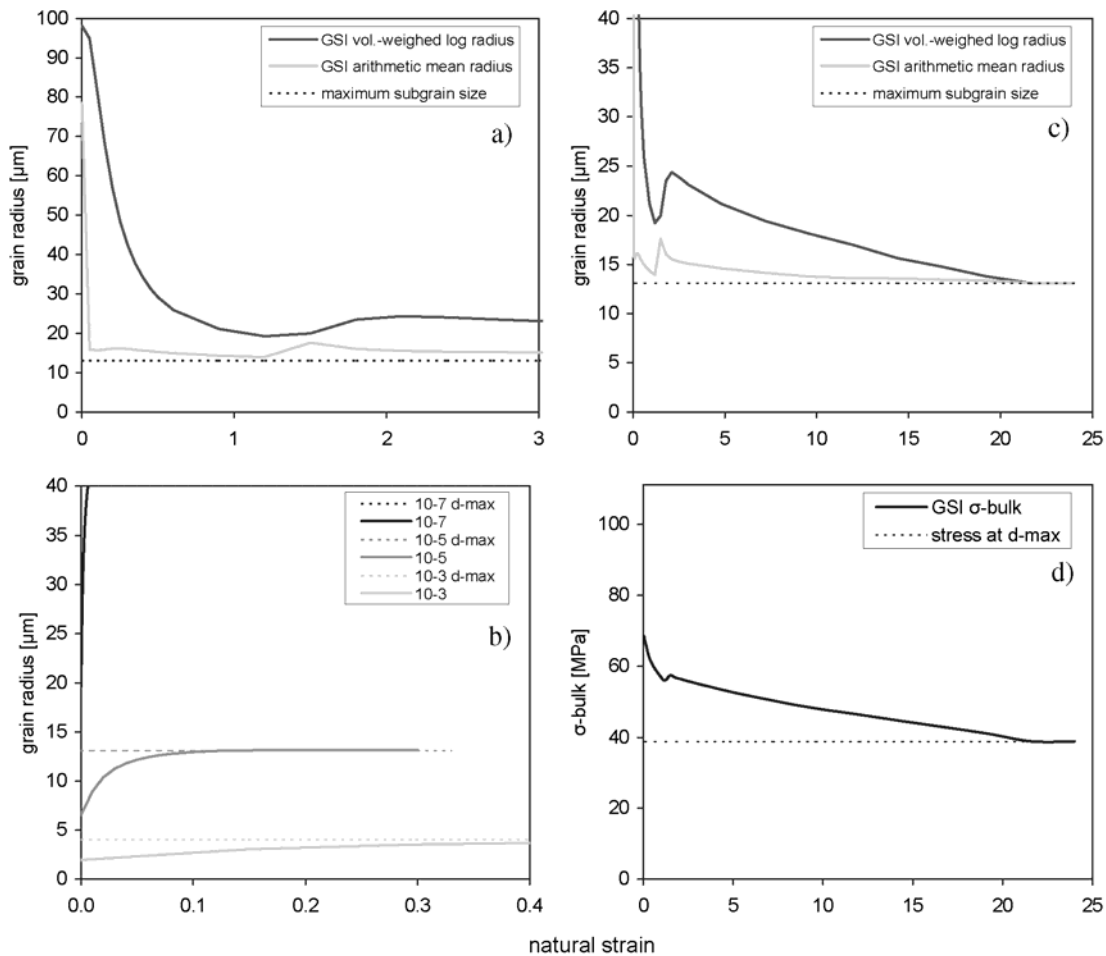


**Figure 2.9.** Results of recrystallization tests at a strain rate of  $10^{-3} \text{ s}^{-1}$  and  $T = 1250^\circ\text{C}$  a) Evolution of arithmetic mean grain radius, volume-weighted log grain radius and maximum subgrain size up to a natural strain of 3.0 for a test starting in the GSI creep field. b) Evolution of arithmetic mean grain radius and maximum subgrain size up to a natural strain of 4.5 for a test starting in the GSS creep field. c) Similar to a) up to a natural strain of 24.0. d) Local stress at the maximum subgrain size and evolution of the bulk stress up to a natural strain of 24.0 for a test starting in the GSI creep field.

The distinct features of the complex evolution in a grain radius distribution for tests at  $10^{-5} \text{ s}^{-1}$  (fig. 2.7) are also observed for tests at strain rates of  $10^{-3}$  and  $10^{-7} \text{ s}^{-1}$ , though the evolution for tests starting in the GSI creep field at a strain rate of  $10^{-7} \text{ s}^{-1}$  is slightly different. It appears that at this strain rate, GBM and  $\nu$  are more strongly dominated by surface energy driven grain growth, causing the initial distribution (peak C as in fig. 2.7a) first to migrate towards larger grain radii. At a strain of  $\sim 0.1$  migration of peak C is balanced again by an increasing nucleation rate and peak C starts to migrate back again towards lower grain sizes. However migration back occurs at such a slow rate that no steady state is yet reached in our (time consuming) model runs at a strain of 24.

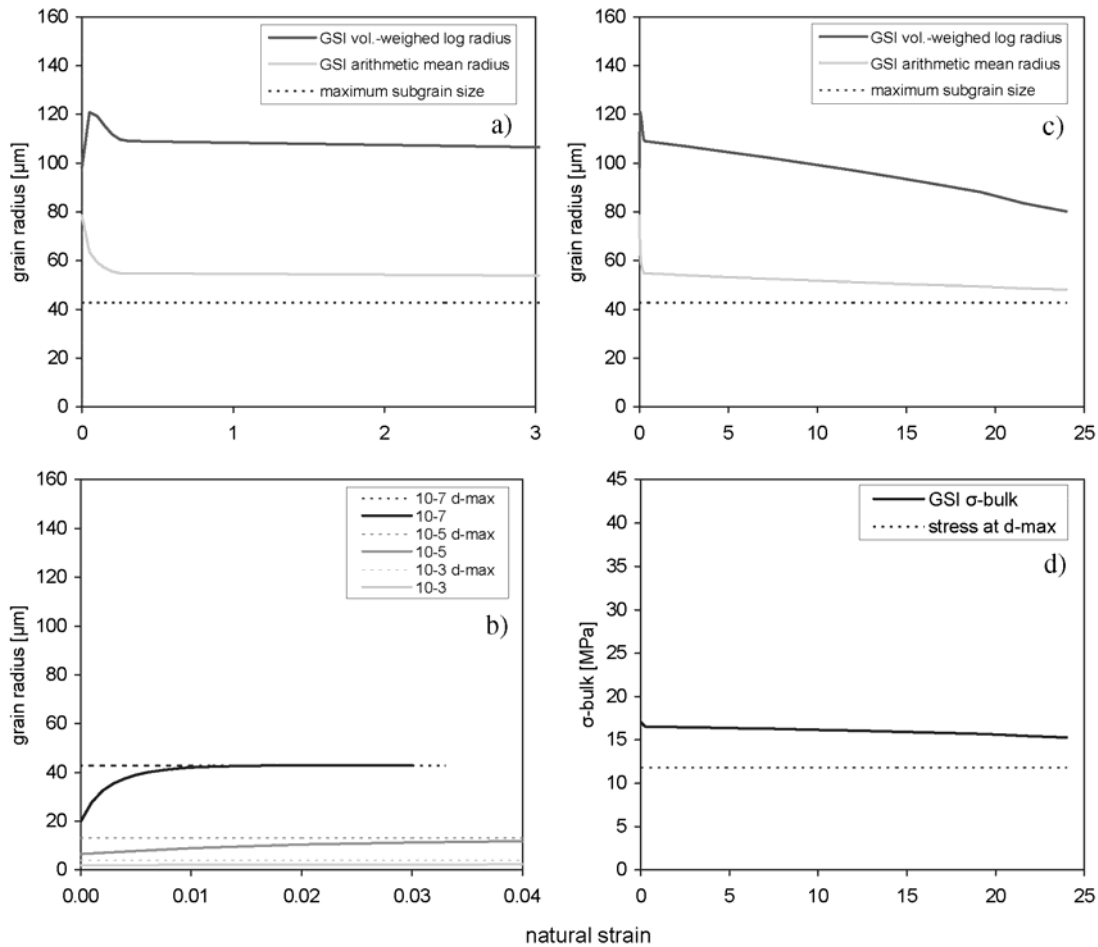
#### Evolution of average grain size and flow stress

Fig. 2.9, 2.10 and 2.11 summarize the evolution of the arithmetic mean radius, volume-weighted log radius and stress with strain for all tests at strain rates of  $10^{-3}$ ,  $10^{-5}$ , and  $10^{-7} \text{ s}^{-1}$ , respectively. For the recrystallization tests starting in the GSI creep field, we observe that the arithmetic mean radius decreases rapidly towards the maximum subgrain size whereas the volume-weighted log radius decreases much less rapid (fig. 2.9a, 2.10a) or even increases (fig.



**Figure 2.10.** Results of recrystallization tests at a strain rate of  $10^{-5} \text{ s}^{-1}$  and  $T = 1250^\circ\text{C}$  a) Evolution of arithmetic mean grain radius, volume-weighted log grain radius and maximum subgrain size up to a natural strain of 3.0 for a test starting in the GSI creep field. b) Evolution of arithmetic mean grain radius and maximum subgrain size up to a natural strain of 0.3 for a test starting in the GSS creep field. Results at other strain rates are also shown for comparison c) Similar to a) up to a natural strain of 24.0. d) See fig. 2.9d

2.11a). This diversion between the arithmetic mean and volume-weighted log radius is a statistical expression of the tri-modal distribution being developed at the onset of deformation (see fig. 2.7). The discussed marked change in distribution evolution for the GSI recrystallization test at  $10^{-5} \text{ s}^{-1}$  between 1.2 to 1.5 strain is also visible as a temporal increase in both arithmetic mean and volume-weighted log radius (fig. 2.10a and 2.10c). A similar, but less prominent increase in only the arithmetic mean radius between  $\varepsilon = 1.0$  and 1.3 is observed for the test at strain rate  $10^{-3} \text{ s}^{-1}$  (fig. 2.9a and 2.9c). A similar feature is absent for the test at  $10^{-7} \text{ s}^{-1}$  (fig. 2.11a and 2.11c). Also note that comparing fig. 2.7 versus fig. 2.10 shows the sheer contrast in level of complexity when presenting microstructural evolution either as full GSDs or as some mean value. For  $\varepsilon > 2$ , both the arithmetic mean and volume-weighted log radius continue to decrease. For strain rates at  $10^{-3}$  and  $10^{-5} \text{ s}^{-1}$  this decrease causes the arithmetic mean and volume-weighted log radius to merge and reach steady state at the maximum subgrain size at a natural strain of  $\sim 21$ . However, no steady state is reached for the test at the strain rate of  $10^{-7} \text{ s}^{-1}$  up to a strain of  $\sim 24$ , since the arithmetic mean and volume-weighted log radius do not yet merge nor reach the maximum subgrain size and show ongoing decrease.



**Figure 2.11.** Results of recrystallization tests at a strain rate of  $10^{-7} \text{ s}^{-1}$  and  $T = 1250^\circ\text{C}$  a) Evolution of arithmetic mean grain radius, volume-weighted log grain radius and maximum subgrain size up to a natural strain of 3.0 for a test starting in the GSI creep field. b) Evolution of arithmetic mean grain radius and maximum subgrain size up to a natural strain of 0.03 for a test starting in the GSS creep field. Results at other strain rates are also shown for comparison. c) Similar to a) up to a natural strain of 24.0. d) See fig. 2.9d.

Relative to the GSI recrystallization tests, the volume-weighted log radius in GSS recrystallization tests grows quite quickly, i.e. within 0.01 to 1 natural strain, towards the maximum subgrain size for all three strain rates (fig. 2.9b, 2.10b and 2.11b). The distribution when starting in the GSS creep field develops a bimodal distribution, which has a less extreme spread in grain radii compared to GSI recrystallization tests. Therefore only the volume-weighted log radius is shown, since the evolution in arithmetic mean radius is close to identical. Note that since the increase in grain size is largely governed by surface energy driven GBM, the grain growth is actually time-dependent rather than strain dependent.

Obviously, tests starting in the GSS creep field show a stress increase according to the increase in grain size, i.e. reaching steady state at a stress value that is representative for the maximum subgrain size (fig. 2.9d, 2.10d and 2.11d). Similarly, stress evolution for recrystallization tests starting in the GSI creep field also follows quite closely the evolution in volume-weighted log grain radius. In other words the evolution in flow stress shows gradual but persistent weakening up to considerable high strains before steady state stress is reached at the maximum subgrain size stress relation. This illustrates that a contribution of GSS creep to the overall stress is closely related to the volume fraction of fine grained material, rather

then to the arithmetic mean grain size of the total GSD, especially when the distribution is multi-modal. Up to natural strains of 24 flow stress experienced 58, 44, and 10% weakening for tests at strain rates of  $10^{-3}$ ,  $10^{-5}$ ,  $10^{-7}$   $s^{-1}$ , respectively. Note again that at a natural strain of 24 still no steady state flow stress is reached for the test at strain rate  $10^{-7}$   $s^{-1}$ .

#### 2.4.4 Comparison with experimental studies

Fig. 2.12 forms a final synopsis of the results of the model runs plotted within a deformation mechanism map. Included in the map are the GSS-GSI mechanism boundary, the used subgrain-size stress relation, the recrystallized grain size-stress relation of Van der

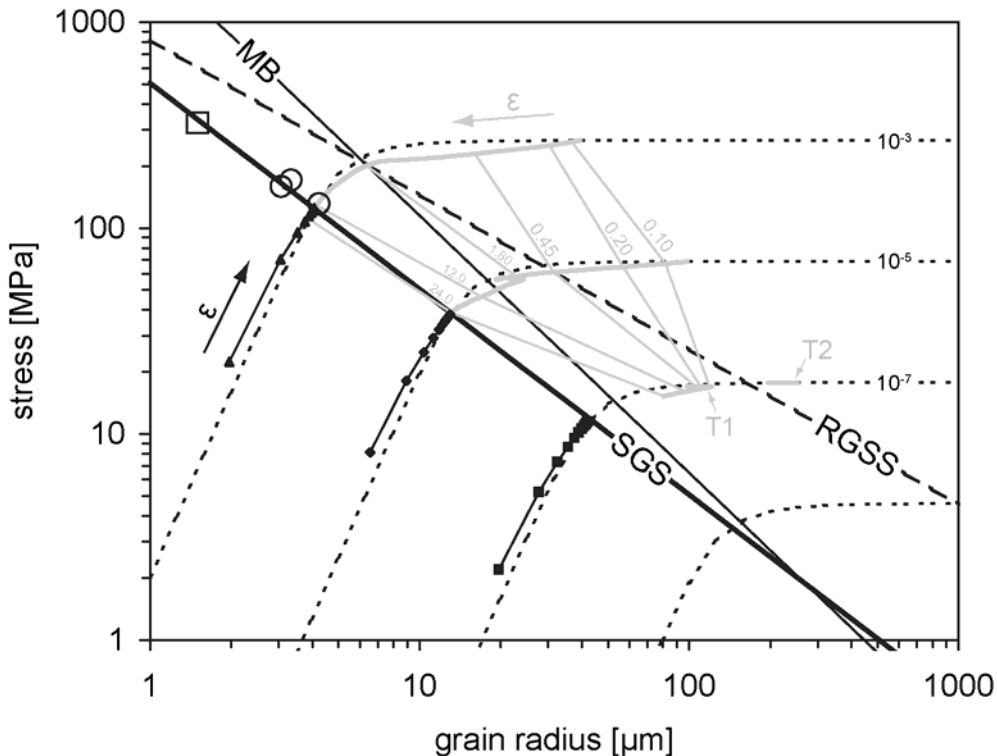


**Figure 2.12.** Deformation mechanism map for the applied composite rheology (see table 2.2 for details on used flow law parameters) at  $T = 1250^{\circ}C$ . Dashed lines are contours for strain rates of  $10^{-3}$ ,  $10^{-5}$ ,  $10^{-7}$ , and  $10^{-9}$   $s^{-1}$ .  $r_v - \sigma$  traces of the recrystallization tests that start in the GSS creep field are shown in black with black closed triangles, diamonds and squares at fixed strain intervals of 0.15, 0.01 and 0.001, respectively. The  $\epsilon$ -labeled black arrow indicates the direction of strain ( $\epsilon$ ) increase.  $r_v - \sigma$  traces of the recrystallization tests that start in the GSI creep field are shown as bold gray lines. These traces are connected by thin gray lines at similar strains, thus forming strain (labeling) contours. The  $\epsilon$ -labeled gray arrow indicates the direction of strain increase. MB = the deformation mechanism boundary, where  $\dot{\epsilon}^{diff} = \dot{\epsilon}^{disl}$ , RGSS = the recrystallized grain size - stress relation after Van der Wal et al. (1993) and SGS = is the inverse subgrain size - stress relation modified after Karato et al. (1980). The open circles represent high strain ( $>0.5$ )  $\bar{D}/2 - \sigma$  data points of Zhang et al. (2000) and the open square represents a  $\bar{D}/2 - \sigma$  data point of a high strain (1.9) torsion experiment of Bystricky et al. (2000).

Wal et al. (1993) and the recrystallized grain size-stress data from Zhang et al. (2000) and Bystricky et al. (2000). Fig. 2.12 shows volume-weighted log radius versus bulk stress trends for runs at  $10^{-3}$ ,  $10^{-5}$ ,  $10^{-7}$   $s^{-1}$ . At strain rates of  $10^{-3}$  and  $10^{-5}$   $s^{-1}$  steady state is reached at about the same strain, although starting from different initial distributions. Furthermore two runs at



a similar strain rate of  $10^{-3} \text{ s}^{-1}$ , but with different starting volume-weighted log grain radius of 98 and 40  $\mu\text{m}$ , shows steady state is reached at about the same natural strain of  $\sim 21$ . This suggests the position of the starting distribution in the GSI creep field hardly affects the evolution of grain size and stress with strain for tests at the higher strain rates. At a lower strain rate of  $10^{-7} \text{ s}^{-1}$  the position of the starting distribution does seem to have a significant effect as trends for two tests (indicated as T1 and T2) with different starting distributions do not start to overlap up to high strains. This indicates that at this strain rate the position of volume-weighted log radius versus stress data at a specific strain is strongly influenced by the position of the starting distribution. The fact that the recrystallized grain size for the  $10^{-3} \text{ s}^{-1}$  strain rate model runs plots below the subgrain-stress relation at  $\varepsilon = 24$  is solely due to the relative large grain radius interval used for the discrete GSD. For tests starting in the GSI creep field trends are connected at similar strains forming strain contours. For strain rates between  $10^{-3}$  and  $10^{-5} \text{ s}^{-1}$  the recrystallized grain size-stress relation, calibrated from samples strained to  $\sim 0.1$  natural strain (Van der Wal et al., 1993), plots between natural strain contours of 0.45 to 1.8 according to the model. The model thus predicts that to reach the recrystallized grain sizes found in experiments, strains are required that are a factor 4 to 18 larger than actually imposed. Realize, however, that this is a particular rough comparison, since in contrast to our modeled grain size data, the experimentally recrystallized grain sizes do not represent distributions of the complete aggregate. Instead, experimental grain size data were measured from selected areas within sample microstructures, i.e. areas ‘considered’ to be fully recrystallized. Future recrystallization tests with  $f$  being varied within the range constrained by the mean subgrain misorientation and measurement of full grain size distributions obtained in experiments are thus needed. This will allow a better comparison and further fine-tuning of the position of model strain contours with respect to experimental data. Since the position of the volume-weighted log radius – stress – strain data at  $10^{-7} \text{ s}^{-1}$  strain rate are dependent on where the initial distribution resides, the strain contours between  $10^{-5}$  and  $10^{-7} \text{ s}^{-1}$  strain rate are less straightforward to interpret. Although we acknowledge the problem of starting distribution dependency, we still may suggest the general trend that the recrystallized grain radius at the (maximum) subgrain size -stress relation is more rapidly approached (in terms of strain) at higher strain rates according to the model. As a consequence, experimental data gathered to calibrate a recrystallized grain size stress relation obtained from samples deformed to a fixed relative low strain like the data of Van der Wal et al. (1993) might be biased towards larger grain sizes at lower strain rates/stresses. Zhang et al. (2000) already noted their recrystallized grain sizes produced at natural strains  $>0.5$  plotted below the relation of Van der Wal et al. (1993). Here we show the data of Zhang et al. (2000) and Bystricky et al. (2000) plot surprisingly close to the subgrain size stress relation used here. We suggest that the higher strains reached by Zhang et al. (2000) and Bystricky et al. (2000) explain why their microstructures reduced more in grain size than the recrystallized grain size versus stress data of Van der Wal et al. (1993).

#### 2.4.5 Future improvements

The model in its present form predicts that grain radius distributions tend to recrystallize towards the subgrain size-stress relation, rather than to the mechanism boundary of De Bresser et al. (2001) or the recrystallized grain size-stress relation determined for  $\varepsilon < 0.1$  by Van der Wal et al. (1993). Our model might overestimate this strong attraction towards the subgrain size-stress relation, since it assumes that subgrains form instantaneously the moment the grain radius becomes greater than the subgrain radius that it would produce according to the subgrain size-stress relation. In general, recrystallized microstructures show

that small subgrains are dominantly produced in considerable larger grains. Future detailed inspection of recrystallized microstructures may further constrain at what minimum relative grain radius subgrains start to form. If, for example, subgrains will only form in grains that are at least 2-times larger, this would shift the modeled recrystallized grain size stress relation towards at position near the mechanism boundary at strain rates between  $10^{-3}$  and  $10^{-5} \text{ s}^{-1}$ .

Another important point to be treated here is the slope of the subgrain size-stress relation. In case of olivine, we refitted subgrain stress data of Karato (1980) to a slope (i.e. stress-dependence) of -1 (see section 2.4.1) with a correlation coefficient similar to the original calibration of Karato (1980), giving a slope of -0.67. Note the slope of the mechanism boundary is at -0.8. Considering the suggestion that recrystallization may lead to a mechanism switch and significant weakening (see section 1) it is thus crucial to constrain the slope of the subgrain stress relation at utmost precision as these slope differences determine to what extent a recrystallized grain size stress relation is expected to penetrate the GSS creep field at high stresses/strain rates or the GSI creep field at low stresses/strain rates.

In addition to the subgrain size-stress relation several other material-dependent parameters in the model appear to be poorly constrained by available literature in case of olivine material. These are: 2) the critical misorientation,  $\theta_c$ , for a subgrain boundary to become a high angle grain boundary, 3) the fraction of excess dislocations contributing to progressive subgrain misorientation, and 4) the grain boundary mobility  $M$ . On the one hand model predictions in terms of e.g. a recrystallized grain size-stress relation will gain confidence with an improved experimental calibration and theoretical evaluation of these parameters. On the other hand future model tests that explore in more detail the effect of varying e.g. the value of  $f$  will better constrain the range in parameter values, which produces realistic predictions that are comparable to experimental data.

The chosen method of calculating the subgrain driven GBM (i.e. the gradient between the *local* and *average* subgrain energy) causes grain size distributions to evolve towards a single-valued recrystallized grain size. It is generally thought that an aggregate at steady state shows some degree of distributed grain sizes (Shimizu, 1998, 1999; Ter Heege et al., 2003, 2005) and the model may thus be further improved on this point in future development. Also no topological constraints are taken into account yet with respect to GBM. Such constraints may become rather important as soon as a multimodal distribution is developed, representing actually a ‘core-mantle’ microstructure. Grain neighbors in a fine-grained mantle are far from the ‘average’ environment for the complete aggregate and GBM may thus be better modeled with a driving force taking the local ‘mantle’ average into account.

These first model results probably overestimate the amount of strain needed to reach steady state. The strain contours (fig. 2.12) represent significant larger absolute strains than the relation of Van der Wal et al. (1993) and the data of Zhang et al. (2000) and Bystricky et al. (2000). Still the trend in strain contours can explain why lower recrystallized grain sizes (at constant stress) are found at higher strains.

## 2.5 Conclusions

We have developed a microphysically based model that allows a numerical evaluation of the large strain transient evolution of both GSD and flow stress towards a recrystallized steady state. Here recrystallization results from a dynamic competition between nucleation by progressive subgrain rotation and GBM driven by free energy differences across grain boundaries. From the first results of model runs applied to olivine material the following conclusions can be drawn:

1. In static surface energy driven GBM tests the model produces normal grain growth kinetics and time-invariant GSD-shapes that are in good agreement with theoretical evaluations and experimental data on olivine material.

2. Transient evolution of GSD showed the development of bi- and complex multimodal distributions. This suggests that to establish a unique relation between flow stress and a steady state recrystallized microstructure full GSDs need to be measured. Measurement of only a mean value from selected recrystallized areas in a microstructure seems inadequate. Overall, GSD tends to migrate towards larger grain sizes when starting in the GSS creep field and tends to migrate towards smaller grain sizes when starting in the GSI creep field.
3. High strain is needed to reach a steady state recrystallized microstructure. Perhaps the model predicts strains that are too high, but the trend is there and is consistent with observations of generally smaller recrystallized grain sizes found by Zhang et al. (2000) and Bystricky et al. (2000) compared to the data of Van der Wal et al. (1993).
4. Both the gradual increase in stress with strain for tests starting in the GSS creep field and the gradual decrease in stress for tests starting in the GSI creep field are proportional to the evolution in volume-weighted log grain radius  $r_v$ . This illustrates that a contribution of GSS creep to the overall stress is closely related to the volume fraction of fine grained material, rather than to the arithmetic mean grain size of a GSD, especially when the distribution is multi-modal. Analogous to the high strains necessary to reach a steady state microstructure, flow stress may experience up to 60% weakening when going to sufficient high strains.
5. The attraction towards the inverse relation between subgrain size and flow stress causes the initial discrete GSD to narrow and reach steady state as a single grain size interval at the inverse subgrain size - stress relation. In order to prevent that initial GSD's reach steady state in a single grain size interval, an improved method is needed for calculating subgrain energy driven GBM, which remains a topic for future work.
6. Considering the observed attraction towards the inverse relation between subgrain size and flow stress, it is emphasized that this relation needs to be further evaluated in theory and experiments, such that it's position with respect to the deformation mechanism boundary in experiments and nature is better understood. This knowledge is essential when one seeks to assess a reliable steady recrystallized grain size stress relation with the present model.
7. Evolution of distributions approaching steady state from the GSS creep field appears far less complex than when starting in the GSI creep field. Moreover steady state is reached at relative low strains if grain growth is sufficiently rapid. This suggests that calibration of a recrystallized grain size-stress relation through performing experiments that start in the GSS creep field may produce data less biased towards larger grain sizes for the slowest strain rates stresses.

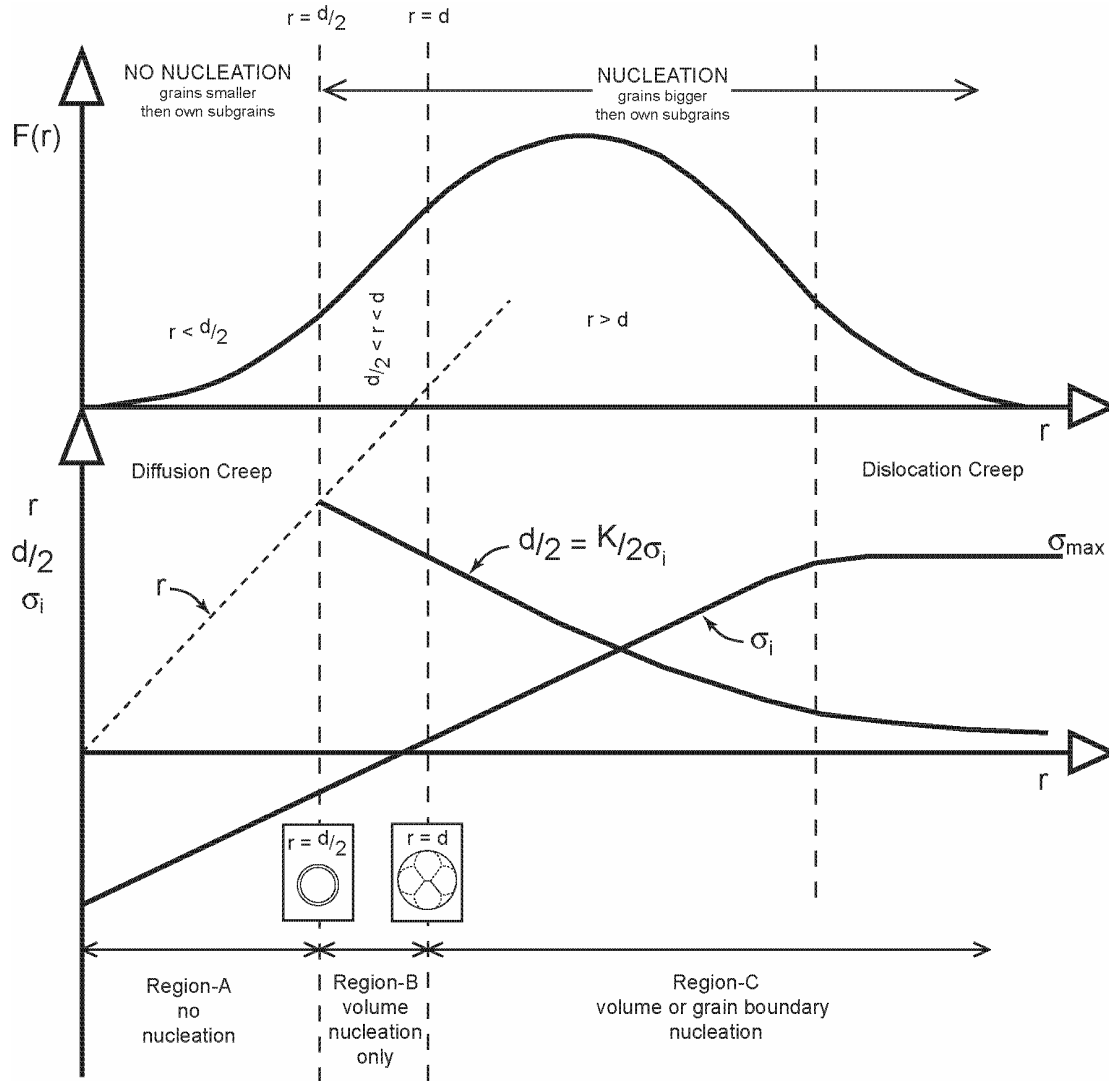


**Figure A1** Schematic illustration of the grain radius distribution and the variation of  $\sigma_i$  and the subgrain radius ( $d/2$ ) with  $r$ . Three regions (A, B and C) in grain radius are distinguished for which different nucleation,  $\dot{N}_g$ , criteria apply. See text for further explanation.

## Appendix A:

### Constraints on nucleation rate in individual grains

Prior to employment of the model as it is set out in section 2.3, a number of additional constraints on the nucleation rate in individual grains have to be built-in. This is required in order to prevent production of subgrains at unrealistic regions in the grain size distribution. First constraints are considered on nucleation rate in (daughter) grains  $\dot{N}_g$  of size  $r$ , followed by constraints on nucleation rate in parent grains  $(\dot{N}_g)_p$  of size  $r_p$  producing subgrain/new-grains of size  $r$ .

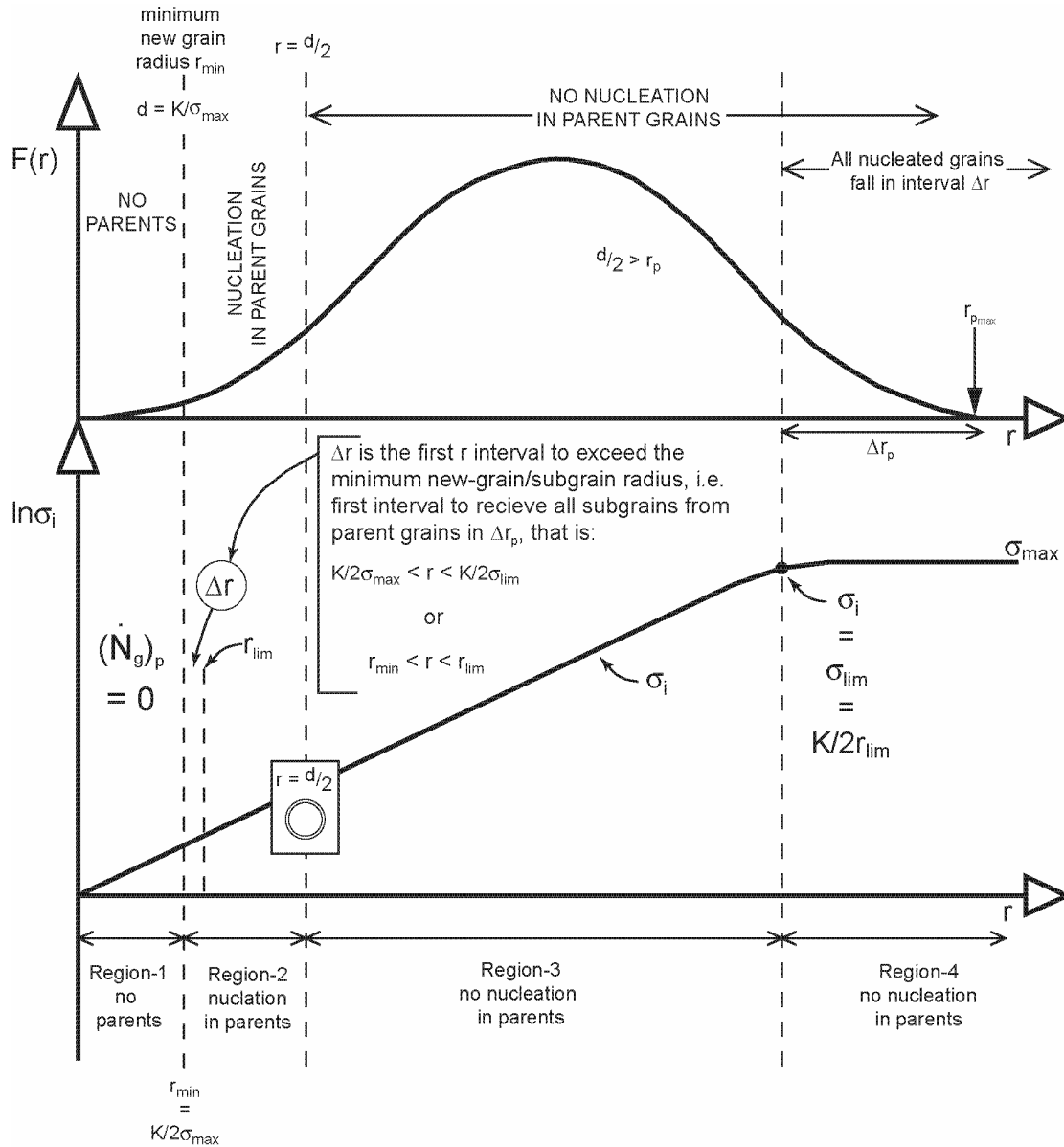


**Figure A2.** Similar schematic illustration as in fig. 4, but now showing four distinct regions (1-4) for which different parent grain nucleation,  $(\dot{N}_g)_p$ , constraints apply. See text for further explanation.

Constraints on  $\dot{N}_g$ .

Recall that the diameter,  $d$ , of subgrains nucleating in a given grain size interval  $\delta r$  is related to the stress,  $\sigma_i$ , for that particular grain size interval, according to relation (21), where  $\sigma_i$  is the solution to relation (6). Fig. A1 shows schematically how  $\sigma_i$ , and subgrain radius ( $= d/2$ ) vary with  $r$ . Starting at the smallest grain size fraction, three regions, which require different criteria on the application of  $\dot{N}_g$ , can be distinguished with increasing grain radius  $r$  (also see fig. A1):

Region-A. In this region grains are smaller than the subgrains they would produce according to the combination of relation (6) and (21). This is not possible and therefore  $\dot{N}_g$  has to be set to zero, that is:

$$\text{If } r \leq d/2 \quad \rightarrow \quad \dot{N}_g = 0 \quad (\text{A1})$$

This constraint is feasible and close to what occurs in nature, since in this region is thought to deform at very low stresses dominated by diffusion creep and thus involving little dislocation activity.

Region-B. In this region grains are larger than the subgrains/new-grains they produce, but are smaller than  $\sim 2$  times the radii of their subgrains/new-grains (i.e.  $d$ ). This means that the produced subgrains will approximately fill the complete grain volume, regardless what type of nucleation, i.e. volume or grain boundary, is considered. We will therefore use the following constraint:

$$\text{If } d/2 < r \leq d \quad \rightarrow \quad \dot{N}_g = \dot{N}_g \text{ for volume nucleation} \quad (\text{A2})$$

Region-C. In this region grain radii are larger than  $\sim 2$  times the radii of the subgrains they produce. Therefore both volume and grain boundary nucleation can be applied, that is:

$$\text{If } r > d \quad \rightarrow \quad \dot{N}_g = \dot{N}_g \text{ for gb or volume nucleation} \quad (\text{A3})$$

In computation the lower bound value of the grain size interval  $\delta r$  will be taken in applying the above criteria.

### Constraints on $(\dot{N}_g)_p$ .

Recall  $(\dot{N}_g)_p$  is the nucleation rate per parent grain (radius  $r_p$ ) delivering subgrains/new-grains of (daughter) radius  $r$ . The diameter,  $d$ , of the subgrains (new-grains) developed in a given parent grain size interval  $\delta r_p$  is  $2r$ . Therefore the stress in the parent grain size,  $\sigma_p$ , is given by relation (70). The parent grain radius,  $r_p$ , producing subgrains of radius  $r$  is thus given by relation (71). If in relation (71) the dislocation creep component starts to dominate the total strain rate, the parent grain radius,  $r_p$ , rapidly approached infinity (fig. A2). Thus  $r_p$  is very sensitive to  $r$  in the dislocation creep regime. Starting at the smallest grain size fraction, four regions, which require different limitations on  $(\dot{N}_g)_p$ , can be distinguished with increasing grain radius  $r$  (see fig. A2):

Region-1. In this region the grain radius is smaller than the minimum new grain radius,  $r_{min}$  (which corresponds to  $d_{min}/2$ ), which can be produced by the maximum parent grain size. So no parent grains exist within the distribution that could produce subgrains/new-grains in this region. Therefore the following constraint applies:

$$\text{If } r < r_{min} \quad \rightarrow \quad (\dot{N}_g)_p = 0 \quad (\text{A4})$$

Region-2. In this region grains are larger than the minimum new grain radius,  $r_{min}$ , and the parents producing grains of this size  $r$  are themselves larger than  $r$ , i.e.  $r < r_p$ . So nucleation occurs in parent grains producing new-grains of radius  $r$ . The nucleation rate in the parent grains will then be according to the choice of volume or grain boundary nucleation. Therefore the following constraint applies:

$$\text{If } r_{min} < r < r_p \quad \rightarrow \quad (\dot{N}_g)_p = (\dot{N}_g)_p \text{ for gb or volume nucleation} \quad (\text{A5})$$

Note that the total number of nuclei collected in the first interval  $\Delta r$  to exceed  $r_{min}$ , is given by the sum of all nucleation events in  $\Delta r_p$  at  $\sigma_{lim} < \sigma_p \leq \sigma_{max}$  (see fig. A2).

Region-3. In this region grains nucleated at size  $r$  would be larger than their parent grains, which is not possible. Therefore no nucleation is possible in parent grains:

$$\text{If } r_p < r \quad \rightarrow \quad (\dot{N}_g)_p = 0 \quad (\text{A6})$$

Region-4. In this region grains nucleated at size  $r$  would still be larger than their parent grains, which is not possible. So the similar constraint (A6) applies as for region-3. Note all nucleation in these grains contributes to new grain addition to the interval  $\Delta r$ .





## Chapter 3

### Deformation induced grain growth in forsterite aggregates

*This chapter has been submitted for publication to Physics of the Earth and Planetary Interiors as: Kellermann Slotemaker, A., de Bresser, J.H.P., Spiers, C.J., and Drury, M.R., Deformation induced grain growth in forsterite aggregates.*

**Abstract.** Coarse-grained olivine materials that are experimentally deformed to high strain show substantial weakening before steady state mechanical behavior is approached. This weakening may be attributed to progressive reduction of the grain size through dynamic recrystallization, resulting in a change in deformation mechanism. On the other end of the deformation spectrum, the deformation of initially fine-grained materials may show hardening related to grain growth. With respect to olivine, broad knowledge is lacking regarding deformation and microstructural evolution of fine-grained aggregates. This is the focus of the present study. We have experimentally investigated the behavior of fine-grained ( $\sim 1 \mu\text{m}$ ) forsterite aggregates containing  $\sim 0.5 \text{ wt}\%$  water and  $10 \text{ vol}\%$  enstatite. Samples were axially compressed to varying strains up to a maximum of  $\sim 45\%$ , at  $600 \text{ MPa}$  confining pressure and a temperature of  $950^\circ\text{C}$ . Microstructures were characterized by analyzing full grain size distributions and textures using SEM/EBSD. Our stress-strain curves showed continuous hardening. When straining was temporally interrupted for short time intervals, no difference in flow stress was observed before and after the interruption. The observed stress vs. strain rate behavior suggests that deformation took place by a grain size sensitive process. Deformed samples showed an increase in grain size with strain up to values twice the starting value. In contrast, grain sizes of samples heat treated without deformation showed only minor increase in grain size. We relate the observed increase in flow stress with strain to grain coarsening, which must be deformation induced. A dynamic grain growth model involving an increase in cellular defect fraction (i.e., fraction of non-hexagonal grains) seems best applicable to the grain growth observed in this study.

### 3.1 Introduction

Meaningful modeling of the geodynamics of the outer Earth requires a detailed understanding of the flow properties of the Earth's upper mantle. Since olivine is the most abundant and weakest mineral in the upper mantle, its flow behavior and the different microstructural processes operating during deformation have been the objective of many laboratory studies. These have yielded mechanical data and microstructural observations that point to grain size sensitive (GSS) diffusion creep and grain size insensitive (GSI) dislocation creep as important deformation mechanisms, with (dynamic) recrystallization being a significant process accompanying GSI creep (e.g., Chopra and Paterson, 1984; Hirth and Kohlstedt, 1995a; 1995b; Karato et al., 1986; McDonnell et al., 1999; Mei and Kohlstedt, 2000a; 2000b; Jackson, 2002). In addition to the effects of temperature, strain rate and stress, laboratory studies on olivine have also included exploration of the effects of pressure, oxygen fugacity, partial melting and the presence of water. Furthermore, mechanical data combined with grain size analysis of plastically deformed samples have been used to calibrate a recrystallized grain size versus stress relation (Van der Wal et al., 1993), forming a very useful tool for estimating paleostress in upper mantle rocks (e.g., Jaroslow et al., 1996; Dijkstra et al., 2002).

Most early experiments on olivine involved deformation to relatively low strains (natural strain  $\sim 0.1$ - $0.2$ ), but it was generally assumed that steady state was attained. Accordingly, low strain 'steady state' flow laws have been used in numerical modeling studies, the rheology being further constrained using the stress-recrystallized grain size relationship for olivine (e.g., Govers and Wortel, 1995; Kameyama et al., 1997; Braun et al., 1999; Yamasaki, 2004). However, recent high shear strain investigations by Zhang et al. (2000) and Bystricky et al. (2000), up to equivalent natural strains of 2, have demonstrated that significant weakening can occur after an initial quasi steady state part of the stress-strain trajectory. This weakening has been mainly attributed to ongoing pervasive dynamic recrystallization and related grain size refinement, leading to a change in deformation mechanism. In the case of olivine materials with a relatively large starting grain size, grain refinement may induce a switch from dominant GSI dislocation to deformation mainly by GSS creep (cf. Rutter and Brodie, 1988). The high strain studies show that progressive change in microstructure is likely to result in a gradual change in flow strength before reaching steady state, implying that for modeling studies constraints are needed on the transient, evolving character of large strain flow.

While the evolution from GSI towards GSS creep through grain size reduction appears well established, broad knowledge is lacking regarding deformation of fine-grained olivine that starts in the GSS creep field. In that case, grain coarsening by grain growth may be the prime cause of microstructural modification influencing large strain transient creep. The question then arises as to whether grain coarsening in deforming aggregates follows a normal grain growth law or if strain significantly affects the growth of grains. The present study is focused on this question. To date, grain growth in olivine material has either been studied under static conditions, i.e. involving heat treatment without straining (e.g., Karato, 1989; Nermond et al., 1993; Nichols and Mackwell, 1991), or it was assumed that normal grain growth could explain the observed increase in grain size during experimental deformation (e.g., Hirth and Kohlstedt, 1995a; Mei et al., 2000a). The one exception where the influence of strain was specifically investigated, to our knowledge, is that of a single low strain experiment on synthetic fine-grained ( $<20 \mu\text{m}$ ) starting material performed by Karato et al. (1986) (run 4765,  $T = 1300^\circ\text{C}$ , their fig. 3.5). In that experiment, flow stress gradually increased during deformation. Straining was interrupted during the run, and when deformation was resumed the flow stress was found to have increased following the trend established before the static interval. Since grain growth during the experiment was substantial, the authors concluded that time rather than strain caused the hardening. Hence, either there was no strain dependent component of grain growth or it was fully insignificant compared with grain coarsening following conventional time dependent normal growth.

The aim of the present study was to further explore the effect of microstructural modification on the flow behavior of polycrystalline olivine deforming initially in the GSS creep field. In particular, we focused on the interaction of grain growth with deformation during deformation to relatively high strains. In order to achieve our goals, we built upon previous experience with very fine grained ( $\sim 1 \mu\text{m}$ ), wet, synthetic forsterite ( $\text{Mg}_2\text{SiO}_4$ ) aggregates containing 10 vol% enstatite ( $\text{MgSiO}_3$ ) (McDonnell et al., 1999; 2002). Choosing this Fe-free material avoids complications regarding control of oxygen fugacity, as is essential for Fe-bearing systems. The material needs to be wet since dry forsterite only shows elastic behavior under the desired experimental conditions. After normal grain growth during initial hot isostatic pressing (HIP) for 24 hours at a temperature of  $950^\circ\text{C}$ , the forsterite-enstatite material shows little further grain growth if heat treatment is continued at similar or lower temperature. Consequently, any effects of strain on grain growth during deformation at such temperature should be resolvable. We deformed the aggregates to various axial shortening strains up to a maximum of 45% (i.e. 0.6 natural strain), at a temperature ( $T$ ) of

950°C, a confining pressure ( $P$ ) of 600 MPa, and a strain rate of  $5.0 \times 10^{-6} \text{ s}^{-1}$ . Under these conditions, the forsterite aggregates deform by GSS creep involving grain boundary sliding (GBS) (McDonnell et al., 1999). For comparison, static (heat treatment only) experiments were done at similar experimental conditions ( $P$ ,  $T$ , duration of runs). Grain growth behavior in the deformed and undeformed samples were compared using scanning electron microscopy (SEM/EBSD) and quantitative image analysis techniques.

## **3.2 Experimental method**

### **3.2.1 Material and sample preparation**

Billets of synthetic forsterite plus 10 vol% enstatite were produced employing a sol-gel based fabrication method described previously (McDonnell et al., 2002). In brief, this involved the preparation of a diphasic gel using high purity MgO powder and tetraethyl orthosilicate. The gel was dried, reaction sintered at 875°C for 2 hours, cold isostatically pressed with 2.5 wt% organic binder at 100 MPa pressure, and finally reaction sintered in air at 1400-1450°C. All samples used in the present study were produced from the same gel batch. Samples were cored from the sintered billets to yield cylinders 8 or 11 mm in diameter and 5, 15 or 16 mm in length. An overview of all samples studied is given in Table 3.1. The porosity of the starting material before HIP, measured by conventional Archimedes method, was ~8 % for samples Fo39-44 and ~1% for HIP4-5. The average grain size of the material at the stage prior to HIPing and deformation testing was ~ 0.6  $\mu\text{m}$ . All samples were jacketed in a gold tube of 0.2 mm wall thickness, and water (~ 0.5 wt%) was added. Standard length of the tubes was chosen such that these precisely fitted samples of 16 mm length. In case of shorter samples, small compensation pistons (50% forsterite + 50% enstatite ceramic at theoretical density) were included. The tube ends were closed with welded-in cups made from 0.25 mm thick gold foil.

### **3.2.2 Deformation apparatus, experiments and data acquisition**

The jacketed samples were first HIPed and then, in most cases, deformed in axial compression at constant displacement rate, in a constant volume, internally heated argon medium apparatus (McDonnell, 1997; McDonnell et al., 1999). This deformation apparatus consists of a water-cooled 1 GPa pressure vessel with a three zone Kanthal-AF wire furnace. The vessel is mounted in a horizontally placed Instron 1362 servo controlled testing machine, which supplies the axial force to the sample during deformation. The force is measured both externally, using an Instron 100 kN load cell, and internally, using an internal force gauge (100 kN full scale, ~20 N resolution). The internal force gauge is a Heard type load cell based on a linear variable differential transformer (LVDT), fully calibrated in terms of load sensitivity and influence of pressure. Piston position is measured externally with the use of an LVDT (2  $\mu\text{m}$  resolution). Temperature is measured using three Pt/10%Rh (type S) thermocouples located next to the gold jacket. From previous calibrations, temperature variation within the sample is known to be in the order of 1-2° (McDonnell et al., 1999).

Four types of experiments were performed (Table 3.1): a) HIP only, b) HIP followed by deformation at a constant strain rate, c), HIP followed by deformation at constant strain rate but interrupted for two intervals of a few hours, and d) HIP followed by deformation with strain rate stepping. All experiments were conducted at a fixed temperature of 950°C

(1223 K) and a confining pressure of 600 MPa. The HIP-only experiments, and HIP-parts of all other tests, involved hot isostatic pressing for time spans varying from 3 to 40 hours. The HIP+deformation experiments were carried out at constant piston displacement rate corresponding to a strain rate of about  $5 \times 10^{-6} \text{ s}^{-1}$ , reaching axial shortening strains between 15 and 45% (natural strains 0.16-0.60) within 10 to 30 hours. Note that imposing a constant piston displacement rate implies that the strain rate gradually increases by a factor of 1.8 by the time 45% sample shortening is reached. Reproducibility of mechanical results was checked by repeating one run (Fo39 vs. Fo40, Table 3.1).

Experiments were terminated as follows. In the case of deformation experiments, displacement was first halted and the deformation piston was pulled back to unload the sample. To initiate quenching in both deformation and static runs, the furnace was then switched off. This caused the sample to cool down to  $\sim 100^\circ\text{C}$  and the pressure to decrease to  $\sim 400$  MPa within  $\sim 10$  minutes. The remaining argon pressure was then released from the vessel at slow pace ( $\sim 10$  MPa/min). Subsequently, the deformed samples were removed from the vessel. Finally, the capsules were opened and the final dimensions of the samples were measured. All measured signals for internal and external axial force, position, pressure and temperature were logged using an A/D converter and PC. Raw data were processed to obtain values for axial stress ( $\sigma$ ), displacement (corrected for apparatus stiffness), strain, strain rate ( $\dot{\epsilon}$ ) and average temperature, assuming homogeneous deformation and constant volume. The very low strength of the gold jacket has been neglected in the processing of the data. The error in measured stress was estimated to be  $\sim 5\%$ .

### 3.2.3 Microstructural analysis

Microstructural imaging was carried out using a scanning electron microscope (SEM) operated in orientation contrast (OC) and Electron Backscattered Diffraction (EBSD) modes. Samples were sectioned parallel to the compression direction and prepared for SEM analysis by Syton<sup>TM</sup> (colloidal silica) polishing the section for at least 1 hour. The SEM (a Philips XL30 Field Emission Gun) was operated at an acceleration voltage of 20 to 25 kV, a sample tilt of  $70^\circ$  and a working distance of 20 to 15 mm. In order to perform grain size analysis the grains in the OC images were traced manually using photo-editing software or transparencies. Quantitative analysis of the traced grain boundary maps was conducted using the image-analyzing program Leica Qwin Pro (version 2.3). The analysis included measurement of median and arithmetic mean grain size (expressed as equivalent circular diameter, ECD), standard deviation of the distribution, grain aspect ratio (i.e., Feret 90/Feret0 ratio: the width and height of the grains measured perpendicular and parallel to the sample long axis / load direction). In addition, the mean pore diameter (expressed as ECD) and the total percentage of the imaged area taken up by pores were measured. We manually counted the coordination number of each grain, i.e. the number of neighboring grains as seen in 2D section. On the basis of these counts, the average 2D coordination number for the (olivine + enstatite) aggregate was determined as well as the fraction of non-hexagonal grains (called the “cellular defect fraction”, after Hillert, 1965).

To measure lattice-preferred orientation (LPO) two samples were analyzed using EBSD. Polished sections were coated with a thin layer of carbon to prevent charging during EBSD analysis. Automated indexing scans at a step size of  $\sim 0.5 \mu\text{m}$  were performed and crystallographic pole plots were made using the post-processing software package Channel 5 (HKL Ltd).

Table 3.1 Characteristics of the experiments and measured microstructural parameters<sup>1</sup>

Sample number	Start	Fo39	Fo40	Fo41	Fo43 <sup>5</sup>	Fo49	Fo42	Fo44	HIP4	HIP5
Type of experiment <sup>2</sup>	-	H+D	H+D	H+Di	H+Ds	H+D	H+D	H	H	H
Initial sample length x diameter [ $\mu\text{m}$ ]	-	16 x 8	16 x 8	16 x 8	16 x 8	15 x 8	5 x 8	16 x 8	5 x 11	5 x 11
HIP-duration [hrs]	-	3	24	234	15	20	14	17	9	40
Deformation-duration [hrs]	-	17.8	18.8	17.9	35.4	9.1	30.2	-	-	-
Total duration of experiment [hrs]	-	20.8	42.8	40.6	50.4	29.1	44.2	17	9	40
					4.8					
					9.3					
Strain rate [ $10^{-6} \text{ s}^{-1}$ ]					1.13					
					5.23					
					10.8					
	-	5.07	5.01	5.12	1.26	5.29	5.85	-	-	-
					17.3					
					31.3					
Flow stress <sup>3</sup> [MPa]					9.9					
					41.1					
					83					
	-	32.7	33.9	25	31.6	35.4	28.9	-	-	-
Axial shortening strain [%]	-	28	27.9	27.1	28.4	15.5	45.6	-	-	-
Number of grains	301	281	300	297	294	677	147	556	917	810
Mean grain size [ $\mu\text{m}$ ]	0.65	1.35	1.32	1.34	1.36	0.93	1.88	0.89	0.78	0.85
Standard error of mean grain size [ $\mu\text{m}$ ]	0.02	0.04	0.04	0.04	0.04	0.02	0.07	0.01	0.01	0.01
Standard deviation of grain size [ $\mu\text{m}$ ]	0.31	0.65	0.71	0.71	0.65	0.39	0.91	0.36	0.37	0.37
Median grain size [ $\mu\text{m}$ ]	0.61	1.26	1.17	1.2	1.2	0.87	1.71	0.84	0.71	0.78
Average Feret90/Feret0 ratio	1.17	1.21	1.15	1.12	1.09	1.2	1.2	1.1	1.23	1.13
Standard error of average Feret ratio	0.01	0.03	0.03	0.02	0.02	0.01	0.03	0.02	0.01	0.01
% area of porosity	6.2	0.9	1.6	2.1	0.6	0.9	0.6	2.3	4.3	3.5
Mean pore diameter [ $\mu\text{m}$ ]		0.37	0.23	0.29	0.21	0.18	0.22	0.23	0.24	0.24
Defect fraction	0.78	0.805	0.833	0.821	0.813	0.795	0.84	0.753	0.803	0.798
Average coordination number	4.96	5.59	5.34	5.38	5.53	5.61	5.64	5.48	5.29	5.31

<sup>1</sup>All experiments were done at constant temperature (950 °C) and pressure (600 MPa).

<sup>2</sup>H = HIP only, H+D = HIP followed by deformation, H+Di = HIP plus interrupted deformation, H+Ds = HIP plus strain rate stepping.

<sup>3</sup>value at 15% strain for all samples except for steptest Fo43 where average values are given for each step.

<sup>4</sup>includes two periods of ~7 hrs in which straining was interrupted, at strains of ~6% and ~24%.

<sup>5</sup>see Figure 3 for strain intervals of this step test.

## 3.3 Results

### 3.3.1 Mechanical behavior

The mechanical data ( $\sigma, \dot{\epsilon}$ ) obtained and the experimental conditions used are summarized in Table 3.1. Selected stress-strain curves of the deformation experiments performed at constant strain rate are shown in fig. 3.1. The stress-strain curves start with a rapid, quasi-elastic increase in flow stress up to 10-30 MPa in the first 1-2% strain. Then, after yielding, continued increase in flow stress follows at a slower rate. The rate of hardening increases with increasing strain, except in experiment Fo42, which employed the shortest sample tested. Fig. 3.2 shows the stress evolution as a function of time for

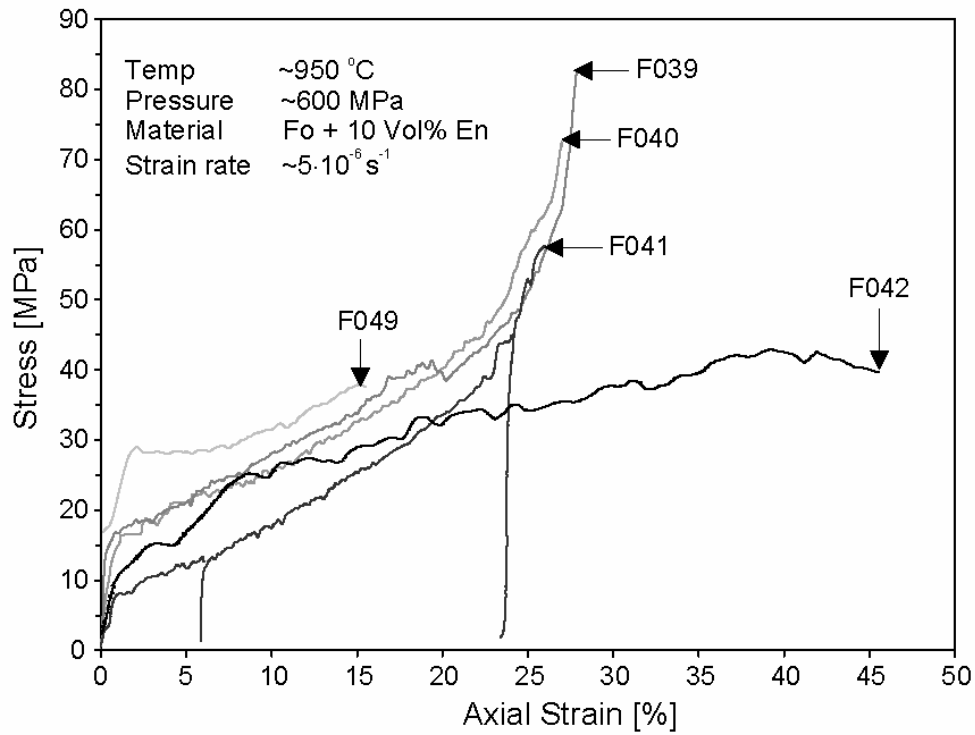


**Figure 3.1.** Stress-strain curves for experiments F039-42 and 49. Stress drops during experiment F041 indicate periods of unloading, see fig. 3.2.

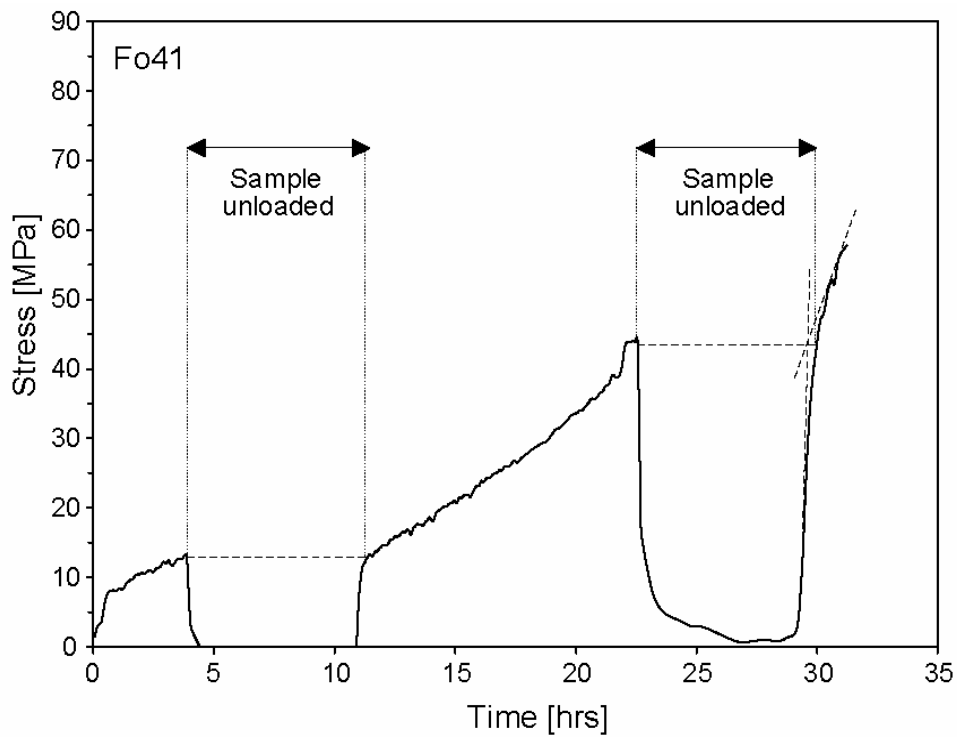


**Figure 3.2.** Stress-time curve for the annealing experiment F041; sample was unloaded twice during experimentation and left at high temperature/pressure.

experiment Fo41, which was unloaded twice, at strains of ~6% and ~24% (see also fig. 3.1). On reloading, deformation continued at nominally the same stress level as measured before the interruption, i.e. the material did not harden during the load-free period.

The strain rate step test Fo43 (fig. 3.3) provides an impression of the strain rate sensitivity of our material (at  $T = 950^\circ\text{C}$ ). Since steady state was not achieved in any of the steps, we determined the strain rate sensitivity by comparing stress values at identical strains (5, 10, 15 and 20 %), using linear extrapolations to higher and lower strains under the assumption of constant hardening within the strain interval under consideration. The results are presented in fig. 3.4, which includes the data obtained in the constant strain rate experiments (Fo39-42). Using a conventional power law type strain rate vs. stress relation ( $\dot{\epsilon} \sim \sigma^n$ ), the stress exponent,  $n$ , was calculated from linear regression least-squares fits to the data at 5, 10, 15 and 20 %. The values for  $n$  range from 1.3 at 5% strain to 1.5 at 20% strain, with an average value of  $n = 1.5 \pm 0.3$ . For comparison, curves for the flow law calibrated by McDonnell (1997), with  $n \sim 2.14$  (calibrated at 5 % strain) are shown for two grain sizes, i.e. 0.5 and 1.0  $\mu\text{m}$ . Note that this flow law was calibrated for similar synthetic forsterite aggregates as used in our study, but with lower enstatite content (2.5 instead of 10 vol% enstatite in this study).

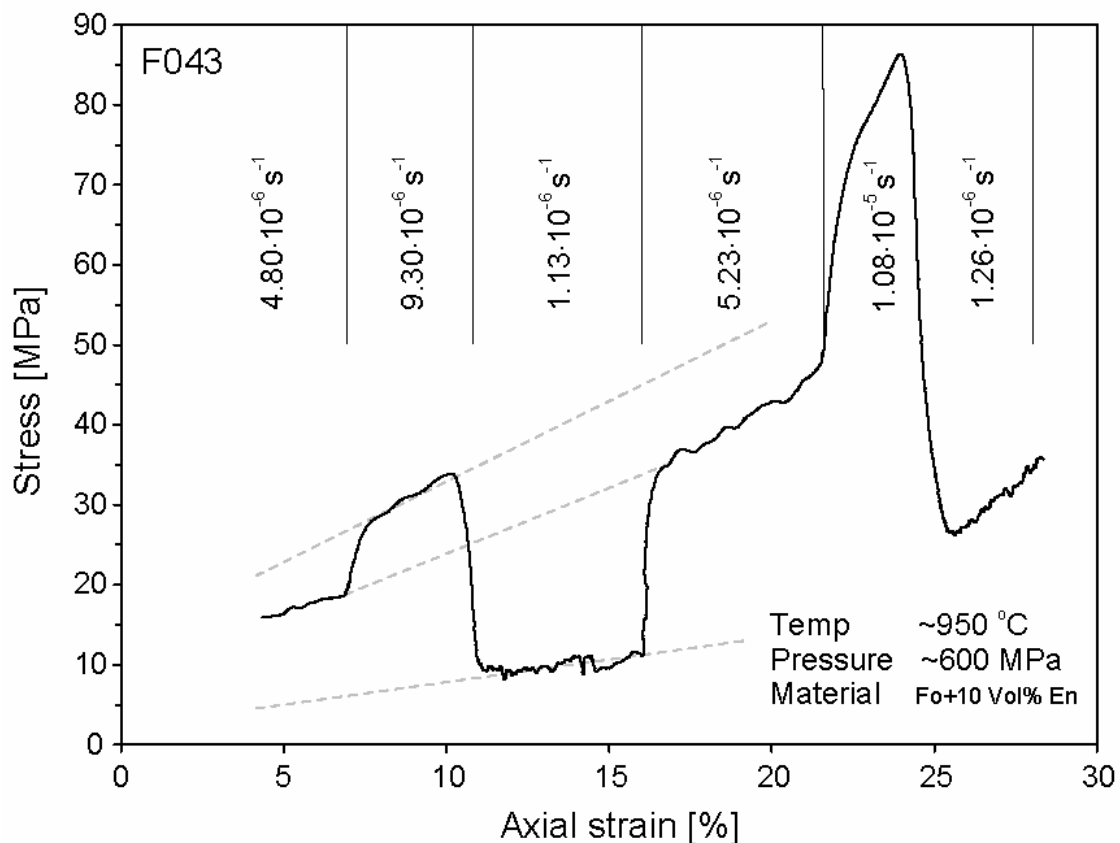


**Figure 3.3.** Stress-strain curve for strain rate stepping experiment Fo43; note no data were recorded for the first 4% strain due to a logging error. Strain rates are indicated for each step, flow stresses for the different steps are linearly inter- and extrapolated, indicated by light dashed gray lines, to determine stress estimates at fixed strains for each strain rate.

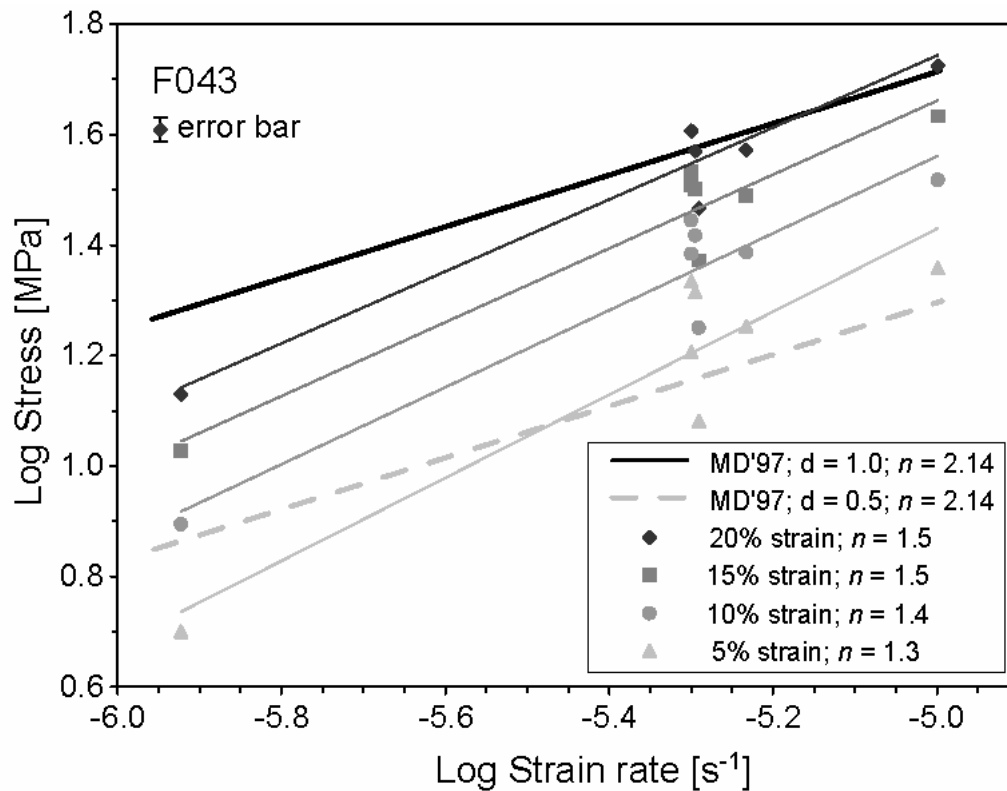


**Figure 3.4.** Stress (extrapolated) versus strain rate data at different strains (5, 10, 15 and 20 %) for all experiments. Error bar indicates a maximum error in stress of 5%. Average values for stress exponent  $n$  are indicated in the legend for each strain value. For comparison, 'model' lines calculated using the flow law of McDonnell (1997) are also shown (heavy black and dashed heavy grey lines) for different grain sizes (0.5 and 1.0  $\mu\text{m}$ ).

### 3.3.2 Microstructures

The deformed samples were found to have retained a near cylindrical shape, except for some minor distortion at the samples ends, indicating relatively homogeneous deformation. Fo42 is an exception, showing more visible barreling, probably related to the shorter initial sample length and some deformation of the compensation pistons used to fill up the capsule. The SEM microstructures of all samples show a fine-grained, homogeneous foam structure (fig. 3.5). The grains contain very little internal structure and have predominantly equidimensional shapes. Grain boundaries are straight or gently curved and triple junctions of  $120^\circ$  are common (see also McDonnell (1997) and McDonnell et al. (1999)). Small, 3- or 4-sided grains often show outwardly curved grain boundaries. Intergranular pores can easily be recognized on the SEM images, but enstatite grains are less clearly distinguished. The representative microstructures seen in fig. 3.5 qualitatively demonstrate that the average grain size of a HIP+deformed sample (fig. 3.5b) is larger than that of a HIPed-only sample (fig. 3.5a), at similar experimental duration. Abnormally large grains have not been seen in any of the samples.

**Figure 3.5.** SEM orientation contrast (OC) micrographs showing (a) microstructure of grain growth test (Fo44) and (b) microstructure of  $\sim 28\%$  strained material (Fo39); compression is horizontal at close to identical experimental duration. Pores are visible as solid black (b) or clear white (a; inverted image) elements in the micrographs.



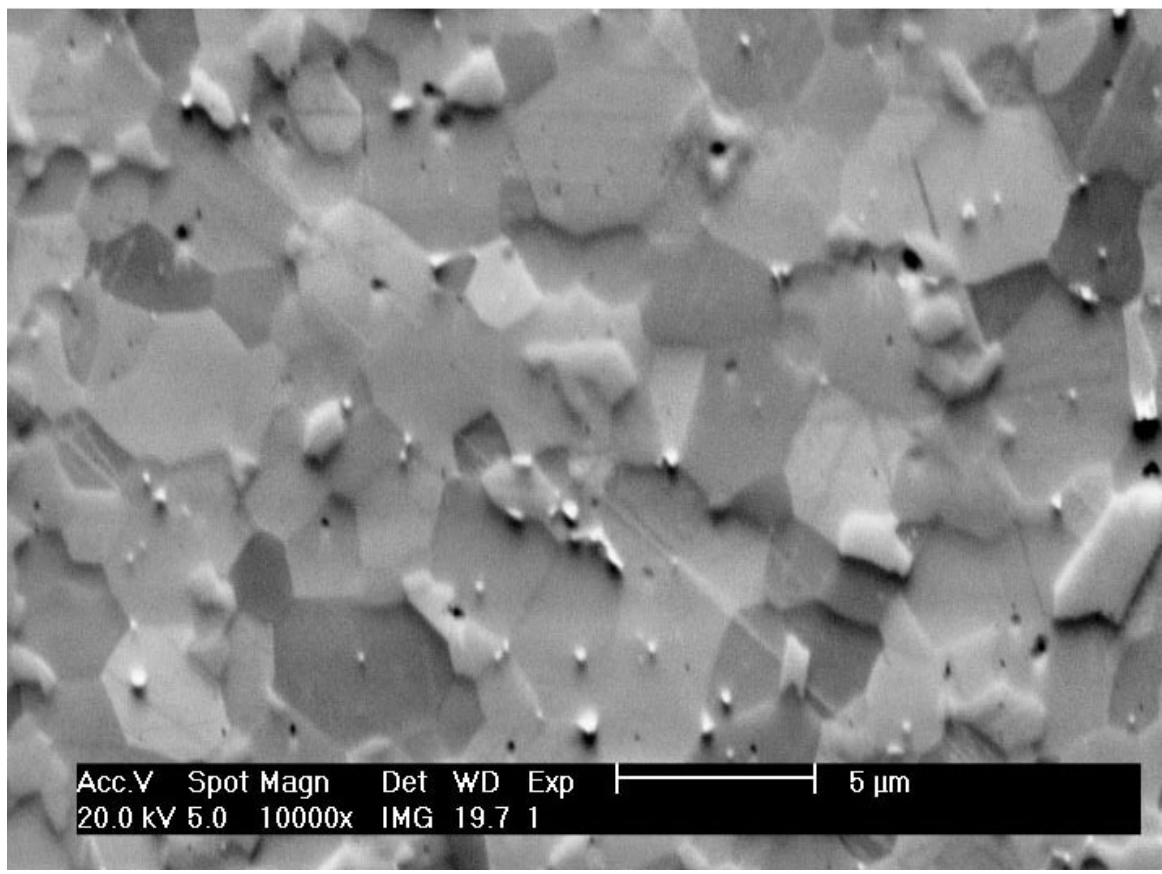
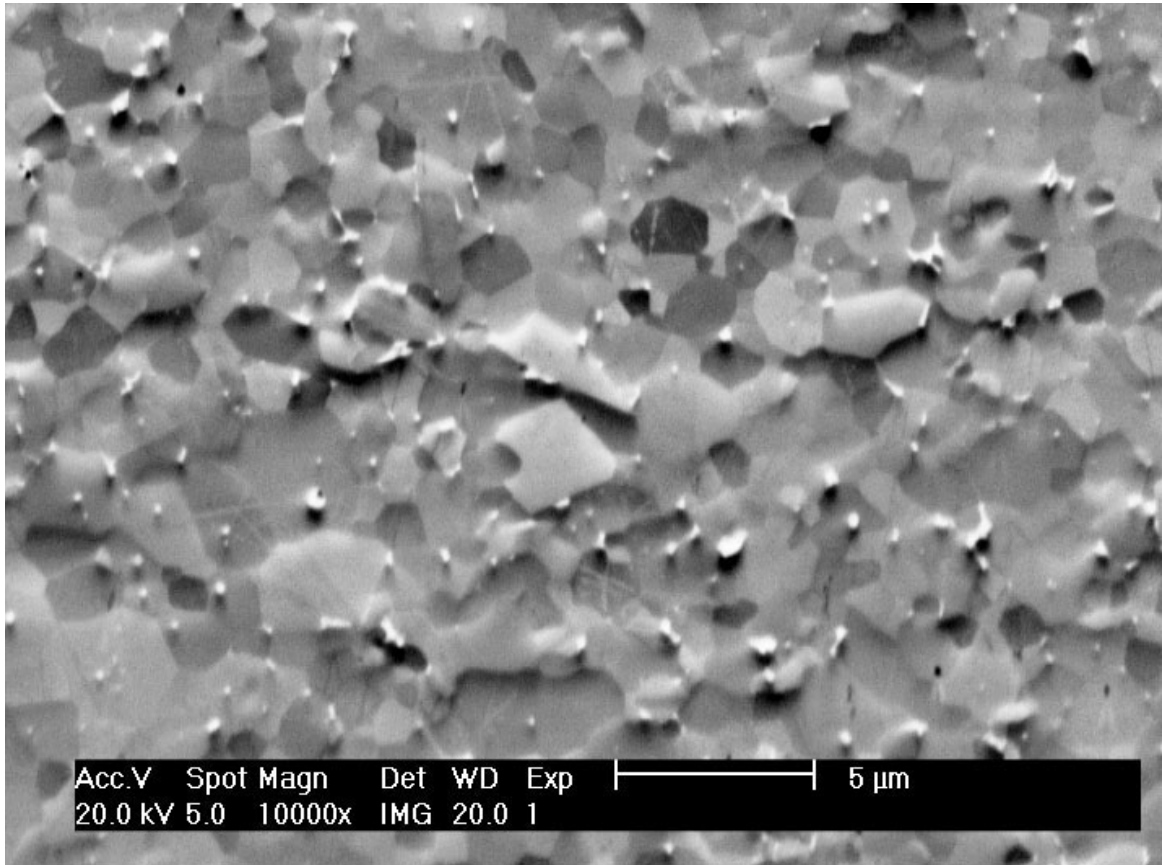


**Figure 3.5**

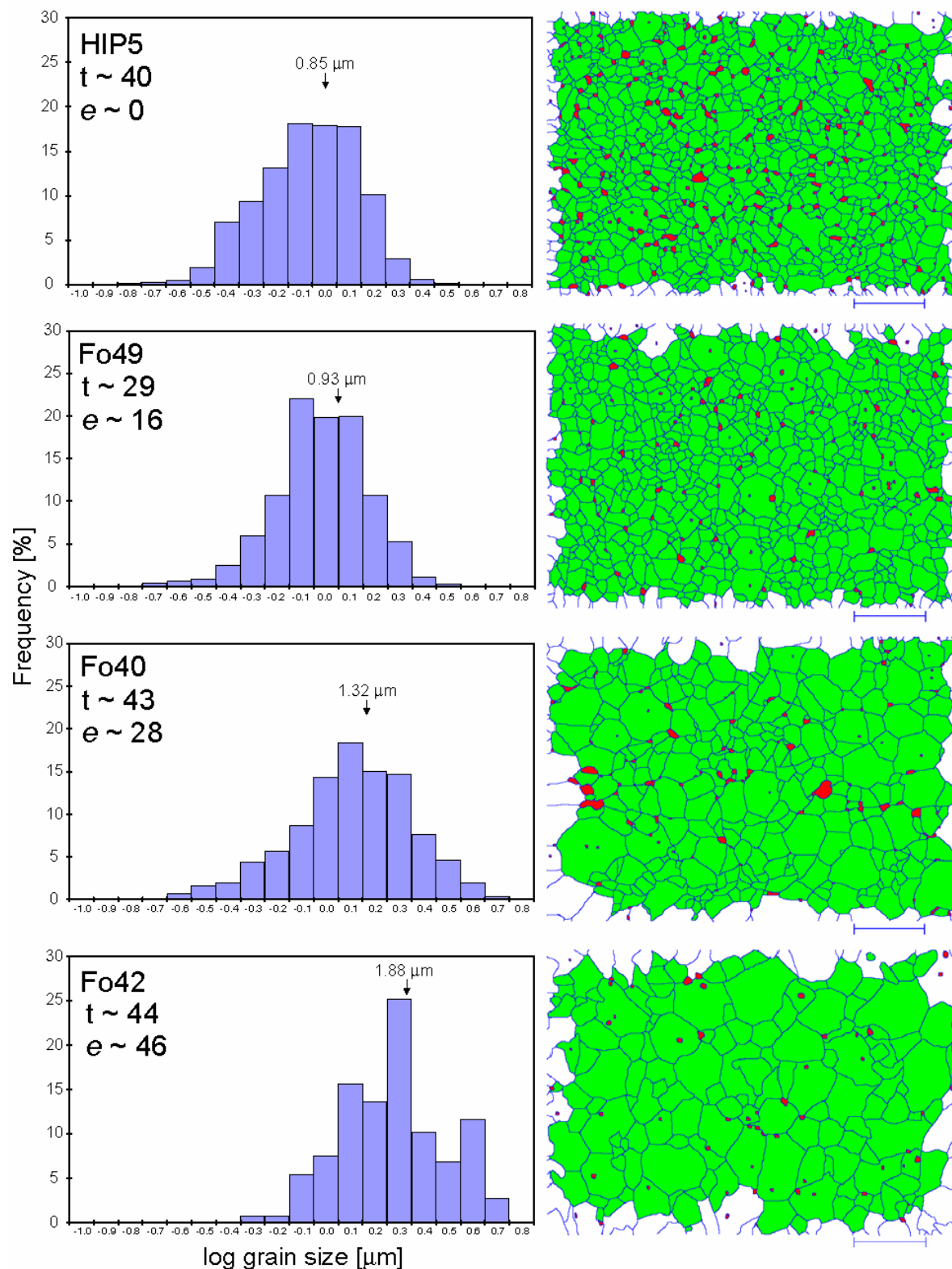


**Figure 3.6.** Logarithmic grain size (ECD) frequency distributions with accompanying grain boundary tracing maps for representative samples. Bin size 0.1. Vertical arrows indicate the arithmetic mean value for each distribution;  $t$  and  $e$  indicate total experimental duration in hrs and axial shortening strain in %, respectively.

### 3.3.3 Quantitative microstructural analysis

Traced grain boundary maps and frequency histograms of (logarithmic) grain size distributions of samples representing the full range of sizes are presented in fig. 3.6. Values for the measured microstructural parameters are given in Table 3.1. No distinction was made between forsterite and enstatite grains, since these are similar in size (cf. McDonnell et al., 1999; 2000) The arithmetic mean grain size (in linear space) varies from 0.6  $\mu\text{m}$  for the starting material (pre-HIP) to 1.9  $\mu\text{m}$  for sample Fo42 deformed to 45% strain. The mean grain sizes for all experiments have been plotted as a function of total experiment duration in fig. 3.7. The figure shows that HIPing at 950°C results in an increase in mean grain size from 0.65  $\mu\text{m}$  to  $\sim 0.9$   $\mu\text{m}$  in the first 10-15 hours, together with a decrease in porosity (see Table 3.1), but that ongoing heat treatment (up to 40 hrs) at pressure does not result in any further increase in grain size. Note that the sample HIPed and deformed to 15% strain ended up with a grain size slightly larger than that of HIP-only samples ( $0.93 \pm 0.01$   $\mu\text{m}$  and  $0.85$ - $0.89 \pm 0.01$   $\mu\text{m}$ , respectively; HIP > 15 hrs). Moreover, the forsterite aggregates HIPed and subsequently deformed to higher strains showed grain sizes substantially larger than that of equivalent HIP-only samples (fig. 3.7). This is best seen in the data for a total experiment duration of  $\sim 40$  hrs (fig. 3.7), where the samples deformed to 30% or 45% strain show a grain size of 1.6 to 2.4 times that of the HIP-only sample. Strikingly, the mean grain size for the samples deformed to 30% strain does not appear to have been influenced by the total duration of the experiment, at least not for periods ranging 20-50 hours.

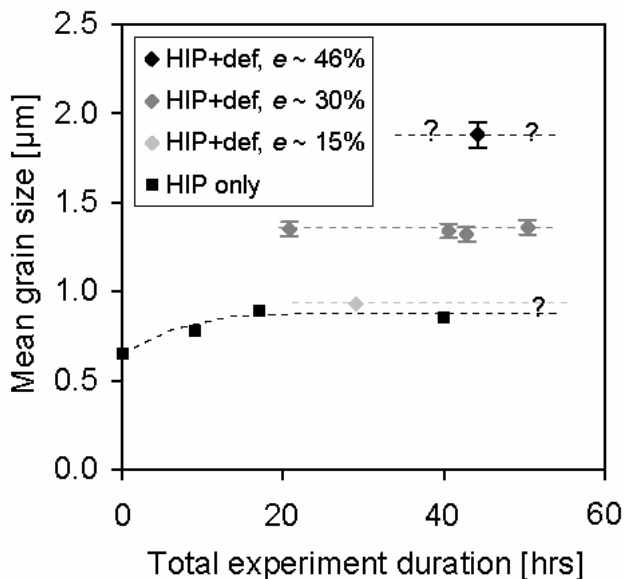


**Figure 3.7.** Arithmetic mean grain size vs. total experiment duration; error-bars show standard errors of the mean; error bars are smaller than symbols for all HIP-only tests and Fo49.

The effect of strain on grain size is corroborated by fig. 3.8a, for samples HIPed beyond the time required to obtain a stable grain size in HIP-only samples (i.e. HIP > 10 hours – see fig. 3.7). However, the grain aspect ratio (expressed as Feret90/Feret0) hardly changed as a function of strain (fig. 3.8b). In other words, the sample strain is not visible in the average grain shape after deformation. The average 2D coordination number (fig. 3.9a) shows no systematic trend with strain, but the fraction of non-hexagonal grains clearly increases, from  $\sim 0.78$  in undeformed samples to 0.84 at 45% strain (fig. 3.9b).

The porosity measured from the SEM images (area% - Table 3.1) decreased from  $\sim 6\%$  in the starting material to 2-4% after HIP, and was further reduced to 0.5-2% during deformation. The porosity decrease during deformation appears to take place in the first 15%

of straining; no systematic change in porosity has been observed at progressively higher strain.

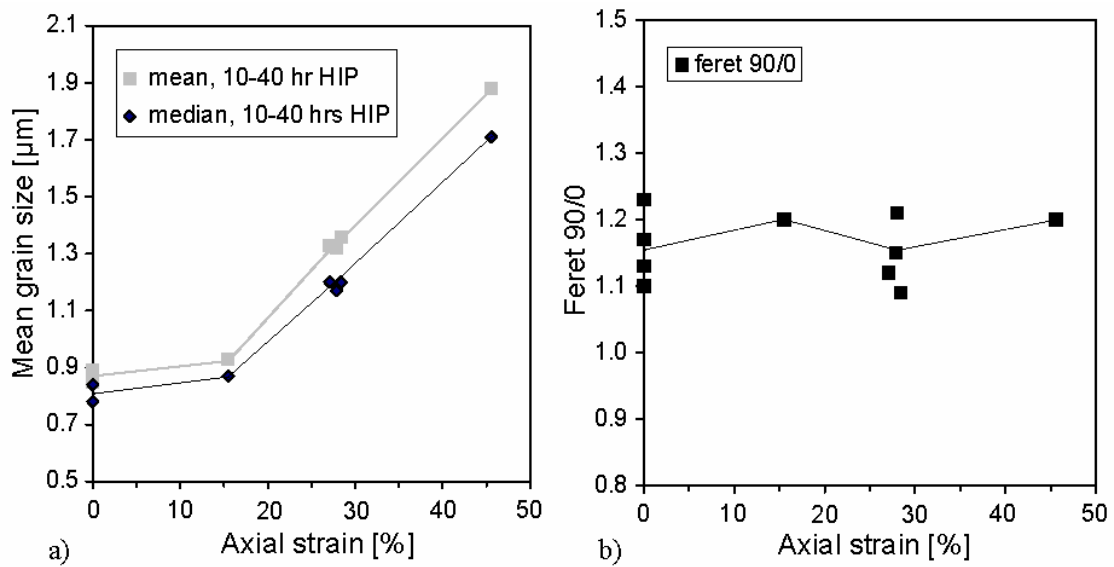


**Figure 3.8.** a) Mean grain size (arithmetic and median) vs. axial strain (pre deformation HIP times > 10 hrs). b) Aspect ratio's (Feret 90/Feret0) as a function of axial strain. 'Ty-lines' are drawn between mean values at fixed strain.

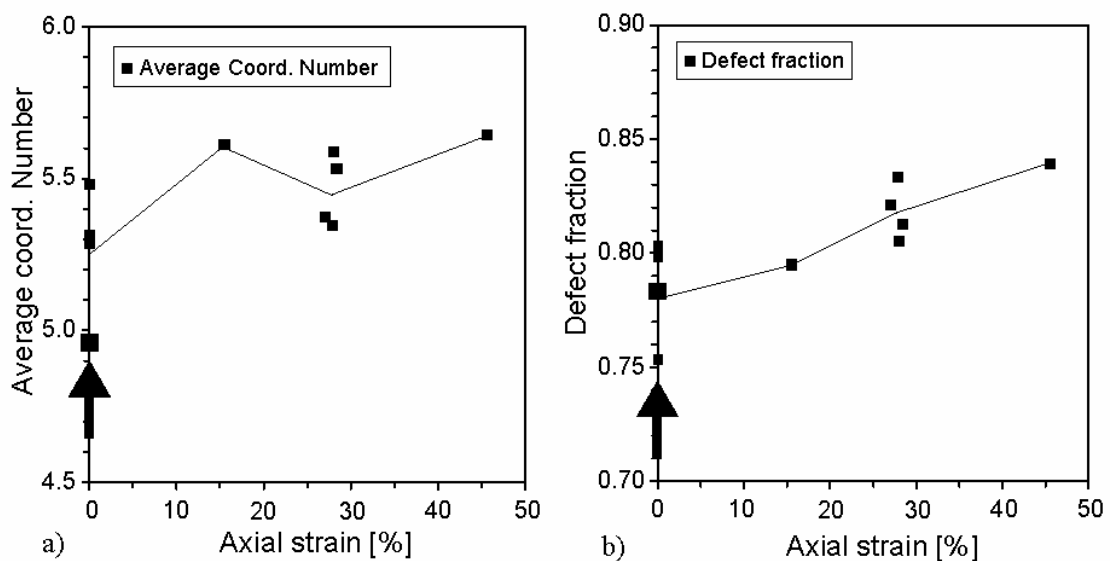
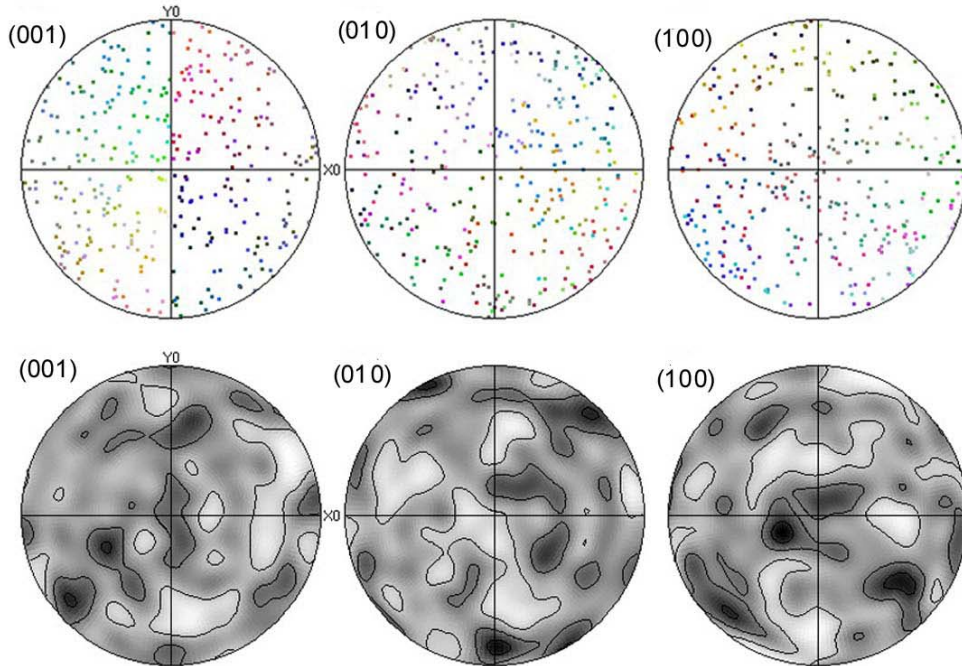
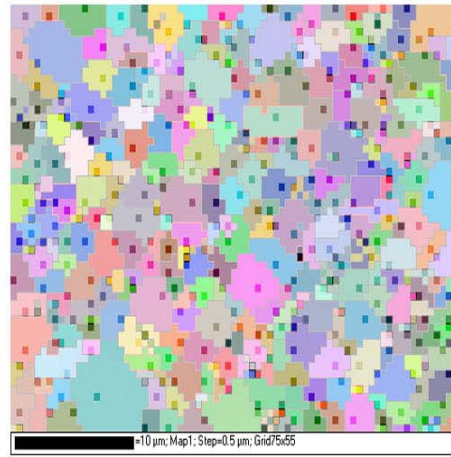
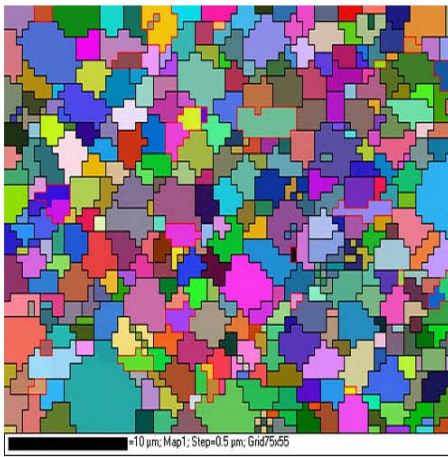
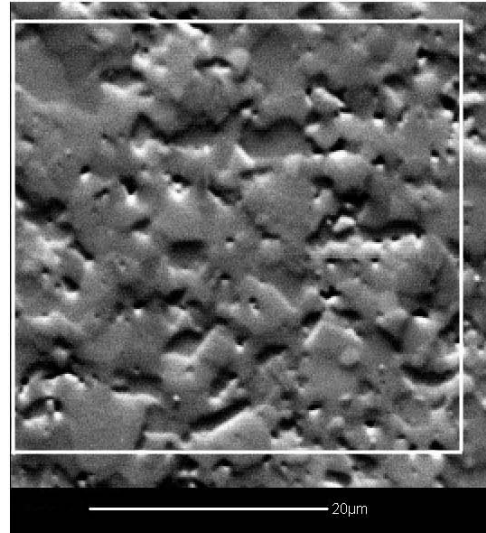


**Figure 3.9.** Average coordination number (a) and cellular defect fraction (fraction of non-hexagonal grains) (b) as a function of strain. 'Ty-lines' are drawn between mean values at fixed strain. Black arrows indicate position of the HIP-only tests and the starting material (larger black square symbol).

**Figure 3.10.** EBSD-map and pole figures (upper hemisphere, equal area projection) for sample Fo39. The EBSD-map is accompanied by an OC image, showing location of map. Compression direction in the figures is horizontal; the analysis includes 342 fo grains. Pole density contour-lines are drawn at every 2/3 MUD (Multiples of Uniform Density), with 14.4° Half-width and 5° cluster size.



*Grain growth in forsterite aggregates*



### 3.3.4 Crystallographic preferred orientation analysis

Color-coded EBSD maps and pole figures were made for two deformed samples (Fo39 and Fo40). Maps and plots for Fo39 are shown in fig. 3.10. The results for Fo40 are very similar to those for Fo39. Note that the spatial step size chosen for the EBSD analysis was such that grains smaller than  $0.5\ \mu\text{m}$  have not been analyzed (i.e., grains from the left tail of the histogram of fig. 3.6a were not included). From inspection of fig. 3.10, it is evident that the positions of the scattered density maxima show no systematics, and that the contour plots have density maxima that do not rise above 2 MUD (multiples of uniform density). The EBSD measurements thus show that the samples have little or no lattice preferred orientation.

## 3.4 Discussion

### 3.4.1 Time-dependent vs. strain-dependent grain growth

The HIP-only samples showed that a more or less stable average grain size of  $\sim 0.9\ \mu\text{m}$  develops within the first 10-15 hours of hot pressing at  $950^\circ\text{C}$  and 600 MPa pressure. Continued heat treatment at high pressure did not result in significant further growth of the grains. We can compare the observed grain growth in our HIP-only forsterite aggregates with grain growth kinetics observed by Karato (1989) for dense fine-grained (wet) aggregates of San Carlos olivine, heat treated at  $1200\text{-}1300^\circ\text{C}$  and 300 MPa pressure. If we extrapolate the olivine grain growth law calibrated by Karato to our working temperature of  $950^\circ\text{C}$ , a starting grain size of  $0.65\ \mu\text{m}$  (Table 3.1) is predicted to evolve to  $\sim 20\ \mu\text{m}$  in 50 hours. Obviously, grain growth in our material is far slower, suggesting pinning of the grain boundaries by small pores or the larger scale enstatite grains present in our samples. In addition to differences in character of the olivine material, the external pressure might play a role in this (300 MPa in Karato's work vs. 600 MPa in our study), since it is known from materials science that the pressure required for densification at the same time can suppress grain growth during HIP. For example, Park and Park (2001) describe grain growth of alumina that was inhibited during extended HIP treatment compared to sintering during pressure-less heating.

Regarding the HIP+deformed samples, the following lines of observation are important. First, deformed samples showed average grain sizes that were larger than seen in the HIP-only samples for similar experimental time spans (fig. 3.7). Second, the average values for the grain size increased with increasing strain (figs. 8), while the total time taken to perform the HIP and subsequent deformation step was not of influence (see data for 30% strain in fig. 3.7). Third, along with the increasing grain size, the HIP+deformed samples showed a continuous increase in flow stress with increasing strain (except for the last part of Fo42 – fig. 3.1), suggesting that grain growth caused the hardening. However, the experiment in which straining was interrupted for a couple of hours (fig. 3.2) did not show an increase in flow stress after resuming deformation, indicating that the hardening was directly related to strain and not to time. On the basis of these points, we conclude that grain growth in our synthetic forsterite aggregates, at time spans above 15 hours (i.e. after initial HIP), is strain rather than time dependent. In other words, the material shows microstructural evolution governed by dynamic grain growth.

The strain-dependent nature of grain growth in our samples differs from the grain growth behavior seen in the experiments of Karato et al. (1986) on synthetic olivine, mentioned above. Karato et al. concluded that time was the main parameter controlling grain

growth during deformation and, hence, that a static grain growth law is sufficient to describe grain size evolution during GSS deformation. We speculate that normal grain growth in Karato's olivine samples was not hindered by pinned grain boundaries, so that a dynamic component might well have been present, but if so may have been too small to be noted. In contrast, our approach involving HIPing of porous (wet) aggregates followed by extended heat treatment at high pressure of the densified material resulted in subdued normal grain growth, allowing a dynamic contribution to be noticeable.

### 3.4.2 Deformation mechanism and hardening

The low value obtained for the power law stress exponent holding for our data,  $n = 1.5 \pm 0.3$  at  $T = 950$  °C (fig. 3.4), compares well with  $n = 1.7$  at 950°C for synthetic wet forsterite with 2.5 wt% enstatite obtained in a previous study (McDonnell et al., 1999). In that study,  $n$ -values changed with temperature, with an average value of  $n = 2.1 \pm 0.3$  holding for the temperature range 850-1000°C. The flow behavior was inferred to be dependent on grain size via a relation of the form  $\dot{\epsilon} \propto d^{-3}$ . On the basis of a comparison of experimental data with theoretical creep models it was concluded that a GSS, possibly grain boundary sliding (GBS) dominated deformation mechanism best explains the observed behavior (see also Chopra, 1986; Karato et al., 1986; Lee et al., 2002). Our findings regarding the lack of any change in average grain aspect ratio with increasing strain (fig. 3.8b) and the near random lattice orientations of grains in the deformed material (fig. 3.10) strongly support a GSS+GBS creep mechanism.

To gain insight into the strain hardening effect seen in our experiments, the flow law parameters of McDonnell et al. (1999) have been used to calculate  $\sigma$ - $\dot{\epsilon}$  isotherms for grain sizes close to values characterizing the starting and deformed microstructures reported in this study, i.e. 0.5 and 1  $\mu\text{m}$ , respectively. These isotherms, included in fig. 3.4, more or less bound the stress-strain rate isotherms obtained for different strains from experiment Fo43. This suggests that the strain hardening of the material and the strain-induced growth of the forsterite grains are related, as already suggested in section 4.1. We can estimate the amount of hardening during a given experiment assuming that a creep rate equation of the form  $\dot{\epsilon} = A \cdot d^{-p} \cdot \sigma^n$  holds, with grain size  $d$ , flow stress  $\sigma$ , and with  $p = 3$  for GSS flow (McDonnell et al, 1999) and  $n = 1.5$  (this study, fig. 3.4). Two effects need to be accounted for: a) the change in grain size with increasing strain, and b) the increase in strain rate caused by keeping the piston displacement rate constant in the experiment (section 2.2) while the sample is progressively shortened (factor 1.4-1.8 for 30-45% strain). For samples deformed to 30% strain (Fo39-Fo41), with a 1.6 fold increase in grain size (Table 3.1), the flow stress is predicted to increase by a factor of  $\sim 3.5$ , i.e. a 20 MPa stress at yield is increased to  $\sim 70$  MPa at 30% shortening. This estimate is in good agreement with the actual hardening as seen in the experiments (fig. 3.1), supporting the inferred relation between strain hardening of the fine-grained olivine samples and the strain dependent (dynamic) grain growth.

Experiment Fo42 did not show hardening in the same way as observed in the other experiments. We believe that this is related to the substantially inhomogeneous deformation (barreling) of the sample and the observed deformation of the pistons used in the sample assembly to compensate for the short initial length of the sample.

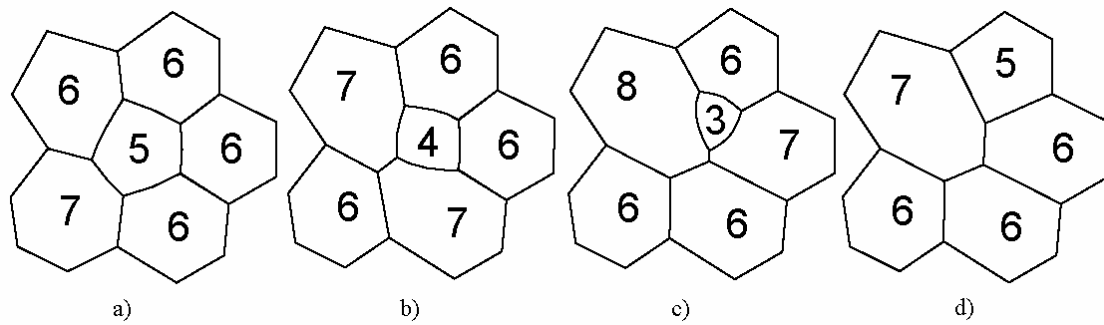


**Figure 3.11.** Schematic representation of surface energy driven grain boundary migration, showing, in four stages, climb of a cellular dislocation, i.e. the 5-7 combination in (a). In (b) the continued shrinking of the central 5-sided grain in (a) has resulted in a neighbor switch (arrow). The now 4-sided central grain continues to shrink leading to another neighbor switch in (c) (see arrow). In (d) the resulting 3-sided grain disappeared and the original 5-7 combination in (a) has climbed one level upwards.

### 3.4.3 Mechanism of strain-dependent grain growth: the role of cellular defects

In ceramic materials and metals it is often observed that GSS, GBS dominated flow (or superplasticity) is accompanied by dynamic (strain dependent) grain growth. Various models for dynamic grain growth have been put forward (Bate, 2001; Clark and Alden, 1973; Holm et al., 1977; Rabinovich and Trifonov, 1996; Sato et al., 1990; Seidensticker and Mayo, 1998b; Sherwood and Hamilton, 1994; Wilkinson and Caceres, 1984). Although varying in detail, the majority of these models are built upon topological changes occurring during deformation by GBS, in particular grain neighbor switching events and related changes in coordination number distribution and cellular defect fraction (fraction of non-hexagonal grains). Ashby and Verrall (1973) were amongst the first to propose grain switching during GBS. This can be referred to as dynamic grain switching and involves material (grain) translation and rotation. Earlier, Hillert (1965) had proposed the concept of varying grain coordination number or “cellular dislocations” being responsible for normal grain growth, which involves static grain switching through grain boundary reconfiguration, but without deformation. In 2-D array of grains, a cellular dislocation is defined as the combination of a 5-sided grain neighboring a 7-sided grain (see fig. 3.11). A single non-hexagonal grain is called a ‘defect’ within an array of grains. Others extended the Hillert’s model to 3-D and showed a geometric analogy with crystallographic dislocation theory (Cahn and Padawar, 1965; Morral and Ashby, 1974). Viewed in this framework, a cellular dislocation can climb via multiple grain switching events, causing normal grain growth (fig.11). Hillert (1965) already pointed out that for normal grain growth to occur, the microstructure must be characterized by a log normal distribution of grain sizes. Also a fixed normal distribution in grain coordination number is generally observed during normal grain growth (Seidensticker and Mayo, 1998b). Hillert (1965) quantitatively evaluated this, concluding that the defect fraction in a 2-D microstructure should be  $\sim 0.75$  for normal grain growth. Combining the original models of Hillert and Ashby and Verrall, Sato (1990) was the first to suggest that GBS in combination with movement of cellular dislocations can lead to dynamic grain growth. Sato’s (1990) hypothesis is that deformation will assist static grain switching, resulting in enhanced (static + dynamic) grain switching, which according to Sherwood and Hamilton (1992) may increase the defect fraction. A higher defect fraction will enhance grain growth as well considering the original normal grain growth model of Hillert (1965). Based



upon this, Sherwood and Hamilton (1992; 1994) propose the following relation between the dynamic grain growth rate,  $\dot{d}_{dyn}$ , and the strain rate,  $\dot{\epsilon}$  :

$$\dot{d}_{dyn} = \lambda \cdot d \cdot \dot{\epsilon} \quad (1)$$

where  $\lambda$  is a function of strain rate and strain, but is sometimes shown to be a constant of order unity (Sherwood and Hamilton, 1992),  $d$  is the instantaneous average grain size, being a function of time and strain. If  $\lambda$  is constant and if static grain growth is negligible, relation (1) integrates to (after Sherwood and Hamilton, 1994):

$$d = d_0 \cdot \exp(\lambda \cdot \epsilon) \quad (2)$$

where  $d_0$  is the initial grain size. According to Sherwood and Hamilton (1992; 1994), rate parameter  $\lambda$ , in (1) and (2), largely depends on the defect fraction  $X_d$ . That is the higher the defect fraction the larger is  $\lambda$ , giving:

$$\lambda = k \cdot X_d \quad (3)$$

where  $k$  is a scaling constant that is complexly dependent on the model geometry (e.g. the fraction of strain rate taken up by GBS). Seidensticker and Mayo (1998a) approximate the DGG rate  $\dot{d}_{dyn}$  in (1) by an average grain growth rate using:

$$\dot{d}_{dyn} \approx \left( \frac{d_f - d_{stat}}{t} \right) \quad (4)$$

where  $d_f$  is the final grain size after deformation,  $t$  is the time of deformation and  $d_{stat}$  is the (predicted) grain size for only static grain growth within the same time interval. Seidensticker and Mayo (1998a) normalized the dynamic grain growth rate in (1) and (4) by the instantaneous grain size  $d$ , rewriting (1) as

$$\frac{\dot{d}_{dyn}}{d} = \lambda \cdot \dot{\epsilon} \quad (5)$$

Equation (5) allows easy comparison of experimental dynamic grain growth data for a wide range of materials, both metals and ceramics. Convincing support was found by Seidensticker and Mayo (1998a) for relation (1), with  $\lambda$  varying between 0.04 and 1. Looking now at our data, the observed trends of increasing defect fraction and increasing grain size with increasing strain (fig. 3.8a & 9b, respectively) are in qualitative agreement with models relating deformation induced grain growth to enhanced neighbor switching and increase in defect fraction during GBS. The question then arises as to the value for  $\lambda$  (equation (1)-(3)) for our Fo-samples, and whether or not  $\lambda$  can be regarded constant. Existing models do not provide any constraints on either  $\lambda$  (0.04-1) or defect fraction (0.75-1). However, our data show that the defect fraction in our samples increases with strain from  $\sim 0.78$  after HIP-only to 0.84 at 45% shortening (see Fig.9b), which according to equation (3) implies that  $\lambda$  is not constant for the range of strains covered. Another way of looking into this is by applying relation (2). With the initial assumption of a constant  $\lambda$ , fig. 3.12a shows a non-linear best-fit

line through our grain size versus natural strain data using (2), with an initial grain size  $d_0$  of 0.85 and a  $\lambda$  of 1.33. Inspection of fig. 3.12a shows that while at 30 and 45% strain the data fall close to the best fit, the data point at 15% strain (i.e.  $\sim 0.16$  natural strain) falls below it. The latter data point better fits equation (2) with  $\lambda = 0.5$ . We speculate that  $\lambda$  might be constant only at high strains, i.e. above natural strain 0.3. Fig. 3.12b shows our normalized dynamic grain growth rate data, calculated using relation (4), versus strain rate. Here lines of normalized dynamic grain growth rate versus strain rate for constant  $\lambda$  are shown using relation (5) for the minimum and maximum  $\lambda$ -values observed by Seidensticker and Mayo (1998a). The data for experiments up to 30 to 45% fall close to a high  $\lambda \sim 1.0$ , while the experiment up to only 15% strain shows  $\lambda$  must be significantly lower. The relative high  $\lambda$ -value found here is most likely a material related property, since the  $\lambda$ -range reported by Seidensticker and Mayo (1998a) is also based on a range of different metallic and ceramic materials, where some show a significant higher or lower  $\lambda$  than the average of 0.13.

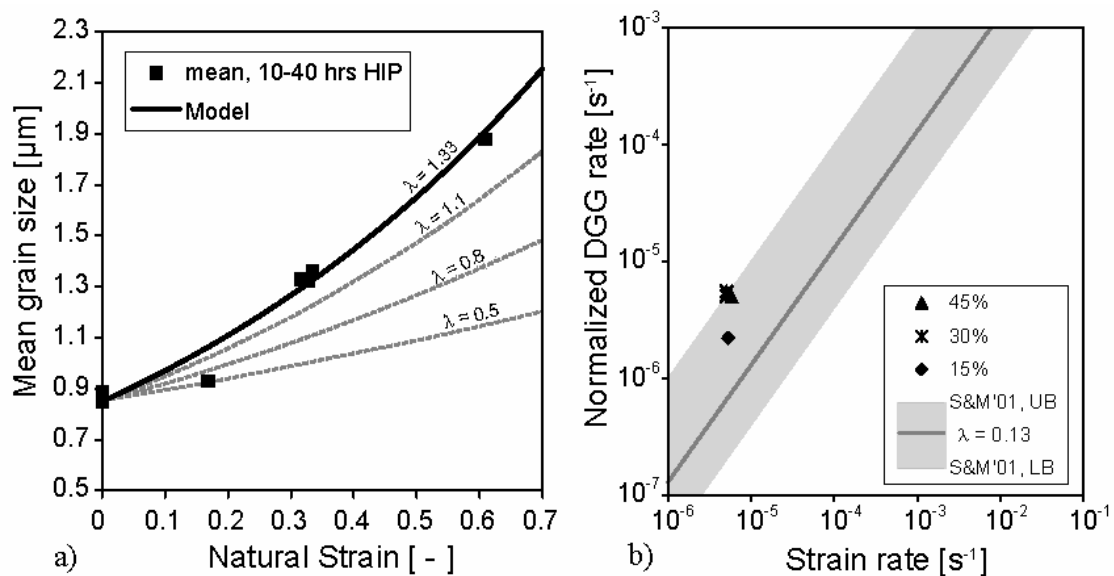


**Figure 3.12.** a) Mean grain size versus natural strain data for tests with HIP durations between 10 and 40 hrs. A non-linear best fit of the data to relation (2) is shown by the solid line. b) Normalized dynamic grain growth rate versus strain rate data, with upper and lower bound trend lines, fitted to relation (5), shown for the range in  $\lambda$  reported by Seidensticker and Mayo (1998a).

### 3.4.4 Alternative dynamic grain growth models

Seidensticker and Mayo (1998b) proposed a model for DGG to explain relation (1) based on faster shrinking of small grains parallel to the load direction during diffusion creep, which in turn, they suggest, leads to faster disappearance. In the model grain switching is more or less regarded as a byproduct, and changes in 3-D topology and defect fraction are not considered. Seidensticker and Mayo (1998b) do, however, note grain switching is biased in their model, i.e. after shrinking and disappearance of a 4-coordinated small grain, the 2 grains which are aligned parallel to the load direction are preferred to become direct neighbors over the 2 grains which are aligned perpendicular to the load direction. Our observation of a changing defect fraction with strain is inconsistent with the model of Seidensticker and Mayo (1998b), since that model predicts that the coordination number distribution remains constant during dynamic grain growth. Furthermore, we question if faster shrinking of small grains

parallel to the load direction can really lead to faster disappearance of these grains. That is grain boundary migration perpendicular to the load direction and towards the center of shrinking small grains, is retarded by material transfer in the opposite direction due diffusion creep accommodated deformation.

Wilkinson and Caceres (1984) suggest that GBS could induce dislocations through plastic deformation at triple junctions, in turn producing recovery of dislocations by boundary migration or bulging. Other models (Clark and Alden, 1973; Rabinovich and Trifonov, 1996) suggest that the production of excess vacancies, or an increase in the density of dislocations in the grain boundary region during GBS, can give rise to increased boundary mobility and therefore grain growth. As none of our observations point to major dislocation activity, these models do not appear applicable to our data.

The effect of second phases and/or porosity on grain growth was briefly mentioned in Section 1, with porosity probably forming the main reason for the sluggish static grain growth observed in this study. During deformation, the porosity was reduced during the first 15% of strain, but we did not observe any systematic change in porosity at higher strain (Table 3.1). Further, the mean pore size remained more or less constant with increasing strain (see also Table 3.1). In other words, there is little evidence that deformation-related porosity evolution in our samples influenced grain growth up to high strain, in the sense that progressively decreasing porosity reduced the force of so-called Zener pinning and possibly increased the grain growth rate (cf. Bate, 2001; Herwegh and Berger, 2004). Although this inference is based on relatively little data, our results of a separate study on the microstructural evolution of Fe-bearing forsterite-enstatite aggregates corroborate the conclusion that it is not a change in pore structure that controlled dynamic grain growth in our synthetic olivine material.

In order to investigate in more detail the grain switching model (evolution of grain coordination number distribution and defect fraction) under conditions of both grain growth and deformation, we have performed 2-D microstructural simulations for a range of strain rates, using the ELLE 2D microstructural modeling program. A full description of the simulation results is presented in separate paper (Kellermann Slotemaker and De Bresser, in press). Nevertheless, our simulations did provide evidence for changing defect fraction with strain concomitant with enhanced grain growth. Such microstructural modeling also allows incorporation of a discrete second phase or porosity, which will enable us to extend previous work on the role of Zener-pinning in dynamic grain growth (Bate, 2001), thereby evaluating whether this effect was involved in our experiments. In the mean time, we infer that the grain switching model offers the most likely explanation for our experimental results.

### 3.4.5 Implications for geodynamic modeling

GSS creep is believed to be an important flow mechanism in the upper mantle, (Drury, 2003; Hirth and Kohlstedt, 2003; Lee et al., 2002; Jaroslow et al., 1996; Vissers et al., 1995). Normal grain growth has been considered as a process which might inhibit GSS creep in the upper mantle (Karato 1989, Drury et al. 1991). Our results indicate that the effects of dynamic grain growth may also be capable of inhibiting GSS creep as a result of microstructural evolution when large strains are involved. This is particularly important with respect to localization. Localization of deformation in upper mantle shear zones is commonly inferred to control geodynamics in various tectonic settings (Hopper and Buck, 1993; Drury et al., 1991; Levin and Park, 2000; Van Wees and Beekman, 2000; Vissers et al., 1995). One means of initiating localization frequently put forward in the literature is a mechanism switch from GSI creep to GSS creep (Rutter and Brodie, 1988; Vissers et al., 1995; Braun et al.,

1999). Grain size refinement by dynamic recrystallization or reaction-nucleation can realize this switch, while Zener-pinning by pores or second phases can prevent static grain growth from causing a switch back to dominant GSI creep, or can lead to mixed GSS-GSI creep at the mechanism boundary (De Bresser et al; 2001). The prevention of grain growth by Zener pinning has been put forward as the key mechanism by which dynamic recrystallization leads to grain refinement, weakening and shear localization (Drury et al., 1991; Vissers et al., 1995; Evans, 2001). However, dynamic grain growth is much less restrained by Zener-pinning (Bate, 2001). As a consequence, Zener pinning may allow dynamic grain growth to dominate over static grain growth. Thus, beyond a certain critical strain (and not time), dynamic grain growth should produce sufficient grain coarsening in a weak, recrystallizing shear zone to push the microstructure back to the boundary between GSI and GSS creep fields. This scenario allows shear zones to form through the combined effect of grain size reduction, a switch to GSS creep and Zener pinning preventing static grain growth. However, the lifetime of a shear zone would be restricted to a finite amount of shear strain, beyond which dynamic grain growth will coarsen the grain size and increase the flow stress as dislocation creep processes become important again. Equation 2 provides a first order means to build this effect into geodynamic models in future, assuming a suitable value of  $\lambda$ .

### 3.5 Conclusions

We have studied the microstructural evolution of fine-grained ( $\sim 1 \mu\text{m}$ ), synthetic forsterite aggregates containing  $\sim 0.5 \text{ wt}\%$  water and  $10 \text{ vol}\%$  enstatite. The initially porous samples were hot isostatically pressed at  $950^\circ\text{C}$  and  $600 \text{ MPa}$  confining pressure to create dense aggregates, followed by axial compression to strains in the range  $15\text{-}45\%$ . The aim was to determine if grain growth in fine-grained olivine is influenced by deformation (i.e. strain) or is dependent only on temperature and time. This is important for geodynamic models involving grain size dependent creep of mantle rock. We have come to the following conclusions:

1. Under the experimental conditions employed, The material investigated shows minor static grain growth during an initial stage of heat treatment ( $\sim 10 \text{ hrs}$ ). Beyond this, growth more or less ceases, probably due to Zener-pinning by remaining porosity and the presence of the enstatite phase.
2. During deformation following initial heat treatment, grain growth is dominantly strain dependent rather than time dependent and thus can be characterized as dynamic (or deformation enhanced) grain growth.
3. Lack of evidence for dislocation activity, lack of formation of a shape and/or crystallographic preferred orientation, and the observed stress vs. strain rate behavior suggest that our samples deformed by a grain size sensitive process. Continuous hardening of the material during deformation is dominantly due to the dynamic grain growth effect.
4. Undeformed (heat treated) material has an average defect fraction, i.e. the fraction of non-hexagonal grains (in 2-D section), of  $\sim 0.78 \pm 0.02$ . During straining and dynamic grain growth, we found that the defect fraction increases during the first  $30\%$  axial strain from  $0.78$  at the start up to  $0.84$ . At axial strain  $>30\%$  defect fraction seems to remain constant.
5. The deformation enhanced grain growth occurring in our experiments can best be explained by grain neighbor switching models for dynamic grain growth, written  $d = d_0 \cdot \exp(\lambda \cdot \varepsilon)$  ; where  $d$  is the grain size,  $\varepsilon$  is the strain,  $d_0$  is the initial grain size and  $\lambda$  is a constant. In our experiments on fine-grained forsterite-enstatite aggregates, the

parameter  $\lambda$  has a value of  $\sim 1$  at axial strains  $\geq 30\%$ . At lower strains  $\lambda$  is  $< 1$ , indicating a possible coupling between  $\lambda$  and the defect fraction, as proposed by the grain neighbor switching based models for dynamic grain growth.

6. The grain size – strain evolution law indicated in the conclusion above may be used in geodynamic modeling to account for the effect of dynamic grain growth, assuming static grain growth is negligible and the value of  $\lambda$  is known and constant.



## Chapter 4

### On the role of grain topology in dynamic grain growth - 2D microstructural modeling

*This chapter has been accepted for publication in the Deformation mechanisms, Rheology and Tectonics volume 2005, Tectonophysics as: Kellermann Slotemaker, A., and de Bresser, J.H.P., On the role of grain topology in dynamic grain growth - 2D microstructural modeling.*

**Abstract.** Microstructural modification processes like dynamic recrystallization and grain growth can have a major effect on the transient and (semi-) steady state flow behaviour of deforming materials. Work on metals and ceramics suggests that deformation-enhanced changes in grain topology and the corresponding increase in fraction of non-hexagonal grains, called cellular defect fraction, can promote grain growth during deformation. The present study tests this hypothesis, by investigating the evolution of the cellular defect fraction during deformation, accompanied by grain growth, of aggregates with distributed grain sizes. For this purpose, we made use of the ELLE 2D microstructural modeling package. We simulated and quantified microstructural evolution under conditions where both surface energy driven grain boundary migration (GBM) and homogeneous deformation or grain size sensitive (GSS) straining were allowed to occur. The simulations show that contemporaneous GBM and simple geometrical straining of grain aggregates with distributed grain size and coordination number lead to extra grain neighbor switching, an increase in defect fraction, and enhanced grain growth. An increase in defect fraction was also found in a selected set of natural calcite mylonites that, with increasing temperature, show an increase in grain size and contribution of GSS creep. Analysis of defect fraction thus appears to be a good microstructural tool to establish whether or not a material has experienced normal static (defect fraction  $\sim 0.7$ ) or dynamic grain growth (defect fraction  $\sim 0.8$ ).

#### 4.1 Introduction

##### 4.1.1 Background and general problem statement

Microstructural modification processes like dynamic recrystallization and grain growth can have a major effect on the transient and (semi-)steady state flow behaviour of deforming materials. For example, high strain (torsion) experiments on coarse-grained olivine (Bystricky et al., 2000) and calcite materials (Schmid et al., 1987; Rutter, 1995, 1998; Pieri et al., 2001; Barnhoorn et al., 2004) have demonstrated transient strain weakening related to grain refinement by dynamic recrystallization. Relatively high shear strains were needed to approach steady state flow. Materials with relatively small starting grain sizes may, on the other hand, show strain hardening related to ongoing grain coarsening (e.g., olivine materials: Karato et al., 1986; Hirth and Kohlstedt, 1995). Evidently, meaningful modeling of large strain flow in the Earth must take into account microstructural evolution effects that cause rheological changes (e.g., Braun et al., 1999; Urai and Jessell 2001; Montesi and Hirth, 2003; Yamasaki, 2004). This requires a mechanism-based understanding of microstructure modification processes.

In a recent experimental study (Kellermann Slotemaker et al., 2004, chapter 3), we deformed fine-grained synthetic forsterite aggregates at a strain rate of  $5 \times 10^{-6} \text{ s}^{-1}$ , 600 MPa

confining pressure and a temperature of 950°C. Under these conditions, the forsterite material deforms by a grain size sensitive (GSS) creep mechanism involving grain boundary sliding (GBS), after McDonnell et al. (1999). We observed strain hardening in the stress-strain curves as well as an increase in grain size during the experiments. More importantly, comparison of the results of the deformation tests with heat treatment (static) tests showed that grain growth was strain-dependent (i.e. dynamic) rather than time-dependent (cf. static grain growth). No lattice preferred orientation developed in the samples (Kellermann Slotemaker et al., 2004; chapter 3) and only little evidence was found for dislocation activity on TEM scale (McDonnell et al., 1999). We thus concluded that grain boundary migration (GBM) in the material, resulting in dynamic grain growth (DGG), was dominantly surface energy driven. It is known from metals and ceramics that DGG and GSS creep, with a strong GBS signature, are intimately related processes (Seidensticker and Mayo, 1998a). Models by Sato (1990) and Sherwood and Hamilton (1992; 1994) propose that grain (neighbor) switching during GBS (after Ashby and Verrall, 1973) may increase the probability of high-sided grains coming in contact with low-sided grains, in turn stimulating grain growth. Sherwood and Hamilton (1992; 1994) hypothesized that deformation-induced grain neighbor switching results in changes in grain topology, i.e. an increase in the fraction of non-hexagonal grains (in 2D), called the cellular defect fraction (originally defined by Hillert, 1965). Indeed, measurements of grain topology in the forsterite samples showed an increase of the cellular defect fraction with increasing strain, consistent with the increase in grain size and related strain hardening.

The results of the experimental study on synthetic forsterite (Kellermann Slotemaker et al., 2004) corroborate the importance of understanding microstructure modification during flow of Earth materials. However, it is as yet not clear if analysis of the cellular defect fraction is a useful and generally applicable tool to identify DGG in relation to grain neighbor switching and deformation. It is the broad objective of this chapter to shed light on this. We used the 2-D numerical modeling package ELLE (Jessell et al., 2001) to simulate combined deformation and surface energy driven GBM, specifically aiming a) to investigate the evolution of cellular defect fraction with strain and time in relation to grain growth with or without contemporaneous deformation, and b) to test the hypothesis that extra neighbor switching induced by deformation causes an increase in cellular defect fraction, which in turn leads to enhanced grain growth. In our approach, we tested homogeneous ‘geometrical’ deformation as well as simulated inhomogeneous GSS creep. By ‘geometrical’ deformation we simply mean bulk homogeneous straining of the complete aggregate, i.e. as if the grain boundaries are completely passive elements in the aggregate. This deformation type is useful since it allows a straightforward approach to investigate the effect of changes in grain boundary geometry on grain growth. The effects of inhomogeneous GSS creep are less straightforward to interpret but are more applicable to the results of the forsterite work and other experimental studies on real materials.

Limited previous modeling work has been performed on combined homogeneous or inhomogeneous deformation and GBM. Bons and Urai (1992) studied simultaneous operation of surface energy driven GBM and homogeneous area-conservative deformation using a simple 2-D network model. They demonstrated that syndeformational grain growth slows down the progressive increase in aspect ratio normally associated with development of a shape-preferred orientation during homogeneous straining. However, they also found that if a grain shape preferred orientation is present, it slows down grain growth. Using a similar type of 2-D modeling, Bate (2001) focused on the effect of deformation on GBM in nominally Zener-pinned microstructures and observed DGG, which he ascribes to deformation induced perturbations of the grain boundary geometry. The present study forms the next step forward by applying a modeling approach similar to Bons and Urai (1992) and Bate (2001), but



looking in detail at (and quantifying) geometrical changes in grain topology, in particular defect fraction, which in turn link up with analytical neighbor switching models of Sherwood and Hamilton (1992, 1994) and Sato (1990).

In this study we explicitly excluded any grain size reduction mechanism contributing to grain size evolution. As such, the results are not directly applicable to (high) strain zones where dynamic recrystallized grains resulted from competition between grain size reduction and grain growth. The results could, however, apply to shear zones, which experienced significant grain size reduction causing rocks to switch in deformation mechanism to dominant GSS creep. Rather than ongoing grain size reduction, the continued microstructural evolution in such a shear zone would dominantly involve normal (or dynamic) grain growth (e.g. Herwegh et al., 2005).

The paper starts with a brief overview of dynamic grain growth theories presented in the literature, followed by an outline of our modeling approach. We then present the results of the modeling runs and assess how the present and previous modeling studies relate to the analytical approaches of grain neighbor switching. Finally, we discuss what factors need to be considered in future studies of DGG and make a comparison with natural rocks through defect fraction analysis on microstructures of selected carbonate mylonite samples, which were already extensively studied by Herwegh et al. (2005).

#### 4.1.2 Dynamic grain growth models

Various experimental and modeling studies on grain growth behaviour during deformation have been performed (e.g. geological materials: Schmid et al. 1977; Karato et al. 1986 and Walker et al. 1990; metals and ceramics: Holm et al., 1977; Holm et al., 1993; Sherwood and Hamilton, 1994; Seidensticker and Mayo, 1998a; modeling studies: Wilkinson and Caceres, 1984; Sato et al., 1990; Sherwood and Hamilton, 1992, 1994; Rabinovich and Trifonov, 1996; Seidensticker and Mayo, 1998b; Kim et al., 1999; Kim and Hiraga, 2000; Bate, 2001; Haslam et al., 2003). The following points emerged as being important in explaining DGG: *a)* GBM kinematics, *b)* deformation mechanisms, *c)* deformation ‘mode’, i.e. homogeneous vs. inhomogeneous, and aspect ratio formation, and *d)* topological changes. These points will be discussed in more detail below, with particular emphasis on the last aspect, in line with the aims of our study.

*a) GBM kinematics.* In materials that show fast grain boundary migration under static conditions, a dynamic component induced by deformation may contribute little to the overall grain growth and, hence, will be hard to recognize. Consequently, DGG is usually recognized in materials in which static grain growth is very slow or pinned due to the presence of one or more pinning phases (Seidensticker and Mayo, 1998a; Bate, 2001). Zener pinning can be established by the presence of relatively small-scale solutes and impurities at the grain boundary or by larger scale discrete particles or pores included within the grain matrix (Evans et al., 2001). Depending on the size of a pinning phase relative to the average matrix grain size, an average uniform (small sized pinning phase) or varying non-uniform (large sized pinning phase) Zener drag must be accounted for. In turn this variation in pinning geometry may have a large effect on the net result of combined deformation and GBM (Bate, 2001). In materials with fast static grain growth, a dynamic component might well be present, but may contribute little to the overall grain growth. In natural rocks, Zener pinning is a common feature (Olgaard, 1990; Mas and Crowley, 1996; Krabbendam et al., 2003; Herwegh and Berger, 2004). In such rocks, dynamic grain growth may provide a significant contribution to the total grain growth.

b) *Deformation mechanisms.* Some DGG models specifically focus on how physical properties of GSS (diffusion) creep, whether or not combined with GBS, can result in enhanced migration of grain boundaries on the grain scale (Kim et al., 1999; Kim and Hiraga, 2000) and down to the atomistic scale (Haslam et al., 2003; Haslam et al., 2004). Other models focus on the effects of accommodation by GBS. This mechanism may induce excess vacancies or dislocations in the grain boundary region, which can increase grain boundary mobility (Clark and Alden, 1973; Rabinovich and Trifonov, 1996) or the driving force for GBM (Wilkinson and Caceres, 1984). Since our motivation for doing the current study came from the results on forsterite, which did not show evidence that production of dislocations or excess vacancies in the grain boundary region played a role, it will not be considered further in this chapter.

c) *Deformation ‘mode’ and aspect ratio formation.* Homogeneous ‘geometrical’ deformation is a simplified way of strain accumulation and is not related to a deformation mechanism with a specific microphysical basis. Nevertheless, this type of deformation allows straightforward straining of grain aggregates resulting in an increasing aspect ratio and associated development of a grain shape preferred orientation. In combination with GBM, homogeneous deformation has been shown to cause accelerating (Bate, 2001) as well as decelerating effects (Bons and Urai, 1992) on grain growth. More realistic modeling of deformation necessarily needs to take into account inhomogeneous straining to some extent, assuming a distributed grain size and a specific GSS (diffusion with or without GBS) or GSI (dislocation) creep mechanism. This will introduce a variable level of heterogeneity in the accommodation of strain between and/or within grains, which also may influence aspect ratio formation (Bate, 2001).

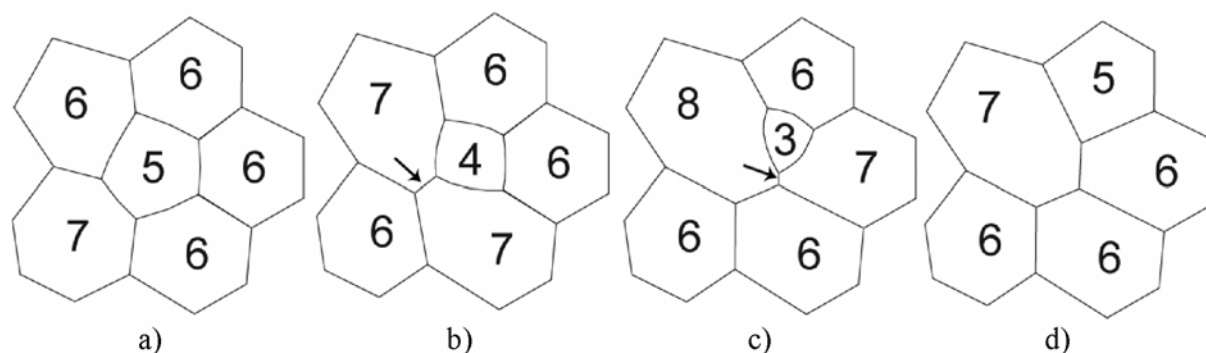


**Figure 4.1.** Schematic drawing showing the evolution of a group of six grains undergoing surface energy driven GBM and neighbor switching, resulting in normal grain growth (after fig. 4 of Hillert 1965); coordination number is shown within each grain. Average coordination number remains 6 at all shown stages. Defect fraction is shown at each stage. a) The initial state with two defects, i.e. one 5- and one 7-sided grain,  $X_d = 2/6 = 0.33$ , b) The 5-sided grain has become 4-sided due to a neighbor switch (arrow),  $X_d = 3/6 = 0.50$ , c) The 4-sided grain has become 3-sided due to another switch (arrow),  $X_d = 3/6 = 0.50$ , d) Finally the 3-sided grain has disappeared and thus net grain growth has taken place  $X_d = 2/5 = 0.40$ . Note a 5- and a 7-sided grain are still present in the final state.

d) *Topological changes.* Related to this are the various forms of grain neighbor switching ‘events’ and changes in distribution of grain coordination number and cellular defect fraction (Sato et al., 1990; Sherwood and Hamilton, 1992). Grain neighbor switching related models on static and dynamic grain growth specifically base their grain growth (rate) relations as a function of time (Hillert, 1965), strain (Sato et al., 1990) and strain rate

(Sherwood and Hamilton, 1992; 1994; Seidensticker and Mayo, 1998b) on the various ways of grain neighbor switching. Such switching events can be considered as variants of defect ‘climb’ and glide’ in analogy to the atomistic dislocation theory. Measures to describe grain topology are the arithmetic mean and second moment, i.e. the standard deviation, of the coordination number distribution (eg. Weaire and Kermode, 1983; Anderson, 1988; Bons, 1993). Defect fraction is an additional way to describe the state of the coordination number distribution with a single value. Recalling Von Neumann’s rule (1952), in two dimensions a 5-sided or lower coordinated grain will tend to shrink while a 7 or higher sided grain will tend to grow (fig. 4.1). After a neighbor-switching event, there is a chance that grains changed their coordination number, resulting in a higher or lower defect fraction. According to Hillert (1965), neighbor switching during normal grain growth (fig. 4.1), i.e. surface energy driven GBM without any deformation, occurs at a characteristic constant defect fraction of 0.75. Note that, although the defect fraction is constant, the absolute number of defects must decrease, given that the total number of all grains in the system decreases with net grain growth. Individual grains may switch back and forth from defect (non-hexagonal) to hexagonal coordination, depending on the evolution of migrating boundaries of neighboring grains. When deformation, e.g. by some combination of GBS and diffusion creep, occurs alongside normal grain growth, this can introduce extra neighbor switching events (fig. 4.2), resulting in a change in defect fraction away from the steady state value of 0.75 for normal grain growth. If a higher fraction is produced, enhanced grain growth is expected.

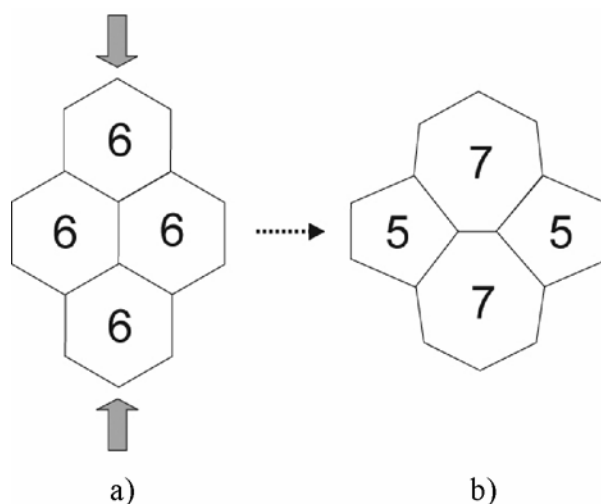


**Figure 4.2.** Schematic illustration of deformation (GBS + diffusion) induced neighbor switching; coordination number is shown within each grain. a) Initial state with four 6-sided grains under vertical compression,  $X_d = 0/4 = 0.0$ , b) State after deformation and neighbor switching; top and bottom grains are now direct neighbors and both gained an extra side; the two middle grains separated and both lost a side,  $X_d = 4/4 = 1.0$  (after Sherwood and Hamilton, 1994, their fig. 6).

The latter forms the rationale for an analytically derived relation between strain rate and DGG rate presented by Sherwood and Hamilton (1992; 1994), expressed as:

$$\dot{d}_{dyn} = \lambda \cdot d \cdot \dot{\epsilon} \quad (1)$$

where  $\dot{d}_{dyn}$  is the DGG-rate,  $\lambda$  is a rate-parameter,  $d$  is the instantaneous average grain size and  $\dot{\epsilon}$  is the strain rate. Note that  $d$  can vary between different grain growth experiments as well as within a single experiment. Thus, in practice, data are best compared by normalizing (1) by the instantaneous average grain size (Seidensticker and Mayo, 1998a):

$$\frac{\dot{d}_{dyn}}{d} = \lambda \cdot \dot{\epsilon} \quad (2)$$

According to the model of Sherwood and Hamilton (1992), the value of the rate-parameter  $\lambda$  largely depends on the defect fraction,  $X_d$ , as they show that:

$$\lambda = k' \cdot X_d \quad (3)$$

where  $k'$  is a scaling constant.

From the above list of parameters that are of importance in DGG, we concentrate on changes in topology and, to a lesser extent, on changes in aspect ratio (and related deformation ‘mode’), since these are potentially useful as measurable microstructural parameters. In the approach of Sherwood and Hamilton (1992), DGG is simply a response to extra neighbor switching and increasing defect fraction induced by some deformation event, irrespective of which physical processes are actually involved in the neighbor switching. Therefore, as a first order approach, it appears reasonable to model GBM in combination with simple homogeneous deformation, which allows an unambiguous investigation of geometric effects of deformation on defect fraction evolution and grain growth. Moreover, results are directly comparable to studies by Bons and Urai (1992) and Bate (2001), which have already proven this to be a successful way to simulate static grain growth and DGG. However, these investigations did not include quantitative analysis of topological changes during their simulations. A logical next step would be to perform GBM combined with inhomogeneous GSS creep simulations, which potentially predict more realistic topological changes. The theory of Sherwood and Hamilton (1992; 1994) on DGG predicts extra neighbor switching by GBS and possible related changes in coordination number distribution and defect fraction for dynamically grown material. However, to our knowledge, not many constraints are yet established on the dependence of defect fraction on deformation, leaving the value of  $\lambda$  in (1)-(3) with a large uncertainty. Our approach will supply a first order calibration of such variation in defect fraction,  $X_d$  (3).

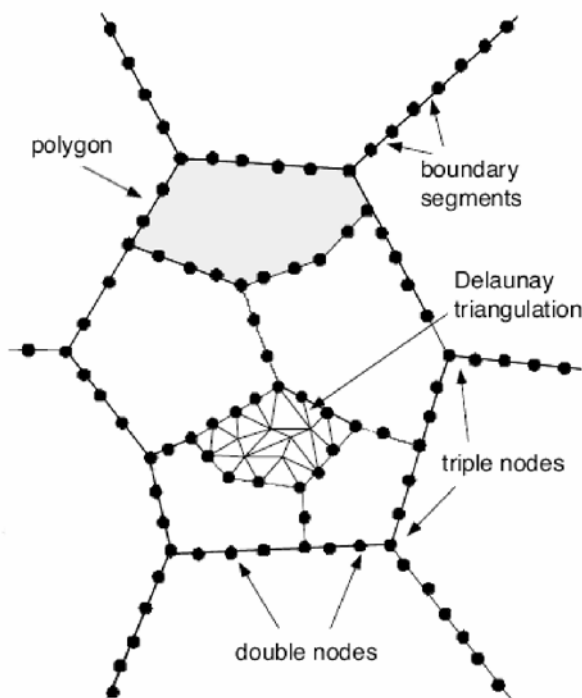


**Figure 4.3.** Representation of the 2D finite element map of a grain aggregate (modified after Piazzolo, 2001, see her fig. 3.2). Each polygon domain (e.g. the light-gray area) forms a grain, which can be assigned a number of properties, such as viscosity. All polygons can, if desired, be triangulated to smaller elements using a Delaunay triangulation routine. This triangulation is, in contrast to the polygons, nodes and boundary segments, not permanent and can be used temporarily e.g. for the basal deformation routine. Triangulation elements may also have individual properties, including the stress and strain state during deformation.

## 4.2 Method

### 4.2.1 General Approach

Grain microstructures of heat-treated and deformed material can be analyzed to quantify defect fraction using conventional image analysis techniques. Similarly, 2-D simulations allow quantification and systematic investigation of various microstructural parameters, like defect fraction, and their evolution. Such microstructural analysis forms a powerful tool to test neighbor switching based DGG theories and verify/calibrate the variation in defect fraction under conditions of combined GBM and deformation. We concentrated on single-phase material.

We used the 2-D microstructural modeling package ELLE to perform the simulations. This package provides a variety of routines to simulate individual microprocesses. In principle, ELLE is based upon a two-dimensional network structure in which grains are represented by polygons, and polygons are in turn defined by a closed set of connected nodes (see fig. 4.3, modified after Piazzolo, 2001). Straight boundary segments connect the nodes, of which there are two types, i.e. double nodes, connected to two neighboring nodes and triple nodes, connected to three neighboring nodes (fig. 4.3). The latter reside at a triple point, where boundaries between three neighboring grains merge into one point. Average distance between nodes is controlled by user-defined parameters. The minimum allowed distance between two nodes, referred to as ‘*switchdistance*’, is set to a fixed value in all tests and maximum node separation is defined as  $2.2 \times \textit{switchdistance}$ . In the general case where separation is lower or higher than this range, nodes are removed or added, respectively. If separation between two triple nodes is below the minimum they will switch neighbors rather than remove one of the triple nodes. The modeled area is a square finite element map (area set to 1000) with periodic boundaries, i.e. it is continuous on opposite sides of the frame. In this way, boundary effects are avoided as long as the modeled polygonal network is sufficiently fine-grained. For more detailed information on the Elle system, the reader is referred to Jessel et al. (2001) and the Elle website (<http://www.microstructure.info>).

We effectively simulated contemporaneous activity of deformation and GBM by iteratively combining small strain and time steps of each separate process. To perform small steps of homogeneous deformation we used an ELLE routine named *elle\_manuel*. This routine simulates homogeneous simple shear deformation. Shear strain step size is set as a displacement-value in the x-direction of the finite element map. The ELLE routine *elle\_gg* is used to simulate surface energy driven GBM. *elle\_gg* allows a quick (short computation times) evaluation of surface energy driven GBM, without the need to specify values for time, temperature and pressure, or material parameters like grain boundary mobility and activation energy for GBM. For a single boundary node, local boundary curvature,  $w$ , is defined as  $1/R$ , where  $R$  is the radius of an imaginary circle fitted through the specific node and its 2 neighboring boundary nodes. This curvature,  $w$ , forms the local driving force for GBM and is used to calculate the node-displacement, *movdist*, per *stage* (i.e. the time-unit) according to the following relation:

$$\textit{movdist} = w \cdot M \quad (4)$$

where  $M$  is a rate-constant comparable to GBM mobility, defined as:

$$M = \textit{speed\_up} \cdot \textit{switchdistance}^2 \cdot 0.02 \quad (5)$$

In (5) *speed\_up* limits the distance a node may move in any one *stage* and 0.02 is a fixed constant allowing the value for *speed\_up* to vary within the range 0.3 - 1. As *switchdistance* is kept constant in all simulations, the value of *M* can only be varied by artificially changing the *speed\_up*-value. In (4) a maximum value for *movdist* is set at 0.2 x *switchdistance* to prevent large node movements, in case of strong acute angles between nodes, which could destabilize the network. The movement calculation is done for each boundary node within each *stage*, where a ‘GBM time step’ consists of a specified number of *stages*. The program outputs mean statistics on grain size, grain shape and other parameters at a preset interval of stages.

We used *basil*, which is a finite element code for calculating viscous deformation developed separately from the Elle code (Barr and Houseman, 1992; 1996), to simulate inhomogeneous GSS deformation. During a *basil* deformation step, the polygonal network temporarily requires Delaunay triangulation (see fig. 4.3. *basil* simulates simple shear deformation like *elle\_manuel*, but rather than homogeneously deforming the microstructure (i.e. applying uniform viscosity), the program permits a spatially variable Newtonian (or non-Newtonian) viscosity. This way *basil* can model deformation of an aggregate with variable internal viscosity as also done by previous workers (Bons et al., 1997; Piazzolo et al., 2002; Jessell et al., 2004; Jessell et al., in press). Each grain in a (starting) microstructure can be assigned a specific viscosity-value depending on user-defined parameters. Using this approach Piazzolo (2001) and Piazzolo et al. (2002) calculated a dislocation density dependent viscosity for each grain as:

$$\eta = \eta_{base} + \rho^{1/2} \quad (6)$$

where  $\rho$  is the dislocation density and  $\eta_{base}$  is a base viscosity specific to temperature, pressure conditions, and mineral species. In the present study, it was not our intention to model real values for viscosity corresponding to a specific material and natural conditions. Rather, our goal was to get a crude impression of the effect of spatially variable viscosity in comparison to simple homogeneous deformation. We applied the same approach as in (6) (by Piazzolo et al., 2002), and calculated a grain size dependent viscosity, according to the following relation:

$$\eta = c \cdot d^3 \quad (7)$$

where  $d$  is the grain size, calculated as the equivalent circular diameter of the grain area, and  $c$  is a scaling-factor (arbitrarily set to  $10^4$ ). The grain size exponent is chosen to be 3, a typical value for grain boundary diffusion controlled creep. In practice, the approach in relation (7) allowed us to model deformation with relative viscosity differences between larger and smaller grains up to four orders of magnitude (for the fine-grained starting microstructure), similar to grain size dependent Newtonian creep. It is emphasized that this sort of modeling of GSS deformation is not based on any specific physical process; we simply imply grain size dependence through an intrinsic variable viscosity definition. After each GBM step, and before the following *basil* deformation step, we recalculated the viscosity value for each grain, as some grains may have grown, while others may have shrunk. *basil* requires input of boundary conditions on traction (stress) and/or velocity. Maximum strains of the order of 100% are possible.

During every simulation, intermediate output files were saved at regular time intervals such that the evolution of grain size, grain coordination and grain shape can be evaluated. Dynamic grain growth rate,  $\dot{d}_{dyn}$ , was calculated according to the following relation (after Seidensticker and Mayo, 1998a):

$$\dot{d}_{dyn} = (d_{total} - d_{static}) / t_{total} \quad (8)$$

where  $d_{total}$  is the grain size resulting from both static and dynamic contributions to grain growth, and  $d_{static}$  is the statically grown grain size over a similar period of time,  $t_{total}$ .

A single starting microstructure has been used for all simulations. It was made artificially, contains 1500 grains, and is single phased with zero porosity (see fig. 4.4). The starting microstructure has close to lognormal grain size distribution and normal grain coordination number distributions (see fig. 4.4b-c), similar to our forsterite microstructure (McDonnell et al., 1999; Kellermann Slotemaker et al., 2004; Kellermann Slotemaker et al., in prep.). The microstructure is similar to microstructures commonly observed in natural rocks (e.g. Ranalli, 1984; Michibayashi, 1993; Dijkstra, 2001) and synthetically prepared materials (Karato et al., 1986; Rabinovich and Trifonov, 1996; Bergmann et al., 1998; Fayad et al., 1999; Ter Heege et al., 2005; Zhilyaev et al., 2005).

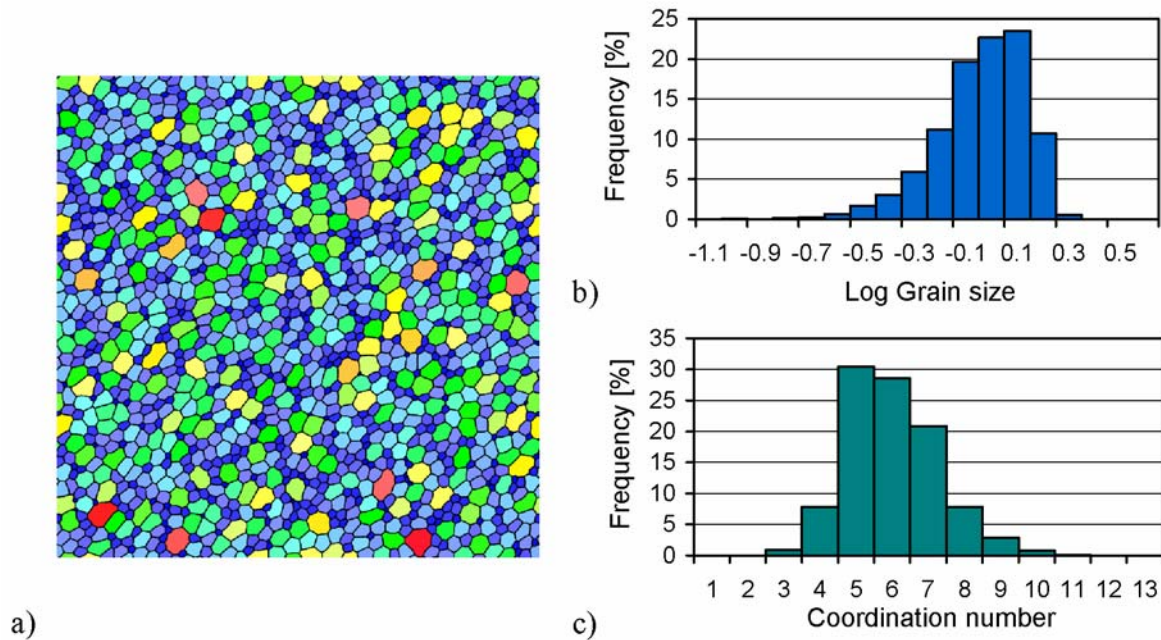


**Figure 4.4.** a) Starting microstructure used for all simulations. gray-tones represents grain size dependent viscosity variation. b) Starting grain size distribution, showing a close to log-normal shape. c) Starting coordination number distribution of approximate normal shape (cf. Fayad et al. 1999).

## 4.2.2 Simulations

As described above, simultaneous activity of GBM and deformation is modeled by iteratively combining small time and shear strain steps of each process respectively. Time is defined as the number of computational GBM *stages* that have elapsed. A time step has a prescribed number of GBM *stages* and is followed by a shear strain step with a preset size. Shear strain rate is then calculated as the ratio of shear strain step-size (dimensionless) over GBM time step-size (i.e. no. of *stages*) resulting in a unit of 1/*stage*. The GBM stage-unit used in the modeling could be converted to an absolute amount of time if constraints are

available for the grain boundary mobility of the relevant material. Two simulation types (**A** and **B**) of combined deformation and GBM were performed:

**Type A:** We used *elle\_manuel* for small steps of homogeneous deformation and *elle\_gg* for small time-steps of GBM. In total 16 constant shear strain rate simulations were done up to a shear strain of 2, where shear strain rate was varied over 2 orders of magnitude.

**Type B:** We used *basil* for small steps of GSS creep and again *elle\_gg* for small steps of GBM. 7 constant shear strain rate simulations were performed up to a shear strain ( $\gamma$ ) of 2, with strain rate being varied one order of magnitude.

Table 1. List of all simulations and specific preset test-conditions

Test no. <sup>a)</sup>	Simulation type <sup>b)</sup>	Shear Strain-step-size [-]	GBM Time-step-size [stages]	Shear Strain rate [1/stage]	GBM Speed_up factor
test33	A	1.0E-04	1	1.0E-04	0.3
test16	A	2.0E-04	1	2.0E-04	0.3
test19	A	4.0E-04	1	4.0E-04	0.3
test17	A	1.0E-03	1	1.0E-03	0.3
test15	A	2.0E-03	1	2.0E-03	0.3
test20	A	4.0E-03	1	4.0E-03	0.3
test18	A	1.0E-02	1	1.0E-02	0.3
test14	A	2.0E-02	1	2.0E-02	0.3
test34	A	5.0E-04	5	1.0E-04	1
test32	A	1.0E-03	5	2.0E-04	1
test31	A	2.0E-03	5	4.0E-04	1
test30	A	5.0E-03	5	1.0E-03	1
test29	A	1.0E-02	5	2.0E-03	1
test13	A	2.0E-02	5	4.0E-03	1
test25	A	5.0E-02	5	1.0E-02	1
test27	A	1.0E-01	5	2.0E-02	1
test23	B	4.0E-03	1	4.0E-03	0.3
test21	B	1.0E-02	1	1.0E-02	0.3
test22	B	2.0E-02	1	2.0E-02	0.3
test28	B	1.0E-02	5	2.0E-03	1
test11	B	2.0E-02	5	4.0E-03	1
test24	B	5.0E-02	5	1.0E-02	1
test26	B	1.0E-01	5	2.0E-02	1

<sup>a)</sup> Note that each test number refers to both a combined GBM plus deformation test and a complementary single GBM test. All tests started with the same microstructure.

<sup>b)</sup> A = homogeneous ‘geometrical’ deformation; B = heterogeneous GSS deformation

GBM time-step-size and shear strain step-size both can change the strain rate, but the smaller the time step the more close truly contemporaneous activity of GBM and deformation is simulated, i.e. smaller time steps give higher resolution. Thus to investigate grain growth behaviour at varying strain rates it is most practical to only vary strain step-size and keep the time-step-size constant at a small value, maintaining a constantly high resolution. On the



other hand, at constant strain rate, a larger GBM time-step allows a larger deformation-step size, giving lower computation time. In about half of all simulations, we used the smallest possible time step size of 1 *stage*, but for practical (calculation-time) reasons the other half was done using a time step size of 5 *stages*. This also gave us the chance to check how sensitive the simulations were to a (5-fold) decrease in resolution. Furthermore, to detect the presence of possible large statistical uncertainties caused by a significant decrease in number of grains over long time periods (when imposing slow strain rates), we also varied the *speed\_up* parameter in (5), setting its value to 1 or 0.3. This resulted in two combinations of preset test parameters for both type A and B simulations. We will refer to them as respectively the ‘5&1’ and the ‘1&0.3’ combination, where the first number refers to the GBM time step size (5 or 1) and the second number to the *speed\_up* value (1 or 0.3). In addition, complementary static grain growth tests were done for each combined GBM + deformation simulation over similar periods of time, to be able to compare grain growth behaviour with and without contemporaneous deformation. A complete list of all simulations and specific preset conditions is given in Table 1. In the following, we will refer to a combined GBM-deformation simulation as ‘testXX-dyn’ and to a complementary static grain growth simulation as ‘testXX-st’.

## 4.3 Results

### 4.3.1 Normal grain growth

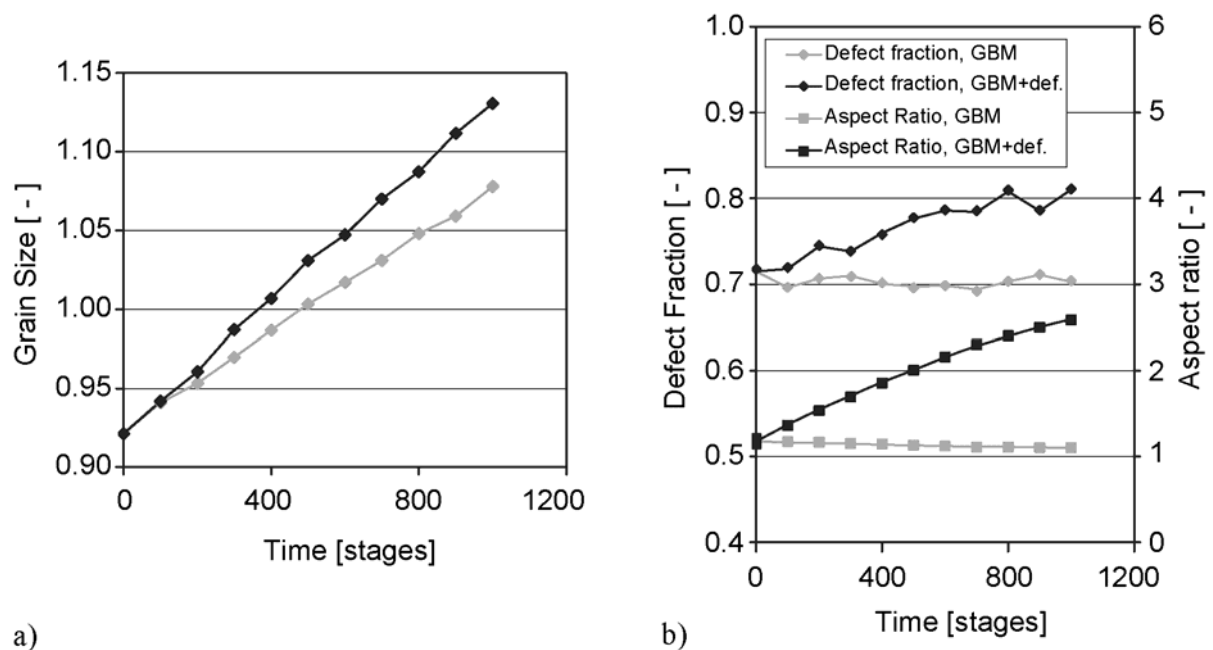
A representative example of grain growth (test15-st) produced when only GBM is allowed to occur is shown in fig. 4.5a. To show that this and other simulations produced realistic static grain growth kinetics, we used the conventional grain growth law (after Burke and Turnbull, 1952; Atkinson, 1988; Evans et al., 2001) given by:

$$d_{static}^n - d_o^n = k \cdot t \quad (9)$$

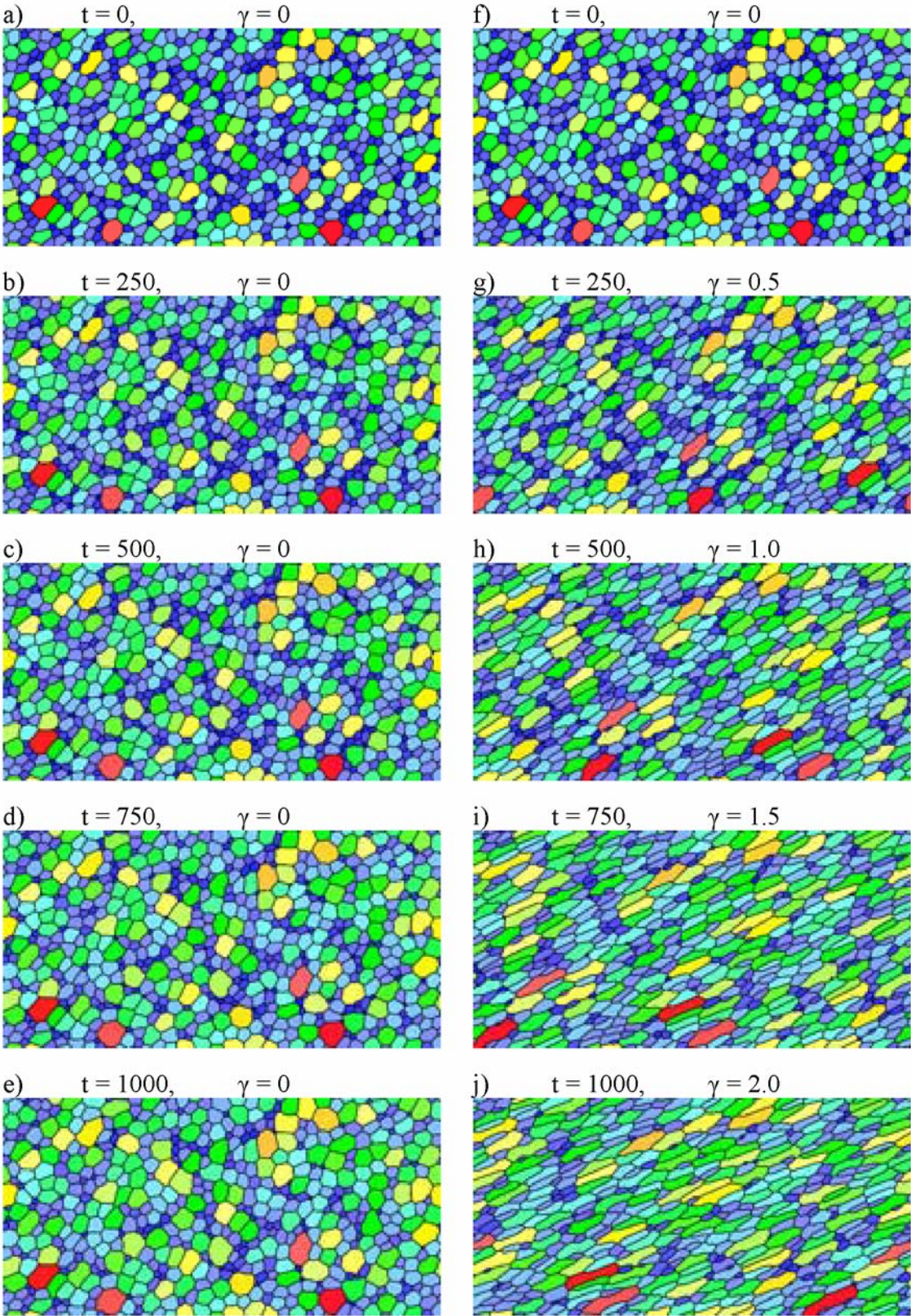
where  $d_o$  is the initial grain size,  $t$  is time,  $n$  is the grain growth exponent (typically varying between 2 and 5; Evans et al., 2001), and  $k$  is a temperature-dependent rate constant. Using linear regression analysis in  $d_{static}^n - d_o^n$  versus  $t$  space, and taking  $k$  as a constant, a best fit of the growth data of test15-st to equation (9) gives  $n = 2.0$ , with a correlation coefficient,  $R^2$ , of 0.9990. Considering all static grain growth tests with a minimum duration of 500 *stages*, we found the average best-fit  $n$ -value is  $2.3 \pm 0.3$ . More pronounced variation occurs in shorter duration tests, i.e. for  $t < 500$  *stages*. Thus, following an initial transient stage, static grain growth conforms well to the theoretical ‘exponential’ law (equation (9)). Furthermore, defect fraction and aspect ratio are both more or less constant during normal grain growth, as shown by characteristic plots of both parameters versus time for test15-st in fig. 4.5b. For a quantitative overview of the microstructural parameters for all tests see Table 2. In general, defect fraction only slightly varies between 0.67 and 0.72, with an exception for a few tests with a *duration*  $\geq 5000$  *stages*, where its value can drop as low as 0.54 (Table 2). Microstructural evolution during static grain growth (test15-st) is shown in fig. 4.6a-e at time intervals of 250 *stages*.

Table 2. Quantitative overview of main simulation results for all tests.

Test no.	Duration [stages]	Final values GBM test (static grain growth)				Final values GBM + def test (dynamic grain growth)					Average DGG-rate [1/stage]
		No. of grains	Average grain size	Defect Fraction	Shear Strain	No. of grains	Average grain size	Defect Fraction	Aspect ratio	DGG-Fraction [%]	
test33	20000	213	2.44	0.54	2.0	199	2.53	0.75	2.05	5.26	$8.03 \cdot 10^{-7}$
test16	10000	355	1.89	0.69	2.0	319	2.00	0.72	2.12	9.66	$4.61 \cdot 10^{-6}$
test19	5000	559	1.51	0.72	2.0	496	1.60	0.81	2.24	13.66	$1.14 \cdot 10^{-5}$
test17	2000	849	1.22	0.68	2.0	770	1.29	0.8	2.42	16.81	$2.61 \cdot 10^{-5}$
test15	1000	1096	1.08	0.70	2.0	996	1.13	0.81	2.59	25.23	$4.97 \cdot 10^{-5}$
test20	500	1265	1.00	0.70	2.0	1184	1.04	0.8	2.97	29.17	$8.33 \cdot 10^{-5}$
test18	200	1401	0.95	0.71	2.0	1333	0.98	0.8	3.69	42.87	$1.22 \cdot 10^{-4}$
test14	100	1438	0.94	0.70	2.0	1397	0.95	0.77	4.45	41.09	$1.57 \cdot 10^{-4}$
test34	20000	84	3.89	0.71	2.0	76	4.09	0.68	1.95	6.3	$4.73 \cdot 10^{-6}$
test32	10000	159	2.83	0.62	2.0	140	3.02	0.68	2.02	8.88	$4.19 \cdot 10^{-6}$
test31	5000	244	2.28	0.59	2.0	235	2.33	0.77	2.05	3.08	$4.92 \cdot 10^{-6}$
test30	2000	468	1.65	0.71	2.0	424	1.73	0.81	2.18	10.29	$2.90 \cdot 10^{-5}$
test29	1000	694	1.35	0.68	2.0	615	1.44	0.8	2.32	16.3	$5.05 \cdot 10^{-5}$
test13	500	922	1.18	0.70	2.0	841	1.23	0.82	2.44	17.89	$1.05 \cdot 10^{-4}$
test25	200	1210	1.03	0.70	2.0	1117	1.07	0.8	2.73	28.6	$2.23 \cdot 10^{-4}$
test27	100	1341	0.97	0.71	2.0	1253	1.01	0.81	3.19	38.78	$3.63 \cdot 10^{-4}$
test23	450	1284	1.00	0.70	1.8	1204	1.03	0.82	2.84	30.41	$8.03 \cdot 10^{-5}$
test21	160	1412	0.95	0.70	1.6	1376	0.96	0.79	3.27	30.39	$7.76 \cdot 10^{-5}$
test22	90	1449	0.94	0.70	1.8	1407	0.95	0.79	3.94	46.35	$1.36 \cdot 10^{-4}$
test28	1000	694	1.35	0.68	2.0	585	1.48	0.8	2.12	21.81	$7.65 \cdot 10^{-5}$
test11	500	922	1.18	0.70	2.0	798	1.26	0.83	2.3	25.75	$1.56 \cdot 10^{-4}$
test24	200	1210	1.03	0.70	2.0	1161	1.05	0.78	2.73	17.02	$2.23 \cdot 10^{-4}$
test26	100	1341	0.97	0.71	2.0	1277	1.00	0.81	3.21	31.24	$2.51 \cdot 10^{-4}$



**Figure 4.5.** a) Increase in grain size (i.e. average equivalent circular diameter) resulting from simulation test15-st for static grain growth (gray symbols and line) and for the combined deformation plus GBM simulation (black symbols and line). b) Evolution of defect fraction and aspect ratio for test15. Defect fraction and aspect ratio remain more or less constant at their starting values during the static grain growth simulation, while they show gradual but significant increase for the combined deformation plus GBM simulation.



**Figure 4.6.** Microstructural evolution during test15 of a)-e) the static grain growth simulation and f)-j) the combined deformation plus GBM simulation.



## 4.3.2 Combined GBM and homogeneous deformation

### 4.3.2.1 Dynamic grain growth and evolution of grain geometry

In the case of combined GBM and homogeneous deformation, a component of extra ‘dynamic’ grain growth is observed compared to the static grain growth curve. This is well illustrated by the results of test15-dyn (fig. 4.5a). Both defect fraction and aspect ratio significantly increase with time (and strain) compared to the semi-constant values measured during normal grain growth (figs. 4.5b and 4.6f-j). Increase of defect fraction (from an initial value of 0.71) is gradual and reaches values up to 0.81 at the end of the runs, where  $\gamma = 2$ . This microstructural evolution is consistently found to be the same in all of the combined deformation plus GBM tests. Final defect fraction values of all simulations are summarized in Table 2.

### 4.3.2.2 Dynamic grain growth rate and effect of strain rate

The rate of DGG is evaluated for all simulations using relation (2). The normalized DGG rate shows more or less constant behaviour with ongoing strain/time at constant strain rate after an initial period of transient DGG rates (fig. 4.7). For most simulations, a continuous slight decrease in DGG rate is observed at shear strains above 1.0. This is best seen in the higher strain rate tests. However, this decrease of normalized DGG-rate with time is small compared to the increase in DDG rate with increasing strain rate (cf. test14-dyn to test33-dyn; fig. 4.7). To get a better picture of how DGG-rate increases with strain rate, we calculated the average normalized DGG-rate for each test, using only data for  $\gamma = 1$  and higher, i.e. when the dynamic grain growth rate is more or less constant. The increase of the averaged normalized DGG rate with strain rate is shown in fig. 4.8. The two different curves in fig. 4.8 correspond to the two different combinations of ‘GBM time-step size’ and ‘*speed\_up*’ – values (see Table 1). As long as  $\lambda$  and  $k$  in equation (1)-(3) are constant, a linear relation with a slope of 1 can be expected between DGG rate and natural strain rate (in the log-log space of fig. 4.8). This appears to be the case for intermediate values of strain rate, where both types of GBM + deformation combinations overlap. At higher strain rates, data lie below this linear trend, implying decreasing values for  $\lambda$  (cf. equation (2)). This is more pronounced for the 1&0.3 combination. Also at low strain values, the data do not follow the linear trend of the intermediate strain rates, the 5&1.0 value being anomalously different.

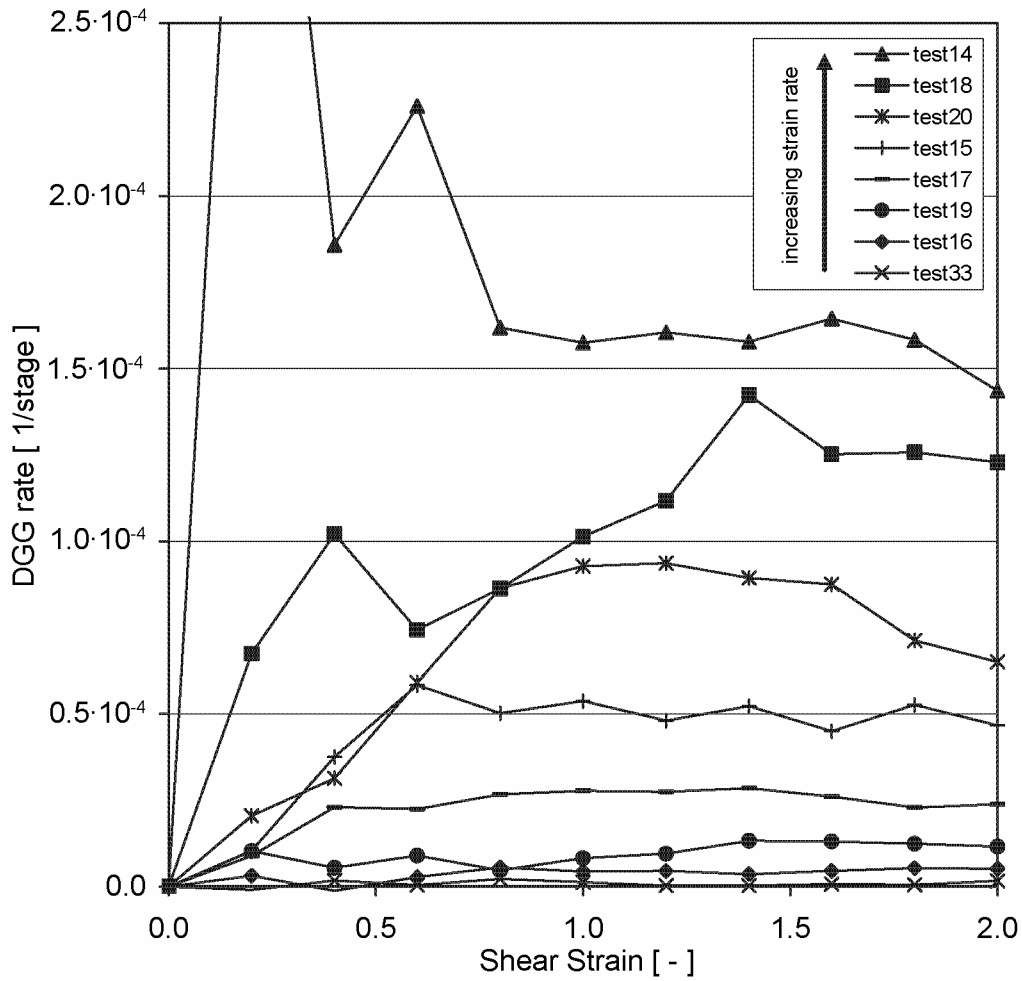


Figure 4.7. Evolution of normalized DGG rate with strain for all Type A, 1&0.3-combination tests.

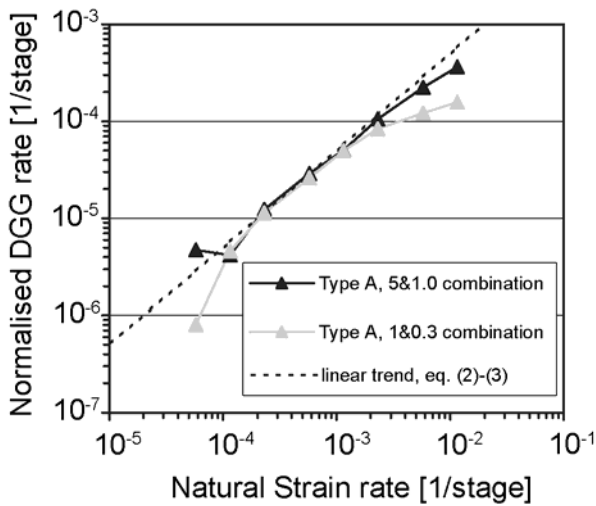
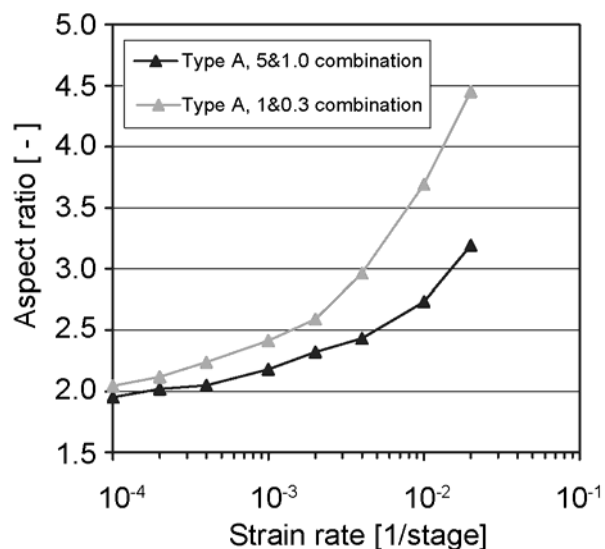


Figure 4.8. Log-scale plot of average normalized DGG rate versus natural strain rate for all Type A, i.e. homogeneous deformation plus GBM, combined tests. A linear trend line is shown for equation (2), if  $\lambda$  and  $k'$  in (3) are constant.

Fig. 4.9 shows the final average aspect ratio of the grains at  $\gamma = 2$  as a function of strain rate. We observe more flattening (increase in aspect ratio) when the strain rate is higher. Moreover, fig. 4.9 shows that for high resolution but low *speed\_up* (1&0.3) there is significantly more increase in aspect ratio, especially at the highest strain rates, compared to lower resolution but higher *speed\_up* (5&1.0).



**Figure 4.9.** Dependence of aspect ratio on strain rate for all Type A tests, i.e. homogeneous plus GBM. Aspect ratios taken at shear strain of 2.

The evolution of defect fraction with strain, as a function of strain rate, is shown in fig. 4.10. There is some scatter in defect fraction evolution with varying strain rate, but no systematic dependence on strain rate emerges from the data (fig. 4.10a, c). At shear strains above  $\sim 1.4$ , a constant value for the defect fraction is approached within the range 0.76 - 0.81. While trends are clearly defined at fast strain rates, defect fractions for both single GBM and GBM plus deformation irregularly vary and reach lower values as a function of strain at low shear strain rates, i.e.  $\leq 4.0 \times 10^{-4}$  (figs. 10b, d and Table 2).

### 4.3.3 Combined GBM and GSS deformation

#### 4.3.3.1 Dynamic grain growth and evolution of grain geometry

Test28-dyn (Table 2) is a representative example of combined GBM and GSS deformation at an intermediate strain rate. In this test we observed more DGG during GSS deformation compared to homogeneous deformation (test29-dyn) (fig. 4.11a). The evolution of defect fraction is similar to that in the homogeneous case, but less increase in aspect ratio is observed (fig. 4.11b). Qualitatively, small grains in the distribution seem to develop a stronger grain shape preferred orientation than larger grains, but with decreasing grain size at the final shrinking stages, this stronger aspect ratio diminishes again (fig. 4.12).

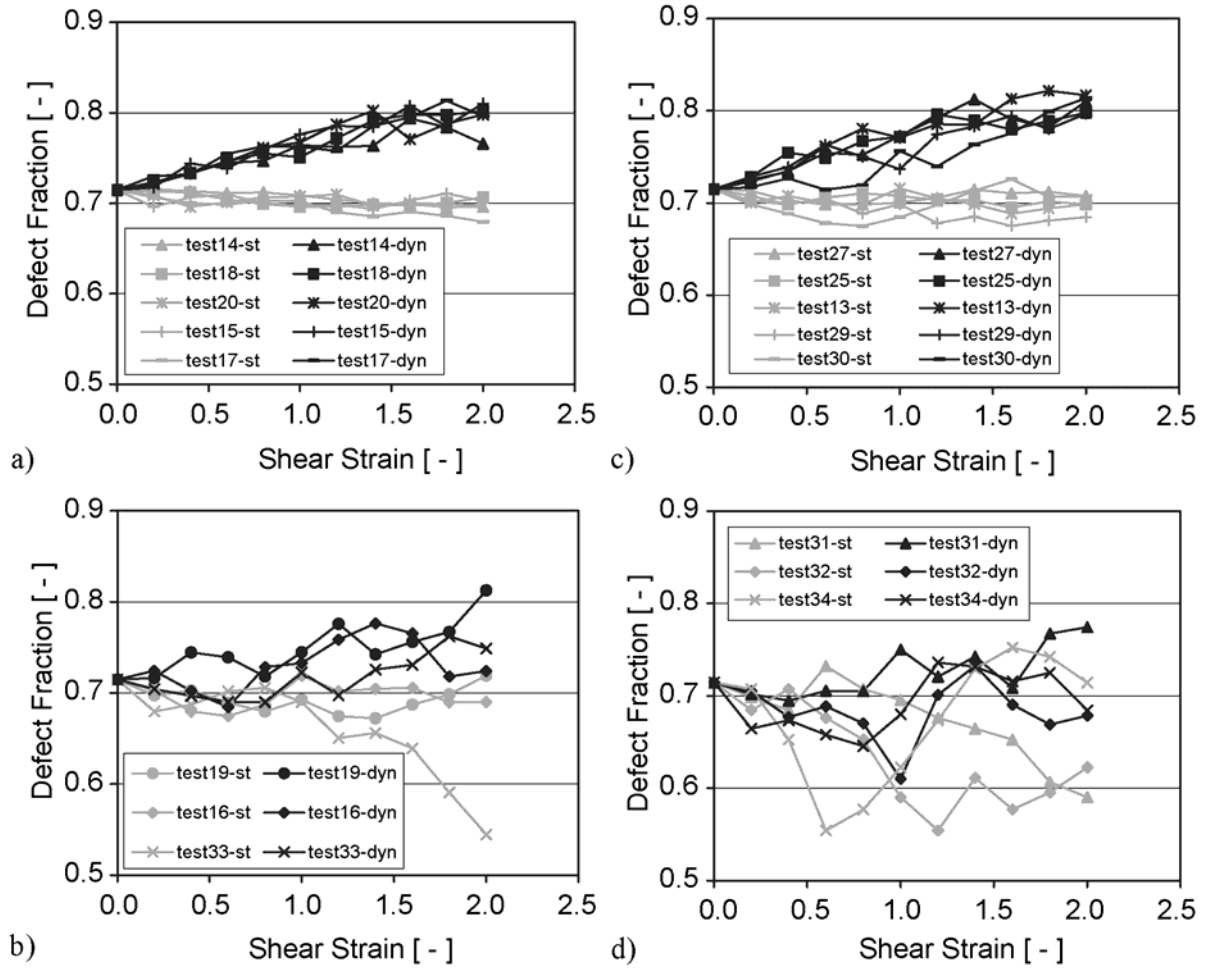


**Figure 4.10.** Evolution of defect fraction,  $X_d$ , with strain for all Type A tests; a) 1&0.3-combination tests with shear strain rate  $> 4.0 \times 10^{-4}$  b) 1&0.3-combination tests with shear strain rate  $\leq 4.0 \times 10^{-4}$  c) 5&1.0-combination tests with shear strain rate  $> 4.0 \times 10^{-4}$  b) 5&1.0-combination tests with shear strain rate  $\leq 4.0 \times 10^{-4}$ .

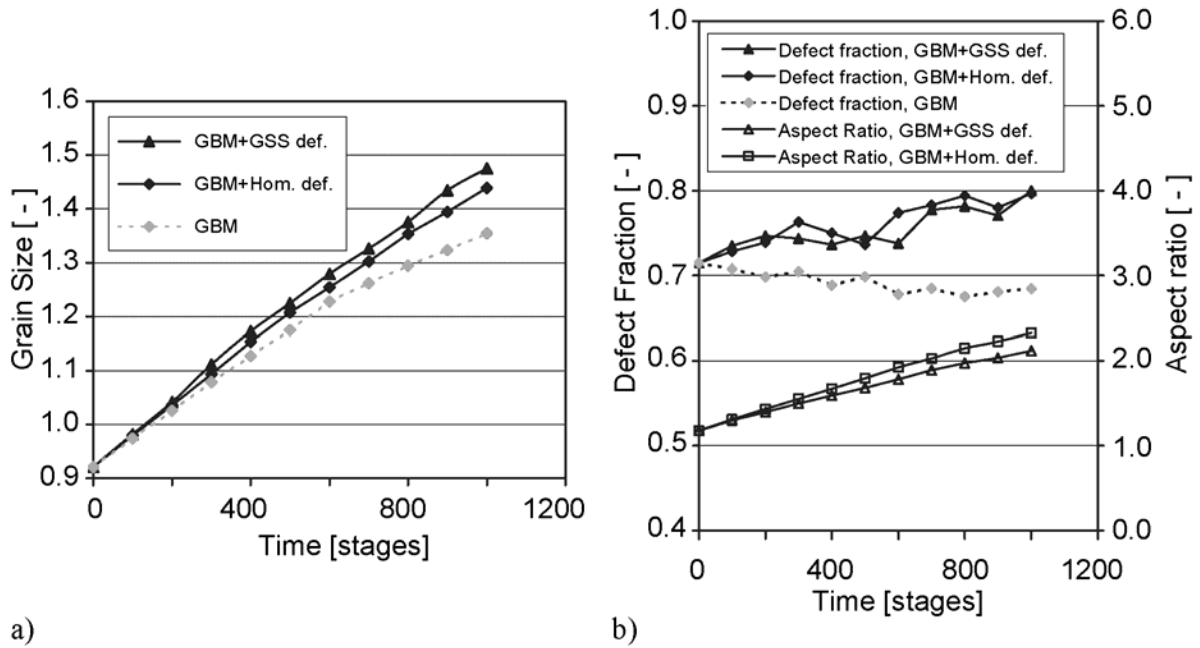


**Figure 4.11.** a) Evolution of grain size with time for static grain growth (GBM) (dotted line and diamond gray symbols, test28-29), combined GBM plus homogeneous deformation (continuous line and diamond black symbols, test29), and combined GBM plus GSS deformation (continuous line and triangle symbols, test28). Note enhanced grain growth in the GBM plus GSS deformation run (test29) compared with the other types of simulation. b) Evolution of defect fraction and aspect ratio for GBM plus deformation (homogeneous or GSS); both show gradual but significant increase.

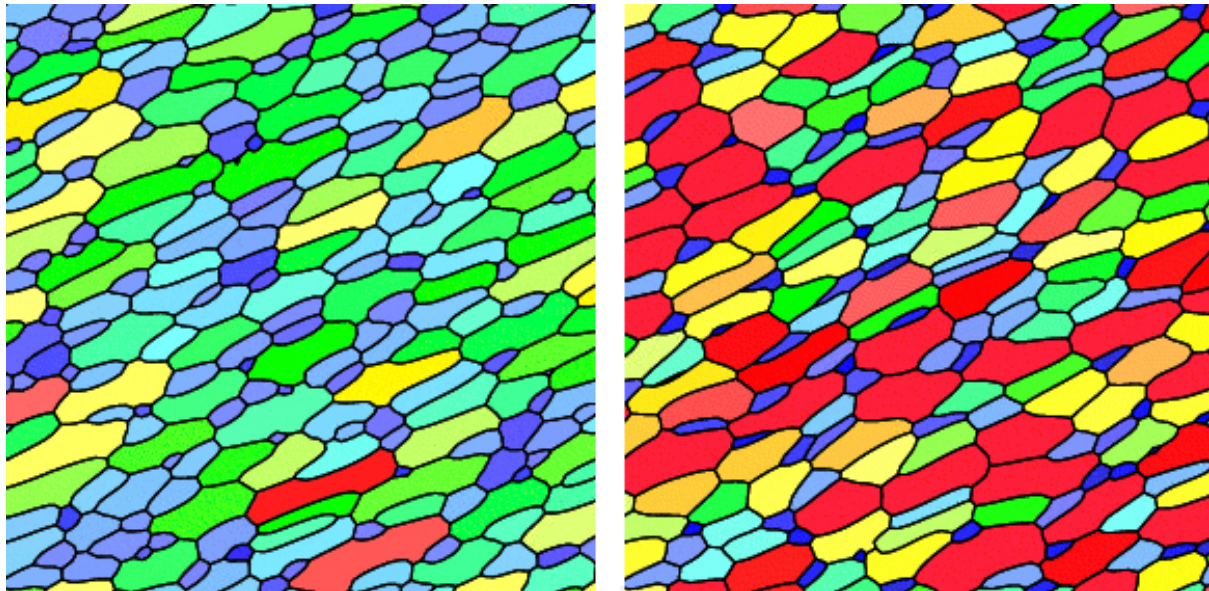


**Figure 4.12.** Microstructures (lower left quarter of modeled square cell) of test13 (left image) and test11 (right image) at a shear strain of 2. Test13 is a homogenous deformation plus GBM combined simulation showing a clear homogenous flattening of all (large and small) grains. Test11 is the equivalent GSS deformation plus GBM combined simulation showing that, in comparison to test13, larger grains are less flattened, while smaller grains have higher aspect ratios. Note the few smallest grains that show a more or less equidimensional shape.



## 4.3.3.2 Dynamic grain growth rate and effect of strain rate

Fig. 4.13 shows the dependence of DGG rate on strain rate for all GSS deformation plus GBM combined simulations. For the type B 5&1.0-combination, the usual increasing trend in DGG rate with increasing strain rate is observed, but at higher strain rates there is a strong deviation from the linear trend expected if  $\lambda$  (and  $k'$ ) is constant (fig. 4.13). All type B 1&0.3 simulations show lower DGG rates and no real trend can be observed. This is partly due to the fact that the range in strain rate is small and restricted to the higher values: because of rapidly increasing calculation times it became impractical to perform type B simulations at lower strain rates. It is only at the lowest two applied strain rates for the type B 5&1.0-combination, i.e. test28-dyn and test11-dyn, that we observe a higher DGG rate when compared to the equivalent homogeneous deformation tests. All remaining GSS deformation tests show a lower or equal DGG rate (fig. 4.13), suggesting lower or equal  $\lambda$ -values. Similarly, aspect ratio analysis only shows significantly lower values for test28-dyn and test11-dyn (fig. 4.14). The microstructure developed in the higher strain rate tests (test21-dyn to test24-dyn and test26-dyn) shows that small grains locally develop unrealistically large aspect ratios. Furthermore, only a few small grains seem to be able to shrink enough for them to regain a more or less equidimensional shape (fig. 4.15). This delayed their final disappearance.

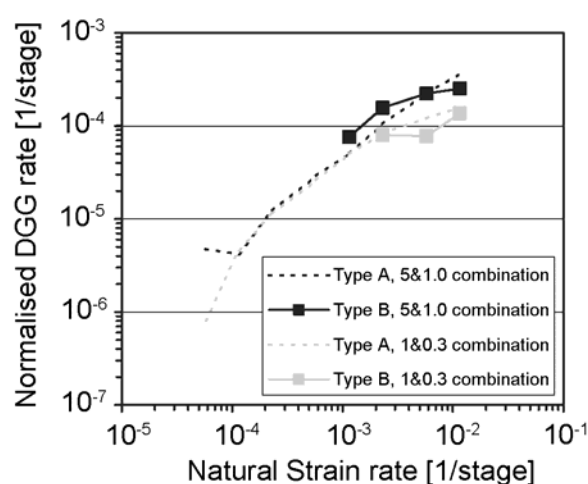


**Figure 4.13.** Log-scale plot of average normalized DGG rate versus natural strain rate for all type B, i.e. GSS deformation plus GBM, combined tests. Type A tests are also shown as lines without symbols for comparison (taken from fig. 4.8).

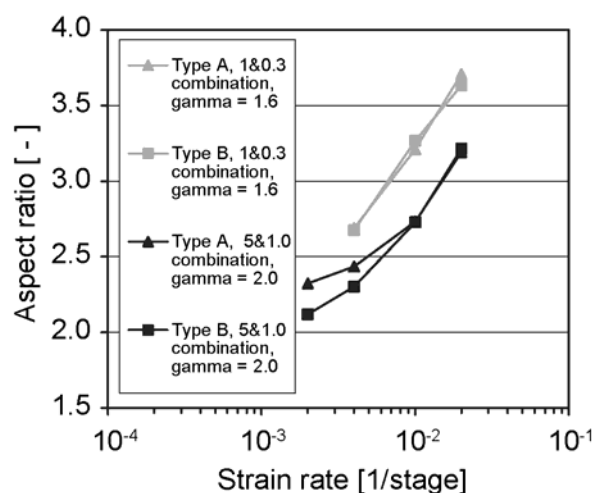


**Figure 4.14.** Dependence of aspect ratio on strain rate for all type B, i.e. homogeneous plus GBM, combined tests at constant shear strain of 1.6 for the 1&0.3 combination and at a shear strain of 2 for the 5&1.0 combination. Equivalent type A values are also included for comparison.

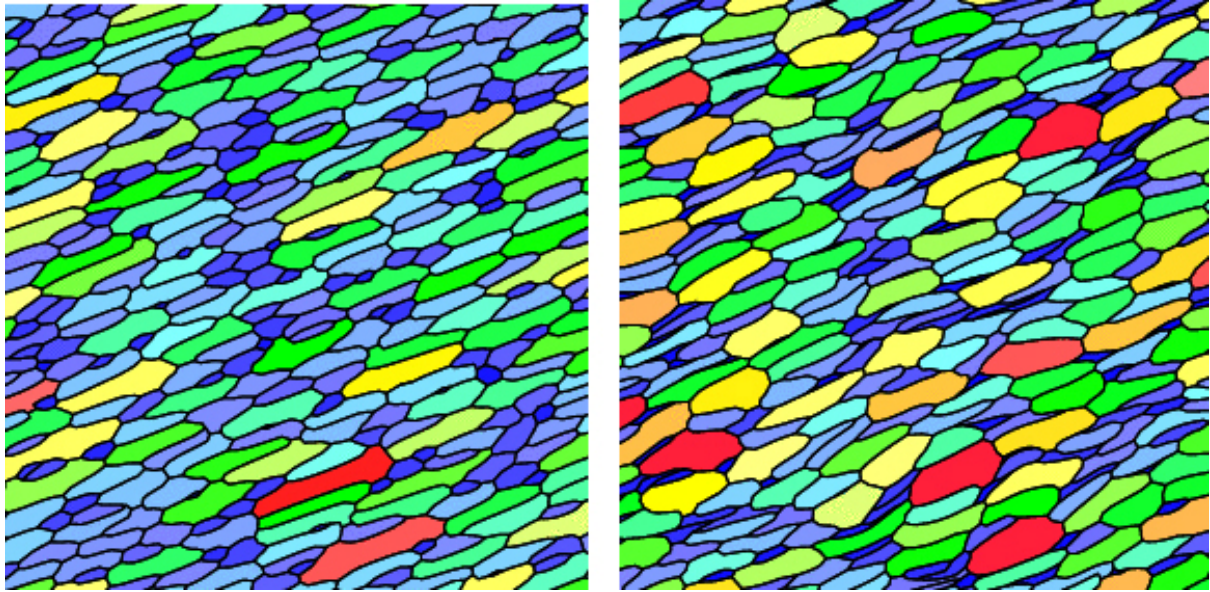


**Figure 4.15.** Microstructures (lower left quarter of modeled square cell) of test27 (left image) and test26 (right image) at a shear strain of 2 and higher strain rate than in fig. 4.12. Test27 is a homogenous deformation plus GBM combined simulation showing a clear homogenous flattening of all (large and small) grains. Test26 is the equivalent GSS deformation plus GBM combined simulation showing that, in comparison to test27, larger grains are less flattened, while smaller grains have higher aspect ratios. Moreover differences in aspect ratio between large and small grains have become more pronounced, such that now also most of the smallest grains show significant flattening.

## 4.4 Discussion

### 4.4.1 Mechanism of modeled DGG

Using 2D microstructural modeling to combine simple homogeneous (or inhomogeneous GSS) deformation and GBM, we observed a component of grain growth not seen under static conditions. In other words, we produced strain induced (dynamic) grain growth. In association with the dynamic grain growth, a systematic increase in cellular defect fraction,  $X_d$  (3), as a function of strain was observed (figs. 5b and 10). A change in defect fraction, and hence in grain topology, together with a change in average grain size, implies that extra grain neighbor switching must have taken place. Our modeling thereby demonstrates the general validity of the hypothesis that extra neighbor switching induced by deformation causes an increase in cellular defect fraction, which in turn leads to enhanced grain growth. Our modeling involved homogeneous or inhomogeneous straining of grains rather than GBS plus accommodating diffusion creep (cf. fig. 4.2). Grain neighbor switching in our deforming aggregates with distributed grain size and coordination number can be envisaged as depicted in fig. 4.16. Here it is schematically shown how extra deformation-induced neighbor switching can take place compared to static GBM. Compared to one switching event in fig. 4.1b, two switching events occurred in fig. 4.16d, leading to a higher defect fraction and more rapidly shrinking small grains. For example, compare the 3-sided grain in fig. 4.16d with the larger 4-sided grain in fig. 4.1b.

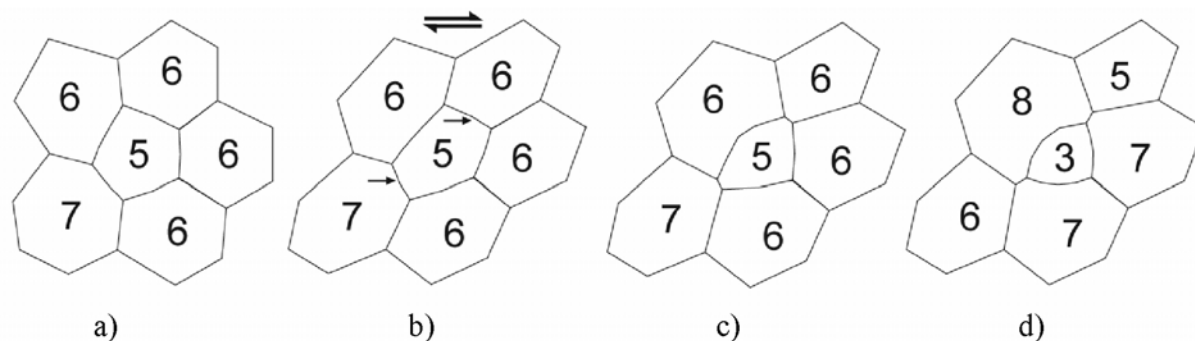


**Figure 4.16.** Schematic drawing of geometrical strain plus GBM induced grain neighbor switching in an aggregate with distributed grain size and coordination number. a) Initial microstructure similar to Fig. 4.1a,  $X_d = 2/6 = 0.33$ , b) Sheared microstructure, small arrows indicate grain boundary segments of the 5-sided grain, which are bounded by distorted triple junctions, i.e.  $\neq 120^\circ$  angles,  $X_d = 2/6 = 0.33$  c) The unstable triple junctions have moved toward each other via GBM to regain a stable geometry,  $X_d = 2/6 = 0.3$  d) Ongoing GBM has led to 2 switching reactions and the 5-sided grain has become 3-sided. Only one six-sided grain remains, giving a defect fraction of 0.83 in this particular microstructure.

Any 2D grain neighbor switching event is preceded by a stage in which the grain boundaries involved form a quadruple point. There are various ways to develop a quadruple point. One scenario, proposed by Bons and Urai (1992; their fig. 4.10), showed how homogeneous flattening of a group of 4 equally-sized ideal hexagonal grains (fig. 4.2a) can result in (extra) surface-energy-driven GBM, leading to strain-induced neighbor switching without grain growth. In their approach, the evolution of grain boundary geometries up to ca. 40 % shortening (0.5 natural strain) results in an unstable stage when two triple points merge into a quadruple point, where the boundaries intersect at  $60^\circ$  and  $120^\circ$  angles. In this evolution, grains develop an elongated shape (aspect ratio  $>1$ ). Pure grain boundary or lattice diffusion (Coble or Nabarro-Herring) creep can produce a similar quadruple point. These diffusion mechanisms change the shape of the grains, as is the case in the Bons and Urai (1992) scenario, but do not disturb the  $120^\circ$  equilibrium angles at triple points. Although the theories behind conventional Coble and Nabarro-Herring GSS creep do not explicitly include any grain switching, such microstructural modification is inevitable for the 4 grain-aggregate with ideal hexagonal grains as used by Bons and Urai (1992), as can be seen in fig. 4.2a. Ashby and Verrall (1973) explicitly incorporate neighbor switching in a model for diffusion-accommodated GBS and also predict a quadruple point stage at ca. 40 % shortening (cf. Bons and Urai, 1992). In contrast to the above scenarios, in their model all boundaries are now at  $90^\circ$  angles, and no elongated grain shape develops. Further, Ashby and Verrall's model presumes a completely different flow pattern on the grain scale, i.e. less volume displaced per unit strain and a shorter length of diffusion pathways compared to conventional GSS creep. Irrespective of how a quadruple point develops, the geometry will be unstable and will be modified by a subsequent stage of GBM to re-equilibrate grain boundaries. As a result, a single indistinguishable grain boundary geometry develops, with equal-sized and equidimensional hexagonal grains. We suggest it is reasonable to assume that all types of deformation-related neighbor switching lead to similar changes in topology of aggregates with distributed grain size and distributed coordination number (in contrast to an idealized honeycomb network). This may affect two measurable microstructural parameters: (1) it can increase the defect fraction, following Sherwood and Hamilton (1992), and (2) it can enhance the grain growth. Both of these effects are observed in all our tests. Two important caveats to

the above must be dealt with. First, the homogeneous flattening as modeled in the present study lacks a true physical basis in terms of a specific deformation mechanism. Thus process rates as seen in the modeling, for instance the number of grain switching events per strain or time increment, might be very different from nature. However, from the above it appears that flattening plus GBM, as applied in simulations (Bons and Urai, 1992), will produce neighbor switching at roughly the same strain as predicted for theoretically based diffusion-accommodated GBS or conventional GSS creep. The amount of strain necessary to induce a neighbor switching, obviously, controls the number of switching events per time unit (at a certain strain rate) and thus most likely effects the resulting dynamic grain growth rate. We therefore do not expect large differences in dynamic grain growth rate to be produced by the present modeling, in experiments, or in nature. A second point is that the present modeling produces a strong grain shape preferred orientation with increasing strain. However, in real materials and natural rocks deformed by dominant GSS creep, a large component of GBS is frequently inferred and grain-shapes are more or less equidimensional even if large strains were reached. This marked difference between the present modeling and nature does result in dissimilar (dynamic) grain growth rates, which will be discussed further below.

#### 4.4.2 Microstructural evolution and strain rate effects

Together with a gradual increase in defect fraction, we also observed an increase in aspect ratio with strain (fig. 4.5b). Bons and Urai (1992) performed similar combined GBM plus deformation simulations to those of our study and observed that GBM tends to impede the increase in aspect ratio when compared to deformation without GBM. They further concluded that the presence of a strong aspect ratio slows down grain growth. This conclusion was based on the comparison of results from two modeling runs with different starting microstructures. In one run, an initial microstructure was homogeneously flattened first, before static grain growth was allowed. In the other run, the same initial microstructure was allowed to grow without prior deformation. Our approach was different, since grain growth and flattening occurred (quasi) simultaneously. Nevertheless, we confirm the conclusion of Bons and Urai (1992) as shown by our observation of a small but systematic decrease in DGG rate with strain (i.e. flattening) at constant strain rate (see fig. 4.7), together with a prominent decelerating increase in DGG-rate with increasing strain rate (see fig. 4.8). This correlates well with a strain- and strain rate-dependent increase of aspect ratio (see figs. 4.6 and 4.9). In our simulations, the retarding effect of aspect ratio formation on grain growth does not result in less net grain growth compared to the static tests. This is because of the enhancing effect of deformation on grain growth related to neighbor switching, which probably dominates the impeding effect of aspect ratio increase.

The divergence between the 5&1.0 and 1&0.3 combinations in fig. 4.8 at higher shear strain rates ( $2 \times 10^{-3}$  -  $2 \times 10^{-2}$ ) appears strongly related to stronger aspect ratio formation at a lower *speed\_up*-value (or GBM mobility), as shown in fig. 4.9. At lower intermediate shear strain rates ( $4 \times 10^{-4}$  -  $2 \times 10^{-3}$ ), both combinations overlap and the DGG rate parameter  $\lambda$  in relations (1)-(3) is more or less constant (fig. 4.8). In addition, we found a very consistent increase in defect fraction,  $X_d$  (3), which approaches a constant level around 0.81 at these strain rates (see 3.6a, c). In other words, both rate parameter  $\lambda$  and defect fraction remain constant with increasing (intermediate) strain rate. Moreover, the decrease in  $\lambda$  at the lowest shear strain rates ( $1 \times 10^{-4}$  -  $4 \times 10^{-4}$ ) correlates well with the decreasing trend in defect fraction for static grain growth tests and with the greater variability and smaller increase in defect fraction for combined GBM plus deformation tests (figs. 10b, d). This supports the hypothesis that  $\lambda$  is strongly related to defect fraction,  $X_d$ , as in equation (3). At lower strain

rates, the increased variability in defect fraction is probably an artifact of the decrease in number of grains after long periods of time. This causes statistical inconsistencies in the distributions in grain size and coordination number of the strongly coarsened modeled aggregate. This must also have triggered the anomalous high DGG-rate at the lowest strain rate for the 5&1.0 combination (test34-dyn), as this microstructure experienced the greatest amount of grain growth of all the simulations; in fact only 76 grains remained from the 1500 grains at the start (see also Table 2).

#### 4.4.3 The effect of GSS deformation

In order to obtain a crude impression of the effect of GSS deformation, we invoked viscosity decrease with decreasing grain size in our model, so that smaller grains were more easily deformed and flattened than larger grains (fig. 4.12). Compared to grains undergoing homogeneous deformation, this resulted in a more heterogeneous evolution of aspect ratio and grain shape preferred orientation, which can explain higher DGG rates at slower strain rates and lower DGG rates at higher strain rates. At intermediate strain rates, the local strain heterogeneities between larger and smaller grains result into a lower overall aspect ratio (test28-dyn and test11-dyn, fig. 4.14) and thus higher DGG rates compared to homogeneous deformation under the same conditions. The higher strain rates and/or lower *speed\_up* values in all other GSS tests result in similar aspect ratios compared to homogenous deformation. Nevertheless, the strain heterogeneities are perhaps even more prominent in these tests (fig. 4.15) and we propose that, in this case, GBM of the now strongly flattened smallest grain size fraction cannot keep up with the deformation (see also Bate, 2001). This may impede final shrinkage and may prevent disappearance of these smallest grains (fig. 4.15), leading to lower DGG rates compared to homogeneous deformation. Advances in modeling techniques eventually will allow more physically based simulation of GSS creep, possibly including accommodation by GBS and grain rotation (e.g. Ford et al., 2002) to be incorporated in ELLE. This will limit the formation of a strong aspect ratio and its significant effect on DGG behaviour at high strain rates and would make the results better applicable to interpreting the behaviour of natural rocks and superplastically deformed materials. Our goal in the present study was only to investigate whether GBM plus geometrical (in)homogeneous deformation could induce extra neighbor switching, resulting in a higher defect fraction and in enhanced grain growth.

As noted above, an increase in aspect ratio is found to have a strong decelerating effect on the rate of dynamic grain growth. We further emphasize that in this study we did not include dislocation activity, related grain size reduction, formation of interconnected weak layers, or other development of organized strain heterogeneities. In case these processes are active, an increasing dynamic grain growth rate with increasing strain rate will be difficult to interpret, in particular because faster strain rate generally gives higher stresses resulting in smaller (!) recrystallized grain sizes. In the following sections we will further elaborate on the relevance of the model results for natural systems and experiments on real materials.

#### 4.4.4 Comparison to existing models and experimental work

The various theoretical, modeling and experimental studies on DGG have indicated a range of values for the strain rate sensitivity of rate parameter  $\lambda$  in (1)-(3), from 0.13 (Seidensticker and Mayo, 1998a) up to  $\sim 1$  (Wilkinson and Caceres, 1984). Seidensticker and Mayo (1998a) summarized DGG data on a wide range of metallic and ceramic materials

tested within over a large range of temperatures and found surprisingly consistent strain rate dependency. The compiled data of Seidensticker and Mayo (1998a) fall within a band of linear strain rate sensitivity  $\lambda$  with upper and lower limits of 0.04 and 1, respectively (average 0.13). A comparison of our data to the calibration by Seidensticker and Mayo (1998a) is shown in fig. 4.17. Our simulation data for  $\lambda$  (figs. 8, 11 and 17) vary between 0.07 and 0.01, and are positioned near the lower limit of the range for real materials of Seidensticker and Mayo (1998a). This first order agreement of the modeling results with experimental data on real materials gives confidence in the general validity of our conclusions. If anomalous aspect ratio development in future modeling can be reduced (see section 4.4.3) DGG rate might very well reach the average  $\lambda$  of 0.13. At the highest strain rates, the experimental record shows incipient breakdown of the linear relationship due to a supposed deformation mechanism switch from superplasticity to dislocation creep (Wilkinson and Caceres, 1984). This nicely agrees with the lower DGG rate values predicted in this study at the highest strain rates. If such a mechanism switch is accompanied by an increase in aspect ratio formation, our modeling may provide a good approximation of this breakdown in the linear trend of natural strain rate vs. normalized DGG rate.

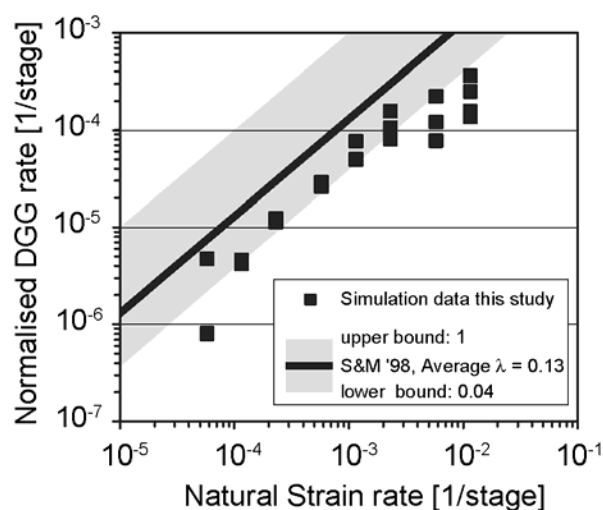


**Figure 4.17.** Log-scale plot of average normalized DGG rate versus natural strain rate for all simulations of this study (of figs. 6 and 13) compared to the average linear relationship calibrated by Seidensticker and Mayo (1998) and the upper and lower bounds of this calibration.

The microstructural modeling study of Bate (2001) investigated GBM during deformation of uniform Zener-pinned aggregates and produced higher DGG rates and  $\lambda$  (0.4 to 0.5) than those from the compilation of Seidensticker and Mayo (1998a) or from our simulation runs. This suggests that if Zener-pinning could be introduced into our simulations, the component of dynamic grain growth may well be significantly larger. We aim to take this into account in future modeling, as our forsterite microstructures (Kellermann Slotemaker et al., 2004) also showed definite effects of grain boundary pinning. It is worth noting that the ELLE system has the potential to model non-uniform Zener-drag by introducing an unconnected distribution of discrete second phase grains into the microstructure, which would be even more realistic than the applied uniform Zener-drag by Bate (2001).

#### 4.4.5 Relevance of the model results to natural rocks

The results of the ELLE 2D microstructural modeling suggest that analysis of the fraction of non-hexagonal grains in a deformed material represents a way to establish if dynamic grain growth has occurred. Recognizing this process in natural rocks can be of great

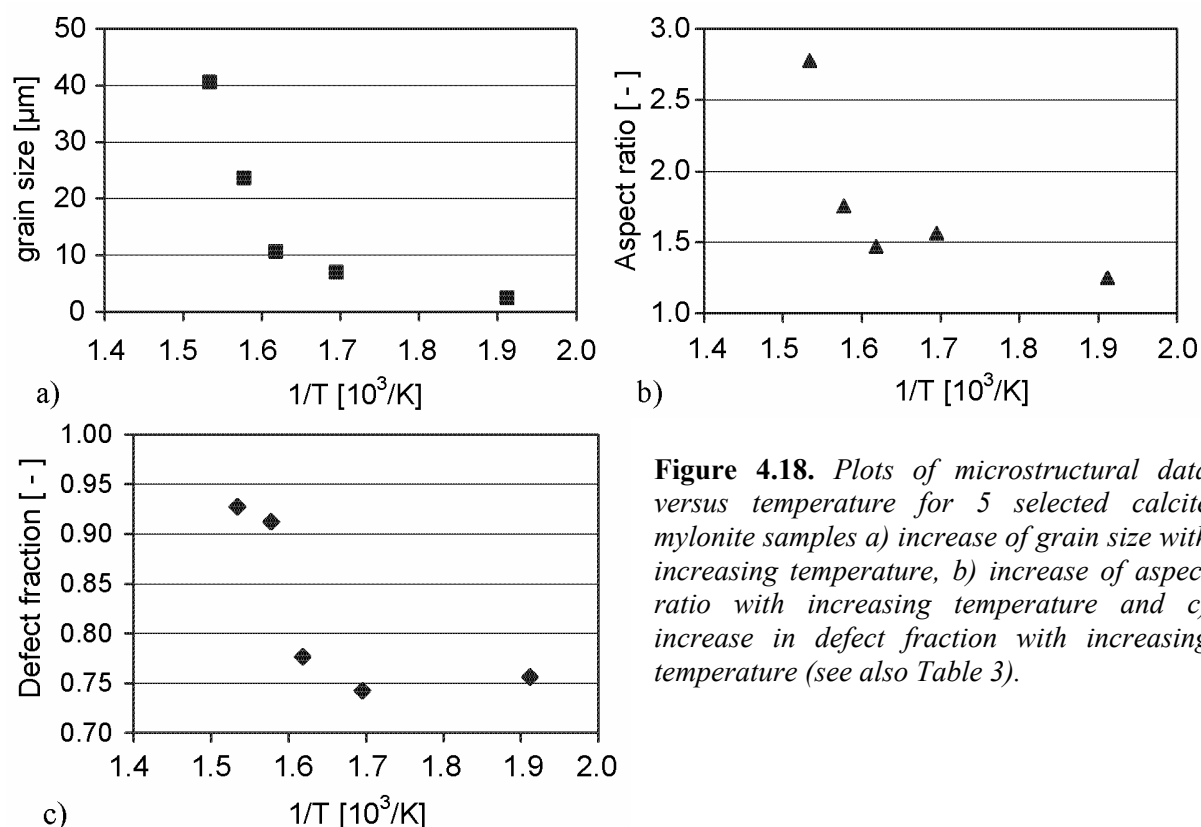
help in the interpretation of the rheological behaviour in a geodynamic context. In order to test and illustrate the potential of defect fraction analysis, we measured defect fractions in some natural calcite mylonites from the Helvetic Alps, Switzerland. The samples were selected from a suite of calcite rocks that show significant syndeformational grain growth, analyzed in detail by Herwegh et al. (2005). The mylonites come from thrust planes in a nappe stack consisting of the Doldenhorn, Gellihorn and Wildhorn nappes. The initially fine-grained limestones were inferred to have been deformed at a strain rate of about  $10^{-11} \text{ s}^{-1}$  and a temperature between 250 and 379 °C. With increasing deformation temperature, the grain size and grain aspect ratio increases (Table 3, fig. 4.18), while the crystallographic preferred orientation of calcite c-axes remains of similar strength. Rheological modeling using full grain size distributions and composite flow laws for GSS and grain size insensitive (GSI) creep (see Ter Heege et al., 2004) indicate an increase in the GSS component of the overall creep rate with increasing temperature (see Table 3). From the measurements and modeling, Herwegh et al. (2005) concluded that with increasing temperature a) grain growth became the major microstructure modification process in the fine-grained rocks, and b) enhanced mass transfer / diffusion processes occurred, rather than increased activity of dislocation mechanisms.

Table 3. Data overview natural calcite mylonites

sample	temp, T [°C]	1/T [10 <sup>3</sup> /K]	grain size [μm]	aspect ratio [-]	%GSS <sup>a)</sup> [%]	defect fraction [-]
Ge-3	250	1.91	2.5	1.25	~0.3	0.76
Wi-16	317	1.69	7.0	1.56	~2.0	0.74
Do-8	345	1.62	10.7	1.47	93-100	0.78
Do-28	361	1.58	23.7	1.75	60-100	0.91
Jung-986	379	1.53	40.6	2.78	31-87	0.93

<sup>a)</sup> %GSS indicates the relative contribution of GSS creep to the total. Calculation of %GSS depends on the character of the grain size distribution, chosen experimentally calibrated flow laws and assumptions regarding homogeneous stress or homogeneous strain rate through the aggregate (see Herwegh et al., 2005).

The same (2D) grain boundary maps as used by Herwegh et al. (2005) were taken to measure grain coordination numbers and to determine defect fractions (Table 3, fig. 4.18). The defect fraction was found to be relatively low (~ 0.75) at low temperature, in samples dominantly deformed by GSI mechanisms. Given that these samples were highly strained, but show small grain sizes and low aspect ratios, competition between grain growth and grain size reduction must have kept the grains relatively small and close to equidimensional. This produced a microstructure that looks ‘static’, which is consistent with the low defect fraction. In contrast, the calcite mylonites deformed at higher temperature show high defect fractions (~ 0.9). The increase in defect fraction corresponds to the change in slope in the grain size vs. temperature and aspect ratio vs. temperature trends (fig. 18). Following Herwegh et al. (2005), these microstructure modifications indicate an increased contribution of grain growth to the grain size stabilization process. Apparently, anisotropic grain growth becomes more prominent at higher temperature, related to a more pronounced contribution of GSS mechanisms to the overall creep. The higher defect fraction at higher temperature is fully consistent with this, suggesting grain neighbor switching played an important role in the deformation.



**Figure 4.18.** Plots of microstructural data versus temperature for 5 selected calcite mylonite samples a) increase of grain size with increasing temperature, b) increase of aspect ratio with increasing temperature and c) increase in defect fraction with increasing temperature (see also Table 3).

In summary, the increased component of syndeformational grain growth and the enhanced contribution of GSS creep mechanisms to the overall creep inferred by Herwegh et al. (2005) for the Helvetic limestones are reflected in an increase in fraction of non-hexagonal grains. An analysis of defect fractions therefore helps in interpreting the development of natural microstructures.

## 4.5 Conclusions

We used a 2-D microstructural modeling approach to investigate the evolution of defect fraction (i.e. the fraction of non-hexagonal grains) during combined grain boundary migration and deformation to test the hypothesis that strain-induced neighbor switching can result in enhanced grain growth. We conclude the following.

1. Using simple 2-D microstructural modeling of grain growth during deformation we were able to produce a component of grain growth not seen under static conditions.
2. This (component of) dynamic grain growth correlates well with a systematic increase in defect fraction,  $X_d$ . Starting with a value of 0.71, the defect fraction gradually increases with strain, approaching a constant level around 0.80 at shear strains above  $\sim 1.4$ .
3. Non-linear strain rate sensitivity of dynamic grain growth rate at the lowest and highest strain rates can be linked to microstructural changes in grain topology and geometry, namely varying defect fraction and aspect ratio. This supports the hypothesis that the rate parameter  $\lambda$  in the relation  $\dot{d}_{dyn} = \lambda \cdot d \cdot \dot{\epsilon}$  is strongly related to defect fraction ( $\dot{d}_{dyn}$  = dynamic grain growth rate,  $d$  = grain size and  $\dot{\epsilon}$  = strain rate).



4. At relatively low strain rates, dynamic grain growth rate is faster if straining is simulated via inhomogeneous GSS creep rather than by simple homogeneous deformation.
5. At intermediate strain rates, we found a good correlation between our dynamic grain growth rate and strain rate data and already published models and experiments on dynamic grain growth. Both show a constant rate parameter  $\lambda$ . The linear strain rate sensitivity and constant defect fraction ( $\sim 0.8$ ) observed at intermediate strain rates in this study provides preliminary constraints on the variation of the rate parameter  $\lambda$ .
6. Analysis of defect fraction appears to be a good microstructural tool for establishing whether or not a material has experienced normal static (defect fraction  $\sim 0.7$ ) or dynamic (defect fraction  $\sim 0.8$ ) grain growth.



## Chapter 5

### Flow behaviour and microstructural evolution of Fe-bearing synthetic forsterite-enstatite aggregates

**Abstract.** Upper mantle dynamics are for a large part controlled by the flow-behaviour of olivine, which is the most abundant and, under a wide range of conditions, the weakest mineral species present. In general, natural upper mantle derived olivine is iron bearing ( $fo_{-90}$ ). A number of previous experimental investigations focused on the flow behaviour of samples containing natural olivine, but more recently, several experimental creep studies used synthetic olivine samples prepared from high purity components. Most of these synthetic samples were composed of the pure magnesium end member of olivine ( $fo_{100}$ ). A comparison between the results on natural  $fo_{-90}$  and synthetic  $fo_{100}$  would basically provide insight into the role of Fe in creep of olivine, but drawing conclusions at present is hindered because of differences in experimental conditions between the studies and differences in microstructure and, possibly, impurity content of the materials used. Further, recent work has shown that more attention is needed on the relation between microstructural evolution and surface energy driven grain growth (rather than dynamic recrystallization) during GSS creep. The importance of this lies in the potential role of GSS creep in localization. To investigate both the effect of Fe on flow behaviour of olivine aggregates and on high strain microstructural evolution during grain size sensitive (GSS) flow behaviour, we have conducted new deformation and heat-treatment tests on synthetic fine-grained wet  $fo_{90}$  material at 850-1000°C and 600 MPa pressure. Compared to data for synthetic wet  $fo_{100}$  at similar conditions, no difference in flow behaviour was observed. Furthermore, similar to  $fo_{100}$ , a deformation induced component of grain growth was observed. Microstructural analysis showed this enhanced grain growth can best be related to a change in fraction of non-hexagonal grains.

## 5.1 Introduction

### 5.1.1 General aim

Experimentally calibrated flow laws for olivine bearing aggregates supply rheological constraints for meaningful construction of geodynamic models, aimed to investigate the state of stress, strain (rate) and flow behaviour in the upper mantle region for various geodynamical settings (Hopper and Buck, 1993; Karato and Wu, 1993; Govers and Wortel, 1995; Wang et al., 2005). In general, natural upper mantle derived olivine contains iron, with a Fe to Fe + Mg molar ratio of  $\sim 0.1$ , also referred to as  $fo_{90}$ . Previous work suggested that a strength difference exists between  $fo_{90}$  and  $fo_{100}$  (i.e. the magnesium end member material) notably with respect to its grain size sensitive (GSS) flow behaviour (Mei and Kohlstedt, 2000a&b). However, a definite conclusion on the effect of Fe on flow behaviour of olivine cannot yet be made since different methods have been employed in preparing samples and since the various materials have not been tested at similar temperature-pressure conditions. Furthermore, new results on  $fo_{100}$  (chapter 3) have shown a component of deformation enhanced grain growth under conditions of GSS deformation, as opposed to pinned grain growth under static conditions. This dynamic grain growth affects the strength of  $fo_{100}$ , but the effect of Fe on grain coarsening at otherwise similar conditions is unknown. Considering these issues, the study presented in this chapter aims to 1) directly compare the GSS flow behaviour of synthetic Fe-bearing olivine to that of Fe-free forsterite prepared by the same

procedure and deformed at similar conditions, and 2) to investigate if microstructural evolution of Fe-bearing material deformed in the GSS regime results in deformation enhanced grain growth similar to forsterite. The following subsections give further background on why these aims can best be treated through experiments on synthetic fo<sub>90</sub>.

### 5.1.2 Role of Fe in the GSS diffusion creep field

McDonnell et al. (1999) investigated the flow behaviour of very fine-grained synthetic forsterite aggregates, fo<sub>100</sub>, in the presence of H<sub>2</sub>O and observed dominant GSS creep with a strong component of grain boundary sliding. This Fe-free material appears significantly stronger than Fe-bearing olivine material deforming by GSS creep (Karato et al., 1986; Hirth and Kohlstedt, 1995a; Mei and Kohlstedt, 2000a). Several workers mention the potentially large effect of Fe on point defect chemistry and related flow behaviour of olivine (Hitchings et al., 1989; Mei and Kohlstedt, 2000a; Ji et al., 2001). We will first treat this point in more detail below, before going into differences that exist in sample preparation and imposed experimental conditions between studies on Fe-bearing versus forsterite materials.

*Point defect chemistry in olivine.* The concentrations of the various point defect species (e.g. vacancies and interstitials) in a crystal lattice as a function of thermodynamic state constitute a material's point defect chemistry. In general, the point defect species that are highest in concentration control the charge neutrality condition, i.e. the sum of the concentrations that regulate charge balance in the material. The concentrations of all additional diffusing species (i.e., of lower concentration) in a crystal lattice are thought to be strongly sensitive to this charge neutrality condition. This means invoking a change in charge neutrality condition (e.g. through addition of Fe to the olivine crystal structure) might also alter the concentrations of additional diffusing species. This is of importance, since it is well known that during diffusion creep, strain rate is controlled by diffusion of the slowest species (generally low in concentration) diffusing along its fastest path, i.e. through the crystal lattice or along grain boundaries.

In dry Fe-free olivine (fo<sub>100</sub>), magnesium Frenkel defects are the major point defects (Smyth and Stocker, 1975), such that  $[Mg_i^{••}] = [V_{Mg}^{//}]$  (using notation after Kröger and Vink, 1956) forms the charge neutrality condition (Mackwell and Kohlstedt, 1986). In the above, the Kröger and Vink (1956) notation defines  $[Mg_i^{••}]$  as the concentration ([]) of magnesium (Mg) on interstitial sites (subscript: i) with an electrical charge of 2+ (superscript: ••). The notation  $[V_{Mg}^{//}]$  indicates the concentration of vacancies (V) on magnesium sites (subscript: Mg) with an electrical charge of 2- (superscript: //). When comparing diffusivities of silicon, oxygen and magnesium through the crystal lattice of dry fo<sub>100</sub> (i.e. volume diffusion, Anderson et al., 1989), silicon appears to be the slowest diffusing species, followed by oxygen and magnesium (i.e.  $D_{Si} \ll D_O \ll D_{Mg}$ ). In contrast, grain boundary diffusion data of silicon (Farver and Yund, 2000) and magnesium (Farver et al., 1994) in dry fo<sub>100</sub> show diffusion rate of magnesium is about an order of magnitude less than silicon, at least at temperatures below ~ 1200°C. Above this temperature the difference is within the error of the obtained diffusion rates. No specific diffusion data exists for grain boundary diffusion of oxygen in dry fo<sub>100</sub>.

The effects of water-related defect species on the charge neutrality condition in wet fo<sub>100</sub> and on diffusion rates of the different species have not been systematically investigated to date. However, Yund (1997) found grain boundary diffusion rates must be a factor of 28 greater for wet compared to dry samples, based on growth rates of enstatite and forsterite

reaction rims, though the controlling diffusing component was unknown. Braithwaite (2002) presented a theoretical study of potentially important hydrogen related defects in Fe-free olivine, which all are associated with magnesium. These hydrogen related defects associated to Mg are then considered to be present in high concentrations suggesting that all other defects related to Si or O could potentially be the slowest diffusing species.

Turning now to Fe-bearing olivine, various experimental studies (see Mei and Kohlstedt, 2000a, for a review) have shown that ferric iron ( $\text{Fe}^{3+}$ ) on metal sites,  $\text{Fe}_{\text{Me}}^{\bullet}$ , and metal vacancies,  $\text{V}_{\text{Me}}^{\prime\prime}$ , are the major point defects in dry material, such that electroneutrality is given by  $[\text{Fe}_{\text{Me}}^{\bullet}] = 2[\text{V}_{\text{Me}}^{\prime\prime}]$ . Furthermore, based on *dry* volume and grain boundary diffusion data (Ryerson et al., 1989; Houlier et al., 1990; Watson, 1991; Fislser and Mackwell, 1994; Hirth and Kohlstedt, 1995a; Farver and Yund, 2000; Gaetani and Watson, 2000), Hirth and Kohlstedt (2003) argue that silicon grain boundary diffusion will control GSS creep in dry experiments and at any conditions in a dry upper mantle at a grain size  $< 1\text{m}$ . This means silicon diffusion is the slowest species (compared to O, Mg and Fe) in both grain volume and grain boundaries, and grain boundaries form the fastest pathway up to grain sizes of  $\sim 1\text{m}$ .

Lack of *wet* diffusion data for Fe-bearing olivine precludes a full detailed analysis for hydrous conditions. Nevertheless, Mei and Kohlstedt (2000a) preliminarily evaluated the charge neutrality condition in wet Fe-bearing olivine by measuring the exponential dependency of GSS flow behaviour on water fugacity. They compared the measured range in water fugacity exponent (0.7-1.0) with theoretical values predicted on the basis of various possible charge neutrality conditions. Additional constraints provided by FTIR spectra and defect energies led them to argue that under hydrous conditions charge neutrality is controlled by concentrations of ferric iron and OH ions associated with metal vacancies, i.e.  $[\text{Fe}_{\text{Me}}^{\bullet}] = [\text{H}_{\text{Me}}^{\prime}]$ . With this charge neutrality condition, silicon diffusivity would increase linearly with water fugacity and most likely rate limits diffusion creep of wet Fe-bearing olivine, similar to dry material.

In summary, since addition of Fe will introduce ferric iron ( $\text{Fe}^{3+}$ ) as a major point defect in the olivine crystal lattice, fo<sub>90</sub> and fo<sub>100</sub> will have significantly different point defect chemistries at both hydrous and anhydrous conditions. Charge neutrality for fo<sub>90</sub> and fo<sub>100</sub> will be governed by different major point defect species. At dry conditions, the charge balance is thought to be controlled by Fe-related species in fo<sub>90</sub> and by Mg-related species in fo<sub>100</sub>. At wet conditions, OH-associated defects with Fe and Mg for fo<sub>90</sub> and fo<sub>100</sub>, respectively, provide charge neutrality. This difference in point defect chemistry may or may not have important consequences for the diffusive properties of both materials. First, it may cause creep to be different when controlled by *different slowest diffusing species*, e.g. Si- versus Mg-controlled grain boundary diffusion creep for fo<sub>90</sub> and fo<sub>100</sub>, respectively, at dry conditions. Second, it may cause *different concentrations* of the same slowest diffusing species, e.g. higher Si defect species in fo<sub>90</sub> compared to fo<sub>100</sub>, which may also lead to different creep rates. Third, although having different point defect chemistries, the difference in concentration of slowest diffusing species might be minor and not lead to different flow behaviour.

Mei and Kohlstedt (2000a) pointed out that due to the differences in point defect chemistry, solubility of water is higher in Fe-bearing olivine. Moreover, Zhao et al. (2004) showed that water solubility increases exponentially with the mole fraction of Fe and that extrapolations to zero Fe-content predict solubility levels for forsterite that are even greater than those observed experimentally. Following Mei and Kohlstedt (2000a), Hirth and Kohlstedt (2003), and Karato (2003) suggest that strain rate increases approximately linearly with water concentration (or fugacity). Thus Fe-bearing olivine is expected to be weaker than forsterite at similar hydrothermal conditions.

### 5.1.3 Microstructural evolution in the GSS creep field

The effect of microstructure modifying processes accompanying deformation of rocks forms an important issue in the description of large strain transient to steady state flow behaviour. This has previously emerged in few high strain experimental studies of materials with relatively large starting grain sizes. For example, high strain torsion experiments on coarse grained olivine (Bystricky et al., 2000) and calcite materials (Pieri et al., 2001; Barnhoorn et al., 2004) have demonstrated dominant grain size insensitive (GSI) dislocation creep and transient strain weakening related to grain refinement by dynamic recrystallization. Relatively high shear strains were needed to approach steady state flow and related steady state microstructure. In addition to GSI dislocation creep, GSS diffusion creep is also known to be an important deformation mechanism. Considering the spatial and temporal range in upper mantle conditions, switching between GSI and GSS creep or contemporaneous operation of both mechanisms seems very well reasonable (Karato and Wu, 1993; Ter Heege et al., 2004). Several experimental studies reported that materials with relatively small starting grain sizes deforming by GSS creep at relative high upper mantle temperatures (1000-1300°C) may show strain hardening related to ongoing grain coarsening (e.g., olivine materials: Karato et al., 1986; Hirth and Kohlstedt, 1995a; Mei and Kohlstedt, 2000a) as opposed to strain weakening related to grain size reduction during GSI creep. Showing close correspondence to static grain growth rates presented by Karato (1989), these deformation studies fitted the grain coarsening during experimentation to a conventional time-dependent grain growth law. Presence of second phases, like enstatite in olivine dominated mantle rock, can considerably reduce or completely impede static grain growth, particularly at lower temperature (<1000°C) conditions. The results on  $fo_{100}$  presented in chapter 3 of this thesis showed that, under conditions where time-dependent grain growth is largely inhibited, grain coarsening related to GSS deformation may still occur. Under these conditions we observed a systematic effect of *strain* rather than *time* on microstructural modification. Here, the presence of enstatite and finely distributed porosity in  $fo_{100}$  material played an important role in pinning static grain growth. The extra component of grain growth during GSS deformation, referred to as dynamic grain growth, was considered to be caused by grain switching and a related increase in cellular defect fraction, i.e. the fraction of non-hexagonal grains as seen in a 2-dimensional section. However, evolution with strain of the distribution of either porosity or enstatite, might also play a role in deformation related grain growth. In our work on  $fo_{100}$  (chapter 3), too few data were available to rule out the possibility that strain induced changes in porosity and/or enstatite distribution (i.e. mean particle size and volume fraction, expressed by means of a Zener parameter) caused the extra component of grain growth during deformation.

### 5.1.4 Material choice

Various approaches can be adopted to prepare olivine samples for deformation tests. A straightforward method is to simply collect a single crystal of olivine (Mackwell et al., 1985) or dunite rock from nature (Post, 1977; Chopra and Paterson, 1981; 1984) and core out a sample in the desired shape and orientation. These are referred to as '*natural*' samples. Another approach is to first crush and grind a natural dunite or single crystal to powder and then handpick olivine grains of desired dimensions. This way, presence of any secondary phases in the new aggregate can be avoided. The obtained olivine powder can be further

processed to high density aggregates through stages of cold- and hot isostatic pressing (Karato et al., 1986; Hirth and Kohlstedt, 1995a; 1995b; Mei and Kohlstedt, 2000a; 2000b). Such produced specimens are generally referred to as synthetic samples, though they still contain olivine of natural origin. We thus prefer to refer to these as ‘*synthetic-natural*’ samples. Truly synthetic olivine samples can be produced by means of a ‘sol-gel’ technique (Beeman and Kohlstedt, 1993; McDonnell et al., 1999; Jackson et al., 2002; McDonnell et al., 2002). This technique involves mixing and reaction of industrially supplied starting ingredients like MgO, FeO and an organic-silicon compound called tetraethylorthosilicate (TEOS) through several stages of solution, gelation and heat-treatment to a pure very fine-grained olivine aggregate.

Now, we will argue what material choice and preparation method best fits to the aims set in 5.1.1. Many natural olivine rocks experienced several stages of metamorphism, partial melting, and deformation before being exhumed to the earth surface (e.g. Drury and Fitz Gerald, 1996; Wirth, 1996). Such a complex exhumation history can leave pronounced markings in the chemistry and texture of the exhumed mantle rock. These markings may affect its flow behaviour when subsequently used in lab experiments. In synthetic-natural specimens a relict metamorphic or deformational microstructure will be more or less obliterated by the grinding, though original intragranular dislocation structures might remain present. However, grinding itself can introduce mechanical damage to grains (e.g. new dislocations) and often produces angular grains with a wide distribution in grain size. Therefore, subsequent annealing and grain growth during hot pressing is necessary to arrive at a microstructurally homogeneous material. In practice, this means the procedure for fabrication of synthetic-natural samples limits the smallest achievable grain size to ~10 µm. Furthermore, a persistent dislocation structure can still be present in such annealed synthetic-natural olivine material (e.g. Karato, 1989). Though the presence of secondary phases can be largely avoided in synthetic-natural material, impurities/solutes of other or chemical elements within the olivine structure are often found in synthetic-natural material (Chopra and Paterson, 1981; Ricoult and Kohlstedt, 1985; Karato et al., 1986; Beeman and Kohlstedt, 1993; Jackson et al., 2002; Hiraga et al., 2004). In a recent study, Hiraga et al. (2004) found proof of significant thermodynamic driven segregation of incompatible solutes, like Ca and Al, from grain interiors into grain boundaries in both natural and synthetic-natural olivine aggregates. Such solutes/impurities bound to the crystal lattice or within grain boundaries may have a large effect on point defect chemistry and thus may affect flow behaviour of natural olivine material (Hiraga et al., 2004).

Synthetically fabricated Fe-bearing olivine, fo<sub>90</sub> (Jackson et al., 2002), or Fe-free olivine, fo<sub>100</sub> (McDonnell et al., 1999; 2002), is nominally free of any significant impurity content and has not experienced a complicated metamorphic and/or deformation history. The pure synthetic samples have the advantage over the synthetic-natural and natural specimens that there is a much better control on texture, chemistry, phase and impurity/solute content. Since most experimental studies focused on the GSS or GSI flow behavior of natural or synthetic-natural specimens, straightforward conclusions on the effect of Fe (and impurities) on flow behaviour are precluded.

The above considerations formed the basis for us to use fine grained synthetic Fe-bearing olivine, fo<sub>90</sub>, plus 5 vol% enstatite, en<sub>90</sub>, material to perform a new set of deformation experiments at hydrothermal conditions, promoting GSS creep and grain growth. This is the ideal material choice to allow a straightforward comparison with the results on synthetic Fe-free olivine (McDonnell et al. 1999). Results will potentially provide further insight in to the effects of Fe-related point defect chemistry on flow behaviour. In addition to Fe, the presence of enstatite (and porosity) and relative low imposed temperatures (800-1000°C) will impede fast static grain growth. These are ideal conditions to investigate the possible effect of strain

on grain growth behaviour of Fe-bearing material during GSS deformation. Presence of enstatite is necessary to fix the silica activity.

A preliminary investigation on viscosity of Fe-bearing synthetic material has been performed by Jackson et al. (2002) and Faul & Jackson (2004), but was at dry conditions and fairly high temperatures. They observed flow behaviour up to 2 orders of magnitude stronger than synthetic-natural  $fo_{90}$  (Hirth and Kohlstedt, 1995a; Mei and Kohlstedt, 2000a).

Table 5.1 Electron microprobe analyses; values in wt%

Oxide	syn- $fo_{90}$ <sup>a)</sup> This study	syn- $fo_{85}$ BK'93 <sup>b)</sup>	syn- $fo_{90}$ JFGFT'02	SC- $fo_{91}$ BK'93	SC- $fo_{91}$ JFGFT'02	SC- $fo_{91}$ KPF'86	AB- $fo_{93}$ CP'81
SiO <sub>2</sub>	41.79	42.82	40.76	39.66	40.20	40.33	41.31
MgO	47.86	46.28	49.15	51.04	50.29	50.68	51.47
CaO	0.00	0.04	0.00	0.14	0.09	0.12	-
FeO	10.20	15.18	10.08	9.12	8.98	9.34	7.11
MnO	0.00	0.00	0.00	0.03	0.12	0.00	0.00
Cr <sub>2</sub> O <sub>3</sub>	0.00	- <sup>c)</sup>	0.00	-	0.02	0.00	-
NiO	0.01	-	0.00	-	0.32	0.08	0.18
Na <sub>2</sub> O	0.00	0.00	-	0.01	-	-	-
Al <sub>2</sub> O <sub>3</sub>	0.00	0.00	-	0.07	-	-	-
Total	99.87	104.32	99.99	100.07	100.02	100.54	100.07
Mg/(Mg+Fe)	0.89	0.85	0.90	0.91	0.91	0.91	0.93
Impurity Content:	0.02	0.04	0.00	0.25	0.55	0.20	0.18

The analysis for this study is the average of several determinations made on an area of  $\sim 10 \mu\text{m}^2$ , sampling 20 to 100 grains

<sup>a)</sup> syn: 'synthetic' olivine; SC and AB: respectively 'synthetic-natural' San Carlos and Anita Bay olivine

<sup>b)</sup> BK'93: Beeman and Kohlstedt, 1993; JFGT'02: Jackson et al., 2002; KPF'86: Karato et al., 1986; CP'81: Chopra and Patterson, 1981.

<sup>c)</sup> - : not analysed

## 5.2 Experimental method

### 5.2.1 Material and sample preparation

Fine-grained ( $\sim 0.3 \mu\text{m}$ ) Fe-bearing forsterite ( $fo_{90}$ ;  $\text{Mg}_{1.8}\text{Fe}_{0.2}\text{SiO}_4$ ) plus 5 vol% enstatite ( $en_{90}$ ;  $\text{Mg}_{0.9}\text{Fe}_{0.1}\text{SiO}_3$ ) starting material was synthesized in a procedure similar to the sol-gel method for fabrication of *Fe-free*  $fo_{100}$  -  $en_{100}$  ceramics described by McDonnell et al. (2002). The method of McDonnell et al. (2002) was slightly modified for our purposes in order to incorporate Fe. The fabrication procedure involved the preparation of a diphasic gel using high purity  $\text{Fe}_2\text{O}_3$  and MgO powder and tetraethyl orthosilicate. These reagents were mixed in proportions such that the final ceramic consists of  $fo_{90}$  plus 5 vol.%  $en_{90}$  material. The gel was dried and reaction sintered at  $T = 950^\circ\text{C}$  for 2 hours in a controlled oxygen fugacity ( $f_{\text{O}_2}$ ) furnace (for details, see de Kloe, 2001) at  $f_{\text{O}_2} = 10^{-11}$  Pa. The reaction sintered precursor ( $\sim 70\%$  reacted at this stage) was cold isostatically pressed (CIPed) with 2.5 wt% organic binder (glycol) at  $P = 100$  MPa. The CIPed billets of material were fired and fully reaction sintered at  $T = 1250^\circ\text{C}$  and  $f_{\text{O}_2} = 10^{-5}$  Pa. In this very last step, the material significantly densified to arrive at a low porosity ceramic. Samples were produced from 3 gel batches. Using powder X-ray diffraction, the phase content of the final ceramics was qualitatively analyzed through inspection of powder X-ray diffraction patterns, which showed close



similarity to those of fo<sub>100</sub> (see McDonnell, 1997). Bulk chemistry of the final ceramics was analyzed using electron probe microanalysis (EPMA) and results are given in Table 5.1, together with published chemical analyses on synthetic and synthetic-natural materials. The total impurity content (i.e. all cations other than Mg, Fe, and Si) was 0.02 wt%. Samples were cored from the sintered billets to yield cylinders of ~8 mm in diameter and ~10 or 16 mm in length. The porosity of (non-HIPed) starting material was 10 to 12 %, measured using the Archimedes-method. Water (~ 0.3 wt%) was added to the samples before jacketing together with an iron sleeve (0.025 mm thickness) in a gold tube of 0.2 mm wall thickness. The presence of water is necessary to allow straining at sufficiently low flow stresses, i.e. between ~10 to 150 MPa. Note that unmeant dry samples of fo<sub>90</sub> showed elastic loading up to stresses far above values for which wet samples yielded. The iron sleeve is used to control oxygen fugacity at the iron-wüstite buffer level during experimentation (Karato et al., 1986). The tube ends were closed with welded-in cups made from gold foil (0.25 mm thick).

### 5.2.2 Deformation apparatus, experiments and data acquisition.

Samples were hot isostatically pressed (HIPed) and deformed in axial compression in a constant volume, internally heated argon gas medium apparatus (McDonnell, 1997; McDonnell et al., 1999). This deformation apparatus consists of a water-cooled 1 GPa pressure vessel with a three zone Kanthal-AF wire furnace. The vessel is mounted in a horizontally placed Instron 1362 servo controlled testing machine, which supplies the force on the sample during deformation. The force is measured both internally, using a Heard type internal force gauge (100 kN full scale, ~20 N resolution) and externally, using an Instron 100 kN load cell. Piston position is measured externally with a linear variable differential transformer (LVDT, 2  $\mu$ m resolution). Temperature was measured using three Pt/10%Rh (type S) thermocouples located next to the gold jacket. From previous calibrations temperature variation within the sample was known to be in the order of 1° or 2° (McDonnell et al., 1999). The experiments were conducted at temperatures between 850 and 1000°C and at 600 MPa confining pressure. Three types of experiments have been conducted: (a) HIP-only, referred to as ‘heat treatment’ or ‘HIP’ tests, where merely static grain growth occurs, (b) HIP followed by deformation at fixed constant displacement rate, referred to as ‘strain’ tests and (c) HIP followed by deformation at constant displacement rate, which was stepped up or down after specific strain intervals (2 to 5 % shortening) and referred to as ‘step’ tests. We will use constant *strain* rate as referring to constant *displacement* rate, though strictly speaking constant displacement rate will lead to a gradual increase in strain rate (up to a factor of 1.8 at 45% strain).

During the initial stage of all experiments jacketed samples were HIPed for ~18 hrs at fixed temperature-pressure conditions, i.e.  $T = 900^\circ\text{C}$  and  $P = 600$  MPa, in order to densify the material down to ~1 to 2 % porosity. This way a single starting microstructure was obtained at the start of a subsequent deformation (types b and c) or continuing heat-treatment stage (type a). One heat treatment (a) experiment (Fe26) was terminated after 18 hrs to analyze this starting microstructure. A detailed microstructural description of Fe26 is given in section 5.3.3 and 5.3.4. In case of the other heat treatment (a) tests HIPing was continued at 600 MPa pressure and temperatures of 900°C or 1000°C. This secondary HIPing was done at durations and temperatures similar to deformation experiments to allow comparison of the effects of static grain growth to grain growth in the deformation experiments. The deformation part in type (b) experiments was performed at constant strain rates of ~1 or  $3 \cdot 10^{-5}$  1/s for  $T = 900^\circ\text{C}$  and at strain rates of ~0.5 or  $1 \cdot 10^{-5}$  1/s for  $T = 1000^\circ\text{C}$ . Type (b) tests were terminated at strains of ~12, 27 or 45 %. The deformation part in type (c) tests was

carried out at fixed temperatures between 850 to 1000 °C and strain rates being stepped between  $\sim 3 \cdot 10^{-7}$  to  $1 \cdot 10^{-4}$  1/s. These step tests were terminated at  $\sim 14$ , 22 or 28 %. These conditions were chosen to promote dominant GSS creep involving grain boundary sliding (GBS) following previous investigation on similar (but Fe-free) forsterite material (McDonnell et al., 1999).

When the final strain was achieved (deformation tests) or the desired time duration passed (heat treatment tests) experiments were terminated as follows. First, in case of a deformation experiment, the displacement was stopped and the piston was pulled back to unload the sample. Then, applying also to the heat treatment experiments, the furnace was switched off, which allowed the sample to cool down to 100 °C temperature and pressure to decrease to  $\sim 400$  MPa within  $\sim 10$  minutes. The remaining gas pressure was then mechanically released from the vessel at slow pace ( $\sim 10$  MPa/min). Subsequently the deformed samples were removed from the vessel. Last, the capsules were opened and the final dimensions of the samples measured. All measured signals for internal and external axial force, position, pressure and temperature were logged using computers. All measurements are estimated to be accurate to within 5%. Raw data-files were further processed to obtain values for axial stress, displacement (corrected for apparatus stiffness), strain, strain rate and average temperature. Error in measured stress was estimated to be  $\sim 5\%$ .

### 5.2.3 Microstructural analysis.

Microstructural imaging was carried out using a scanning electron microscope (SEM) operated in orientation contrast (OC) mode. Samples were sectioned half, parallel to the compression direction and prepared for SEM analysis by Syton<sup>TM</sup> (colloidal silica) polishing the section for at least 1 hour. The SEM (a Philips XL30 Field Emission Gun) was operated at an acceleration voltage of 20 to 25 kV, a sample tilt of 70° and a working distance of 20 to 15 mm. In order to perform grain size analysis, grains and pores in the OC images were traced manually using photo-editing software. Quantitative two-dimensional analysis of the traced grain boundary maps was conducted using the image-analyzing program Leica Qwin Pro (version 2.3, 1998). The arithmetic mean grain and pore size, grain size distribution and standard deviation are expressed as equivalent circular diameter (ECD). We were unable to reliably distinguish enstatite from forsterite grains using SEM imaging. Thus analyzed grain sizes include both phases. Pore area percentages were calculated as a measure of final porosities for all experiments. Zener parameter values were calculated from data on mean pore size and porosity area fraction. Grain aspect ratios were calculated by dividing the feret (grain width) measured perpendicular to the compression direction by the feret measured parallel to the compression direction and values were averaged according to grain area. Two-dimensional grain topology (grain coordination number) and cellular defect fraction were measured automatically, using a topology-routine (courtesy of Elena Petrishcheva, University of Berlin) written for the program Matlab (version 7.1). To measure lattice-preferred orientation (LPO) one high strain (45%) sample was analyzed using the electron backscatter diffraction technique (EBSD) technique with the same SEM as for OC imaging. Automated indexing scans at step size  $\sim 0.5$  were performed and crystallographic pole plots were made using the post-processing software package Channel 5, commercially available at HKL technology. To prevent charging during EBSD analysis polished sections were coated with a thin layer of carbon.

## 5.3 Results

### 5.3.1 Porosity and fluid pressure

Table 5.2 lists the porosity data for all experiments, measured before (Archimedes) and estimated after each experiment (through image analysis). In addition, the intermediate porosity after the 18 hrs HIP-stage was calculated based on the average amount of volume-decrease (compaction) during HIP-only experiments, which was measured from sample dimensions before and after experimentation. Compaction was found to cease within 18 hrs of HIPing and an average of 9.2 % volume decrease was taken into account for estimation of post-HIP porosity.

The average (pre-HIP) starting porosity was  $10.8 \pm 0.6$  %. Data for Fe26, a HIP test which was terminated after the 18 hrs HIP-stage, shows that porosity decreased about 9 % during the first 18 hrs of HIPing. The compaction-based calculation (i.e. the ‘post-HIP porosity’-column in Table 5.2) and the 2-D image analysis estimate (i.e. the ‘final porosity-column’ in Table 5.2) for Fe26 gave porosity values of 2.0 and 1.8 %, respectively. It thus seems that both methods resulted in similar porosity estimates. The average post-HIP porosity was  $\sim 1.7 \pm 0.7$  % whereas the average final porosity estimates were  $\sim 1.6 \pm 0.9$  % and  $\sim 1.3 \pm 0.5$  % for, respectively, all HIP tests and all HIP plus deformation tests. Thus, on average, no large differences in post-HIP and final porosities were observed between HIP and

Table 5.2 Porosity Data

TestNo.	Batch	test-type <sup>a)</sup>	Starting <sup>b)</sup> Pre-HIP porosity [%]	Post-HIP <sup>c)</sup> porosity [%]	Final <sup>d)</sup> porosity [%]
start			10.0		9.1
Fe26	D4+P6+A2	HIP	11.3	2.0	1.8
Fe30	A2	HIP	11.1	2.1	0.6
Fe18	P6	HIP	10.8	1.8	0.9
Fe28	A2	HIP	11.5	2.5	1.3
Fe25	A2	HIP	11.2	2.1	3.4
Fe27	A2	HIP	11.0	2.0	1.3
Fe29	A2	HIP	10.8	1.8	2.2
Fe01	D4	HIP+def	10.4	1.3	1.0
Fe10	P6	HIP+def	10.0	0.9	0.9
Fe02	D4	HIP+def	10.0	0.9	2.4
Fe19	P6	HIP+def	9.7	0.5	1.3
Fe08	D4	HIP+def	11.6	2.6	0.8
Fe14	P6	HIP+def	9.6	0.4	0.7
Fe07	D4	HIP+def	11.6	2.6	0.6
Fe34	A2	HIP+def	10.4	1.3	1.9
Fe11	P6	HIP+def	9.9	0.8	1.3
Fe05	D4	HIP+def	11.5	2.6	1.5
Fe22	A2	HIP+def	11.8	2.9	1.3
Fe20	P6	HIP+def	10.3	1.2	1.2
Fe17	P6	HIP+def	11.1	2.1	1.9
Fe32	A2	HIP+def	10.5	1.4	2.0
Fe33	A2	HIP+def	10.6	1.5	1.9
Fe24	A2	HIP+def	11.4	2.4	1.5
Fe31	A2	HIP+def	11.0	2.0	1.3
Fe36	A2	HIP+def	11.0	1.9	0.8

<sup>a)</sup> HIP = Hot isostatic pressing; HIP+def = HIP followed by deformation. <sup>b)</sup> Measured by Archimedes method

<sup>c)</sup> Calculated as the difference between the starting porosity and the average HIP-volume reduction (9.22 %) divided by the average volumetric stretch due to HIPing (0.9078). <sup>d)</sup> Estimated as pore-area% from image analysis

HIP plus deformation tests. On the basis of the estimated final porosity and assuming all water (0.3 wt%) present in the sample exists as a pure H<sub>2</sub>O fluid phase the pore fluid pressure and water fugacity have been calculated using the program LONER14 (Bakker, 2003) and data from Steam Tables (Haar et al., 1984). The fluid pressure and water fugacity based on these assumptions have been calculated for all experiments. In case of the final porosity of Fe26 that represents to the microstructure at the onset of deformation or further HIPing this gives values of ~600 and ~660 MPa, for fluid pressure and fugacity near the end of experimentation, respectively. These values correspond to the microstructural state after 18 hrs of HIPing at 900 °C and 600 MPa confining pressure. Most other HIPed and deformed samples also show final fluid pressures near the confining pressure or even >1000 MPa. Few samples show lower values (< 600 MPa). So actually, quite a large range in fluid pressures was observed. This can be attributed to the significant errors in porosity measurement and the low overall porosity values. Still, on the basis of a high fluid pressure found for Fe26, we expect fluid pressure and fugacity to be near the confining pressure in the deformation parts of all tests.

Table 5.3 Characteristics of all experiments <sup>a)</sup>

TestNo.	Batch	test-type <sup>b)</sup>	final <sup>c)</sup>	final	final <sup>c)</sup>	temperature		HIP1	HIP2	total	average	strain rate
			flow	short.	strain	HIP1	HIP2/def.	dur.	or def.	dur.	strain rate	step-range
			stress	strain	rate	stage	stage	dur.				
			[MPa]	[%]	[1/s]	[°C]	[°C]	[hrs]	[hrs]	[hrs]	[1/s]	
Fe26	P6	HIP900	-	-	-	898	-	18.1		18.1	-	-
Fe30	A2	HIP900	-	-	-	898	-	26.6		26.6	-	-
Fe18	P6	HIP900	-	-	-	898	-	30.6		30.6	-	-
Fe28	A2	HIP900	-	-	-	900	-	50.8		50.8	-	-
Fe25	A2	HIP1000	-	-	-	897	998	18	8.8	26.8	-	-
Fe27	A2	HIP1000	-	-	-	899	999	17.1	12.2	29.3	-	-
Fe29	A2	HIP1000	-	-	-	900	996	18	27.3	45.3	-	-
Fe01	D4	step850	77.1	14.6	2.31·10 <sup>-5</sup>	847	853	19.2	2.8	21.9	1.64·10 <sup>-5</sup>	1·10 <sup>-5</sup> - 1·10 <sup>-4</sup>
Fe10	P6	step850	90.1	23	1.04·10 <sup>-5</sup>	900	850	18.5	32.5	51	6.04·10 <sup>-6</sup>	3·10 <sup>-7</sup> - 1·10 <sup>-4</sup>
Fe02	D4	step900	67.2	23.4	1.12·10 <sup>-5</sup>	900	900	18.5	25	43.5	1.66·10 <sup>-5</sup>	3·10 <sup>-7</sup> - 1·10 <sup>-4</sup>
Fe19	P6	step900	139.3	22.6	2.80·10 <sup>-5</sup>	905	895	19.5	31.4	50.9	8.38·10 <sup>-6</sup>	3·10 <sup>-7</sup> - 3·10 <sup>-5</sup>
Fe08	D4	step950	48.7	22	1.01·10 <sup>-5</sup>	898	950	18.9	6.7	25.6	4.44·10 <sup>-5</sup>	3·10 <sup>-6</sup> - 1·10 <sup>-4</sup>
Fe14	P6	step950	59.7	23.3	1.04·10 <sup>-5</sup>	899	950	18.1	32.7	50.8	7.08·10 <sup>-6</sup>	3·10 <sup>-7</sup> - 3·10 <sup>-5</sup>
Fe07	D4	step1000	43.8	22.9	9.90·10 <sup>-6</sup>	903	996	17.8	28.4	46.2	1.00·10 <sup>-5</sup>	3·10 <sup>-7</sup> - 1·10 <sup>-4</sup>
Fe34	A2	step1000	29.6	28.6	1.08·10 <sup>-5</sup>	906	1000	18.6	5.5	24.1	4.21·10 <sup>-5</sup>	1·10 <sup>-5</sup> - 1·10 <sup>-4</sup>
Fe11	P6	strain900R1S1	46.2	12.1	1.09·10 <sup>-5</sup>	899	900	18.2	3.5	21.7	1.07·10 <sup>-5</sup> (R1)	-
Fe05	D4	strain900R1S2	75.7	27.1	1.34·10 <sup>-5</sup>	896	903	18.9	7.7	26.6	1.16·10 <sup>-5</sup> (R1)	-
Fe22	A2	strain900R1S3	85.4	44.3	1.75·10 <sup>-5</sup>	899	899	17.7	12.6	30.3	1.32·10 <sup>-5</sup> (R1)	-
Fe20	P6	strain900R2S1	80.9	12.8	3.36·10 <sup>-5</sup>	899	898	18.5	1.3	19.8	3.19·10 <sup>-5</sup> (R2)	-
Fe17	P6	strain900R2S2	94.6	28	4.09·10 <sup>-5</sup>	899	898	18.4	2.6	21.1	3.54·10 <sup>-5</sup> (R2)	-
Fe32	A2	strain900R2S3	114.5	43.6	4.98·10 <sup>-5</sup>	899	900	18.2	4.2	22.4	3.92·10 <sup>-5</sup> (R2)	-
Fe33	A2	strain1000R1S1	19.5	13	1.11·10 <sup>-5</sup>	904	1000	18.1	3.5	21.6	1.10·10 <sup>-5</sup> (R1)	-
Fe24	A2	strain1000R1S2	37	27.3	1.36·10 <sup>-5</sup>	907	1000	18.2	7.6	25.8	1.18·10 <sup>-5</sup> (R1)	-
Fe31	A2	strain1000R1S3	54.6	46.4	1.82·10 <sup>-5</sup>	904	998	18.2	13	31.2	1.42·10 <sup>-5</sup> (R1)	-
Fe36	A2	strain1000R0S3	41.1	45.4	7.19·10 <sup>-6</sup>	902	999	18.4	31.7	50.2	5.37·10 <sup>-6</sup> (R0)	-

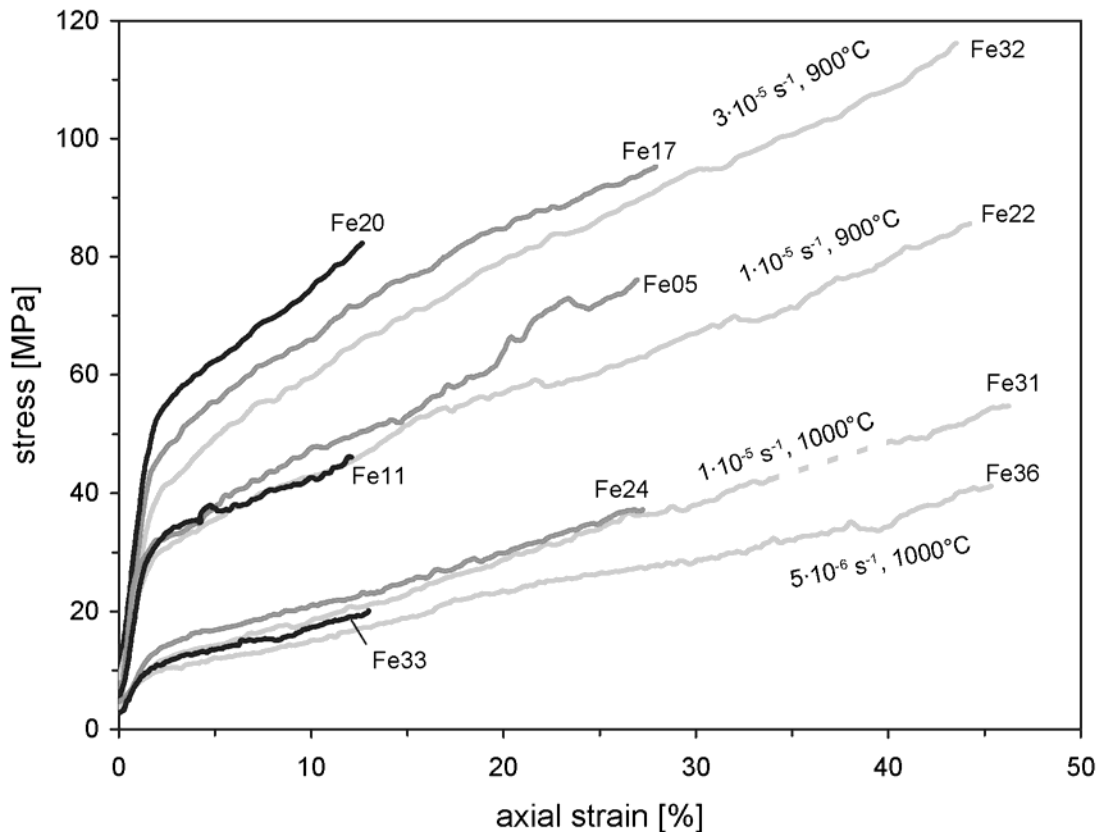
<sup>a)</sup> HIPing (HIP1) at 900 °C and 600 MPa Pressure. Fe01 forms an exception and is HIPed at 850 °C. Pressure is kept constant at ~600 MPa during HIPing and deformation.

<sup>b)</sup> Type (HIP, step or strain) is followed by temperature. HIP = only HIPing (no deformation); step = strain rate is stepped up, down and up again; strain = deformation at a single strain rate (R#) up to ~12 (S1), 28 (S2) or 45 (S3) % shortening strain.

<sup>c)</sup> Flow stress and strain rate measured over the final ~0.3 % strain are quoted.

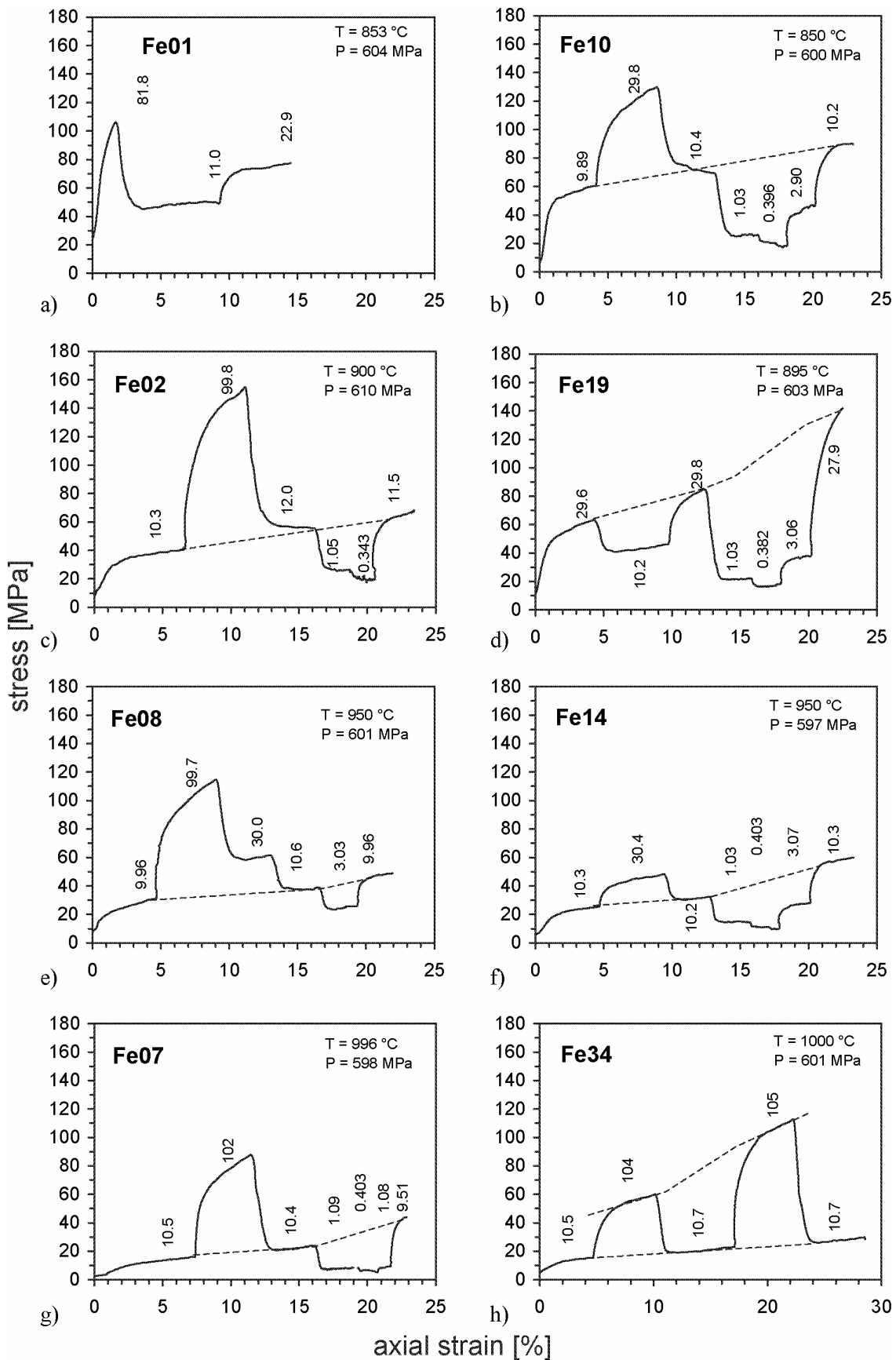
### 5.3.2 Mechanical data

The test conditions and characteristics of all deformation experiments are listed in Table 5.3. Fig. 5.1 shows stress versus strain curves for all constant displacement rate tests stopped at shortening strains of ~12, 27 or 45 %. After yielding at strains of 1-2 % all curves show continuous hardening up to the end of tests. In none of the experiments true steady state was achieved. Flow stresses at similar experimental conditions and sample strains were found to be reproducible within about 20 MPa. Flow stresses increase with increasing strain rate and decrease with increasing temperature (fig. 5.1).

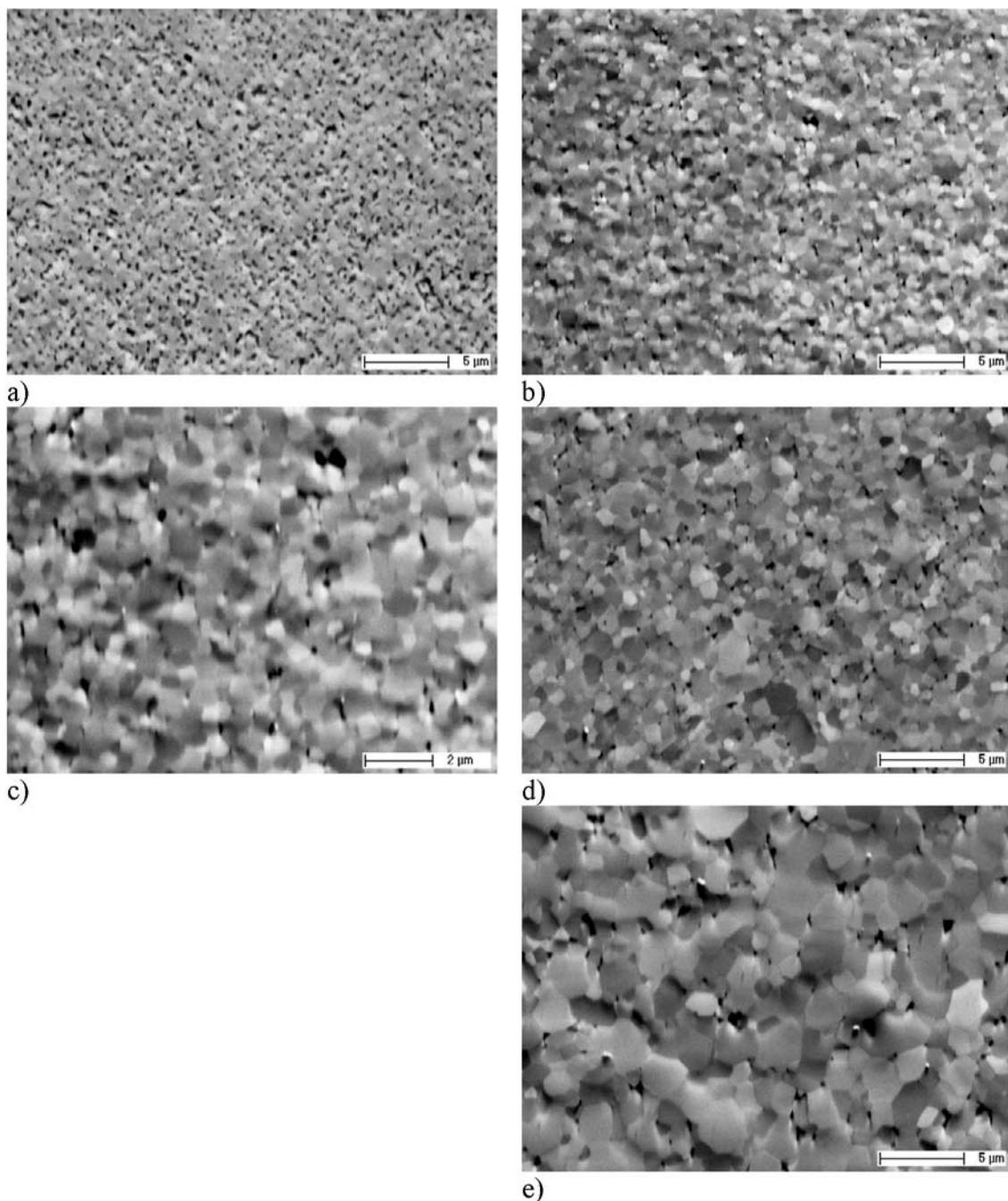


**Figure 5.1.** Stress - strain curves for all constant strain rate experiments. The stress-strain curve of Fe31 is dotted within strain interval 34-40%, because of problems with the displacement control, which were resolved at higher strains.

The complete set of stress - strain curves obtained for the strain rate stepping tests are shown in fig. 5.2a-h. Apart from Fe01 and Fe34, which reached strains of 14.6 and 28.6%, respectively, all step-tests were terminated at a strain of ~ 23 %. Temperature and pressure were kept constant. In none of the steps, true steady state creep was established. Rather, most steps displayed continuous hardening as was found in the constant displacement rate tests. Steps of similar strain rate are connected by dotted lines in fig. 5.2. These correlations indicate near-linear hardening with strain, if low duration steps (i.e. step-duration < 2 hrs at generally fast strain rates) were in between. However, strong deviation from near-linear hardening was observed if long duration steps (i.e. step-duration > 2 hrs at relatively low strain rates) formed part of the experiment.



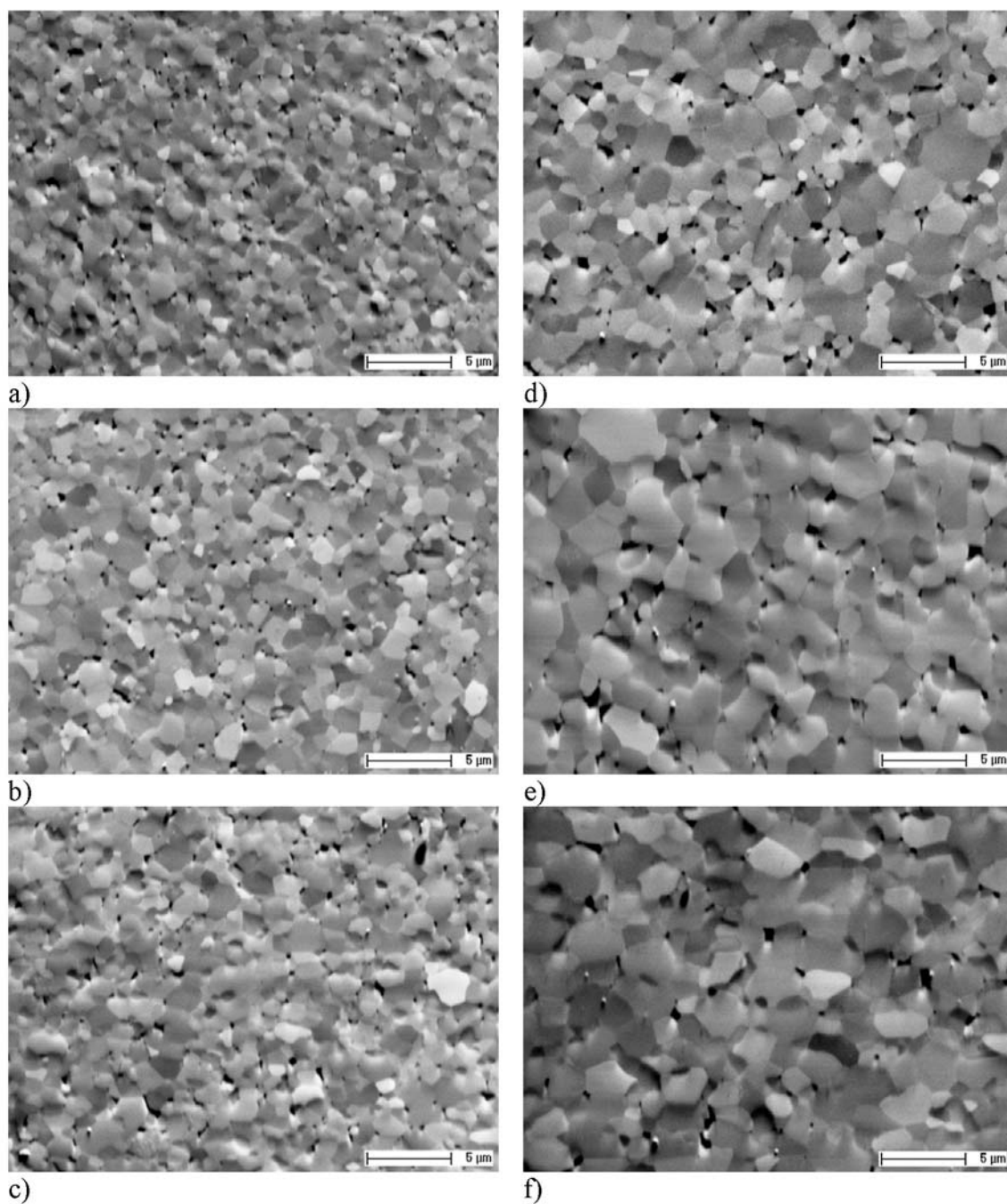
**Figure 5.2.** Stress - strain curves for all stepped strain rate experiments. Average values for temperature and pressure are indicated for each experiment and for each step test the average strain rate (in units of  $10^{-6} \text{ s}^{-1}$ ) is indicated.



**Figure 5.3.** SEM orientation contrast (OC) micrographs showing microstructures of a) starting material and heat-treated samples b-c) Fe26 (900°C, 18 hrs), d) Fe28 (900°C, ~51 hrs) and e) Fe29 (1000°C, ~45 hrs). Pores are visible as solid black elements in the micrographs.

### 5.3.3 Qualitative microstructural observations

Examination of the starting material showed it to be microstructurally very homogeneous and fine grained ( $\sim 0.3 \mu\text{m}$ ; fig. 5.3a). No extraordinary large grains have been observed, i.e. there is no indication of abnormal grain growth during the sintering process. The porosity ( $\sim 11\%$ ) of the un-HIPed starting material appears as a black unconnected phase on SEM images in OC mode.



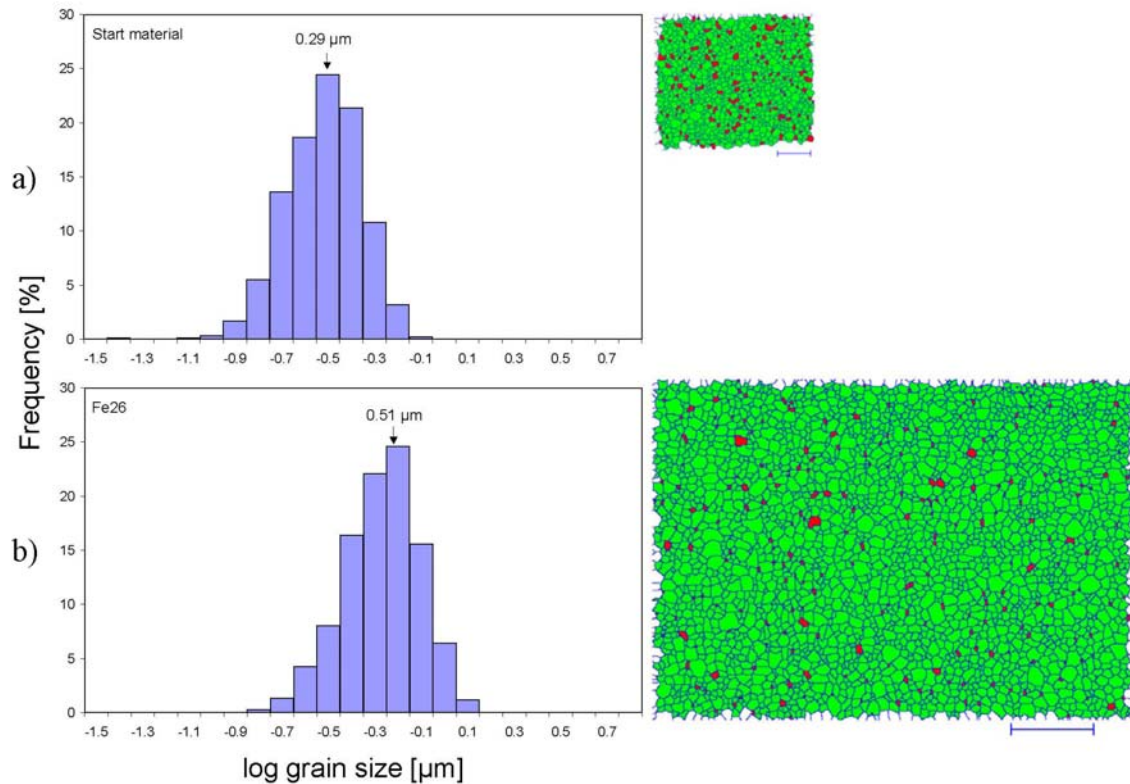
**Figure 5.4.** SEM orientation contrast (OC) micrographs showing microstructures of samples: a) Fe11, b) Fe05 and c) Fe22 deformed to strains of 12, 27 and 44%, respectively, at  $T = 900^{\circ}\text{C}$  and of d) Fe33, e) Fe24, f) Fe31 deformed to strains of 13, 27 and 46%, respectively, at  $T = 1000^{\circ}\text{C}$ . Shortening direction is horizontal, except for c) and f), where shortening direction is vertical.

Fig.'s 5.3b-c show the microstructure of sample Fe26, which experienced 18 hrs of heat treatment at  $T = 900^{\circ}\text{C}$  and  $P = 600\text{ MPa}$ . Significant grain growth and densification occurred during these first 18hrs of HIPing. Compared to the starting material, the porosity reduced from  $\sim 10\%$  to  $\sim 2\%$ . The bulk of the porosity is made up of intergranular pores at grain boundaries, notably at triple junctions. Intragranular pores are occasionally observed. Grain boundaries are generally straight or gently curved and triple junctions commonly display close to  $120^{\circ}$  angles. Continuing heat treatment at  $900^{\circ}\text{C}$  for periods longer than 18 hrs lead



to further grain growth (fig. 5.3d). Grain growth was more significant at 1000 °C (fig. 5.3e). Except for a continued increase in grain size, general changes in the character of the microstructure are minor beyond 18 hrs of HIPing. Therefore, each combined HIP plus deformation test was first subjected to a period of 18 hrs of HIPing at  $T = 900^{\circ}\text{C}$  forming a microstructure similar to Fe26 (fig. 5.3b-c). This microstructure (and corresponding grain size) was considered to represent the general microstructure at the onset of deformation for each HIP plus deformation test.

Micrographs of deformed samples are shown in fig. 5.4. The deformed microstructures have a homogeneous appearance similar to that of the HIP-only material. For shortening strains below  $\sim 30\%$  (at constant strain rate and temperature) the grain microstructure remains that of a strong foam texture, with little or no evidence of grain flattening or grain boundary alignment (fig. 5.4a-b). Samples deformed up to 45% strain, however, show some grain flattening, although grain boundaries remain straight or only gently curved (fig. 5.4c). Qualitatively, the average grain size appears to increase with increasing strain and time. As quantified in section 5.3.1 (Table 5.2), the porosity in the deformed microstructures (fig. 5.4a-c) is more or less similar to its value at the onset of deformation; i.e. no significant change has been observed increasing the strain. No glassy intergranular films or other grain boundary phases have been identified at the scale of (SEM) observation employed. Also, no serrated grain boundaries or subgrains have been observed. Since no distinct fine grain size fraction of particles or secondary phases is observed along grain boundaries, we infer enstatite grains are of similar size to the olivine grains (c.f. McDonnell et al, 1999). Enstatite grains occasionally exhibit lamellae, but are otherwise indistinguishable from the olivine grains when employing OC-imaging.



**Figure 5.5.** Frequency histograms of (logarithmic) grain size distributions and accompanying traced grain boundary maps of a) starting material and b) Fe26 (HIP,  $900^{\circ}\text{C}$ , 18 hrs). Grain size is expressed as equivalent circular diameter (ECD). Long-axis of the sample is vertical (Fe26) or perpendicular to the sectioned area (starting material).

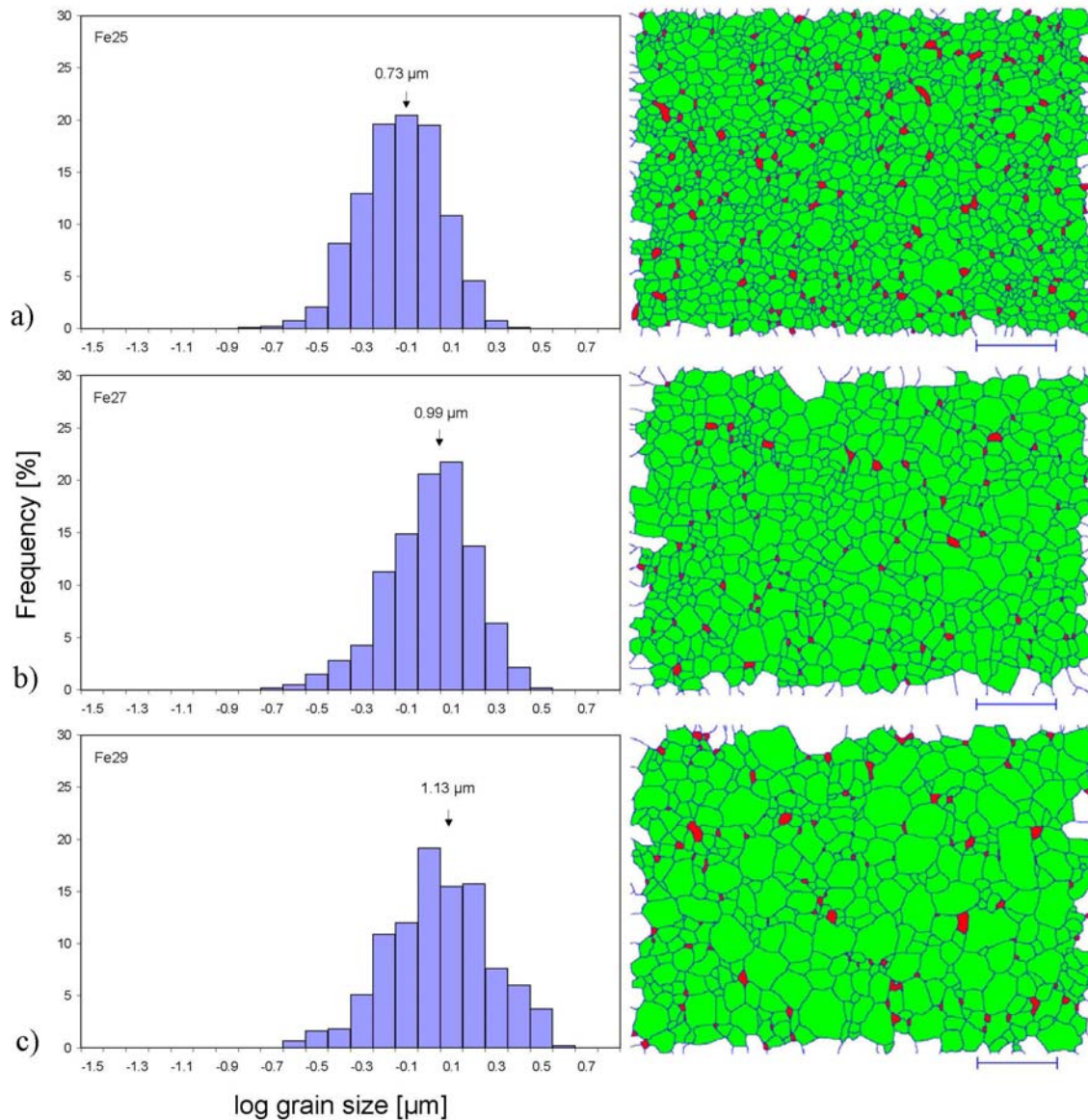
## 5.3.4 Quantitative microstructural observations

Traced grain boundary maps and frequency histograms of (logarithmic) grain size distributions have been produced for all samples, of which a representative selection is shown in figs 5.5 - 5.8. Values for the measured microstructural parameters are given in Table 5.4. The arithmetic mean grain size varies from 0.3  $\mu\text{m}$  for the starting material (pre-HIP) to 1.6  $\mu\text{m}$  for sample Fe36, which resulted from the experiment with the longest experimental duration ( $\sim 50$  hrs, final shortening  $\sim 45\%$ ). The grain size distributions shown in fig. 5.5 - 5.8 were selected to cover the complete range in mean grain size. The mean final grain sizes have been plotted as a function of total experimental duration in fig. 5.9. For clarity, only those step tests were included with similar final strain ( $\sim 23\%$ ), number of strain rate steps (7) and experimental duration ( $>46$  hrs), i.e. Fe10-19-14-07. Fig. 5.9 shows that static HIPing at  $T = 900^\circ\text{C}$  results in an increase in mean grain size from  $\sim 0.3$  to  $\sim 0.5$   $\mu\text{m}$  in the first 18 hours, together with a decrease in porosity (see Table 5.2). Grain size at the onset of deformation is taken as 0.5  $\mu\text{m}$  (sample Fe26, see section 5.3.3) Ongoing static heat treatment after the first 18 hrs (up to 50 hrs), at 600 MPa pressure and temperatures of 900 or 1000 $^\circ\text{C}$  results in further increase in grain size. At 1000 $^\circ\text{C}$  grain growth is noticeably more pronounced than at 900 $^\circ\text{C}$ .

Table 5.4 Microstructural characteristics of all samples

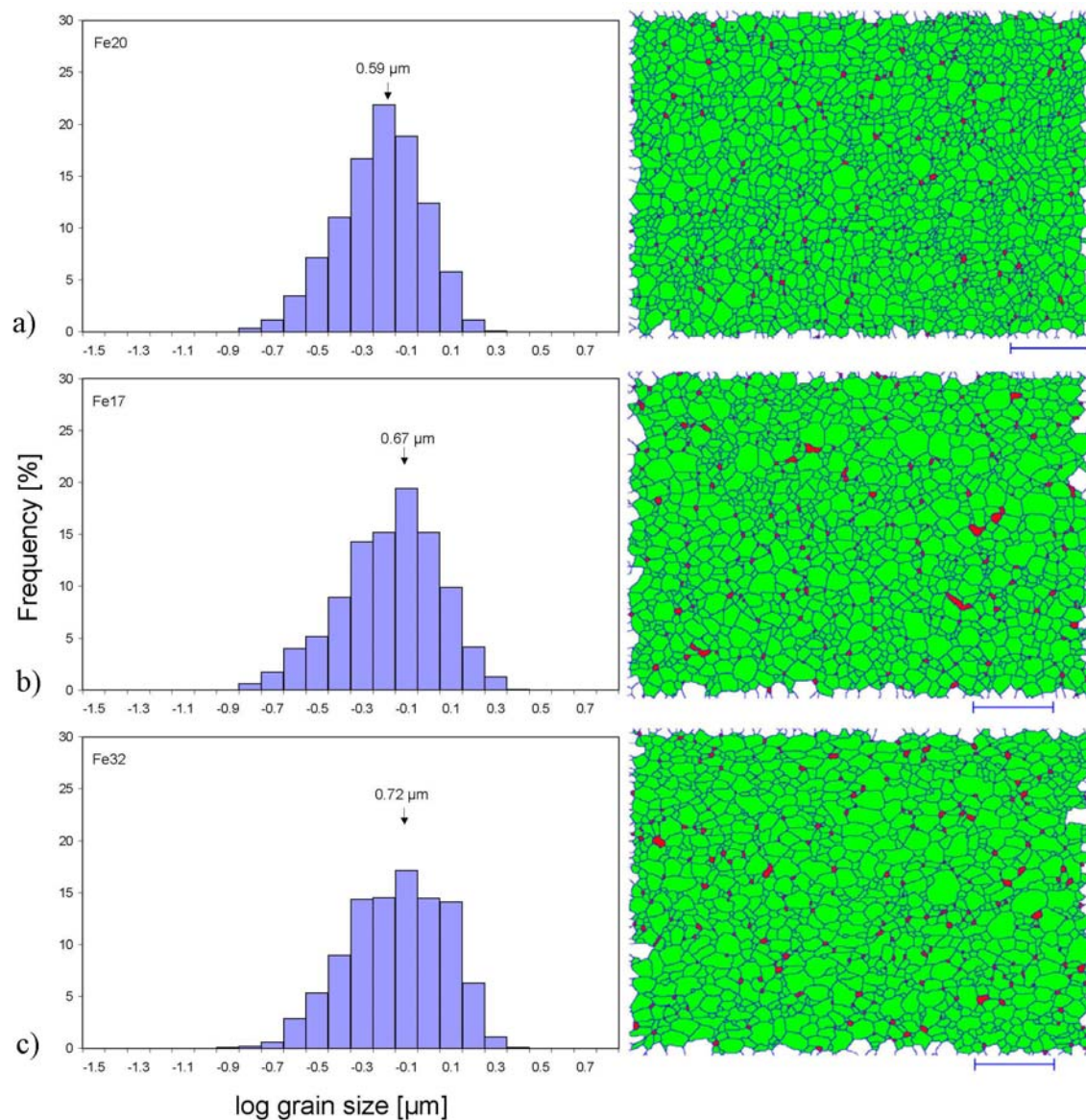
TestNo.	number of grains	median grain size [ $\mu\text{m}$ ]	mean grain size [ $\mu\text{m}$ ]	stand. error	stand. dev.	norm. dyn. g.g. rate [1/s]	area weighed Feret 90/0	stand. error	average coordination number	defect fraction
start <sup>a)</sup>	945	0.28	0.29	0.00	0.10	-	1.13	0.01	5.08	0.805
Fe26 <sup>a)</sup>	2584	0.49	0.51	0.00	0.18	-	1.09	0.01	5.74	0.749
Fe30	1710	0.58	0.62	0.01	0.24	-	1.12	0.01	5.90	0.742
Fe18	1560	0.62	0.65	0.01	0.25	-	1.14	0.01	5.78	0.736
Fe28	1380	0.63	0.68	0.01	0.28	-	1.12	0.01	5.69	0.752
Fe25 <sup>b)</sup>	1174	0.68	0.73	0.01	0.29	-	1.06	0.01	5.53	0.781
Fe27 <sup>b)</sup>	612	0.95	0.99	0.02	0.41	-	1.09	0.02	5.70	0.745
Fe29 <sup>b)</sup>	433	0.99	1.13	0.03	0.59	-	1.11	0.02	5.58	0.836
Fe01	1795	0.58	0.60	0.01	0.23	$1.05 \cdot 10^{-5}$	1.17	0.01	5.82	0.740
Fe10	1279	0.65	0.69	0.01	0.32	$1.52 \cdot 10^{-6}$	1.17	0.01	5.79	0.774
Fe02	1046	0.71	0.75	0.01	0.35	$1.50 \cdot 10^{-6}$	1.05	0.01	5.52	0.783
Fe19	757	0.79	0.87	0.02	0.43	$2.08 \cdot 10^{-6}$	1.04	0.02	5.66	0.818
Fe08	867	0.79	0.84	0.01	0.37	$8.27 \cdot 10^{-6}$	1.07	0.01	5.73	0.756
Fe14	443	1.00	1.10	0.03	0.60	$1.88 \cdot 10^{-6}$	1.04	0.02	5.78	0.832
Fe07	178	1.28	1.57	0.08	1.03	$3.21 \cdot 10^{-6}$	1.10	0.02	5.52	0.848
Fe34	445	1.00	1.09	0.03	0.58	$1.39 \cdot 10^{-5}$	1.05	0.02	5.59	0.810
Fe11	1613	0.60	0.63	0.01	0.26	$7.73 \cdot 10^{-6}$	1.11	0.01	5.70	0.757
Fe05	899	0.78	0.82	0.01	0.36	$9.03 \cdot 10^{-6}$	1.07	0.01	5.61	0.787
Fe22	747	0.84	0.89	0.02	0.42	$7.16 \cdot 10^{-6}$	1.18	0.01	5.67	0.799
Fe20 <sup>c)</sup>	1805	0.56	0.59	0.01	0.25	$1.12 \cdot 10^{-5}$	1.13	0.01	5.75	0.760
Fe17 <sup>c)</sup>	1322	0.63	0.67	0.01	0.32	$1.52 \cdot 10^{-5}$	0.99	0.01	5.62	0.800
Fe32 <sup>c)</sup>	1163	0.66	0.72	0.01	0.34	$1.34 \cdot 10^{-5}$	1.27	0.01	5.61	0.807
Fe33 <sup>d)</sup>	591	0.88	0.97	0.02	0.48	$2.19 \cdot 10^{-5}$	0.99	0.01	5.57	0.810
Fe24 <sup>d)</sup>	415	1.05	1.13	0.03	0.58	$9.96 \cdot 10^{-6}$	1.11	0.02	5.53	0.847
Fe31 <sup>d)</sup>	368	1.03	1.21	0.03	0.67	$4.91 \cdot 10^{-6}$	1.26	0.02	5.64	0.873
Fe36 <sup>d)</sup>	177	1.40	1.64	0.07	0.96	$2.63 \cdot 10^{-6}$	1.15	0.02	5.55	0.831

<sup>a)</sup> Figure 5.5; <sup>b)</sup> Figure 5.6; <sup>c)</sup> Figure 5.7; <sup>d)</sup> Figure 5.8



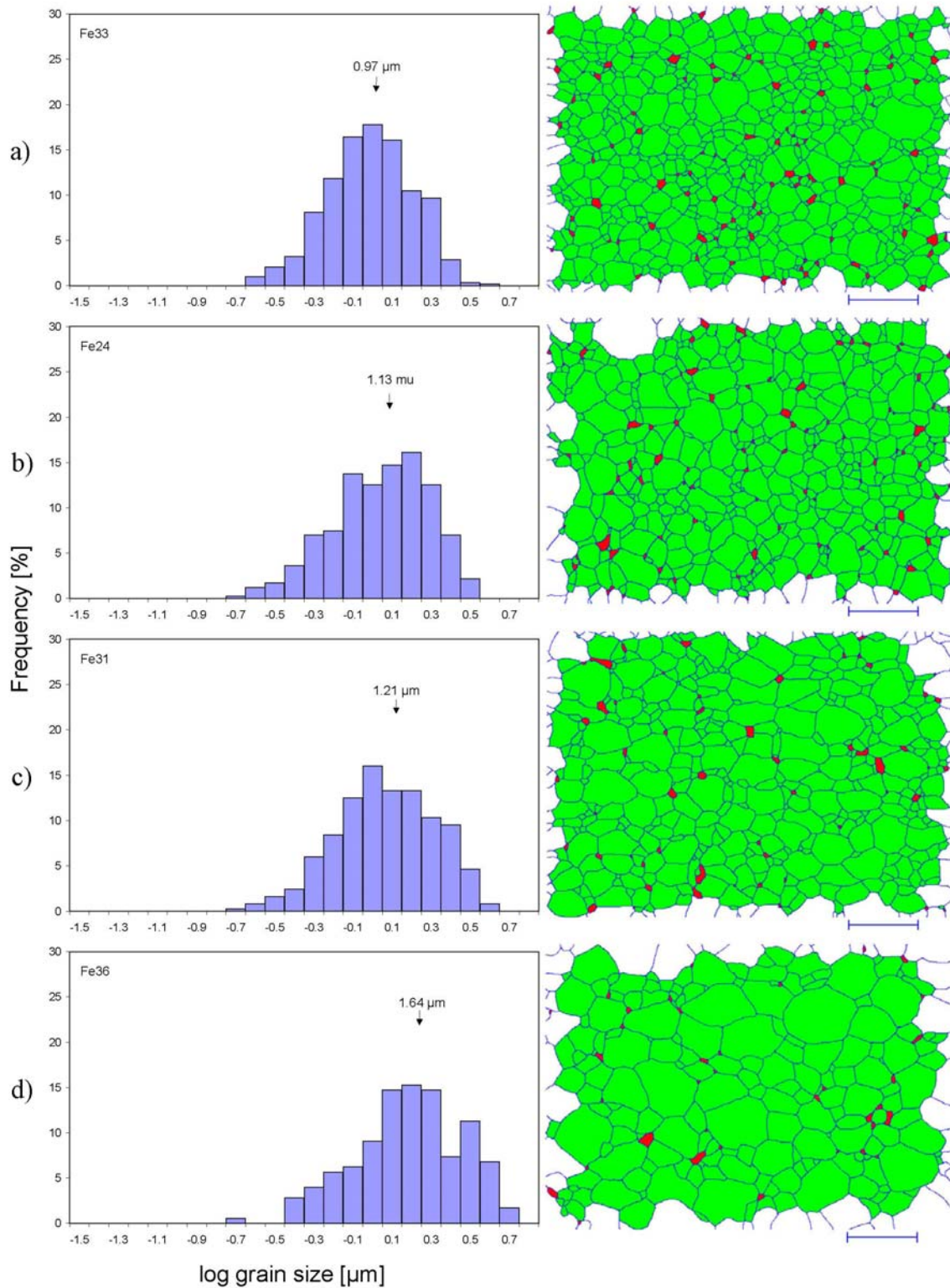
**Figure 5.6.** Frequency histograms of (logarithmic) grain size distributions and accompanying traced grain boundary maps of heat-treated samples a) Fe25 (1000°C, ~27 hrs), b) Fe27 (1000°C, 29 hrs) and c) Fe29 (1000°C, ~45 hrs). Grain size is expressed as equivalent circular diameter (ECD). Long-axis of the samples is horizontal.

Fig. 5.9 includes the experimental duration versus grain size data of the constant strain rate (i.e. non-stepping) tests at 900 and 1000 °C. Comparing the deformation test data with the static data clearly shows that at similar experimental duration and temperature, grain growth is more pronounced in tests with a deformation stage than in plain heat treatment tests. In fig. 5.10a grain growth data for different strain rates (at T = 900°C) can be compared. More grain growth *per unit time* is observed for the higher strain rate tests. When plotting the grain sizes of the constant strain rate tests against strain rather than experiment duration (fig 5.10b), less grain growth *per strain* is observed for the higher strain rate tests. Fig. 5.11 depicts grain size versus temperature data from the same selected step tests (with similar final strain, ~23% and experimental duration, 26 or 44 to 50 hrs) as included in fig. 5.9 and 10b. When compared to static data the enhancing effect of temperature on grain growth appears to be more pronounced in the deformation tests.

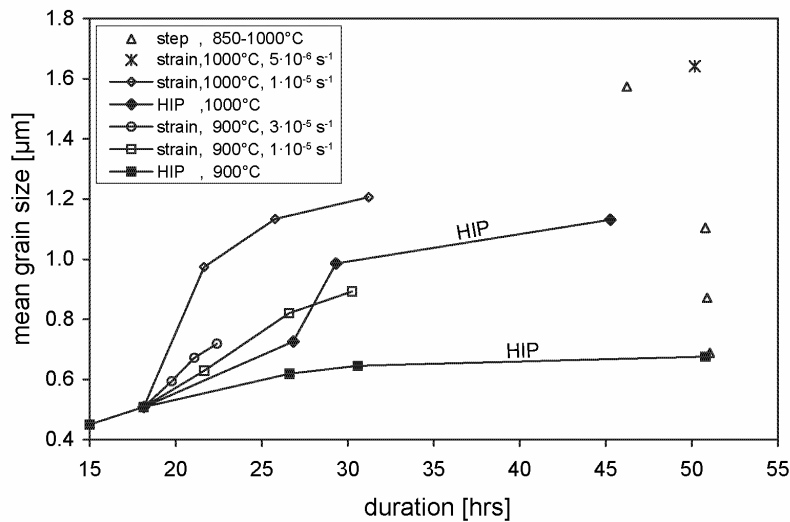


**Figure 5.7.** Frequency histograms of (logarithmic) grain size distributions and accompanying traced grain boundary maps of deformed samples a) Fe20 (900°C,  $\varepsilon \sim 13\%$ ), b) Fe17 (900°C,  $\varepsilon \sim 28\%$ ) and c) Fe32 (900°C,  $\varepsilon \sim 44\%$ ), deformed at constant strain rate of  $\sim 3 \cdot 10^{-5}$  1/s. Shortening direction is horizontal for Fe20 and Fe17 and vertical for Fe32.

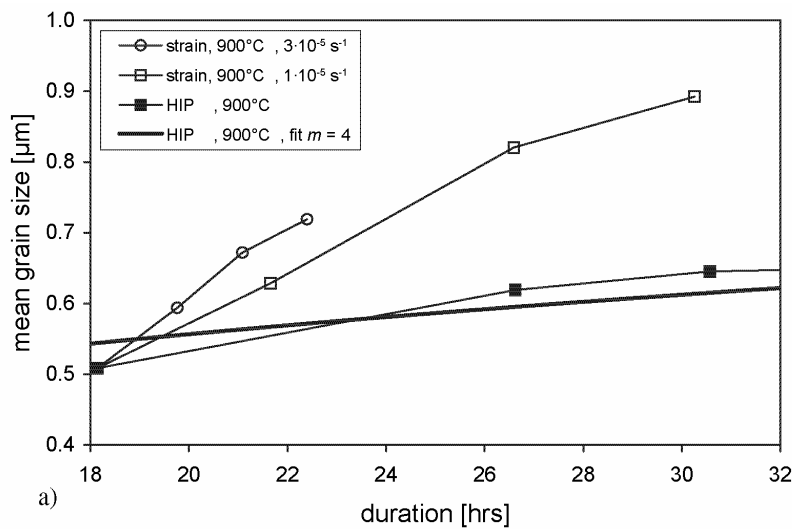




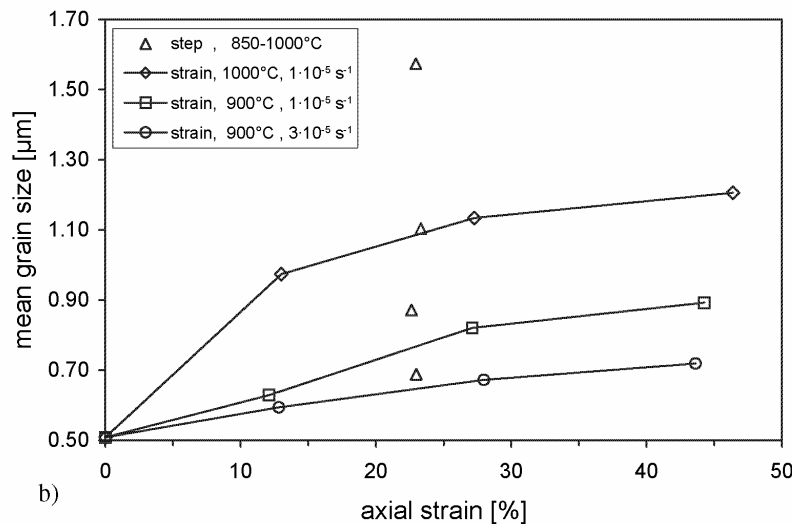
**Figure 5.8.** Frequency histograms of (logarithmic) grain size distributions and accompanying traced grain boundary maps of a) Fe33 (1000°C,  $\epsilon \sim 13\%$ ), b) Fe24 (1000°C,  $\epsilon \sim 27\%$ ) and c) Fe31 (1000°C,  $\epsilon \sim 46\%$ ), deformed at constant strain rate of  $\sim 1 \cdot 10^{-5}$  1/s and d) Fe36 (1000°C,  $\epsilon \sim 45\%$ ), deformed at constant strain rate of  $\sim 5 \cdot 10^{-6}$  1/s. Shortening direction is horizontal for Fe33 and Fe24 and vertical for Fe31 and Fe36.



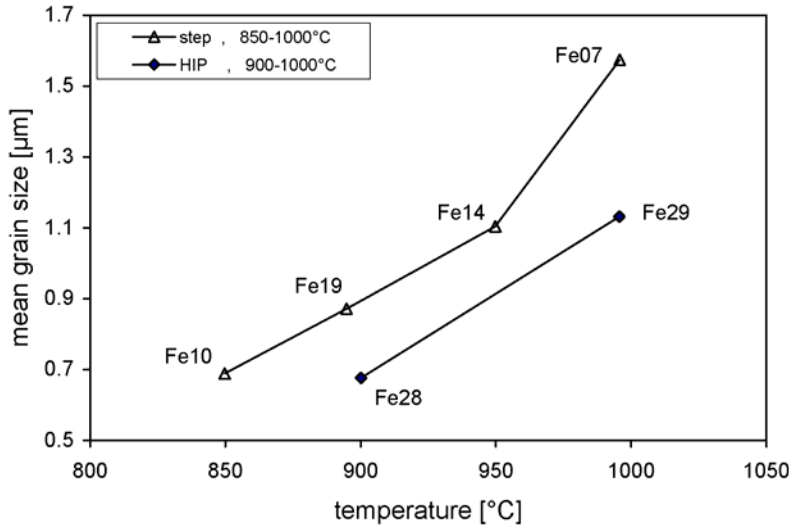
**Figure 5.9.** Mean final grain size versus total experimental duration. Data of strain rate step tests Fe01-02-08-34 are excluded (see text). In the legend ‘HIP’, ‘strain’ and ‘step’ refer to HIP-only, constant strain rate or stepped strain rate tests, respectively, followed by an indication of temperature (and strain rate).



**Figure 5.10.** a) Mean grain size versus experimental duration for static heat treatment tests and constant strain rate tests at a temperature of 900 °C and a strain rate of  $1 \cdot 10^{-5}$  1/s (Fe11-05-22) or  $3 \cdot 10^{-5}$  1/s (Fe20-17-32), b) Mean grain size versus strain for the same tests as in a) plus data from constant strain rate tests at 1000°C and strain rate step tests with alike final strain (~23%), number of strain rate steps (7) and experimental duration (>46 hrs), i.e. Fe07-10-19-14. See caption fig. 5.9 for explanation of the legend.

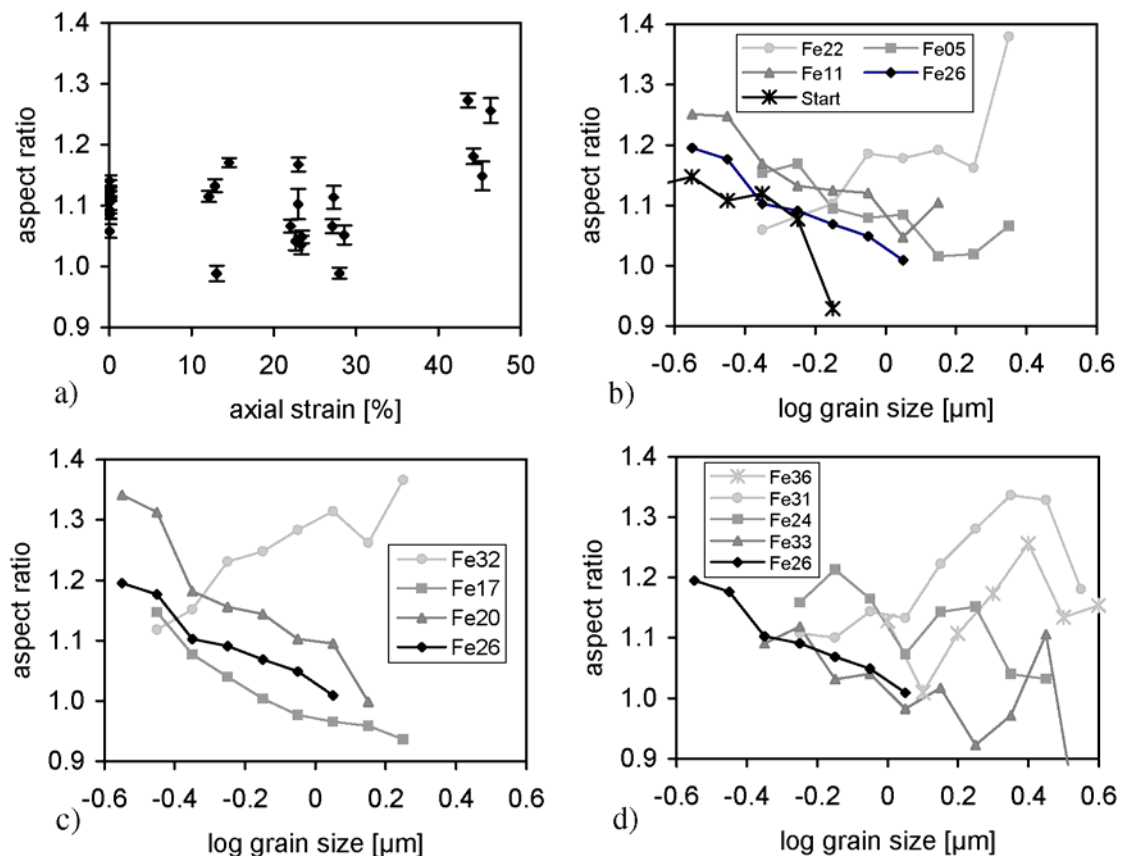


**Figure 5.12.** Area-weighted aspect ratio a) versus strain for the start material and all heat treated and deformed samples and b) versus individual grain size classes of the start material, Fe26 and ‘strain’-tests at  $T = 900^\circ\text{C}$  and strain rate of  $\sim 1 \cdot 10^{-5}$  1/s (Fe11-05-22) or c)  $\sim 3 \cdot 10^{-5}$  1/s (Fe20-17-32) and d) at  $T = 1000^\circ\text{C}$  and strain rates of  $\sim 0.5$  and  $1 \cdot 10^{-5}$  1/s (Fe36 and Fe33-24-31). Note aspect ratios represent the ratio of the grain width (feret) measured perpendicular and parallel to the compression direction. → → → →



**Figure 5.11.** Mean grain size versus temperature for heat treatment (HIP) tests and step tests at close to similar experiment duration (45-50 hrs).

HIP-only and deformed samples up to ~30% strain do not show any systematic variation in area-weighted aspect ratio (see section 5.2.3), where the average value is  $\sim 1.1 \pm 0.1$  (see fig. 5.12a and Table 5.4). Area-weighted aspect ratios for samples deformed up to ~45% strain show higher values than the average at lower strain, up to ~1.3. This difference in aspect ratio between the highest strained samples and the less deformed (and HIP-only) samples is further illustrated in figs 5.12b-d. These figures show the average aspect ratio versus logarithmic grain size classes for all constant displacement rate tests, the start material, and the 18 hrs HIP-only sample Fe26. For the highest strained samples, the average aspect ratio increases with increasing grain size, while the starting material, Fe26 and the lower strain samples show decreasing aspect ratios (down to ~1.0) with increasing grain size.



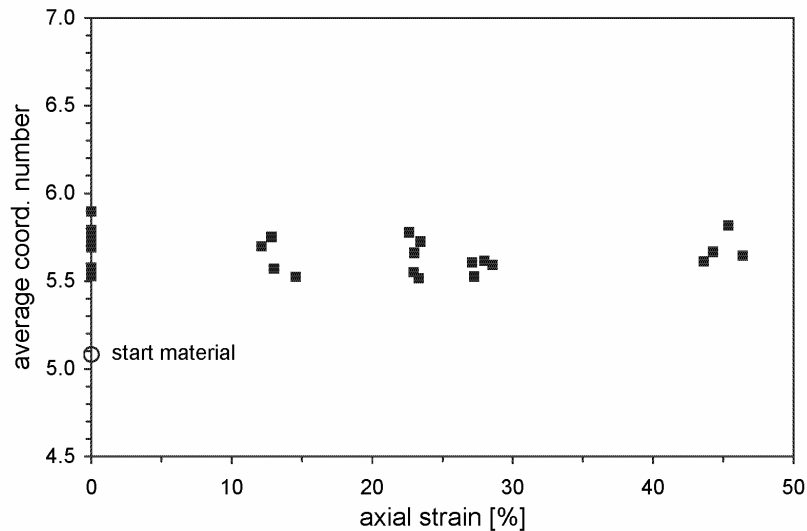


**Figure 5.13.** Average coordination number versus strain for all samples.

The average grain coordination number of the starting material is 5.1. All other samples, HIP as well as HIP plus deformed (fig. 5.13), show an average grain coordination number of  $5.7 \pm 0.2$ . This value does not change with strain (see fig. 5.13 and Table 5.4). In contrast, the (“defect”) fraction of non-hexagonal grains clearly increases with strain, from  $\sim 0.75$  for HIP-only samples, to 0.87 at 45% strain (Fe26 and Fe31; fig. 5.14a and Table 5.4). In fig. 5.14a trends are indicated for similar deformation temperature and strain rate. The figure shows that a 3-fold increase in strain rate only marginally changes the trend in defect fraction. With increasing temperature, however, considerably higher defect fractions are observed at comparable strains and experimental duration. This last point is also illustrated in fig. 5.14c, where defect fractions of step tests with similar strain (and experimental duration) are plotted against temperature. Undeformed samples with area porosities below  $\sim 2\%$  have a consistent defect fraction of  $\sim 0.75$ , i.e. show no change with increasing HIP-duration or temperature (fig. 5.14b). Undeformed samples with porosities over  $2\%$  (starting material, Fe25 and Fe29) show higher defect fractions.

We express the porosity structure by means of a so-called Zener parameter,  $Z$ , defined as (after Herwegh and Berger, 2004):

$$Z = \frac{d_p}{f_p} \quad (1)$$

where  $d_p$  is the mean pore size (diameter) and  $f_p$  is the volume fraction of the pores (In fact area fraction in our analysis). Values of  $Z$  lie in the range 10-45 and do not systematically vary with strain at constant temperature (fig. 5.15a). If grain size is plotted against Zener parameter (fig. 5.15b), a rough trend of increasing grain size with increasing  $Z$  appears for samples modified by dynamic grain growth. In contrast, samples that were only heat treated (HIP900, HIP1000; see Table 5.3) do not show an increase of grain size with  $Z$ , at a given temperature. At the same Zener value, grain sizes resulting from dynamic grain growth are generally larger than grain sizes produced under static conditions.



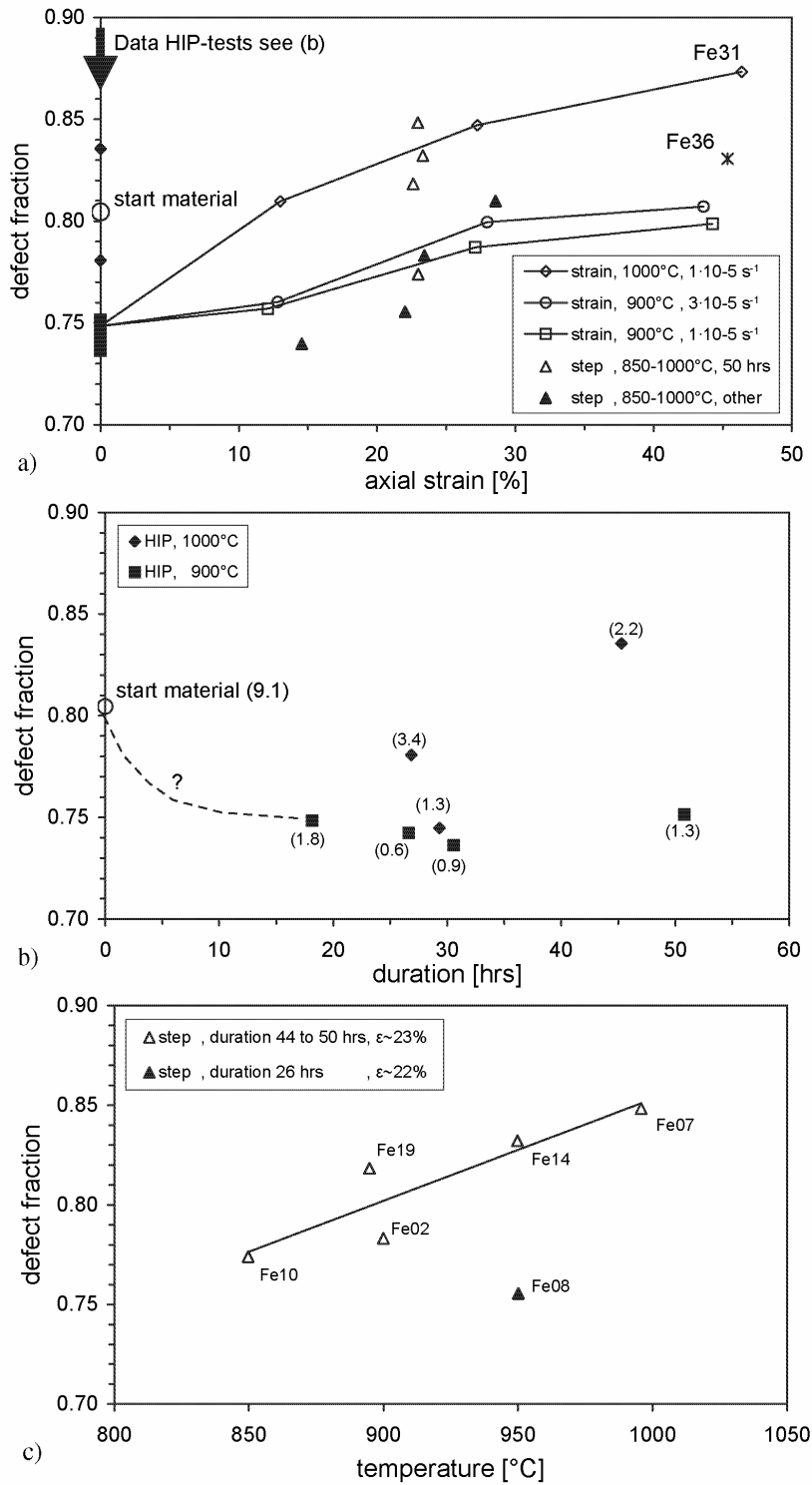


**Figure 5.14.** Defect fraction a) versus strain for HIP and deformation tests, b) versus duration for HIP tests and c) versus temperature for step tests. See caption fig. 5.9 for explanation of the legend. In c), step tests with similar final strain, ~23% and experiment duration, i.e. 44-50 hrs, are shown as open triangles. Step test Fe08 with significantly lower experimental duration (~26 hrs) is also shown.

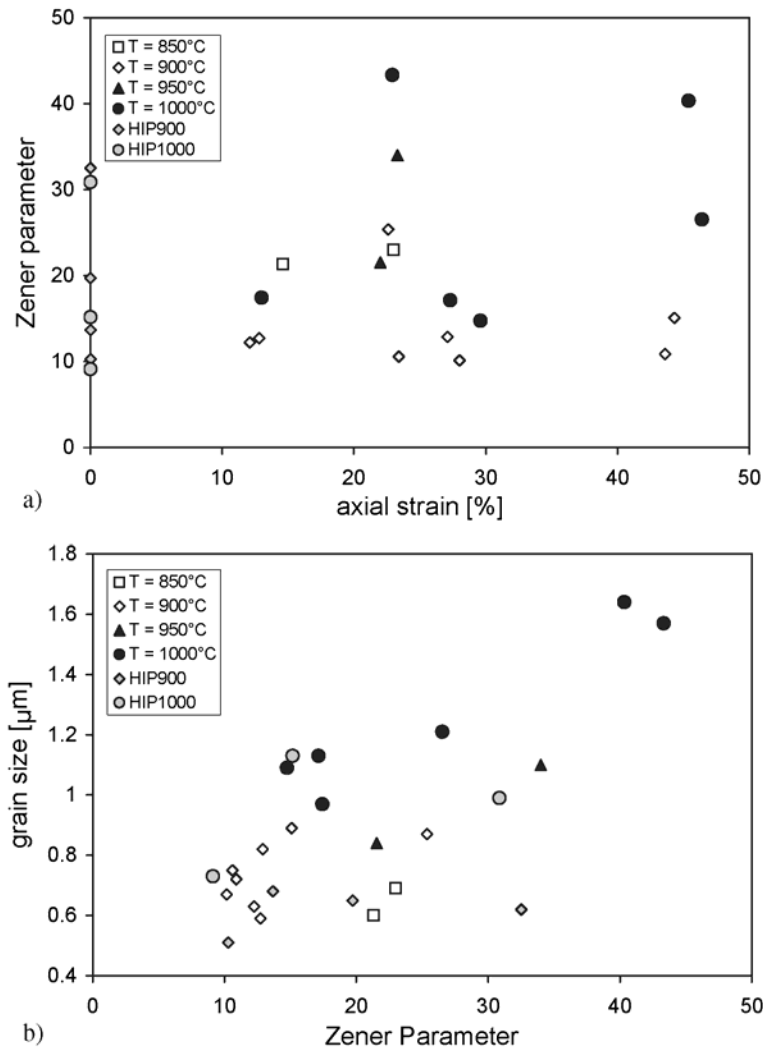


**Figure 5.15.** Plots of a) Zener Parameter versus axial strain data, and b) grain size versus Zener parameter data.

Fig. 5.16 shows pole and contour (pole density) plots obtained from EBSD analysis on sample Fe36 deformed to  $\sim 45\%$  strain at  $1000\text{ }^\circ\text{C}$  at a strain rate of  $\sim 5 \times 10^{-6}\text{ s}^{-1}$ . The poles show a close to random distribution, as also can be seen from the pole density maxima that appear randomly distributed and do not exceed 3 MUD (multiples of uniform density). The poles in fig. 5.16 illustrate the orientation of forsterite grains in the mapped area shown in fig. 5.17. The map shows enstatite grains are well distributed within the aggregates, with similar grain size as the forsterite. No agglomerations of multiple enstatite grains are observed, nor significant proportion of fine grained enstatite is found at forsterite grain boundaries. The area fraction of enstatite in fig. 5.17 ( $\sim 4.3\%$ ) is close to the volume fraction (5%) imposed during preparation of the starting material.

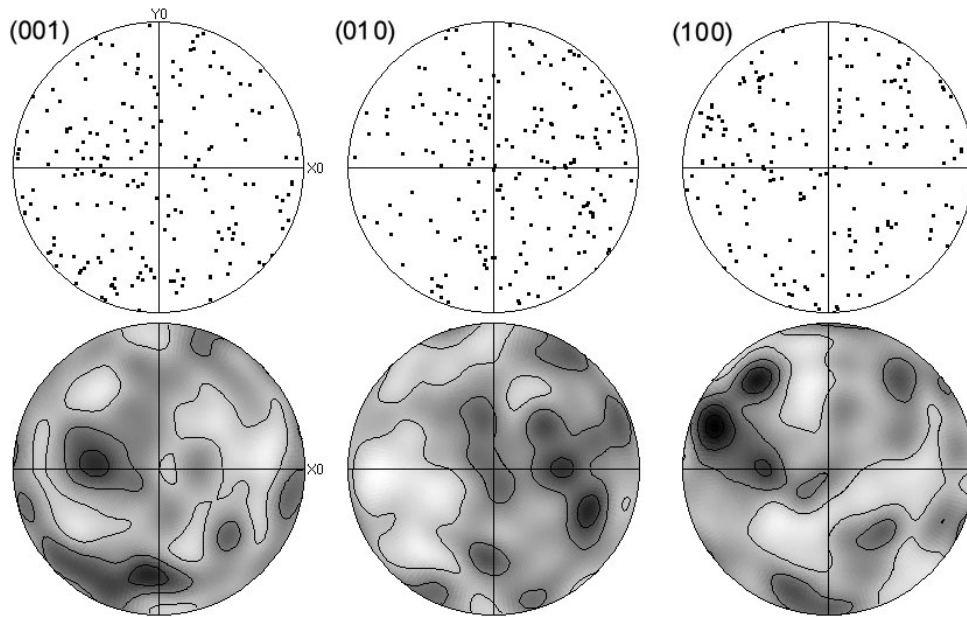


**Figure 5.16.** Crystallographic data of individual grains obtained through EBSD analysis on sample Fe36 deformed to ~45% shortening at  $T = 1000^{\circ}\text{C}$ . About 200 grains were measured. a) Pole plots for specified crystallographic directions (upper hemisphere, equal area projection), and b) contour plots of pole density. Contours drawn every  $2/3$  MUD (multiples of uniform density), with  $19^{\circ}$  Half-width and  $5^{\circ}$  cluster size. Shortening direction is vertical.

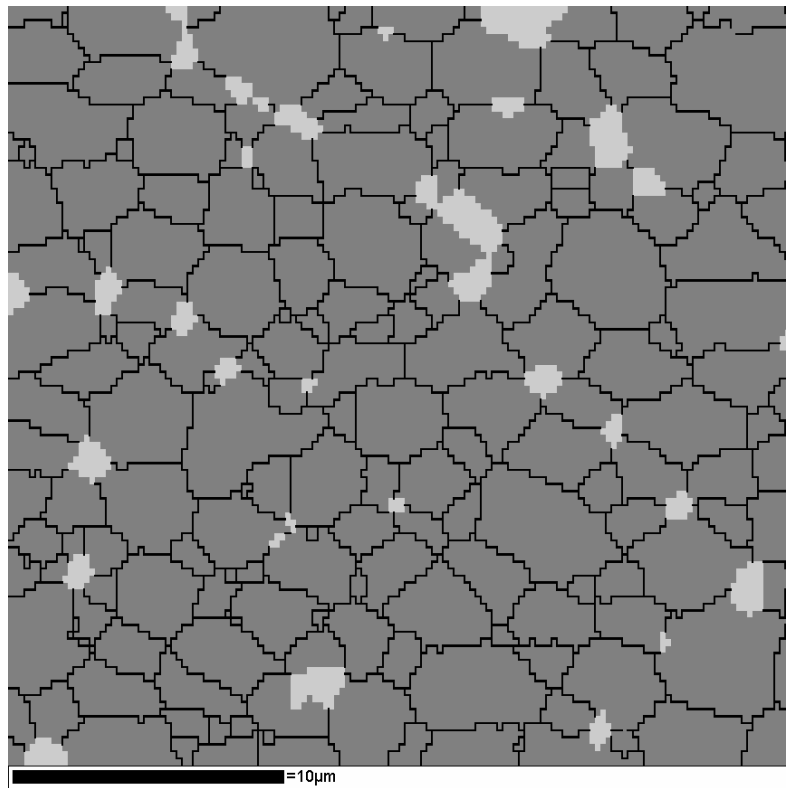


**Figure 5.17.** EBSD map of Fe36 covering the same area as analyzed for fig. 5.16; Gray tones represent grain boundaries (black) and crystal phase, i.e. dark gray is forsterite and light gray is enstatite.

Table 5.5 Experimental conditions, flow stresses & grain sizes for all strain rate steps <sup>a)</sup>

TestNo. step	Temp. [°C]	strain rate [1/s]	stress [MPa]	final grain size [μm]	calculated grain size [μm]	strain [%]
Fe01-1	853	$8.18 \cdot 10^{-5}$	105		0.35	1.8
Fe01-2	853	$1.10 \cdot 10^{-5}$	50		0.41	8.8
Fe01-3	853	$2.31 \cdot 10^{-5}$	77	0.60	0.45	13.5
Fe10-1	850	$9.89 \cdot 10^{-6}$	61		0.50	4.1
Fe10-2	850	$2.98 \cdot 10^{-5}$	129		0.61	8.7
Fe10-3	850	$1.04 \cdot 10^{-5}$	68		0.54	12.9
Fe10-4	850	$1.03 \cdot 10^{-6}$	26		0.60	16.0
Fe10-5	850	$3.96 \cdot 10^{-7}$	18		0.65	18.0
Fe10-6	850	$2.90 \cdot 10^{-6}$	47		0.65	20.2
Fe10-7	850	$1.04 \cdot 10^{-5}$	90	0.69	0.69	22.9
Fe02-1	900	$1.03 \cdot 10^{-5}$	40		0.57	6.2
Fe02-2	900	$9.98 \cdot 10^{-5}$	155		0.72	11.1
Fe02-3	900	$1.20 \cdot 10^{-5}$	56		0.71	15.8
Fe02-4	900	$1.05 \cdot 10^{-6}$	26		0.99	18.2
Fe02-5	900	$3.43 \cdot 10^{-7}$	20		1.24	20.5
Fe02-6	900	$1.04 \cdot 10^{-5}$	67	0.75	0.89	23.4
Fe19-1	895	$2.96 \cdot 10^{-5}$	63		0.52	4.3
Fe19-2	895	$1.02 \cdot 10^{-5}$	46		0.61	9.7
Fe19-3	895	$2.98 \cdot 10^{-5}$	85		0.67	12.3
Fe19-4	895	$1.03 \cdot 10^{-6}$	22		0.83	15.8
Fe19-5	895	$3.82 \cdot 10^{-7}$	18		1.06	18.0
Fe19-6	895	$3.06 \cdot 10^{-6}$	38		0.85	20.2
Fe19-7	895	$3.06 \cdot 10^{-6}$	38	0.87	0.85	22.5
Fe11	900	$1.09 \cdot 10^{-5}$	46	0.63	0.63	12.1
Fe05	903	$1.34 \cdot 10^{-5}$	76	0.82	0.82	27.1
Fe22	899	$1.75 \cdot 10^{-5}$	85	0.89	0.89	44.3
Fe20	898	$3.36 \cdot 10^{-5}$	81	0.59	0.59	12.8
Fe17	898	$4.09 \cdot 10^{-5}$	95	0.67	0.67	28.0
Fe32	900	$4.98 \cdot 10^{-5}$	114	0.72	0.72	43.6
Fe08-1	950	$9.96 \cdot 10^{-6}$	27		0.74	4.7
Fe08-2	950	$9.97 \cdot 10^{-5}$	106		0.88	8.8
Fe08-3	950	$3.00 \cdot 10^{-5}$	60		0.85	13.0
Fe08-4	950	$1.06 \cdot 10^{-5}$	38		0.87	16.6
Fe08-5	950	$3.03 \cdot 10^{-6}$	25		1.02	19.4
Fe08-6	950	$1.01 \cdot 10^{-5}$	49	0.84	1.08	21.9
Fe14-1	950	$1.03 \cdot 10^{-5}$	26		0.61	4.7
Fe14-2	950	$3.04 \cdot 10^{-5}$	48		0.68	9.4
Fe14-3	950	$1.02 \cdot 10^{-5}$	32		0.76	12.7
Fe14-4	950	$1.03 \cdot 10^{-6}$	15		0.97	15.6
Fe14-5	950	$4.03 \cdot 10^{-7}$	10		1.01	17.8
Fe14-6	950	$3.07 \cdot 10^{-6}$	28		1.09	20.1
Fe14-7	950	$1.04 \cdot 10^{-5}$	60	1.10	1.28	23.3
Fe07-1	996	$1.05 \cdot 10^{-5}$	16		0.62	7.2
Fe07-2	996	$1.02 \cdot 10^{-4}$	87		1.07	11.4
Fe07-3	996	$1.04 \cdot 10^{-5}$	24		0.88	16.0
Fe07-4	996	$1.09 \cdot 10^{-6}$	8		0.91	18.9
Fe07-5	996	$4.03 \cdot 10^{-7}$	6		0.94	20.6
Fe07-6	996	$1.08 \cdot 10^{-6}$	9		0.98	21.7
Fe07-7	996	$9.90 \cdot 10^{-6}$	44	1.57	1.53	22.9
Fe34-1	1000	$1.05 \cdot 10^{-5}$	15		0.60	4.7
Fe34-2	1000	$1.04 \cdot 10^{-4}$	60		0.77	10.2
Fe34-3	1000	$1.07 \cdot 10^{-5}$	23		0.85	17.1
Fe34-4	1000	$1.05 \cdot 10^{-4}$	113		1.32	22.2
Fe34-5	1000	$1.08 \cdot 10^{-5}$	30	1.09	1.05	28.5
Fe33	1000	$1.11 \cdot 10^{-5}$	20	0.97	0.97	13.0
Fe24	1000	$1.36 \cdot 10^{-5}$	37	1.13	1.13	27.3
Fe31	998	$1.82 \cdot 10^{-5}$	55	1.21	1.21	46.4
Fe36	999	$7.19 \cdot 10^{-6}$	41	1.64	1.64	45.4

<sup>a)</sup> Steps without a measured final grain size are at INTERMEDIATE strains

### 5.3.5 Description of flow behaviour

The above results show that there is a relationship between mechanical data exhibiting continuous time- and strain-dependent hardening and microstructural data showing (deformation enhanced) grain growth. Considering the lack of microstructural evidence for

significant dislocation activity, this provides a basis to assume that grain growth is the primary cause of hardening. We thus should take grain size into account when describing the collected stress - strain rate data by some rate equation. Although none of the experiments reached true steady state flow behaviour, we will assume that any change in grain size, by whatever mechanism, is immediately reflected in a change in flow behaviour according to a standard (Dorn-type) power law (as done by Hirth and Kohlstedt, 1995a) of the form:

$$\dot{\epsilon} = A_0 \cdot \sigma^n \cdot d^{-p} \exp\left(-\frac{Q_c}{RT}\right) \quad (2)$$

where  $\dot{\epsilon}$  is the strain rate in  $s^{-1}$ ,  $\sigma$  is the flow stress in MPa,  $A$  is a pre-exponential constant  $MPa^{-n} s^{-1} \mu m^p$ ,  $d$  is the grain size in  $\mu m$ ,  $Q_c$  is the apparent activation energy in kJ/mol,  $R$  is the gas constant  $kJ mol^{-1} K^{-1}$ ,  $T$  is the absolute temperature in K,  $n$  is the stress exponent and  $p$  is the grain size exponent. Table 5.5 lists the data of all deformation tests in terms of temperature, final grain size, flow stress and strain rate, which are necessary to determine the stress, temperature and grain size dependence of the creep behaviour. Apart from the final values measured at the end of or after experimentation, Table 5.5 also includes values from strain rate steps at intermediate strains (used later in this section). Nonlinear regression analysis has been carried out to obtain a multidimensional best fit to the data, making use of the software package Axum<sup>TM</sup>. Fitting was achieved using the Marquardt-Levenberg non-linear least squares fitting algorithm (Marquardt, 1963), taking stress as the dependent variable. The Dorn-type equation (2) was first fitted to the set of final grain size values in Table 5.5. The results of this non-linear regression for  $n$ ,  $\log A_0$ ,  $p$ ,  $Q_c$  and  $R^2$  are given in Table 5.6 as flow law parameter set-A. The plot of stress versus strain rate in fig. 5.18a shows the correspondence between the flow law based on parameter set-A and the rheological data obtained at the end or after experimentation, normalised to a grain size of 0.9  $\mu m$ .

Table 5.6 Results of nonlinear regression fitting of relation (2) to the mechanical fo90 data of this study and published flow-parameters on fo100 McDonnell and co-workers.

Data-set	$n$ [-]	$\text{Log}A_0$ [ $MPa^{-n} s^{-1} \mu m^p$ ]	$p$ [-]	$Q_c$ [kJ/mol]	$R^2$ [-]
This study:					
(A) All data	$2.13 \pm 0.34$	$2.99 \pm 1.83$	$2.49 \pm 0.56$	$270 \pm 50$	0.88
(B) $\epsilon = 22-28\%$	$2.34 \pm 0.43$	$1.87 \pm 1.88$	$1.66 \pm 0.71$	$252 \pm 50$	0.93
(C) $\epsilon = 22-28\% + 43-46\%$	$2.29 \pm 0.27$	$1.47 \pm 1.38$	$1.73 \pm 0.47$	$242 \pm 35$	0.95
(D) $\epsilon = 22-28\% + 12-15\%$	$2.30 \pm 0.55$	$3.78 \pm 2.54$	$2.60 \pm 0.81$	$294 \pm 73$	0.86
McDonnell et al. (1997,1999):	$2.14 \pm 0.18$	$4.44 \pm 0.80$	for $d=1.2\mu m$	$302 \pm 21$	-
	constrained: $n=1$	$3.24 \pm 0.88$	for $d=1.2\mu m$	$237 \pm 20$	-
McDonnell et al. (1997,1999):	$2.14 \pm 0.18$	$4.68 \pm 0.80$	constrained: $p=3$	$302 \pm 21$	-

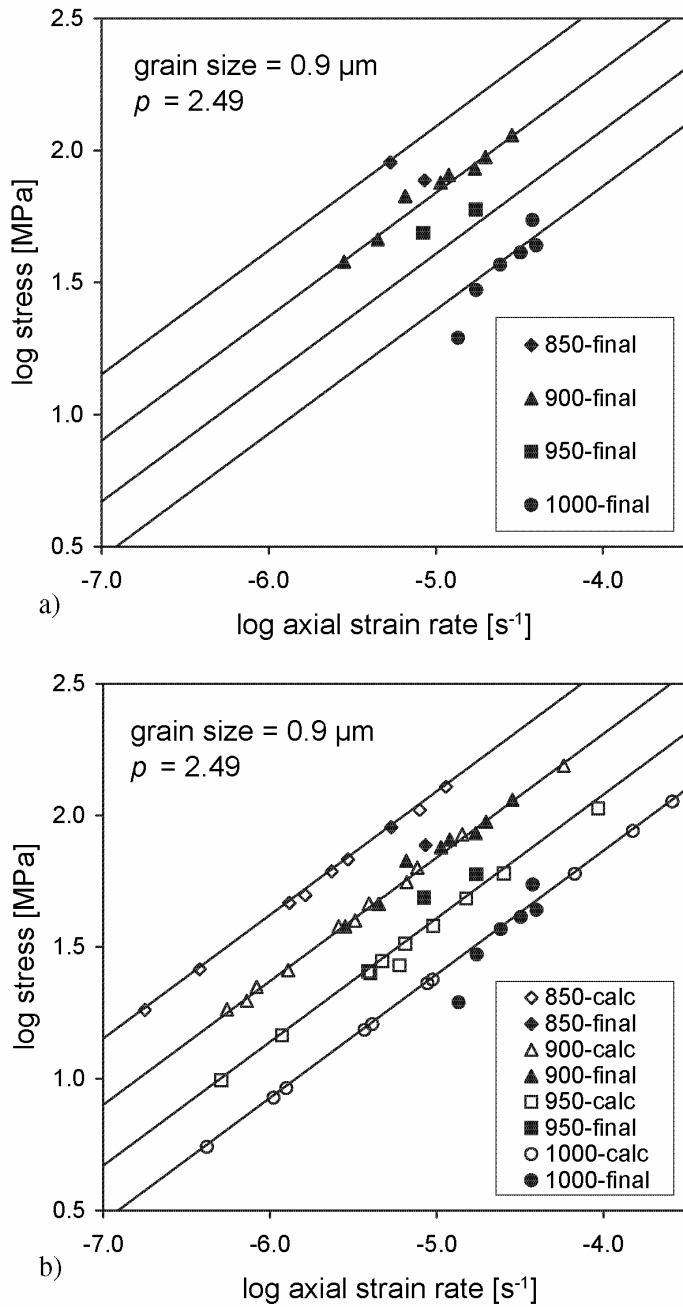


**Figure 5.18.** Stress versus strain rate data and isotherms corresponding to the calibrated flow law (parameter set-A). a) The rheological data obtained at the end or after experimentation, normalised to a grain size of 0.9 μm. b) Similar to a) but including data from intermediate strain rate steps (open symbols).

Next, using these flow law parameters and the observed hardening behaviour, the grain size evolution during every individual experiment can be predicted. In order to do so, relation (2) has been rearranged such that  $d$  becomes the dependent variable:

$$d = \left( A_0 \cdot \sigma^n \cdot \dot{\epsilon}^{-1} \cdot \exp\left(-\frac{Q_c}{RT}\right) \right)^{1/p} \quad (3)$$

Using relation (3) and the parameter set A in Table 5.6, grain size can be predicted for each data point within a single experiment. This approach is reasonable since: a) no dislocation activity that potentially could harden the material has been observed and b) no evidence for processes that can reduce the grain size has been found. Thus, grain growth can be considered

as the sole process causing hardening. Consequence is that the predicted grain size must always increase (with strain or time) and that its evolution must be continuous. Fig. 5.19 shows schematic examples of possible grain size evolutions during step tests for, respectively, dominant strain dependent grain growth, dominant time dependent grain growth, and apparent discontinuous grain growth. Any discontinuous evolution of grain size suggests use of incorrect flow parameters (see fig 5.19d). We assume all experiments had a starting grain size similar to the value measured for Fe26 at the onset of deformation. Fig. 5.20 shows the predicted grain size evolutions as a function of strain for all step tests. The deviation between the measured and predicted starting (after yielding) and final grain sizes is due to the uncertainty in values for the flow parameters. It is shown that grain size indeed increases continuously for steps at intermediate strain rate ( $3 \cdot 10^{-6} \rightarrow 3 \cdot 10^{-5}$ ). At higher strain rates ( $3 \cdot 10^{-5} \rightarrow 1 \cdot 10^{-4}$ ), however, the predicted increase in grain size at the start of the step is not continuous with the previous part of the evolution and if strain rate is stepped down again an almost instantaneous apparent decrease in grain size occurs (e.g Fe07 and Fe34, see also fig 5.19d). Such abrupt steps in grain size are not to be expected, especially not in case of a grain size decrease, since they are not in agreement with time- or strain dependent grain growth. We therefore must conclude that the flow behaviour and grain size evolution at the higher strain rate/stresses is not well represented by the application of the parameter values (set A) in Table 5.6. This suggests that either different flow law parameters have to be used for high and lower strain rates or that the values for set A in Table 5.6 are too inaccurate (see relatively large errors) to properly explain the flow behaviour / grain size evolution for the complete range of conditions covered. From the final and starting grain sizes of lower strain rate steps, respectively preceding and following a higher strain rate step (see fig. 5.20), we do observe grain size increase followed a similar linear trend with strain. This indicates grain coarsening is more a function of strain than of time (see also fig 5.19b and d).

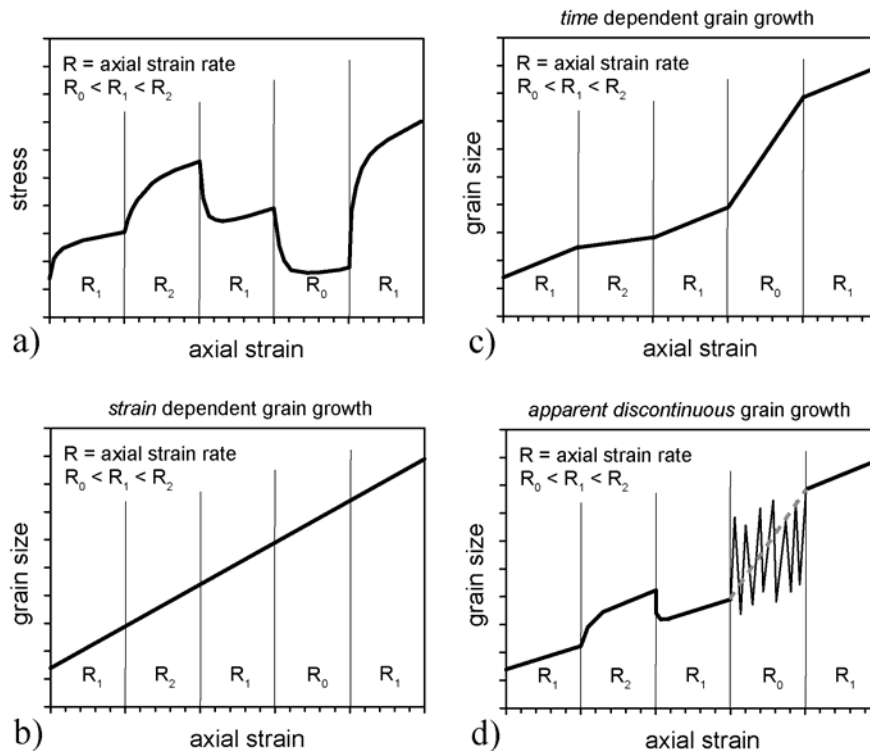


**Figure 5.19.** Schematic (example) plots of a) a stress-strain curve for a typical strain rate step sequence, and possible corresponding grain size - strain evolutions for, respectively, b) dominant strain dependent grain growth, c) dominant time dependent grain growth, and d) apparent discontinuous grain growth.

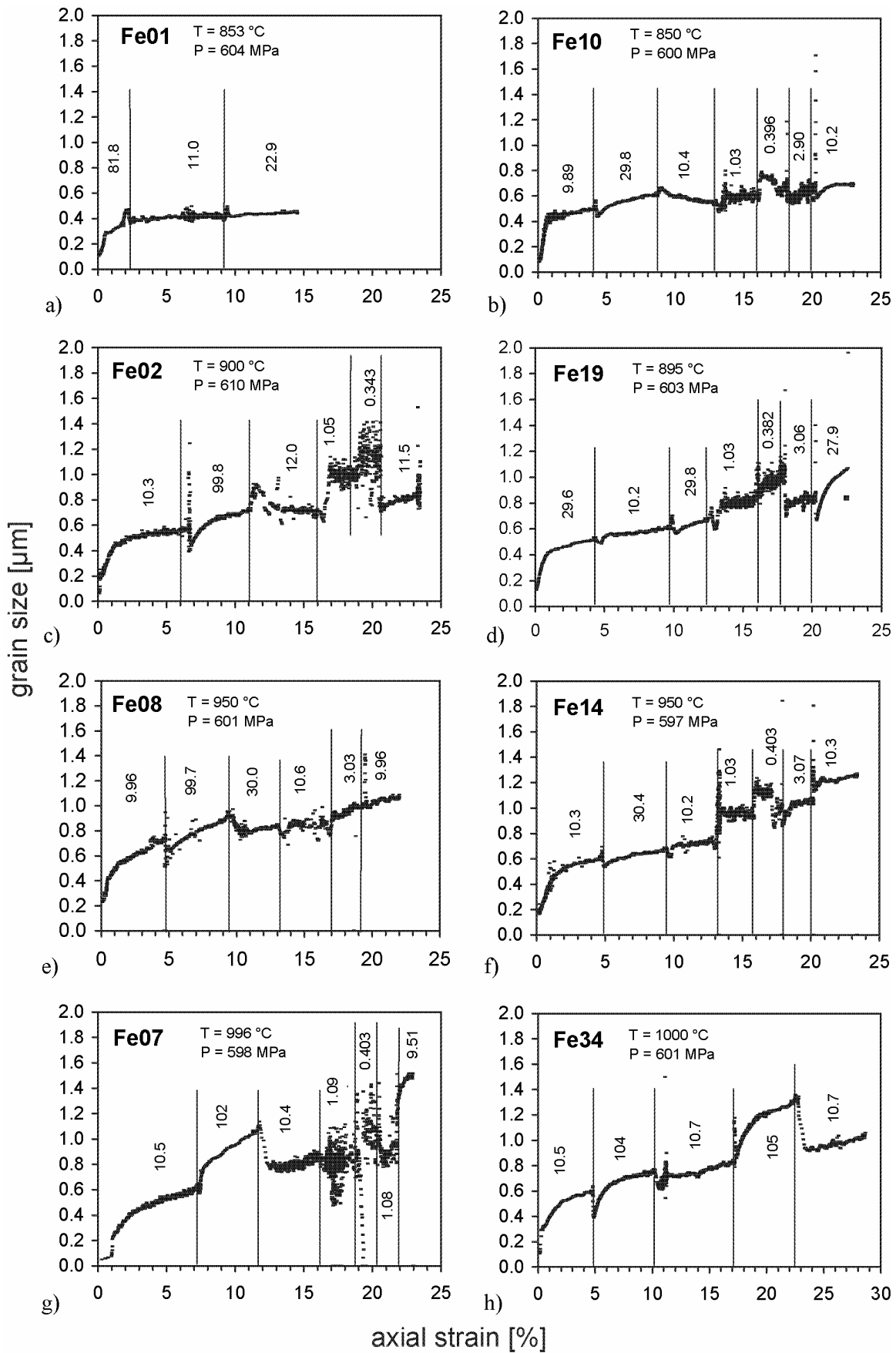


**Figure 5.20.** Predicted grain size evolutions as a function of strain for all step tests. These have been derived using relation (3) and parameter set-A.



At the lower strain rates ( $3.8 \cdot 10^{-7} \rightarrow 3 \cdot 10^{-6}$ ) fig. 5.20 also shows discontinuous and irregular grain size evolution. We infer this indicates that measurements were done at the stress/strain rate resolution limits. Regardless of all the complications, still an evolutionary trend during the slower strain rate intervals can be inferred from the predicted grain size values before and after the specific step (see also fig. 5.19d). Here, Fe08-14-07 clearly show that more grain growth per strain occurred during these slow strain rate steps, indicating again a time dependent component in grain growth (see also fig. 5.19c-d). Apparently, grain growth is both a function of strain and a function of time.

If it is only inaccuracy in parameter set-A (Table 5.6) that causes part of the observed inconsistencies in grain size evolution, there must be a single best-fit flow law within the obtained errors. We followed an iterative approach in an attempt to improve the parameter values of set A. First, a final grain size at the end of each step was calculated using (3) and the first set of parameters in Table 5.6. Then, all data (measured ‘final’ as well as estimated ‘end-of-step’) were included in a new non-linear best fit. This resulted in values for  $n$ ,  $\log A_0$ ,  $p$  and  $Q_c$  that slightly differ from the values (set A) based on the final values only. The new flow parameters were used again to calculate the grain size at the end of each step, and the non-linear best fitting procedure was repeated. We found that, after ~20 iterations, the stress exponent  $n$  continued to decrease to a value outside the error indicated in Table 5.6 for set A (i.e.  $n < 1.79$ ), while values for  $p$ ,  $\log A_0$  and  $Q_c$  increase to values of ~3, ~5.5 and ~310, respectively. In this approach, none of the sets of recalculated parameter values result in more continuous grain size evolutions than shown in fig. 5.20. Since no constant values were reached through this iterative method, we must conclude that no single flow law can satisfactorily describe the data for the range of conditions investigated (stress - strain rate - grain size - temperature). The calibrated flow law given by the parameter set-A best describes the data at the lower strain rates. Fig. 5.18b shows a comparison between the flow law based on parameter set-A and the all the data, including those from intermediate strain rate steps, normalised to a constant grain size of 0.9  $\mu\text{m}$ .

Samples at 0%, 12-15% and 22-28% strain show a more or less constant aspect ratio of ~1.1. The observation of a higher average aspect ratio (1.3) for samples deformed up to the maximum strain of ~45% could indicate that flow behaviour might also change with increasing strain (in addition to strain rate). Therefore we performed non-linear best fits to relation (2) on data selected to represent specific strains. Resulting flow parameters are included in Table 5.6. Individual fits for strains at 12-15% and 43-45% did not produce meaningful results. Compared to the best fit to all the data, the best fit to data at 22-28% strain shows a prominent decrease in  $p$ -value down to 1.85, i.e. close to ~2 (parameter set-B, Table 5.6). Likewise, a fit to both the data at 22-28% and 43-46% strain resulted in a lower  $p$ -value at 1.88 (parameter set-C, Table 5.6). Also, note the higher R-squared values and slightly lower activation energies for fits at 22-28% strain and 22-28% plus 43-46% strain. In contrast, a fit to the data at 22-28% plus the lower strain data at 12-15% leads to a slight increase in  $p$ -value and activation energy (parameter set-D, Table 5.6).

## 5.4 Discussion

### 5.4.1 Flow behaviour of synthetic fo<sub>100</sub> and of fo<sub>90</sub> aggregates

#### Strength of fo<sub>90</sub> relative to fo<sub>100</sub>

In this study, we report the results of 18 deformation experiments on very fine-grained synthetic Fe-bearing (fo<sub>90</sub>) olivine aggregates containing 5 vol% enstatite. The collected mechanical data on this material allow us to evaluate the effect of Fe on flow behaviour

through comparison with data on similarly prepared synthetic but Fe-free ( $fo_{100}$ ) material (chapter 3, and McDonnell, 1997; McDonnell et al., 1999). Such evaluation of the effect of Fe on flow behaviour of synthetic material may also be of use in assessing causes for the observed difference between synthetic and synthetic-natural olivine flow behaviour (Karato et al., 1986; Mei and Kohlstedt, 2000a; Hirth and Kohlstedt, 2003). Note that McDonnell et al. (2000) demonstrated that the strength of their synthetic olivine material decreased substantially if the enstatite content was increased from 0 to 2.5 vol%, but hardly changed with further increase up to 20 vol%. It is thus justified to directly compare our  $fo_{90}$  plus 5 vol% enstatite to McDonnell's  $fo_{100}$  plus 2.5 vol% enstatite. We will further refer to these materials as  $fo_{90}$  and  $fo_{100}$ .

We have found that the flow behaviour of  $fo_{90}$  can be described by applying a Dorn-type power law with a relatively low  $n$ -value ( $2.1 \pm 0.3$ ), a grain size sensitivity  $p = 2.5 \pm 0.6$  and an apparent activation energy  $Q_c = 270 \pm 50$  kJ/mol (see Table 5.6). McDonnell (1997) and McDonnell et al. (1999) calibrated a flow law for  $fo_{100}$  material for a fixed grain size of  $\sim 1.2$   $\mu\text{m}$ , yielding values for  $n$  and  $Q_c$  that, within errors, are identical to the values obtained for  $fo_{90}$ , namely  $n = 2.1 \pm 0.2$  and  $Q_c = 302 \pm 21$  kJ/mol. This flow law for  $fo_{100}$  was made sensitive to grain size by McDonnell and coworkers by fixing  $p = 3$ , based on an analysis of the mechanical results in relation to limited variability in grain size (1-2  $\mu\text{m}$ ). The values for  $n$  and  $Q_c$  remained 2.1 and 302 kJ/mol in this GSS creep law (see Table 5.6). Fig. 5.21 shows calculated isotherms (at  $T = 850$  and  $1000$  °C) in stress versus strain rate space for both synthetic  $fo_{100}$  and  $fo_{90}$  material of grain size 1.2  $\mu\text{m}$ . Flow behaviour of synthetic  $fo_{90}$  olivine appears to be slightly stronger than that of  $fo_{100}$  at the investigated conditions, but the difference is small and cannot be considered as significant given the errors in the flow law parameters ( $n$ ,  $p$ ,  $Q_c$  and pre-exponential constant  $A_0$  - see error-band in fig. 5.21). Therefore, we conclude that the presence or absence of Fe in the olivine structure has no significant effect on its flow behaviour, at least not at the conditions investigated in this study.

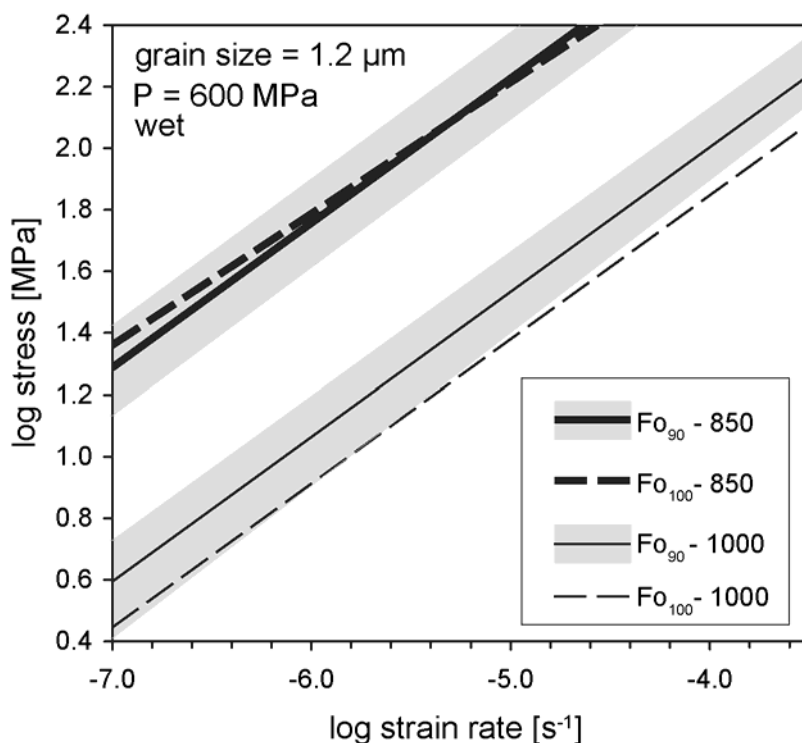


**Figure 5.21.** Calculated isotherms (at  $T = 850$  and  $1000$  °C) in stress versus strain rate space for both synthetic  $fo_{100}$  and  $fo_{90}$  material of grain size 1.2  $\mu\text{m}$ . The error band for  $fo_{90}$  isotherms indicates the maximum possible variation due to errors in the flow parameters (see Table 5.6).

Support for our inference that Fe has little effect on the creep of olivine comes from an analysis by Farver and Yund (2000) on grain boundary diffusion rates in creep experiments. Using the Coble (1963) creep relation, they calculated grain boundary diffusion rates on the basis of the creep data of Hirth and Kohlstedt (1995a) and McDonnell et al. (1999) for synthetic-natural fo<sub>91</sub> and synthetic fo<sub>100</sub>, respectively. Extrapolation of the Hirth and Kohlstedt (1995a) rates to the lower temperature range of the fo<sub>100</sub> data yielded similar grain boundary diffusion rates, implying no large effects of Fe.

Our comparison of the mechanical results on wet synthetic fo<sub>90</sub> and fo<sub>100</sub> has not shown any evidence for the weakening effects of iron proposed by Mei and Kohlstedt (2000a), i.e. higher water solubility and changing point defect chemistry. Several explanations can be put forward. First, the addition of Fe might well alter the point defect chemistry from Mg- to Fe-dominated, but may not cause a switch in controlling slowest diffusing species. Several studies suggested Si to be the slowest diffusing species in both fo<sub>90</sub> (Hirth and Kohlstedt, 2003) and fo<sub>100</sub> (Anderson et al., 1989). If so, then the difference in overall point defect chemistry between fo<sub>90</sub> and fo<sub>100</sub> does not significantly affect the concentration and diffusivity of Si. Alternatively, there is some evidence that Mg (and not Si) is the slowest diffusing species in fo<sub>100</sub> (Farver et al., 1994; Farver and Yund, 2000). In fo<sub>90</sub>, the Fe-induced change in point defect chemistry may cause a switch to Si as the slowest diffusing species, but if the diffusivities of both Si and Mg are not too much different, at the given conditions in wet material, the effect on the creep rate may be small.

### Deformation mechanism

Having established similar mechanical behaviour of wet, fine-grained synthetic fo<sub>90</sub> and fo<sub>100</sub>, we can discuss what deformation mechanism best fits the observed flow behaviour. The microstructure of the deformed olivine is that of dominantly polygonal grains with occasional pores at triple point junctions, and a lack of crystallographic preferred orientation or other evidence of significant dislocation activity (light optical and SEM scale). Taken together with the GSS character of the calibrated flow law, this points to diffusion and/or grain boundary sliding (GBS) as the mechanisms of deformation (e.g., Ashby and Verrall, 1973; Crossman and Ashby, 1975). The stress-exponent  $n \sim 2$  (and not 1) excludes deformation to be governed purely by grain boundary diffusion or lattice diffusion creep (i.e., Coble or Nabarro-Herring creep, respectively). Rather, this value of  $n$  supports a deformation mechanism of grain boundary sliding accommodated by dislocation and/or diffusion creep processes (e.g., Gifkins, 1976; Langdon, 1995).

A wide range of microphysical models exist for GBS, mostly differing in the way accommodation problems are solved during grain sliding (see overview by Hynes and Doremus, 1996). Such accommodation mechanisms include grain boundary and lattice diffusion, dislocation climb, and interface reactions. The value for the grain size sensitivity determined for laboratory creep of fo<sub>90</sub>,  $p = 2.5 \pm 0.6$ , is precisely intermediate between the theoretical values of 2 and 3 representing lattice and grain boundary diffusion, respectively. Taking the error into account, the value for  $p$  does not allow us to determine what kind of diffusion mechanism (lattice or grain boundary diffusion) may have accommodated GBS. It is recalled, though, that fits to the mechanical data at shortening strains  $\geq 22\%$  show a decrease of  $p$  from 2.5 to  $\sim 2$  (Table 5.6). This may hint to lattice diffusion as accommodation mechanism, at the higher strains. On the other hand, it is known that water has a significant weakening effect on the flow behaviour of fo<sub>90</sub>. Similar to fo<sub>100</sub>, unmeant dry samples of fo<sub>90</sub> showed elastic loading up to stresses far above values for which wet samples yielded. Also, the solubility of water in olivine increases substantially with increasing Fe-content (Zhao et al., 2004), but this is not seen back as a difference in strength between fo<sub>90</sub> and fo<sub>100</sub>. In other

words, the weakening of water appears not to be related to an intracrystalline effect, and a  $p$  value of  $\sim 2$  then must imply another mechanism than lattice diffusion.

One possible mechanism explaining  $n = 2$  and  $p = 2$  is given by Gifkins' model (Gifkins, 1976; Hynes and Doremus, 1996). In this model, GBS is accommodated by dislocation motion confined to a mantle zone along the grain boundaries. Dislocation climb is the controlling mechanism, grains can switch neighbours like in the model of Ashby and Verall (1973), but grain interiors remain dislocation free. Though we have not found evidence for dislocation activity in our material, we cannot fully rule out that dislocation processes played a role during creep. For that, TEM work is needed.

So far, we have not discussed any implication of the value of the (apparent) activation energy  $Q_c$  determined for creep of the synthetic wet fo<sub>90</sub>. Within errors, this value does not differ from  $Q_c$  determined for wet fo<sub>100</sub> by McDonnell and coworkers. Following a previous analysis by McDonnell (1997), the temperature dependence implied by the obtained  $Q_c$ -values overlaps with results for dry lattice diffusion (Reddy et al., 1980; Jaoul et al., 1980; 1981; Ando et al., 1981; Oshi and Ando, 1984; Anderson et al., 1989) and with estimates and very limited data on dry and wet grain boundary diffusion data (Tsenn and Carter, 1987; Farver et al., 1994). It thus appears impossible to discriminate between the various types of diffusive process on the basis of  $Q_c$ -values alone, let alone to determine with confidence the rate-limiting diffusing species. However, some relevant information may follow from comparison of dry and wet fo<sub>100</sub>. Farver and Yund (2000) reported a low activation energy of  $\sim 200$  kJ/mol for grain boundary diffusion of Si in dry synthetic fo<sub>100</sub>. This low value leads to an order of magnitude higher grain boundary diffusivity for Si compared to Mg at temperature  $\leq 1200$  °C (Farver et al., 1994). A recent electrical conductivity study by Ten Grotenhuis et al. (2004), performed on synthetic fo<sub>100</sub> material fabricated by the same method as applied by McDonnell et al (2002) confirmed the value for the apparent activation energy for grain boundary diffusion of Mg in dry material of Farver et al. (1994) being  $\sim 350$  kJ/mol. Applied to hydrous conditions, these findings may imply that Mg (and not Si) controls diffusivity of our and McDonnell's material at 850-1000 °C.

#### 5.4.2 Comparison to other studies

Fig. 5.22 compares the flow laws for synthetic fo<sub>90</sub> and fo<sub>100</sub> with previously calibrated flow laws for wet (and dry) GSS flow behaviour of 'natural-synthetic' olivine aggregates (Karato et al., 1986; Mei and Kohlstedt, 2000a; Hirth and Kohlstedt, 2003). We include a flow law for fo<sub>100</sub> in which  $n$  is constrained to 1 (McDonnell, 1997 – Table 5.6), although it is acknowledged that a higher  $n$ -value fits the data better. In order to allow meaningful comparison, we extrapolated a) previous data to our experimental conditions (i.e. to lower temperature, fig. 5.22a), and b) our data to the experimental conditions of previous studies (meaning extrapolation to higher temperature, fig. 5.22b).

In fig. 5.22a 'natural-synthetic' flow laws were used to calculate isotherms for a temperature of 900 °C, a water fugacity of 600 MPa, and a grain size of 1.2  $\mu\text{m}$ . The wet flow laws of Karato et al. (1986) and Mei and Kohlstedt (2000a) predict flow stresses that are up to 2 orders of magnitude lower than hold for fo<sub>90</sub> and fo<sub>100</sub>. However, the most recently proposed wet flow law of Hirth and Kohlstedt (2003), based on a reanalysis of the data of Mei and Kohlstedt (2000a), crosscuts the synthetic-based calibrations and falls close to the fo<sub>100</sub> prediction with  $n$  constrained to 1 (fo<sub>100</sub>-Coble). The resulting higher activation energy (375 kJ/mol) compared to the value (295 kJ/mol) published by Mei and Kohlstedt (2000a) causes a strong increase in flow stresses, up to values comparable to our data. As a reference, fig. 5.22a also includes the dry flow law of Karato et al. (1986) forming an upper stress

bound. In fig. 5.22b the flow laws for synthetic  $fo_{100}$  and  $fo_{90}$  are extrapolated to higher temperature (1300 °C), and grain size (10  $\mu\text{m}$ ). Similar to the lower temperature (900°C) situation, the wet flow laws of Karato et al. (1986) and Mei and Kohlstedt (2000a) indicate significantly lower flow stresses. At 1300 °C, the wet flow law of Hirth and Kohlstedt (2003) also predicts significantly lower stresses than the flow laws for synthetic  $fo_{100}$  and  $fo_{90}$ , i.e. comparable to the strongest Mei and Kohlstedt (2000a) flow law. Even the dry flow law of Karato et al. (1986) predicts lower stresses than the synthetic prediction with  $n$  constrained to 1, which now forms the upper stress bound.

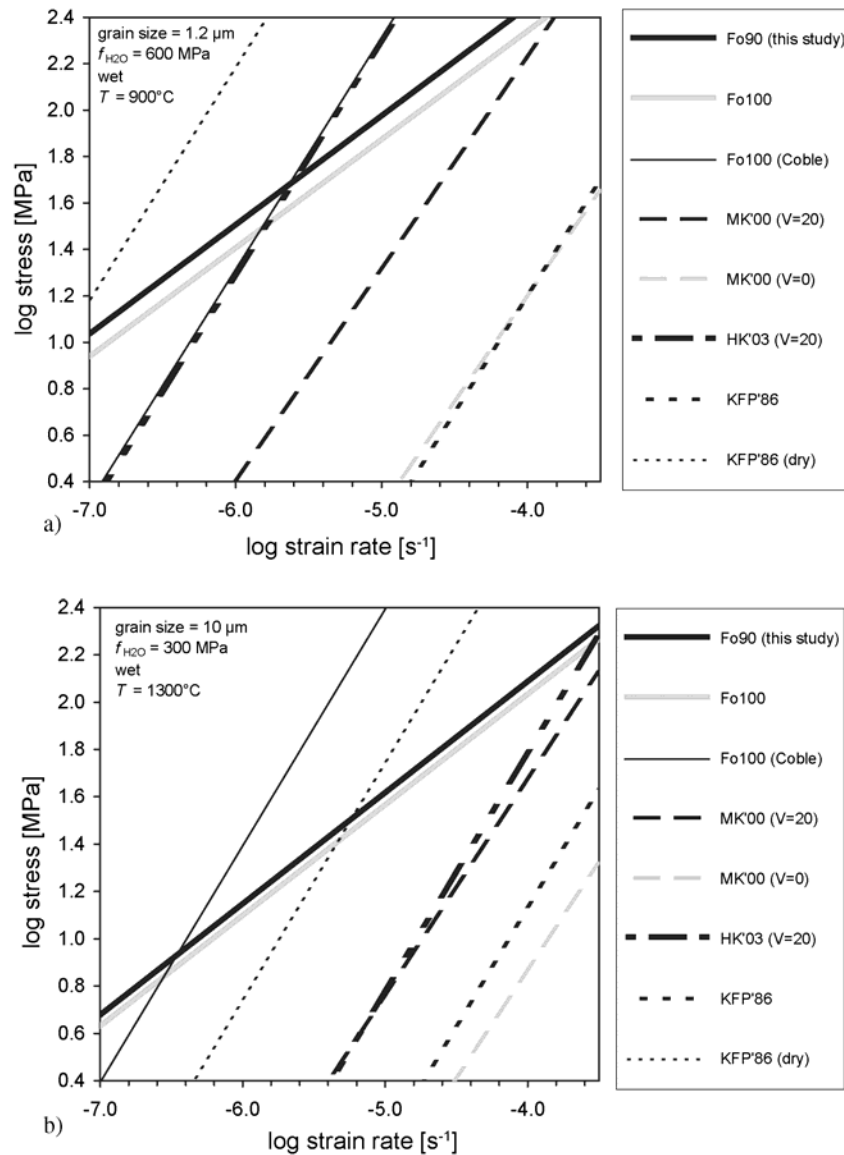


**Figure 5.22.** Comparison of flow laws for wet synthetic  $fo_{90}$  and  $fo_{100}$  with previously calibrated flow laws for wet (and dry) GSS flow behaviour of ‘synthetic-natural’ olivine aggregates. In a) previous data are extrapolated to our experimental conditions (i.e.  $T=900^\circ\text{C}$ , grain size= $1.2 \mu\text{m}$ ,  $f_{\text{H}_2\text{O}}=600 \text{ MPa}$ ) and in b) our flow laws are extrapolated to the experimental conditions of previous studies (i.e.  $T=1300^\circ\text{C}$ , grain size= $10 \mu\text{m}$ ,  $f_{\text{H}_2\text{O}}=300 \text{ MPa}$ ). MK'00 = Mei and Kohlstedt 2000 ( $V$  is activation volume in  $\text{cm}^3/\text{mol}$ ), HK'03 = Hirth and Kohlstedt, 2003, KPF'86 = Karato et al. 1986.

Fig. 5.22 shows that extrapolation of our data to higher temperature and of previous data to lower temperature result in substantial differences in predicted strengths of the olivine material. Of course, the difference in flow behaviour might simply mean that the low and high temperature creep (our and previous materials, respectively) is controlled by different GSS mechanisms. Upon extrapolation, a mechanism boundary then is crossed, not accounted for in creating the graphs of fig. 5.22. Still, the flow laws for synthetic-natural material predict generally lower flow stresses when compared to flow laws for synthetic fo<sub>100</sub> and fo<sub>90</sub>. Since our data show that adding Fe does not result in a significant change in strength of the olivine, it seems unlikely that it is the Fe-content that can explain the difference in flow behaviour between synthetic-natural and synthetic material, as was suggested by Mei and Kohlstedt (2000a). Few data from supplementary studies on synthetic fo<sub>90</sub> in the dry diffusion to dislocation creep field (Beeman and Kohlstedt, 1993; Faul and Jackson, 2004) also show up to 2 orders of magnitude stronger flow behaviour compared to synthetic-natural fo<sub>90</sub> (Hirth and Kohlstedt, 1995a; Mei and Kohlstedt, 2000a). This difference is quite similar to the above discussed difference at 900 and 1300°C for wet material. We infer that a chemical property difference between synthetic and synthetic-natural material other than the presence of Fe must be the reason for the difference in flow behaviour.

One prominent chemical difference between synthetic-natural and synthetic material is their solutes/impurities content (see Table 5.1). Since diffusion rates are very sensitive to changes in point defect chemistry, even small differences in solute/impurity content between materials might strongly influence the flow behaviour. Faul and Jackson (2004) suggest the presence of melt in the nominally melt-free reported samples of Hirth and Kohlstedt (1995a) and Mei and Kohlstedt (2000a) can explain their weaker flow behaviour. Trace amounts of melt ( $\ll 0.1\%$ ) were found by Jackson et al. (2002) in dry ‘synthetic natural’ samples (derived from San Carlos olivine) after mechanical testing in torsion at temperatures up to 1300°C, while no melt was detected in their fully synthetic samples. Melt did not play a role in our samples, but the suggestion of Faul and Jackson forms support to our inference that solutes/impurities might play a bigger role in controlling the rheology of olivine than hitherto thought.

### 5.4.3 Microstructural evolution

In addition to the questions asked above regarding the effects of Fe and impurities on olivine flow behaviour, this study also aimed to investigate microstructural development up to high strain and to test the hypothesis that grain growth can be enhanced by deformation of synthetic Fe-bearing (fo<sub>90</sub>) olivine aggregates as was observed in fo<sub>100</sub> (chapter 3). An extra component of grain growth during deformation can be expressed as the difference between final grain size after a deformation test,  $d_f$ , and the grain size reached during static (high pressure) heat-treatment,  $d_{stat}$ , at similar experimental duration and  $P$ - $T$  conditions.

Table 5.7 Results of nonlinear regression fitting of relation (4) to the grain growth data.

Temp. [°C]	$d_0$ [ $\mu\text{m}$ ]	$m$	$K_{gg}$ [ $10^{-6} \mu\text{m}^p/\text{s}$ ]	$R^2$
900	0.29	$3.97 \pm 1.36$	$1.26 \pm 0.76$	0.97
	0.29	constrained: $m = 4$	$1.24 \pm 0.12$	0.97
1000	0.51	$2.62 \pm 1.59$	$12.88 \pm 3.81$	0.93
	0.51	constrained: $m = 4$	$14.28 \pm 3.16$	0.91

Table 5.8 Compilation of theoretical values for  $m$  in relation (4.3.2) for the various rate-controlling mechanisms of normal grain growth (from Covey-Crump, 1997).

Mechanism	$m$ [ - ]
Boundary control	
Pure system	2
Impure system	
Coalescence of 2 <sup>nd</sup> phase by lattice diffusion	3
Coalescence of 2 <sup>nd</sup> phase by grain boundary diffusion	4
Pore control	
Surface diffusion around the pore boundary	4
Lattice diffusion through the growing phase	3
Vapour transport across the pore	2-3

#### Calibration of static grain growth law

In order to obtain values for  $d_{stat}$  at experimental durations comparable to  $d_f$ , we make use of a static grain growth law for  $T = 900-1000$  °C, based on the HIP-only tests performed at these temperatures. Non-linear regression of the grain size-time-temperature data has been carried out to find the best fit to a standard grain growth law of the form (after Burke and Turnbull, 1952; and Atkinson, 1988):

$$d^m - d_0^m = K_{gg} \cdot t \quad (4)$$

where  $d$  is the grain size,  $d_0$  is the initial grain size,  $m$  is the grain growth exponent,  $K_{gg}$  is a temperature dependent growth rate constant and  $t$  is time. The temperature dependence of  $K_{gg}$  in (4) can be expressed as:

$$K_{gg} = k_{gg}^0 \exp\left(-\frac{Q_{gg}}{RT}\right) \quad (5)$$

where  $k_{gg}^0$  is a reference growth rate constant,  $Q_{gg}$  is the activation energy for grain growth,  $T$  is the temperature and  $R$  is the gas constant. Fitting all grain growth data (at  $T = 900$ °C and  $1000$ °C to the combination of equations (4) and (5), applying non-linear regression, did not converge to a meaningful answer. This is probably due to the relative small number of data. Fitting the individual datasets for  $T = 900$  and  $1000$ °C to relation resulted in values of  $m = 4.0 \pm 1.4$  and  $2.6 \pm 1.6$ , respectively (Table 5.7). Theoretical values of  $m$  depend on the process controlling the grain growth rate and are integers in the range 2-4 (see Table 5.8 after Covey-Crump, 1997). With  $m = 4$ , grain growth is controlled by coalescence of a second phase by grain boundary diffusion or by surface diffusion around pore boundaries (Covey-Crump, 1997), while for  $m = 3$  lattice diffusion controls grain growth rate if GBM is hindered by the presence of pores or a second phase. The investigated olivine material in this study contains small but significant amounts of both porosity (1-2%) and second phase (5% enstatite). The material as such, thus, does not give conclusive evidence regarding a choice between  $m = 3$  or 4. However, the data for  $900$ °C contain more data points and give a higher  $R^2$ -value, which we use as a rationale to perform additional best-fit analyses focusing on  $m = 4$ . The results are included in Table 5.7, and fig. 5.23 shows how the fits for  $m = 4$  compare to the data. We realize this choice is a bit arbitrary, but the sole purpose of performing the best fit is to

calculate static grain sizes for the conditions and durations applied. Note part of the constrained fit at 900 °C is also included in fig. 5.10a. Using relation (5) and the values of  $K_{gg}$  for  $m = 4$  and  $T = 900$  or  $1000$  °C, values for  $k_{gg}^0$  and  $Q_{gg}$  of  $2.95 \pm 1.45 \cdot 10^{-17} \text{ m}^4/\text{s}$  and  $301 \pm 40 \text{ kJ/mol}$ , respectively, were determined. Compared to published results for  $k_{gg}^0$  (3 to  $3.8$  to  $16 \cdot 10^{-9} \text{ m}^2/\text{s}$  after, respectively, Hirth and Kohlstedt, 1995a; Mei and Kohlstedt, 2000a; and Karato et al., 1989) and  $Q_{gg}$  (190 kJ/mol after Karato, 1989), the values found in our study lead to a significantly lower value for  $K_{gg}$ . This corroborates the suggestion that grain growth experienced significant hindrance due to presence of porosity and (possibly) enstatite as a second phase. Wet olivine samples used in other investigations also contained porosities between 1-2% (Karato et al., 1986; 1989; and Hirth and Kohlstedt, 1995a) and small fractions of enstatite (up to 5 wt%) comparable to this study, but substantial higher temperatures were employed in the experiments. Karato et al. (1989) reported, based on microstructural inspection, a significant fraction of porosity is present within grains (intragranular). This observation combined with a square grain growth law (i.e.  $m = 2$ ), led them to conclude that grain coarsening in their wet grain growth tests at temperatures of 1200 and 1300°C is not controlled by the presence of pores. Since we dominantly observe intergranular porosity, this suggests GBM during experimentation at a lower temperature range (850 –1000 °C) cannot overcome drag forces due to pores and/or enstatite grains resulting in far slower grain growth kinetics. However, we cannot distinguish whether it is the porosity or the enstatite or the combination, which supplies the controlling drag-force.

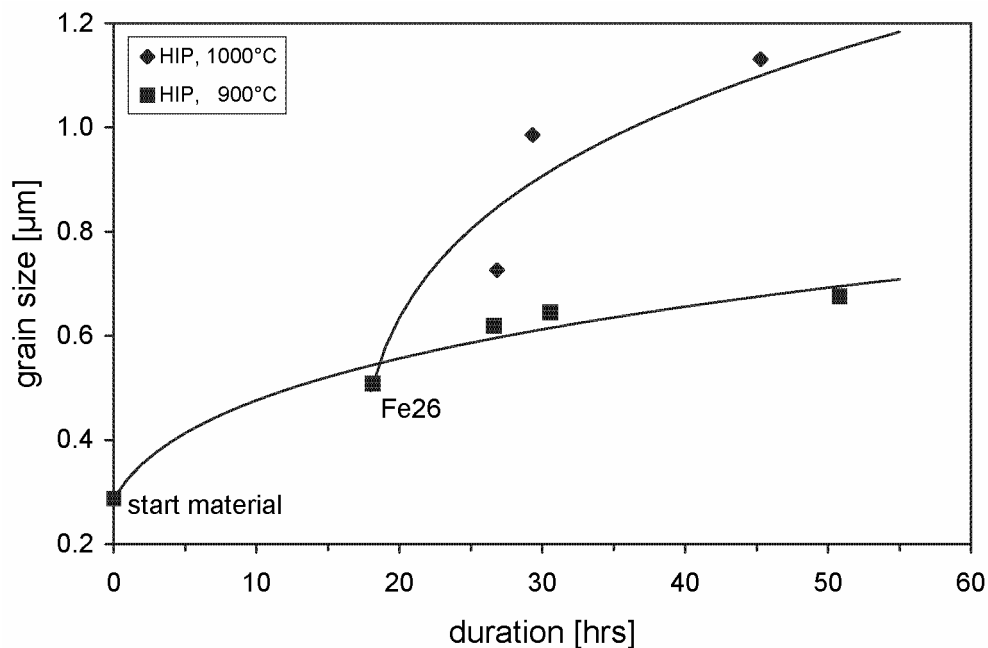


**Figure 5.23.** Grain growth data for static heat treatment tests at 900°C and 1000°C and calibrated fits for  $m = 4$ . Note data point for Fe26 is used both as a starting point in the fit for  $T = 1000$ °C as well as an intermediate point in the fit for  $T = 900$ °C.

#### Dynamic grain growth in fo<sub>90</sub> and comparison to fo<sub>100</sub>

A deformation induced (or dynamic) grain growth rate  $\dot{d}_{dyn}$  normalized with respect to the instantaneous grain size  $d$  can be calculated according to the relation proposed by



Seidensticker and Mayo (1998a) (see also chapter 3):

$$\frac{\dot{d}_{dyn}}{d} \approx \frac{d_f - d_{stat}}{t \cdot d_f} \quad (6)$$

where  $d_f$  is the measured final grain size after a deformation test and  $d_{stat}$  is a calculated static grain size applying the best fit values of Table 5.7 to equation (4) at identical time  $t$ . Using relation (6), we calculated normalized dynamic grain growth rates for all deformation tests at constant strain rate and temperature. Values are listed in Table 5.4 and are plotted versus strain in fig. 5.24. At 900°C, the dynamic grain growth rate appears more or less constant with increasing strain, at strain rate  $1 \cdot 10^{-5}$  and  $3 \cdot 10^{-5} \text{ s}^{-1}$ , but tends to slow down with strain at 1000°C.

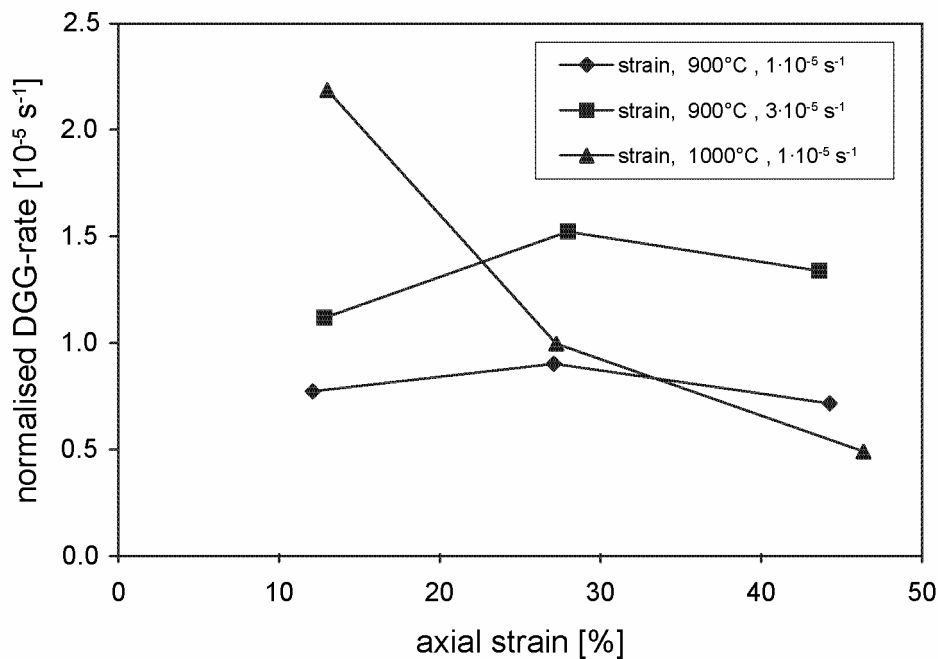


**Figure 5.24.** Normalized dynamic grain growth (DGG) rate versus axial strain for deformation tests at constant strain rate and temperature.

Most models on dynamic grain growth propose that the relation between the dynamic grain growth rate and the strain rate can be described by a general equation (Clark and Alden, 1973; Holm et al., 1977; Wilkinson and Caceres, 1984; Sherwood and Hamilton, 1992; Seidensticker and Mayo, 1998b) of the form:

$$\dot{d}_{dyn} = \lambda \cdot \dot{\epsilon} \cdot d \quad (7a)$$

or

$$\frac{\dot{d}_{dyn}}{d} = \lambda \cdot \dot{\epsilon} \quad (7b)$$

where the rate parameter  $\lambda$  can be a constant or a complex function of time, grain size, strain rate and/or fraction of non-hexagonal grains, depending on the premises of the specific

model. Seidensticker and Mayo (1998a) used relation (7b) to compile the results of a number of studies on dynamic grain growth in metals and ceramics. They found that over a large range in strain rate ( $10^{-8}$  -  $10^1$   $s^{-1}$ ) the data roughly obey the same linear relationship between normalised dynamic grain growth rate and strain rate, i.e.  $\lambda$  is constant with an average value of 0.13 (see also chapters 3 and 4). To compare our data with this finding, we plotted normalized dynamic grain growth rate versus (average) strain rate in fig. 5.25. Data for strain rate *step* tests are also included in the graph, using *single* values for strain rate that were calculated as the average incremental strain rate over all strain rate steps during the respective experiment. Note this average incremental strain rate can only be considered as a first order estimate, since strain rate in these tests varies up to 2 orders of magnitude (see Table 5.3). All data plot between fits to relation (7b) for  $\lambda$  is 0.09 and 2.00. This range in  $\lambda$  is close to the range between 0.04 and 1 and the broadly valid value of 0.13 for  $\lambda$  found by Seidensticker and Mayo (1998a). For comparison, data on synthetic fo<sub>100</sub> (chapter 3) are also included in fig. 5.25. The fo<sub>100</sub> data plot within the range of the new data on fo<sub>90</sub>. The complete data set displays a reasonable spread in strain rates and on average shows an apparent fit to relation (7) at  $\lambda$  of 0.37.

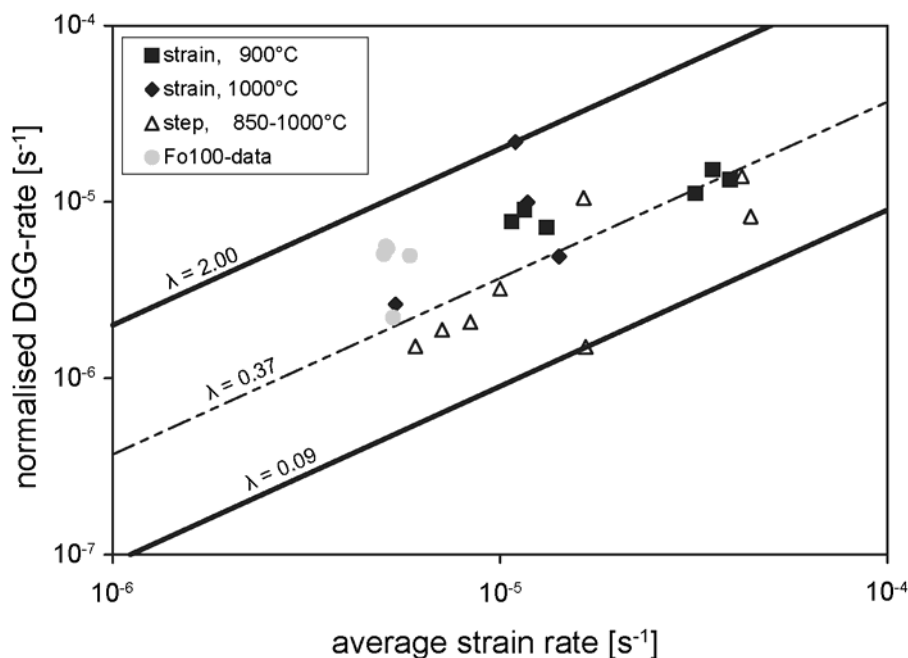


**Figure 5.25.** Normalized dynamic grain growth (DGG) rate versus (average) strain rate for both ‘strain’ and ‘step’ tests. Data on fo<sub>100</sub> are also included for comparison. Lines assuming a linear relationship between DGG-rate and strain rate, that is a constant  $\lambda$  in relation (7), show the average (0.37) and spread (0.09 – 2.00) in  $\lambda$  – values obtained from the fo<sub>90</sub> data.

Normalized- $\dot{d}_{dyn}$  values are found to be comparable between synthetic fo<sub>100</sub> and fo<sub>90</sub>, but the static grain growth behaviour appears to be quite different. Static grain growth in fo<sub>100</sub> was found to be effectively pinned after 15 hrs of heat-treatment at pressure (600 MPa), while grains in the fo<sub>90</sub> material continue to grow after the first 18 hrs of heat-treatment at pressure. It is, thus, possible that addition of Fe to the olivine crystal structure enhances its grain growth kinetics. Note, however, that the growth kinetics of fo<sub>90</sub> might simply appear faster due to the smaller starting grain size ( $\sim 0.3$   $\mu m$ ) of fo<sub>90</sub>, which was about half the starting grain size found for fo<sub>100</sub> ( $\sim 0.6$   $\mu m$ ). Calculating  $K_{gg}$  for  $T = 950^\circ C$  using relation (5) and

using this  $K_{gg}$  together with a starting grain size of 0.6 in relation (4) results in a predicted grain size of  $\sim 0.9 \mu\text{m}$  for fo<sub>90</sub> material after  $\sim 40$  hrs of heat-treatment. This predicted value for fo<sub>90</sub> is close to the experimentally observed values for fo<sub>100</sub>, and thus a true effect of Fe on the grain growth kinetics of synthetic olivine remains unresolved at present.

The observed static grain growth for fo<sub>90</sub> implied that the component of static grain growth could not be neglected in relation (6) for calculating the normalized- $\dot{d}_{dyn}$ , while it was ignored for fo<sub>100</sub>. In relation (6), the normalized- $\dot{d}_{dyn}$  is calculated as an average value by taking the difference between the final grain size and a static grain size over some particular time-interval. Seidensticker and Mayo (1998a) argued that this method of calculating normalized- $\dot{d}_{dyn}$  is actually an approximation, due to the dependency of both static and dynamic grain growth rate on the instantaneous grain size, i.e. the grain size at every instant during its evolution. This prevents an accurate estimation of the true relative contributions of static and dynamic components of grain growth in a single deformation experiment. If the contribution of static grain growth is small or close to zero, the resulting scatter in normalized- $\dot{d}_{dyn}$  will be small, as in case of the fo<sub>100</sub>. At more significant contributions of static grain growth, as for fo<sub>90</sub> material at higher temperature (1000 °C), scatter will be more prominent, as exhibited in fig. 5.25. For fo<sub>90</sub> material, the component of static grain growth during deformation also precludes a description of the final grain sizes as a simple function of strain (as done for fo<sub>100</sub>-material in chapter 3).

#### Evaluation of grain shape

We analyzed changes in grain shape with strain, both in terms of mean value and for individual classes within grain size distributions (see fig. 5.12). The slight increase in aspect ratio (i.e. the ratio of grain length and width, measured perpendicular and parallel to the load direction, see method-section) for samples deformed up to  $\sim 45\%$  might indicate a change in flow behaviour. We investigated this possibility by comparing flow law parameters obtained from data at different strains (compare fits (A), (B), (C) and (D) in Table 5.6). A significant change in flow parameters is observed between data sets with low strain (12-15%) data (fits A & D) and without low strain data (fits B & C). Apparently, some gradual change in mechanism or combination of mechanisms occurs, where both  $Q_c$  and  $p$  reduce to a value of  $\sim 250$  kJ/mol and below a value of 2, respectively. Unfortunately, the strain interval (15-22%) in which this change in parameters occurs does not exactly correspond to the strain interval (30-45%) in which change in aspect ratio appears. Alternative to a change in mechanism causing a change in aspect ratio, one could propose that the combination of a constant strain rate and a decreasing overall grain growth rate (see fig. 5.9 and 5.10) results in the onset of a shape-preferred orientation (SPO) at the highest strains. This very weak SPO at relative high strains (45% shortening) provides, in addition to the obtained flow parameters, further evidence for flow behaviour to be dominated by a GBS mechanism, for which no large grain elongations are expected.

#### Evolution of pore volume and size

The question can be asked if deformation induced changes in pore volume and pore size (expressed by the Zener parameter – relation (1), fig. 5.14) rather than cellular defect fraction affected grain growth during deformation of our fo<sub>90</sub> samples. In microstructures with large volume fractions of pores and small pore sizes (i.e., small  $Z$  values), grain growth can be expected to be hindered by the presence of the pores (Zener drag, e.g., Herwegh and Berger, 2004, Evans et al., 2001). If deformation progressively reduces the total porosity and/or increases the pore size through pore coalescence (i.e.  $Z$  increases), grain growth might be

enhanced compared to the initial stages of the microstructural evolution. This then would be noted as deformation-induced, dynamic grain growth. It is recalled that we, indeed, observed a rather ill defined trend of increasing grain size with increasing  $Z$  for deformed  $fo_{90}$  (fig. 5.14b). Since the porosity volume remained more or less constant in all experiments (see Table 5.2, and section 5.3.1), the higher  $Z$  values imply that the mean pore diameter is larger in samples with larger grain sizes. However, the following three points are to be taken into account: i)  $Z$  does not seem to increase with strain (fig. 5.14a), ii) increasing  $Z$  values in HIP-only samples do not correspond to increasing grain sizes, in contrast to what is observed in deformed samples, and iii) at similar Zener parameter, grain size as measured after deformation tests tends to be larger than grain size resulting from static tests at the same temperature. On the basis of this, we conclude that it is not the porosity structure (Zener parameter) that controlled grain growth in our material. The change in pore structure (notably size) during deformation must be regarded as a by-product of the microstructural modification, rather than a controlling element. Lack of detailed measurements regarding the small fraction of enstatite in the material investigated prevents a Zener parameter analysis to be carried out for this second phase. However, qualitatively comparing the size and distribution of the enstatite grains in  $fo_{90}$  (fig. 5.17) with the microstructural characteristics of the enstatite-bearing material of McDonnell (1997) and McDonnell et al. (2000), little deformation-related change in fraction and grain size of enstatite is to be expected. Note that in this study all samples were prepared with the same 5 vol% of enstatite. In contrast to porosity, this volume percentage is not likely to change due to deformation. If anything, enstatite grains might have become reduced in size (fig. 5.17), lowering the Zener parameter for the second phase. Since enhanced grain growth (higher  $Z$ ) rather than pinning (lower  $Z$ ) was observed, we tentatively conclude that enstatite did not play a role in controlling dynamic grain growth in our synthetic olivine aggregates.

#### The effect of defect fraction

The static heat treatment tests at pressure show defect fraction has a more or less constant value of  $\sim 0.75$  for temperatures at 900 to 1000°C and porosity  $\leq 2\%$ . For higher porosities (starting material, Fe25 and Fe29), higher defect fractions were found, but these lack a systematic relationship with time. The static defect fraction of 0.75 corresponds well to the theoretical value put forward by Hillert (1965). The increase in defect fraction from 0.75 up to 0.87 with strain (see fig. 5.14a) is in correspondence with the data obtained for  $fo_{100}$  (see chapter 3).

Sato et al. (1990) and Sherwood and Hamilton (1992; 1994) present two models for dynamic grain growth that strongly depend on defect fraction. Recall from chapter 3 (and fig. 3.11 therein) that Hillert (1965) inferred climb of a pair of defects in two dimensions (where one grain is 5 and the other is 7-sided) to be the key process for normal grain growth at static conditions, i.e. involving solely surface energy driven GBM. Sato et al. (1990) proposed that deformation by GBS enhances grain switching and accordingly enhances the climb-rate of such defect-pairs. The increased climb-rate results in a higher (deformation-enhanced) grain growth rate that can be expressed in a similar form as relation (7). Based on the deformation enhanced climb mechanism of Sato et al. (1990), Sherwood and Hamilton (1992) proposed the rate parameter  $\lambda$  in (7) can be related to the defect fraction by:

$$\lambda = k \cdot X_d \quad (8)$$

where the scaling constant  $k$  is approximately  $\sim 0.5$ . Substitution of (8) in (7) results in a simple expression in which dynamic grain growth rate is directly proportional to the defect fraction.

In an alternative approach to model dynamic grain growth, Sherwood and Hamilton (1991, 1992) used Hillert's (1965) expression for the grain growth rate, based on the climb process, as a starting point. Hillert (1965) suggested the grain growth rate,  $\dot{d}$ , to be proportional to the defect fraction,  $X_d$ , as in:

$$\dot{d} = \frac{1}{6} \cdot M \cdot X_d \cdot \left( \frac{2\gamma}{d} \right) \quad (9)$$

where  $M$  is the grain boundary mobility,  $\gamma$  is the specific surface energy and  $X_d$  is a constant of value  $0.75 \equiv X_d^0$ . Sherwood and Hamilton (1991; 1992) suggested deformation (by dominant GBS) may lead to production of extra defects such that  $X_d$  becomes  $> 0.75$ . Following (9), a higher defect fraction ( $> 0.75$ ) leads to a higher grain growth rate. They then proposed the component of deformation-enhanced grain growth to be caused by the amount of excess defects or excess defect fraction  $\delta X_d$  on top of  $X_d^0$ , where:

$$\delta X_d \equiv X_d - X_d^0 \quad (10)$$

Substituting  $\delta X_d$  for  $X_d$  in (9) gives an alternative expression for the dynamic grain growth rate (compare with (7)):

$$\dot{d}_{dyn} = \frac{1}{6} \cdot M \cdot \delta X_d \cdot \left( \frac{2\gamma}{d} \right) \quad (11)$$

Note that in contrast to relation (11) the model of Sato et al. (1990) (relations 7 & 8) does not necessarily needs an increase defect fraction for dynamic grain growth to occur. In essence, the model of Sherwood and Hamilton (1991; 1992) assumes dynamic grain growth to result indirectly from an increase in defect fraction due to deformation, while Sato et al. (1990) propose deformation directly increases the rate of defect-pair climb and thus the grain growth rate, without the need of a change in defect fraction.

Before making inferences about whether the model of Sato et al. (1990) or the model of Sherwood and Hamilton (1992; 1994) best applies to our data, we need to discuss in some detail how defect fraction evolves with strain. Moreover, the present data also show an apparent increase in defect fraction with temperature (see fig. 5.14a and c), at similar strains. It thus appears that an increasing temperature speeds up grain neighbor switching events during deformation, such that defect fraction is increased. Temperature, strain rate and time dependence of defect fraction is predicted by the theory of Sherwood and Hamilton (1991; 1992). The theory is based on the idea that an increase in defect fraction results from a change in balance between (grain neighbor) switching that produces defects (non-hexagonal grains) and switching that 'annihilates' defects, i.e. changing grains back to hexagonal grains. The production rate of excess defects (above the steady state fraction,  $X_d^0$ , of  $\sim 0.75$  for normal grain growth) is both strain rate and temperature dependent following an Arrhenius relation. The temperature sensitivity follows from the assumption that energy must be expended to create excess defects, due to the necessary distortion from a perfect hexagonal structure. The annihilation rate of defects increases with the excess defect fraction,  $\delta X_d$ , and the inverse of a characteristic relaxation time,  $\tau$ , of excess defects. Sherwood and Hamilton (1991; 1992) derived the following expression for the variation of total defect fraction with time, under the assumption that  $K_d$  and  $\tau$  are time-independent, given by:

$$X_d = X_d^0 + K_d \cdot \dot{\epsilon} \cdot \tau \cdot (1 - \exp(-t/\tau)) \quad (12a)$$

and,

$$K_d = K_d^0 \cdot \exp(-Q_d / R \cdot T) \quad (12b)$$

where  $t$  is time,  $K_d^0$  is a pre-exponential parameter, and  $Q_d$  is the activation energy for production of defects. Significant uncertainty is contained in values for  $\tau$  and  $K_d^0$  and  $Q_d$ . To date, the only known values for  $\tau$  and  $K_d$  are  $\sim 60$  s, and  $6.8 \cdot 10^{-6}$ , respectively, reported by Sherwood and Hamilton (1994) for Sn-1% Bi material. Also note that if  $t > \tau$ , relation (12) predicts a constant defect fraction with time and strain at constant  $\dot{\epsilon}$  (see fig. 5.14a). Considering only the results of our constant strain rate tests, non-linear fits of the data on defect fraction, strain rate and time to relation (12) resulted in values for  $\tau = 3.30 (\pm 1.1) \cdot 10^4$  s,  $K_d^0 = 1.18 (\pm 2.36) \cdot 10^5$  and  $Q_d = 133 (\pm 20)$  kJ/mol.

Using the best fit values and relations (10) to (12) (model of Sherwood and Hamilton (1991; 1992)) or relations (7), (8) and (12) (model of Sato et al. (1990)), we can now predict the dynamic grain growth rate for olivine at mantle conditions. Note from (12) that the excess defect fraction is linearly proportional to the strain rate. Thus on extrapolation to mantle strain rates, the excess defect fraction will be very small. Taking a strain rate of  $10^{-13}$ , typical for mantle shear zones (Vissers et al., 1995), and a temperature of  $850^\circ\text{C}$ , we obtain for  $\delta X_d$  a value of  $\sim 2.74 \cdot 10^{-10}$ . Thus, the model of Sherwood and Hamilton (1991; 1992) does not predict any significant dynamic grain growth under upper mantle conditions. Completely in contrast to this result, the model of Sato et al. (1990) predicts  $\lambda \sim 0.38$ , at low strain rates, taking  $X_d \sim 0.75$  (see relation (8) with  $k = 1/2$ ). Obviously, our finding that fine grained olivine demonstrates deformation enhanced grain growth may have implications for the grain size evolution in the upper mantle, but more clarity is first needed regarding the details and physical processes of evolution of defect fraction with time at various conditions. As yet, we cannot favour one of the models treated above, i.e. Sato et al. (1990) versus Sherwood and Hamilton (1991;1992).

#### 5.4.4 Geodynamic implications

Temperature in the upper mantle may vary from  $\sim 800$  up to  $1300^\circ\text{C}$ , and grain sizes may vary from as low as submicron up to tens of mm (after Karato and Wu, 1993; Vissers et al., 1995; Evans et al., 2001). A dominant component of GSS diffusion creep in the upper mantle is expected in relative cold and shallow regions (Karato and Wu, 1993) and/or in zones where grain size is relatively small, i.e. submicron to several tens of microns. Also the presence of a significant amount of water may expand the conditions under which diffusion creep dominates (Karato and Wu, 1993). The new flow law for GSS creep of wet synthetic polycrystalline fo<sub>90</sub> olivine presented in this study predicts higher strengths for upper mantle rheology than estimated for wet natural or synthetic-natural fo<sub>90</sub> olivine. Two possible explanations for this difference in flow behaviour are 1) a change in character of the GSS creep mechanism controlling deformation going from relatively high temperature and large grain size to lower temperature and smaller grain size and 2) a difference in chemistry between the synthetic fo<sub>90</sub> material used in this study and the natural and synthetic natural fo<sub>90</sub> used in other studies. Regarding the first explanation, as discussed in section 5.4.1, a change might occur from near pure Coble-type diffusion creep at relatively high temperature ( $1100$ - $1300^\circ\text{C}$ ) and not too small grain size ( $\sim 10 \mu\text{m}$ ) to more dominant grain boundary

sliding (GBS) creep accommodated by diffusion or dislocation mechanisms at lower temperature (850-1000°C) and finer grain sizes (>0.5-1.5 μm). If so, fine-grained shear zones in the shallow upper mantle will be stronger than predicted by the widely used wet diffusion flow law of Karato et al. (1986). This would imply orders of magnitude slower tectonic rates (or higher stresses) if lithospheric extension or compression is governed by such fine grained upper mantle shear zones, as suggested by Vissers et al. (1995). Regarding the second explanation, it could be that the flow behaviour of natural and synthetic-natural material experiences significant weakening effects due to a chemistry which deviates from the pure (Mg<sub>0.9</sub>Fe<sub>0.1</sub>)<sub>2</sub>SiO<sub>4</sub>. Higher amounts of impurities like Ca, Al and Mn might have significant effect on the materials point defect chemistry and diffusivity of relevant species. This difference in chemistry may also cause lower melting temperatures, suggesting (after Faul and Jackson, 2004) the possibility of small amounts of melt in ‘natural-synthetic’ and natural material, reported previously to be nominally melt-free (Hirth and Kohlstedt, 1995a; Mei and Kohlstedt, 2000a). To our knowledge, it is unknown whether or not the impurity/solute content of generally used olivine sources, like San Carlos and Anita Bay dunite, is representative for average abundances in the upper mantle. To this regard, it is not obvious to us whether flow behaviour of natural and synthetic-natural samples would be more representative for the upper mantle than synthetic samples.

The dynamic grain growth observed in the present study shows that grain growth may continue under conditions where static grain growth is retarded (or fully pinned) due to presence of a second phase (or porosity), especially when high strains are involved, as, for example, in large scale upper mantle shear zones. At present, the evolution of olivine grain size as a function of strain cannot yet be included in large-scale geodynamic models in a straightforward way, since the contribution of the non-deformation related (i.e. static) grain growth component is not easily quantified. Nevertheless, one can explore conditions under the assumption that static grain growth is negligible. We then suggest to use the relation for grain size as a function of strain from chapter 3 and substitute the value for λ obtained for fo<sub>90</sub> (i.e. 0.37), which then predicts that grain size can be doubled during ongoing straining within a few million years, assuming a starting grain size of 1 μm.

The contributions of both static and dynamic grain growth can be combined if in an iterative approach, applying small time/strain steps. In such an approach, for each subsequent time step the new calculated grain size is the sum of the previous grain size and the contributions of static and dynamic grain growth. Both contributions are dependent on the previous grain size and are calculated over the small time interval. Thus, the applied time step needs to be small enough, such that the dependency of both static and dynamic grain size on the *instantaneous* grain size is realistically approached. The component of static grain growth can be calculated as the product of the time step size with the growth rate,  $\dot{d}_{static}$ , given by the derivative of the instantaneous grain size,  $d$ , with respect to time,  $t$ , (recall relation (4)):

$$\frac{dd}{dt} = \dot{d}_{static} = \frac{K_{gg}}{m \cdot d^{m-1}} \quad (13)$$

where symbols have similar meaning as in relation (4). Similarly, the component of dynamic grain growth can be included through the product of time step size and dynamic grain growth rate,  $\dot{d}_{dyn}$ , given by relation (7a). Here, again the value for λ of 0.37 calibrated in this study for fo<sub>90</sub> can be used. We propose to include the above approach in geodynamic modeling studies which aim to study localization of deformation in weak fine-grained shear zones. This would allow investigation of the effect of microstructural evolution and a component of deformation induced grain growth on the rheology and lifetime of such shear zones.

## 5.5 Conclusions

We performed heat treatment and uniaxial compression tests at high temperature (850-1000°C) and pressure (600 MPa) on synthetic Fe-bearing olivine ( $fo_{90}$ ) plus 5 vol.% enstatite ( $en_{90}$ ) in the presence of 0.3 wt% H<sub>2</sub>O in order 1) to investigate the effect of Fe on olivine rheology at conditions favoring GSS diffusion creep by comparison with previous data on similarly prepared Fe-free ( $fo_{100}$ ) olivine and 2) to test the hypothesis that deformation affects microstructural evolution in the GSS creep field and enhances grain growth of olivine ( $fo_{90}$ ) similar as for forsterite ( $fo_{100}$ ). We conclude the following:

1. We've experimentally calibrated a standard (Dorn-type) power law for the flow behaviour of material investigated ( $fo_{90}$ ) giving, for the range of conditions applied, a stress exponent  $n = 2.13 \pm 0.34$ , a grain size exponent  $p = 2.49 \pm 0.34$ , a pre-exponential constant  $\text{Log}A_o = 2.99 \pm 0.34$  (MPa<sup>-n</sup> s<sup>-1</sup> μm<sup>p</sup>) and an activation energy  $Q_c = 270 \pm 50$  (kJ/mol).
2. Compared to  $fo_{100}$ , adding Fe to wet synthetic olivine material ( $fo_{90}$ ) has no significant effect on its rheology, at the conditions investigated.
3. The strength of wet synthetic fine grained  $fo_{90}$  (and  $fo_{100}$ ) is higher than that of previously studied wet natural or synthetic-natural fine grained olivine aggregates if compared, by extrapolation, at similar experimental conditions. A change in deformation mechanism upon extrapolation, or the dissimilarity in impurity/solute concentrations and possible presence of melt, might form the reason for this difference in strength rather than Fe-content.
4. We observed minor static grain growth during heat treatment at pressure, indicating the normal grain growth is substantially retarded in the material due to presence of porosity and/or enstatite as second phase.
5. We found that an extra component of grain growth occurred during deformation (i.e. a dynamic grain growth component) when compared to static grain growth behaviour. The calculated dynamic grain growth rate corresponds well to data on  $fo_{100}$  (chapter 3) and metals and ceramics.
6. The observed dynamic grain growth can be related to an increase in fraction of non-hexagonal grains ('cellular defect' fraction) in 2-D microstructures with strain and temperature. These observations corroborate theoretical predictions of defect fraction increase with both strain and temperature. Theory on dynamic grain growth assumes the dynamic grain growth rate to be related to the strain rate by the parameter  $\lambda$ , which in this study was found to be  $\sim 0.37$ . This value can be used, with the appropriate grain growth equation, to build in dynamic grain growth in geodynamic models that rely on meaningful descriptions of the rheology of olivine.



## Chapter 6

### Conclusions and suggestions for further research

#### 6.1 General conclusions

In this study, transient flow behaviour and microstructural evolution towards steady state has been investigated, with emphasis on the effects of dynamic recrystallization and grain growth in olivine aggregates. Theoretical modeling as well as experimental techniques were employed to achieve the aims set in the introduction of this thesis. The general conclusions are:

*On microphysical modeling of dynamic recrystallization:*

1. A microphysical model for dynamic recrystallization has been developed employed in a numerical scheme. The model provides a description of the evolution of bulk flow stress and discrete grain size distributions (GBS's) during straining towards a steady state with fully recrystallized microstructure. Deformation involves both grain size sensitive (GSS) diffusion and grain size insensitive (GSI) dislocation creep. Recrystallization processes involve new grain nucleation by subgrain rotation as well as grain boundary migration (GBM) driven by gradients in surface, dislocation and/or elastically stored energy.
2. The model has been applied to olivine, using appropriate values for the various parameters involved. In static surface energy driven GBM tests, the model predicts normal grain growth kinetics that are in good agreement with theoretical predictions and existing experimental results on olivine material. Dynamic recrystallization tests starting in either the GSS creep field or the GSI creep field, showed the development of bimodal or multimodal grain size distributions, respectively. Overall, the GSD tends to migrate towards larger grain sizes when starting in the GSS creep field and tends to migrate towards smaller grain sizes when starting in the GSI creep field.
3. Models results show that evolving grain size distributions reach steady state when mean values fit the well-known inverse relationship between subgrain size and flow stress. This strong attraction towards the subgrain size - flow stress relation therefore plays a crucial role in positioning the recrystallized grain size - stress relationship in a deformation mechanism map, which, on the basis of experiments, is generally found to lie at higher stresses / larger grain sizes than the relation between subgrain size and flow stress.

*On microstructural evolution of  $f_{0100}$  aggregates during GSS creep:*

4. Static heat treatment and deformation experiments on synthetic fine-grained ( $\sim 1 \mu\text{m}$ ) wet aggregates of  $f_{0100} + 10 \text{ vol\% } e_{100}$  were performed at high pressure (600 MPa) and temperature (950°C) to axial shortening strains of  $\sim 15, 30$  and  $45\%$ . Analysis of the grain size distributions showed that only minor static grain growth occurs during an initial stage of heat treatment during 10 hrs. Beyond this, growth more or less ceases, probably due to Zener-pinning by remaining porosity and the presence of the enstatite phase. However,

during deformation following initial heat treatment, grain growth does occur, and accordingly is strain dependent rather than time dependent. The process, thus, can be characterized as dynamic (or deformation enhanced) grain growth.

5. It was found that the defect fraction, i.e. the fraction of non-hexagonal grains in 2-D section, increases during deformation tests (up to 0.84), while remaining more or less constant during static grain growth tests (at  $\sim 0.78$ ). It is therefore inferred that the observed dynamic grain growth of fo<sub>100</sub> aggregates is related to changes in topological properties, induced by (grain boundary sliding-controlled) GSS deformation.

*On 2-D modeling of deformation enhanced grain growth:*

6. Using simple 2-D microstructural modeling of grain growth during deformation, a component of grain growth was produced not seen under static conditions. This (component of) dynamic grain growth correlates well with a systematic increase in defect fraction,  $X_d$ . Starting with a value of 0.71, the defect fraction gradually increases with strain, approaching a constant level around 0.80 at shear strains above  $\sim 1.4$ . These results are in broad agreement with the findings on fo<sub>100</sub> (points 4-5 above) and confirm the suggestion that deformation-induced changes in topological properties (i.e., defect fraction) can result in dynamic grain growth.
7. At relatively low strain rates, dynamic grain growth rate is faster if straining is simulated by inhomogeneous GSS creep rather than by simple homogeneous deformation. At intermediate strain rates, a good correlation was found between the modeled dynamic grain growth rate ( $\dot{d}_{dyn}$ ) versus strain rate ( $\dot{\epsilon}$ ) data and already published results from models and experiments on dynamic grain growth in a range of materials, following the relationship  $\dot{d}_{dyn} = \lambda \cdot d \cdot \dot{\epsilon}$ , where  $d$  is the grain size and  $\lambda$  is a rate parameter that is strongly related to the defect fraction. A constant defect fraction ( $X_d \sim 0.8$ ) was observed at intermediate strain rates, providing preliminary constraints on the values of the rate parameter  $\lambda$  in the above  $\dot{d}_{dyn} - \dot{\epsilon}$  relationship. These constraints are of importance if dynamic grain growth is to be included in models of microstructural evolution in relation to rheology.
8. Analysis of defect fraction,  $X_d$ , appears to be a good microstructural tool for establishing whether or not a material has experienced normal static ( $X_d \sim 0.7$ ) or dynamic ( $X_d \sim 0.8$ ) grain growth.

*On the GSS flow behaviour of wet fo<sub>90</sub> aggregates:*

9. Deformation experiments on synthetic fine-grained ( $\sim 1 \mu\text{m}$ ) wet Fe-bearing aggregates of fo<sub>90</sub> + 5 vol% en<sub>90</sub> have been performed at strain rates  $3 \cdot 10^{-7}$  to  $1 \cdot 10^{-4}$  1/s, a confining pressure of 600 MPa, and temperatures ranging 850-1000°C. Experiments were stopped at systematically varied strains. A flow law was calibrated with stress exponent  $n = 2.1$ , a grain size exponent  $p = 2.5$ , a pre-exponential constant  $\text{Log}A_o = 3.0$  ( $\text{MPa}^{-n} \text{s}^{-1} \mu\text{m}^p$ ) and an apparent activation energy  $Q_c = 270$  (kJ/mol). Comparison with a previous study on flow behaviour of similar, yet Fe-free fo<sub>100</sub> material, shows that adding Fe to wet synthetic olivine material has no significant effect on its rheology, at least not at the conditions investigated.

10. The strength of wet synthetic fine grained  $fo_{90}$  (and  $fo_{100}$ ) polycrystalline material is higher than that of previously studied natural and synthetic-natural fine grained wet olivine aggregates if compared, by extrapolation, at similar experimental conditions. A change in deformation mechanism upon extrapolation, or the dissimilarity in impurity/solute concentration or possible presence of melt (at temperatures well over 1000 °C) might explain this difference in strength, rather than Fe-content.

*On microstructural evolution of  $fo_{90}$  aggregates at static conditions and during GSS creep:*

11. Static heat treatment tests at pressure on similar  $fo_{90}$  material as used for the deformation experiments, at 850-1000°C, showed minor grain growth, suggesting normal grain growth was substantially retarded due to presence of porosity and/or enstatite as second phase.
12. An extra component of grain growth occurred during deformation (i.e. a dynamic grain growth) when compared to static grain growth behaviour. The calculated dynamic grain growth rate corresponds well to the data on  $fo_{100}$  and data on metals and ceramics, with an average value for  $\lambda \sim 0.37$  (see point 7 above). The observed dynamic grain growth can be related to an increase in fraction of non-hexagonal grains ('cellular defect' fraction) in 2-D microstructures with strain and temperature. These observations corroborate theoretical predictions of defect fraction increase with both strain and temperature. Theory on dynamic grain growth assumes the dynamic grain growth rate to be related to the strain rate by the parameter  $\lambda$ , which in this study was found to be  $\sim 0.37$ . This value can be used in future numerical modeling of mantle flow including transient behaviour of olivine.

## **6.2 Suggestions for further research**

*On microphysical modeling of dynamic recrystallization:*

1. Considering olivine material, values used for several parameters in the theoretical, microphysical model appear to be poorly constrained at present. These are: 1) the constant  $K$  and the stress exponent  $p$ , in the inverse relationship between subgrain size and flow stress, 2) the critical misorientation,  $\theta_c$ , for a subgrain boundary to become a high angle grain boundary, 3) the fraction of excess dislocations  $f$  contributing to progressive subgrain misorientation, and 4) the grain boundary mobility  $M$ . Improved experimental calibration or theoretical evaluation of these parameters is crucial for the models' prediction on where the recrystallized grain size – stress relation might reside relative to the boundary between the GSS and GSI creep fields.
2. In the microphysical model, evolving transient GSD's occasionally reach steady state in a single grain size interval of the distribution. In order to prevent this happening, an improved method for calculating subgrain energy driven GBM is needed. Here, one could think of specific topological constraints that take into account the multi-modal character ('core-mantle' microstructures) of the transient grain size distribution. For example the simulation of GBM could be further improved when a relation between the grain size relative to a local nearest mean and a migration rate factor associated with the grain coordination number is included.

3. Evolution of GSD's approaching steady state starting in the GSS creep field appears far less complex than when starting in the GSI creep field. Moreover, steady state is reached at relatively low strain as long as grain growth is sufficiently rapid. This suggests that calibration of a recrystallized grain size-stress relation through performing experiments that start in the GSS creep field is technically less complex (employing relatively low strains) and may produce data less biased towards larger grain sizes for the slowest strain rates stresses. In case of olivine, previous calibration of the recrystallized grain size-stress relationship was based on experimental results of GSI-deformed samples (Van de Wal et al., 1993); our model results demonstrate that it is unlikely that microstructural steady state was reached. This puts doubt on the applicability of the relationship. It is proposed to recalibrate the recrystallized grain size-stress relationship for olivine, using fine-grained material that starts deforming in the GSS creep field and is free to grow.

*On microstructural evolution during creep of  $f_{0100}$  aggregates:*

4. In line with the above suggestion for calibrating a recrystallized grain size-stress relation through experiments starting deformation in the GSS creep field, future experiments on fine-grained  $f_{0100}$  aggregates should focus on enhancing grain growth kinetics either by applying higher temperatures, i.e.  $> 1000^{\circ}\text{C}$ , or through further reduction of the pinning effects of secondary phases (porosity and enstatite).
5. In those cases that secondary phases appear to play an important role in pinning grain growth, better constraints are needed on the individual role of porosity and enstatite. It is suggested to specifically explore possible changes in defect fraction with strain, since the results presented in this thesis have shown that this parameter is a potentially useful tool in the analysis of grain growth in relation to pinning. Since no real steady state was reached even in the experiments to shortening strains of 45%, this requires experiments to still higher strains, using torsion, saw-cut or direct-shear deformation set-ups.

*On 2-D microstructural modeling of deformation enhanced grain growth:*

6. The grain boundary migration and deformation algorithms used for the 2-D modeling (ELLE) need to be adjusted in order to incorporate Zener-pinning during simulations. Developments in the near future should allow to model non-uniform Zener-drag by introducing an unconnected distribution of discrete second phase grains into the microstructure. Such Zener-pinning is anticipated to produce a significant larger component of dynamic grain growth in simulations than presently observed and will more realistically approach the deformation enhanced grain growth observed in  $f_{0100}$  aggregates. In addition such modeling of non-uniform Zener-drag will provide a direct comparison to the uniform Zener-drag effects investigated by Bate (2001).
7. Also, it is proposed to enforce progress in the (ELLE) simulation of grain size sensitive diffusion creep that accounts for a component of grain boundary sliding (GBS) and associated grain rotation. This will significantly improve realistic modeling of deformation enhanced grain growth related to topological changes. GBS and grain rotation during deformation are expected to increase the rate of grain switching and therefore may further increase the average defect fraction, enhancing grain growth.
8. Tentatively, it is suggested to explore the possibility to integrate (elements of) the theoretical model of dynamic recrystallization of Chapter 2 with the ELLE 2D-

microstructural modeling package (as used in Chapter 4), in order to bring together new insights in the microphysics of microstructure evolution and the spatial distribution of recrystallization processes and grain growth in a deforming aggregate with distributed grain size.

*On rheology and microstructural and mechanical evolution of fo<sub>90</sub> aggregates during wet GSS or GSI creep:*

9. New experimental data on the GSS flow behaviour of wet synthetic fo<sub>90</sub> aggregates as prepared in this study need to be obtained at the temperature - pressure conditions and grain sizes previously applied by Mei and Kohlstedt (2000a), in order to arrive at a comparison between GSS creep behaviour of wet synthetic-natural fo<sub>90</sub> and wet synthetic 'sol-gel' fo<sub>90</sub> material that is no dependent on extrapolation of data. Moreover, it is suggested to particularly focus in future experimental studies on a systematic investigation of the effects of varying impurity/solute chemistry on rheology and melt-behaviour (see also suggestion 5 above) and assessment of the amount of variation in impurity/solute content in mantle-derived natural olivine material.
10. The experiments on Fe-bearing olivine were confined to samples of only one concentration of Fe, i.e. fo<sub>90</sub>. Though fo<sub>90</sub> appears to have a strength that is similar to that of pure forsterite, implying the effect of Fe (if any) is very small, definite conclusions regarding olivine in the mantle should be based on application of a wider range of Fe-contents. The method for fabrication of synthetic Fe-bearing olivine ceramic, as applied in this research, allows to perform future deformation experiments on samples in which the Fe-concentration is systematically varied within a range that is relevant to the olivine rocks of the mantle.
11. As a final suggestion for future research, it is proposed to evaluate the role of dynamic grain growth in upper mantle flow by building in dynamic grain growth in numerical (geodynamic) models, making use of the relationship between dynamic grain growth rate and strain rate established in the present study.



## References

- Anderson, K.G.B., Scherrer, S. and Weber, S., 1989. Self-diffusion in Mg<sub>2</sub>SiO<sub>4</sub> (forsterite) at high temperature - A model case study for SIMS analyses on ceramic surfaces. *Fresenius Z. Anal. Chem.*, 333: 385-385.
- Anderson, M.P., 1988. Simulation of grain growth in two and three dimensions. In: Hansen, N., Jensen, D.J., Leffers, T., Ralph, B. (Eds.), *Annealing processes-recovery, recrystallization and grain growth. Proc. 7th int. Symp. on Metallurgy and Materials Science*, pp. 15-34.
- Ando, K., Kurokawa, H. and Oishi, Y., 1981. Self-diffusion coefficient of oxygen in single-crystal forsterite. *Communications of American Ceramic Society*, C-30.
- Ashby, M.F. and Verrall, R.A., 1973. Diffusion-accommodated flow and superplasticity. *Acta Metallurgica*, 21(2): 149-163.
- Atkinson, H.V., 1988. Theories of normal grain growth in pure single phase systems. *Acta Metallurgica*, 36(3): 469-491.
- Avé Lallement, H.G., 1985. Subgrain rotation and dynamic recrystallization of olivine, upper mantle diapirism, and extension of the Basin-and-range Province. *Tectonophysics*, 119: 89 - 117.
- Bakker, R., 2003. Package FLUIDS 1. Computer programs for analysis of fluid inclusion data and for modelling bulk fluid properties. *Chemical Geology*, 194: 3-23.
- Barnhoorn, A., Bystricky, M., Burlini, L. and Kunze, K., 2004. The role of recrystallisation on the deformation behaviour of calcite rocks: large strain torsion experiments on Carrara marble. *Journal of Structural Geology*, 26(5): 885-903.
- Barr, T.D., Houseman, G.A., 1992. Distribution of deformation around a fault in a non-linear ductile medium. *Geophysical Research Letters* 19 (11), 1145-1148.
- Barr, T.D., Houseman, G.A., 1996. Deformation fields around a fault embedded in a non-linear ductile medium. *Geophysical Journal International* 125, 473-490.
- Bate, P., 2001. The effect of deformation on grain growth in Zener pinned systems. *Acta Materialia*, 49 (8), 1453-1461.
- Beeman, M.L. and Kohlstedt, D.L., 1993. Deformation of fine-grained aggregates of olivine plus melt at high temperatures and pressures. *Journal of Geophysical Research*, 98: 6443-6452.
- Bergmann, R.B., Shi, F.G., Queisser, H.J., Krinke, J., 1998. Formation of polycrystalline silicon with log-normal grain size distribution. *Applied Surface Science* 123-124, 376-380.
- Bird, P. and Piper, K., 1980. Plane-stress finite-element models of tectonic flow in southern California. *Physics of The Earth and Planetary Interiors*, 21(2-3): 158-175.
- Blum, W., 1982. On modelling steady state and transient deformation at elevated temperature. *Scripta Metallurgica*, 16(12): 1353-1357.
- Bons, P., Urai, J.L., 1992. Syndeformational grain growth: microstructures and kinetics. *Journal of Structural Geology* 14 (8/9), 1101-1109.
- Bons, P.D., 1993. Experimental deformation of polyphase rock analogues. *Geologica Ultraiectina* 110 (Ph.D. Thesis, Utrecht University), Utrecht, 207 pp.
- Bons, P.D., Barr, T.D., ten Brink, C.E., 1997. The development of d-clasts in non-linear viscous materials: numerical approach. *Tectonophysics* 270, 29-41.
- Braithwaite, J.S., Sushko, P.V., Wright, K. and Catlow, C.R.A., 2002. Hydrogen defects in forsterite; A test case for the embedded cluster method. *Journal of Chemical Physics*, 116(6): 2628-2635.
- Braun, J., Chéry, J., Poliakov, A., Mainprice, D., Vauchez, A., Tomassi, A. and Daignières, M., 1999. A simple parameterization of strain localization in the ductile regime due to grain size reduction: A case study for olivine. *Journal of Geophysical Research*, 104(B11): 25167-25181.
- Brodie, K.H. and Rutter, E.H., 2000. Deformation mechanisms and rheology: why marble is weaker than quartzite. *Journal of the Geological Society of London*, 157(6): 1093-1096.
- Burke, J.E. and Turnbull, D., 1952. Recrystallization and grain growth in metals. *Progress in Metal Physics*, 3: 220-292.
- Burton, B., 1972. Interface Reaction-Controlled Diffusional-Creep--A Consideration of Grain-Boundary Dislocation-Climb Sources. *Materials Science and Engineering*, 10(1): 9-14.
- Busch, J.P. and van der Pluijm, B.A., 1995. Calcite textures, microstructures and rheological properties of marble mylonites in the Bancroft shear zone, Ontario, Canada. *Journal of Structural Geology*, 17(5): 677-688.
- Bystricky, M., Kunze, K., Burlini, L. and Burg, J.-P., 2000. High Shear Strain of Olivine Aggregates: Rheological and Seismic Consequences. *Science*, 290(5496): 1564-1567.
- Cahn, R.W., and G.E. Padawar, On Hillert's grain growth catalyst, *Acta Metallurgica*, 13, 1091-1092, 1965.
- Casey, M. and Williams, D., 2000. Micromechanical Control of Rheological Anisotropy in Quartz Mylonite. *Physics and Chemistry of the Earth, Part A: Solid Earth and Geodesy*, 25(2): 127-132.
- Chopra, P., 1986. The plasticity of some fine-grained aggregates of olivine at high pressure and temperature., in: *Mineral and rock deformation; laboratory studies; the Paterson volume.*, edited

## References

- by H.C. Heard, pp. 25-33, AGU. Washington, DC, United States.
- Chopra, P.N. and Paterson, M.S., 1981. The experimental deformation of dunite. *Tectonophysics*, 78: 453-473.
- Chopra, P.N. and Paterson, M.S., 1984. The role of water in the deformation of dunite. *Journal of Geophysical Research*, 89 B9: 7861 - 7876.
- Clark, M.A. and Alden, T.H., 1973. Deformation enhanced grain growth in a superplastic Sn-1% Bi alloy. *Acta Metallurgica*, 21(9): 1195-1206.
- Coble, R.L., 1963. A model for boundary diffusion controlled creep in polycrystalline materials. *Journal of Applied Physics*, 34: 1679-1682.
- Covey-Crump, S.J., 1997. The normal grain growth behaviour of nominally pure calcitic aggregates. *Contributions to Mineralogy and Petrology*, 129(2 - 3): 239-254.
- Crossman, F.W. and Ashby, M.F., 1975. The non-uniform flow of polycrystals by grain-boundary sliding accommodated by power-law creep. *Acta Metallurgica*, 23(4): 425-440.
- De Bresser, J.H.P., Peach, C.J., Reijs, J.P.J. and Spiers, C.J., 1998. On dynamic recrystallization during solid state flow: Effects of stress and temperature. *Geophysical Research Letters*, 25: 3457-3460.
- De Bresser, J.H.P., Ter Heege, J.H. and Spiers, C.J., 2001. Grain size reduction by dynamic recrystallization: Can it result in major rheological weakening? *International Journal of Earth Sciences*, 90: 28-45.
- de Kloe, R., 2001. Deformation mechanisms and melt nano-structures in experimentally deformed olivine-orthopyroxene rocks with low melt fractions. PhD Thesis, Utrecht University, Utrecht, 173 pp.
- de Kloe, R., Drury, M.R., Vissers, R.L.M., Newman, J. and Roermund, H.L.M., 2000. Evidence for stable grain boundary melt films in experimentally deformed olivine-orthopyroxene rocks. *Physics and Chemistry of Minerals*, 27: 480-494.
- Derby, B. and Ashby, M.F., 1987. On dynamic recrystallization. *Scripta Metallurgica*, 21: 879-884.
- Derby, B., 1990. Dynamic recrystallization and grain size. In: D.J. Barber and P.D. Meridith (Editors), *Deformation processes in minerals, ceramics and rocks*. Unwin-Hyman, London, pp. 354-364.
- Dijkstra, A.H., 2001. Deformation and melt in natural mantle rocks: The Hilti Massif (Oman) and the Othris Massif (Greece). Ph.D. Thesis, Utrecht University, Utrecht, 164 pp.
- Dijkstra, A.H., Drury, M.R. and Frijhoff, R.M., 2002. Microstructures and lattice fabrics in the Hilti mantle section (Oman Ophiolite); evidence for shear localization and melt weakening in the crust-mantle transition zone? *Journal of Geophysical Research*, 107(B11): 2270, doi:10.1029/2001JB000458.
- Ding, R. and Guo, Z.X., 2001. Coupled quantitative simulation of microstructural evolution and plastic flow during dynamic recrystallization. *Acta Materialia*, 49(16): 3163-3175.
- Drury, M.R. and Fitz Gerald, J., 1996. Grain boundary melt films in an experimentally deformed olivine-orthopyroxene rock: implications for melt distribution in upper mantle rocks. *Geophysical Research Letters*, 23: 701 - 704.
- Drury, M.R. and Fitz Gerald, J., 1998. Mantle rheology: insights from laboratory studies of deformation and phase transition. In: I. Jackson (Editor), *The Earth's Mantle*. Cambridge University press, Cambridge, pp. 503-559.
- Drury, M.R. and Urai, J.L., 1990. Deformation-related recrystallization processes. *Tectonophysics*, 172(3-4): 235-253.
- Drury, M.R., 2005. Dynamic recrystallization and strain softening of olivine aggregates in the laboratory and the lithosphere. *Geological Society, London, Special Publications*, 243: 143-158.
- Drury, M.R., Dynamic recrystallization and strain softening of olivine aggregates in the laboratory and the lithosphere. *Geological Society Special Publications*, 243, 143-158, 2005.
- Drury, M.R., Humphreys, F.J. and White, S.H., 1985. Large strain deformation studies using polycrystalline magnesium as a rock analogue. Part II: dynamic recrystallisation mechanisms at high temperatures. *Physics of The Earth and Planetary Interiors*, 40(3): 208-222.
- Drury, M.R., Vissers, R.L.M., Van der Wal, D. and Hogerduijn Strating, E.H., 1991. Shear localization in upper mantle peridotites. *Pure Applied Geophysics*, 137: 439-460.
- Duyster, J. and Stöckhert, B., 2001. Grain boundary energies in olivine derived from natural microstructures. *Contributions to Mineralogy and Petrology*, 140(5): 567-576.
- Edward, G.H., Etheridge, M.A. and Hobbs, B.E., 1982. On the stress dependence of subgrain size. *Textures and Microstructures*, 5: 127-152.
- Evans, B., Renner, J. and Hirth, G., 2001. A few remarks on the kinetics of static grain growth in rocks. *International Journal of Earth Sciences*, 90: 88-103.
- Farver, J.R. and Yund, R.A., 2000. Silicon diffusion in forsterite aggregates; implications for diffusion accommodated creep. *Geophysical Research Letters*, 27: 2337- 2340.
- Farver, J.R., Yund, R.A. and Rubie, D.C., 1994. Magnesium grain boundary diffusion in forsterite aggregates at 1000°–1300°C and 0.1 MPa to 10 GPa. *Journal of Geophysical Research*, 99(B10): 19809-19819.



- Faul, U.H. and Jackson, I., 2004. The rheology of dry, melt-free polycrystalline Fo90 olivine. *EOS Transactions of the American Geophysical Union*, 85(47): Fall Meet. Suppl., Abstract MR24A-02.
- Fayad, W., Thompson, C.V., Frost, H.J., 1999. Steady-state grain-size distributions resulting from grain growth in two dimensions. *Scripta Materialia* 40 (10), 1199-1204.
- Fisler, D. and Mackwell, S., 1994. Kinetics of diffusion-controlled growth of fayalite. *Physics and Chemistry of Minerals*, 21(3): 156-165.
- Flack, C.A., Klemperer, S.L., McGearry, S.E., Snyder, D.B. and Warner, M.R., 1990. Reflections from mantle fault zones around the British Isles. *Geology (Boulder)*, 18(6): 528-532.
- Ford, J.M., Wheeler, J. and Movchan, A.B., 2002. Computer simulation of grain-boundary diffusion creep. *Acta Materialia*, 50(15): 3941-3955.
- Forsyth, D.W., 1975. The early structural evolution and anisotropy of the oceanic upper mantle. *The Geophysical Journal of the Royal Astronomical Society*, 43(1): 103-162.
- Frederiksen, S. and Braun, J., 2001. Numerical modelling of strain localisation during extension of the continental lithosphere. *Earth and Planetary Science Letters*, 188(1-2): 241-251.
- Freeman, B. and Ferguson, C.C., 1986. Deformation mechanism maps and micromechanics of rocks with distributed grain sizes. *Journal of Geophysical Research*, 91(B3): 3849-3860.
- Furlong, K.P., 1993. Thermal-rheologic evolution of the upper mantle and the development of the San Andreas fault system. *Tectonophysics*, 223: 149-164.
- Gaetani, G.A. and Watson, E.B., 2000. Open system behavior of olivine-hosted melt inclusions. *Earth and Planetary Science Letters*, 183(1-2): 27-41.
- Gaherty, J.B. and Jordan, T.H., 1995. Polarization anisotropy, layering, and small-scale structure with the continental tectosphere. In: Anonymous (Editor), *International Union of Geodesy and Geophysics; XXI general assembly; abstracts. International Union of Geodesy and Geophysics, General Assembly. [publisher varies], [location varies], International*, pp. 2.
- Garofalo, F., Zwell, L., Keh, A.S. and Weissmann, S., 1961. Substructure in iron during creep at 600 °C. *Acta Metallurgica*, 9: 721-729.
- Gifkins, R.C., 1976. Grain-Boundary Sliding and Its Accommodation During Creep and Superplasticity. *Metallurgical Transactions A*, 7a(8): 1225-1232.
- Govers, R. and Wortel, M.J.R., 1993. Initiation of asymmetric extension in continental lithosphere. *Tectonophysics*, 223: 75-96.
- Govers, R. and Wortel, M.J.R., 1995. Extension of stable continental lithosphere and the initiation of lithospheric scale faults. *Tectonics*, 14(4): 1041-1055.
- Guillopé, M. and Poirier, J.P., 1979. Dynamic recrystallization during creep of single-crystalline halite: An experimental study. *Journal of Geophysical Research*, 84(B10): 5557-5567.
- Haar, L., Gallagher, J. and Kell, G., 1984. *NBS/NRC Steam Tables*. Hemisphere Publications Co., Washington.
- Hacker, B.R., Yin, A., Christie, J.M. and Snoke, A.W., 1990. Differential stress, strain rate, and temperature of mylonitization in the Ruby Mountains, Nevada: Implications for the rate and duration of uplift. *Journal of Geophysical Research*, 95(B6): 8569-8580.
- Hall, C.E. and Parmentier, E.M., 2003. Influence of grain size evolution on convective instability. *Geochemistry Geophysics Geosystems*, 4(3): doi:10.1029/2002GC000308.
- Handy, M.R., 1989. Deformation regimes and the rheological evolution of fault zones in the lithosphere: the effects of pressure, temperature, grain size and time. *Tectonophysics*, 163(1-2): 119-152.
- Haslam, A.J., Moldovan, D., Yamakov, V., Wolf, D., Phillpot, S.R. and Gleiter, H., 2003. Stress-enhanced grain growth in a nanocrystalline material by molecular-dynamics simulation. *Acta Materialia*, 51(7): 2097-2112.
- Haslam, A.J., Yamakov, V., Moldovan, D., Wolf, D., Phillpot, S.R. and Gleiter, H., 2004. Effects of grain growth on grain-boundary diffusion creep by molecular-dynamics simulation. *Acta Materialia*, 52(7): 1971-1987.
- Herwegh, M. and Berger, A., 2004. Deformation mechanisms in second-phase affected microstructures and their energy balance. *Journal of Structural Geology*, 26(8): 1483-1498.
- Herwegh, M., De Bresser, J.H.P., Ter Heege, J.H., 2005. Combining natural microstructures with composite flow laws: an improved approach for the extrapolation of lab data to nature. *Journal of Structural Geology* 27 (3), 503-521.
- Hillert, M., 1965. On the theory of normal and abnormal grain growth. *Acta Metallurgica*, 13: 227-238.
- Hiraga, T., Anderson, I.M. and Kohlstedt, D.L., 2004. Grain boundaries as reservoirs of incompatible elements in the Earth's mantle. *Nature*, 427: 699-703.
- Hiraga, T., Anderson, I.M., Zimmerman, M.E., Mei, S. and Kohlstedt, D.L., 2002. Structure and chemistry of grain boundaries in deformed, olivine + basalt and partially molten lherzolite aggregates: evidence of melt-free grain boundaries. *Contributions of Mineralogy and Petrology*, 144: 163-175.

## References

- Hirth, G. and Kohlstedt, D.L., 1995a. Experimental constraints on the dynamics of the partially molten upper mantle: Deformation in the diffusion creep regime. *Journal of Geophysical Research*, 100(B2): 1981-2001.
- Hirth, G. and Kohlstedt, D.L., 1995b. Experimental constraints on the dynamics of the partially molten upper mantle: 2. Deformation in the dislocation creep regime. *Journal of Geophysical Research*, 100(B8): 15441-15449.
- Hirth, G. and Kohlstedt, D.L., 1996. Water in the oceanic upper mantle: implications for rheology, melt extraction and the evolution of the lithosphere. *Earth and Planetary Science Letters*, 144(1-2): 93-108.
- Hirth, G. and Kohlstedt, D.L., 2003. Rheology of the Upper Mantle and the Mantle Wedge: A View from the Experimentalists. In: J. Eiler (Editor), *Inside the Subduction Factory*. Geophysical Monographs. American Geophysical Union, Washington, DC, pp. 83-105.
- Hirth, G. and Tullis, J., 1992. Dislocation creep regimes in quartz aggregates. *Journal of Structural Geology*, 14(2): 145-159.
- Hirth, G., and D.L. Kohlstedt, Rheology of the upper mantle and the mantle wedge: A view from the experimentalists, in *The subduction factory*, edited by J. Eiler, pp. in press, 2003.
- Hirth, G., Teyssier, C. and Dunlap, J., 2001. An evaluation of quartzite flow laws based on comparisons between experimentally and naturally deformed rocks. *International Journal of Earth Sciences*, 90(1): 77-87.
- Hirth, J.P. and Lothe, J., 1982. *Theory of dislocation*. John Wiley and Sons, Inc, 857 pp.
- Hitchings, R.S., Paterson, M.S. and Bitmead, J., 1989. Effects of iron and magnetite additions in olivine-pyroxene rheology. *Physics of The Earth and Planetary Interiors*, 55(3-4): 277-291.
- Holm, E.A., Srolovitz, D.J., Cahn, J.W., 1993. Microstructural evolution in two-dimensional two-phase polycrystals. *Acta Metallurgica et Materialia* 41 (4), 1119-1136.
- Holm, K., Embury, J.D. and Purdy, G.R., 1977. The structure and properties of microduplex Zr-Nb alloys. *Acta Metallurgica*, 25(10): 1191-1200.
- Hopper, J.R. and Buck, W.R., 1993. The initiation of rifting at constant tectonic force: Role of diffusion creep. *Journal of Geophysical Research*, 98(B9): 16213-16221.
- Houlier, B., Cheraghmakani, M. and Jaoul, O., 1990. Silicon diffusion in San Carlos olivine. *Physics of The Earth and Planetary Interiors*, 62(3-4): 329-340.
- Houseman, G.A. and England, P.C., 1986. A dynamic model of lithospheric extension and sedimentary basin formation. *Journal of Geophysical Research*, 91: 719-729.
- Hull, D. and Bacon, D.J., 1984. *Introduction to Dislocations*. Pergamon, Oxford
- Humphreys, F.J. and Hatherly, M., 1996. *Recrystallization and related annealing phenomena*. Pergamon, 497 pp.
- Hynes, A. and Doremus, R., 1996. Theories of creep in ceramics. *Critical Reviews in Solid State and Material Sciences*, 21(2): 129-187.
- Jackson, I., Fitz Gerald, J.D., Faul, U.H. and Tan, B.H., 2002. Grain-size-sensitive seismic wave attenuation in polycrystalline olivine. *Journal of Geophysical Research*, 107(B12): 2360, doi:10.1029/2001JB001225.
- Jaoul, O., Froidevaux, C., Durham, W.B. and Michaut, M., 1980. Oxygen self-diffusion in forsterite: implications for the high-temperature creep mechanism. *Earth and Planetary Science Letters*, 47: 391-397.
- Jaoul, O., Poumellac, M., Froidevaux, C. and Havette, A., 1981. Silicon diffusion in forsterite: A new constraint for understanding mantle deformation. In: F.D. Stacey, M.S. Paterson and A. Nicolas (Editors), *Anelasticity in the Earth*. Geodyn. Ser. Am. Geophys. Union. AGU, Washington, pp. 95-100.
- Jaroslow, G.E., Hirth, G. and Dick, H.J.B., 1996. Abyssal peridotite mylonites: implications for grain-size sensitive flow and strain localization in the oceanic lithosphere. *Tectonophysics*, 256(1-4): 17-37.
- Jessell, M., Bons, P., Evans, L., Barr, T., Stuwe, K., 2001. Elle: the numerical simulation of metamorphic and deformation microstructures. *Computers & Geosciences* 27 (1), 17-30.
- Jessell, M., Bons, P.D., Evans, B., Piazzolo, S., 2004. Numerical experiments into the localization of deformation during recrystallization flow. *Material Science Forum* 467-470, 647-652.
- Jessell, M.W., Siebert, E., Bons, P.D., Evans, L. and Piazzolo, S., 2005. A new type of numerical experiment on the spatial and temporal patterns of localization of deformation in a material with a coupling of grain size and rheology. *Earth and Planetary Science Letters*, 239(3-4): 309-326.
- Ji, S., Wang, Z. and Wirth, R., 2001. Bulk flow strength of forsterite-enstatite composites as a function of forsterite content. *Tectonophysics*, 341(1-4): 69-93.
- Jin, D., Karato, S.-i. and Obata, M., 1998. Mechanisms of shear localization in the continental lithosphere: inference from the deformation microstructures of peridotites from the Ivrea zone, northwestern Italy. *Journal of Structural Geology*, 20(2-3): 195-209.
- Jung, H. and Karato, S.-I., 2001. Effects of water on dynamically recrystallized grain-size of olivine. *Journal of Structural Geology*, 23(9): 1337-1344.
- Kameyama, M., Yuen, D.A. and Fujimoto, H., 1997. The interaction of viscous heating with grain-size dependent rheology in the formation of

- localized slip zones. *Geophysical Research Letters*, 24(20): 2523-2526.
- Karato, S. and Wu, P., 1993. Rheology of the upper mantle. *Science*, 260: 771-778.
- Karato, S., 1989. Grain growth kinetics in olivine aggregates. *Tectonophysics*, 168: 255 - 273.
- Karato, S., Toriumi, M. and Fujii, T., 1980. Dynamic recrystallisation of olivine single crystals during high temperature creep. *Geophysical Research Letters*, 7: 649-652.
- Karato, S., Toriumi, M. and Fujii, T., 1982. Dynamic recrystallization and high-temperature rheology of olivine. In: S. Akimoto and M. Manghnani (Editors), *High pressure research in geophysics. Advances in Earth and Planetary Sciences*. Center for Academic Publications, Tokyo, pp. 171-189.
- Karato, S.-I. and Wu, P., 1993. Rheology of the upper mantle: A synthesis. *Science*, 260: 771-778.
- Karato, S.-I., 2003. Mapping Water Content in the Upper Mantle. In: J. Eiler (Editor), *Inside the Subduction factory*. Geophysical Monograph. American Geophysical Union, Washington, DC, pp. 135-152.
- Karato, S.I., 2003. The dynamic structure of the deep Earth; an interdisciplinary approach. Princeton University Press, Princeton, 241 pp.
- Karato, S.I., Paterson, M.S. and FitzGerald, J.D., 1986. Rheology of synthetic olivine aggregates: influence of grain size and water. *Journal of Geophysical Research*, 91(B8): 8151 - 8176.
- Keen, C.E., MacLean, B.C. and Kay, W.A., 1991. A deep seismic reflection profile across the Nova Scotia continental margin, offshore Eastern Canada. *Canadian Journal of Earth Sciences = Journal Canadien des Sciences de la Terre*, 28(7): 1112-1120.
- Kellermann Slotemaker, A. and De Bresser, J.H.P., On the role of cellular defects in dynamic grain growth - 2D microstructural modeling. *Tectonophysics*, accepted.
- Kellermann Slotemaker, A., De Bresser, J.H.P., Spiers, C.J., Drury, M., 2004. Microstructural evolution of synthetic forsterite aggregates deformed to high strain. *Material Science Forum* 467-470 (Part 1), 579-584.
- Kim, B.-N., Hiraga, K. and Morita, K., 2005. Viscous grain-boundary sliding and grain rotation accommodated by grain-boundary diffusion. *Acta Materialia*, 53(6): 1791-1798.
- Kim, B.-N., Hiraga, K., 2000. Simulation of diffusional creep accompanied by grain growth in two-dimensional polycrystalline solids. *Acta Materialia* 48 (16), 4151-4159.
- Kim, B.-N., Hiraga, K., Sakka, Y., Ahn, B.-W., 1999. A grain-boundary diffusion model of dynamic grain growth during superplastic deformation. *Acta Materialia* 47 (12), 3433-3439.
- Kim, S.-I., Lee, Y., Lee, D.-L. and Yoo, Y.-C., 2003. Modeling of AGS and recrystallized fraction of microalloyed medium carbon steel during hot deformation. *Materials Science and Engineering A*, 355(1-2): 384-393.
- Kirby, S.H. and Wegner, M.W., 1978. Dislocation substructure of mantle-derived olivine as revealed by selective chemical etching and transmission electron microscopy. *Physics and Chemistry of Minerals*, 3: 309-330.
- Krabbendam, M., Urai, J.L., Van Vliet, L.J., 2003. Grain size stabilisation by dispersed graphite in a high-grade quartz mylonite: an example from Naxos (Greece). *Journal of Structural Geology* 25 (6), 855-866.
- Kröger, F.A. and Vink, H.J., 1956. Relations between the concentrations of imperfections in crystalline solids. In: F. Seitz and D. Turnbull (Editors). *Solid state physics*. Academic Press, New York, pp. 307-435.
- Langdon, T.G., 1995. Mechanisms of Superplastic Flow. In: N. Ridley (Editor), *Superplasticity: 60 Years after Pearson*. The Institute of Materials, London, pp. 9-24.
- Lee, K.-H., Jiang, Z. and Karato, S.-i., 2002. A scanning electron microscope study of the effects of dynamic recrystallization on lattice preferred orientation in olivine. *Tectonophysics*, 351(4): 331-341.
- Lehner, F.K., 1990. Thermodynamics of rock deformation by pressure solution. In: D. Barber and P. Meredith (Editors), *Deformation Processes in Minerals, Ceramics and Rocks*. Unwin Hyman, London, pp. 296-333.
- Leibecker, J., Gatzemeier, A., Honig, M., Kuras, O. and Soyer, W., 2002. Evidence of electrical anisotropic structures in the lower crust and the upper mantle beneath the Rhenish Shield. *Earth and Planetary Science Letters*, 202(2): 289-302.
- Levin, V., and J. Park, Shear zones in the Proterozoic lithosphere of the Arabian Shield and the nature of the Hales discontinuity, *Tectonophysics*, 323 (3-4), 131-148, 2000.
- Mackwell, S.J. and Kohlstedt, D.L., 1986. High-temperature deformation of forsterite single crystals doped with vanadium. *Physics and Chemistry of Minerals*, 13(5): 351-356.
- Mackwell, S.J., Kohlstedt, D.L. and Paterson, M.S., 1985. The role of water in the deformation of olivine single crystals. *Journal of Geophysical Research*, 90(13): 11,319-11,333.
- Mareschal, M. et al., 1995. Archaean cratonic roots, mantle shear zones and deep electrical anisotropy. *Nature*, 375: 134 - 137.
- Marquardt, D.W., 1963. An algorithm for least-squares estimation of nonlinear parameters. *Journal of the Society for Industrial and Applied Mathematics*, 11(2): 431-441.
- Mas, D.L., Crowley, P.D., 1996. The effect of second-phase particles on stable grain size in regionally metamorphosed polyphase calcite marbles.

## References

- Journal of Metamorphic Geology 14 (2), 155-162.
- McDonnell, R.D., 1997. Deformation of fine-grained synthetic peridotite under wet conditions. *Geologica Ultraiectina Thesis*, University Utrecht, Utrecht, 195 pp.
- McDonnell, R.D., Peach, C.J. and Spiers, C.J., 1999. Flow behavior of fine-grained synthetic dunite in presence of 0.5 wt% H<sub>2</sub>O. *Journal of Geophysical Research*, 104(B8): 17,823-17,845.
- McDonnell, R.D., Peach, C.J., van Roermund, H.L.M. and Spiers, C.J., 2000. Effect of varying enstatite content on the deformation behavior of fine-grained synthetic peridotite under wet conditions. *Journal of Geophysical Research*, 105: 13535-13553.
- McDonnell, R.D., Spiers, C.J. and Peach, C.J., 2002. Fabrication of dense forsterite-enstatite polycrystals for experimental studies. *Physics and Chemistry of Minerals*, 29(1): 19-31.
- Mei, S. and Kohlstedt, D.L., 2000a. Influence of water on plastic deformation of olivine aggregates 1. Diffusion creep regime. *Journal of Geophysical Research*, 105(B9): 21457-21469.
- Mei, S. and Kohlstedt, D.L., 2000b. Influence of water on plastic deformation of olivine aggregates 2. Dislocation creep regime. *Journal of Geophysical Research*, 105(B9): 21471-21481.
- Meier, L. and Eisbacher, G.H., 1991. Crustal kinematics and deep structure of the northern Rhine Graben, Germany. *Tectonics*, 10(3): 621-630.
- Mercier, J.-C.C., Anderson, D.A. and Carter, N.L., 1977. Stress in the lithosphere: Inferences from steady state flow of rocks. *Pure and Applied Geophysics*, 115: 199-226.
- Michibayashi, K., 1993. Syntectonic development of a strain-independent steady-state grain size during mylonitization. *Tectonophysics*, 222: 151-164.
- Montesi, L.G.J. and Hirth, G., 2003. Grain size evolution and the rheology of ductile shear zones: from laboratory experiments to postseismic creep. *Earth and Planetary Science Letters*, 211(1-2): 97-110.
- Montesi, L.G.J. and Zuber, M.T., 2002. A unified description of localization for application to large-scale tectonics. *Journal of Geophysical Research*, 107(B3): 10.1029/2001JB000465.
- Moresi, L., Dufour, F. and Mühlhaus, H.B., 2002. Mantle Convection Modeling with Viscoelastic/Brittle Lithosphere: Numerical Methodology and Plate Tectonic Modeling. *Pure and Applied Geophysics*, 159(10): 2335-2356.
- Morrall, J.E., and M.F. Ashby, Dislocated cellular structures, *Acta Metallurgica*, 22, 567-575, 1974.
- Nakamura, A. and Schmalzried, H., 1984. On the Fe<sup>2+</sup>-Mg<sup>2+</sup> interdiffusion in olivine. *Ber. Bunsenges. Phys. chem.*, 88: 140-145.
- Nermond, S., J. Ingrin, J.C.C. Mercier, and P. Bertr, Kinetics of grain growth of natural and synthetic olivine polycrystals: experimental study., *Terra abstracts*, 5, 355, 1993.
- Newman, J., Lamb, W.M., Drury, M.R. and Vissers, R.L.M., 1999. Deformation processes in a peridotite shear zone: reaction-softening by an H<sub>2</sub>O-deficient, continuous net transfer reaction. *Tectonophysics*, 303(1-4): 193-222.
- Nichols, S.J., and S.J. Mackwell, Grain growth in porous olivine aggregates, *Physics and Chemistry of Minerals*, 18 (4), 269-278, 1991.
- Nicolas, A., 1978. Stress Estimates from Structural Studies in Some Mantle Peridotites. *Philosophical Transactions of the Royal Society of London A*, 288(NO.1350): 49-57.
- Nicolas, A., Bouchez, J.L., Boudier, F. and Mercier, J.C., 1971. Textures, structures and fabrics due to solid state flow in some European lherzolites. *Tectonophysics*, 12(1): 55-86.
- Olgaard, D.L., 1990. The role of second phase in localizing deformation. In: Knipe, R.J., Rutter, E.H. (Eds.), *Deformation mechanisms, rheology and tectonics*. Geological Society Special Publications. Geological Society of London, London, United Kingdom, pp. 175-181.
- Oshi, Y. and Ando, K., 1984. Oxygen self-diffusion coefficient in single-crystal forsterite. In: I. Sunagawa (Editor), *Materials science of the Earth's interior*. Terra Scientific Pub. Co., Tokyo, pp. 271-280.
- Park, H. and Park, S.Y., 2001. Grain growth behaviour of alumina during sinter-HIP process. *Journal of Materials Science Letters*, 20, 601-603.
- Piazolo, S., 2001. Shape fabric development during progressive deformation. Ph.D. Thesis, Johannes Gutenberg-Universität, Mainz, 251 pp.
- Piazolo, S., Bons, P.D., Jessell, M.W., Evans, L., Passchier, C.W., 2002. Dominance of microstructural processes and their effect on microstructural development: insights from numerical modeling of dynamic recrystallization. In: De Meer, S., Drury, M.R., De Bresser, J.H.P., Pennock, G.M. (Eds), *Deformation mechanisms, Rheology and Tectonics: Current Status and Future perspectives*. Geological Society, London, Special Publications 200, 149-170.
- Pieri, M., Burlini, L., Kunze, K., Stretton, I. and Olgaard, D.L., 2001a. Rheological and microstructural evolution of Carrara marble with high shear strain: results from high temperature torsion experiments. *Journal of Structural Geology*, 23: 1393-1413.
- Pieri, M., Kunze, K., Burlini, L., Stretton, I.C., Olgaard, D.L., Burg, J.-P. and Wenk, H.-R., 2001b. Texture development of calcite by deformation and dynamic recrystallization at

- 1000 K during torsion experiments of marble to large strains. *Tectonophysics*, 330: 119-140.
- Poirier, J.P. and Nicolas, A., 1975. Deformation induced recrystallization due to the progressive misorientation of subgrains, with special reference to mantle peridotites. *Journal of Geology*, 83: 707-720.
- Poirier, J.P., 1985. *Creep of Crystals - High-temperature Deformation Processes in Metals, Ceramics and Minerals*. Cambridge University press, Cambridge, 260 pp.
- Post, R.L., 1977. High-temperature creep of Mt. Burnet dunite. *Tectonophysics*, 42: 75-110.
- Rabinovich, M.K., Trifonov, V.G., 1996. Dynamic grain growth during superplastic deformation. *Acta Materialia* 44 (5), 2073-2078.
- Raj, R. and Ghosh, A.K., 1981. Micromechanical modelling of creep using distributed parameters. *Acta Metallurgica*, 29(2): 283-292.
- Raj, S.V. and Pharr, G.M., 1986. A Compilation and Analysis of Data for the Stress Dependence of the Subgrain Size. *Materials Science and Engineering*, 81(1-2): 217-237.
- Ranalli, G., 1984. Grain size distribution and flow stress in tectonites. *Journal of Structural Geology* 6 (4), 443-447.
- Reddy, K.P.R., Oh, S.M. and Major, L.D., 1980. Oxygen diffusion in forsterite. *Journal of Geophysical Research*, 85: 322-326.
- Reston, T.J., 1990. Mantle shear zones and the evolution of the northern North Sea basin. *Geology (Boulder)*, 18(3): 272-275.
- Ricoult, D.L. and Kohlstedt, D.L., 1985. Experimental evidence for the effect of chemical environment upon the creep rate of olivine. In: R.N. Schock (Editor), *Point defects in minerals*. Geophysical monograph. American Geophysical Union, Washington, D.C., pp. 171-184.
- Riedel, M.R. and Karato, S.-I., 1996. Microstructural development during nucleation and growth. *Geophysical Journal International*, 125: 397-414.
- Ross, J.V., Avé Lallemant, H.G. and Carter, N.L., 1980. Stress dependence of recrystallized-grain and subgrain size in olivine. *Tectonophysics*, 70: 39-61.
- Rutter, E.H. and Brodie, K.H., 1988. The role of tectonic grain size reduction in the rheological stratification of the lithosphere. *Geologische Rundschau*, 77(1): 295-308.
- Rutter, E.H., 1995. Experimental study of the influence of stress, temperature, and strain on the dynamic recrystallisation of Carrara marble. *Journal of Geophysical Research*, 100(B12): 24651-24663.
- Rutter, E.H., 1998. Use of extension testing to investigate the influence of finite strain on the Theological behaviour of marble. *Journal of Structural Geology* 20 (2-3), 243-254.
- Ryerson, F.J., Durham, W.B., Cherniak, D.J. and Lanford, W.A., 1989. Oxygen diffusion in olivine; effect of oxygen fugacity and implications for creep. *Journal of Geophysical Research*, 94: 4105-4118.
- Sato, E., Kuribayashi, K. and Horiuchi, R., 1990. A mechanism of superplastic deformation and deformation induced grain growth based on grain switching. *Materials Research Society Symposium Proceedings*, 196: 27-32.
- Schmid, S.M., 1982. Microfabric studies as indicators of deformation mechanisms and flow laws operative in Mountain Building. In: K.J. Hsü (Editor), *Mountain Building Processes*. Academic Press, London, pp. 95-110.
- Schmid, S.M., Boland, J.N., Paterson, M.S., 1977. Superplastic flow in fine grained limestone. *Tectonophysics* 43 (3-4), 257-291.
- Schmid, S.M., Panozzo, R., Bauer, S., 1987. Simple shear experiments on calcite rocks: rheology and microfabric. *Journal of Structural Geology* 9, 747-778.
- Schmid, S.M., Paterson, M.S. and Boland, J.N., 1980. High temperature flow and dynamic recrystallization in Carrara marble. *Tectonophysics*, 65: 245-280.
- Seidensticker, J.R. and Mayo, M.J., 1998a. Dynamic and static grain growth during the superplastic deformation of 3Y-TZP. *Scripta Materialia*, 38(7): 1091-1100.
- Seidensticker, J.R. and Mayo, M.J., 1998b. A topological rationale for the dependence of grain growth on strain during superplastic deformation. *Acta Materialia*, 46(14): 4883-4893.
- Shankland, T.J., O, C.R.J. and Waff, H.S., 1981. Geophysical constraints on partial melt in the upper mantle. *Reviews of Geophysics and Space Physics*, 19(3): 394-406.
- Sherwood, D.J. and Hamilton, C.H., 1991. A mechanism for deformation-enhanced grain growth in single phase materials. *Scripta Metallurgica et Materialia*, 25(12): 2873-2878.
- Sherwood, D.J. and Hamilton, C.H., 1992. Production of cellular defects contributing to deformation-enhanced grain growth. *Scripta Metallurgica et Materialia*, 27(12): 1771-1776.
- Sherwood, D.J. and Hamilton, C.H., 1994. The neighbourswitching mechanism of superplastic deformation: the constitutive relationship and deformation-enhanced grain growth. *Philosophical Magazine*, 70: 109-143.
- Shimizu, I., 1998. Stress and temperature dependence of recrystallized grain size: A subgrain misorientation model. *Geophysical Research Letters*, 25(22): 4237-4240.
- Shimizu, I., 1999. A stochastic model of grain size distribution during dynamic recrystallization. *Philosophical Magazine A*, 79(5): 1217-1231.
- Smyth, D.M. and Stocker, R.L., 1975. Point defects and non-stoichiometry in forsterite. *Physics of*

## References

- The Earth and Planetary Interiors, 10(2): 183-192.
- Stipp, M. and Tullis, J., 2003. The recrystallized grain size piezometer for quartz. *Geophysical Research Letters*, 30(21): doi: 10.1029/2003GL018444.
- Stipp, M., Stunitz, H., Heilbronner, R. and Schmid, S.M., 2002. The eastern Tonale fault zone: a 'natural laboratory' for crystal plastic deformation of quartz over a temperature range from 250 to 700 [deg]C. *Journal of Structural Geology*, 24(12): 1861-1884.
- Takeuchi, S. and Argon, A.S., 1976. Steady-state creep of single-phase crystalline matter at high temperature. *Journal of Materials Science*, 11: 1542-1566.
- Ten Grotenhuis, S.M., Drury, M.R., Peach, C.J. and Spiers, C.J., 2004. Electrical properties of fine-grained olivine: Evidence for grain boundary transport. *Journal of Geophysical Research*, 109: DOI:10.1029/2003JB002799.
- Ter Heege, J.H., De Bresser, J.H.P. and Spiers, C.J., 2002. The influence of dynamic recrystallization on the grain size distribution and rheological behaviour of Carrara marble deformed in axial compression. In: S. De Meer, M.R. Drury, J.H.P. De Bresser and G.M. Pennock (Editors), *Deformation mechanisms, rheology and tectonics: Current status and future perspectives*. Geological Society, London, Special Publications. The Geological Society of London, London.
- Ter Heege, J.H., De Bresser, J.H.P. and Spiers, C.J., 2004. Composite flow laws for crystalline materials with log-normally distributed grain size: theory and application to olivine. *Journal of Structural Geology*, 26(9): 1693-1705.
- Ter Heege, J.H., De Bresser, J.H.P. and Spiers, C.J., 2005. Dynamic recrystallization of wet synthetic polycrystalline halite: dependence of grain size distribution on flow stress, temperature and strain. *Tectonophysics*, 396(1-2): 35-57.
- Tsenn, M.C. and Carter, N.L., 1987. Upper limits of power law creep of rocks. *Tectonophysics*, 136(1-2): 1-26.
- Twiss, R.J., 1977. Theory and applicability of a recrystallized grain size paleopiezometer. *Pure and Applied Geophysics*, 115: 227-244.
- Urai, J.L., Jessell, M., 2001. Recrystallization and grain growth in minerals: recent developments. In: Gottstein, G., Molodov, D. (Eds.), *Recrystallization and Grain Growth*, Proceedings of the first Joint International Conference. Springer Verlag, RWTH Aachen, Germany, pp. 87-96.
- Urai, J.L., Means, W.D. and Lister, G.S., 1986. Dynamic recrystallization of minerals. In: B.E. Hobbs and H.C. Heard (Editors), *Mineral and Rock Deformation: Laboratory Studies- The Paterson Volume*. *Geophysical Monograph*, Geophys. Monogr. Ser. Am. Geoph. Union, Washington D.C., pp. 161 - 199.
- Van den Berg, A.P. and Yuen, D.A., 1995. Convectively induced transition in mantle rheological behavior. *Geophysical Research Letters*, 22(12): 1549-1552.
- Van den Berg, A.P. and Yuen, D.A., 1996. Is the lower-mantle rheology Newtonian today? *Geophysical Research Letters*, 23(NO. 16): 2033-2036.
- Van den Berg, A.P., Van Keken, P.E. and Yuen, D.A., 1993. The effects of a composite non-Newtonian and Newtonian rheology on mantle convection. *Geophysical Journal International*, 115: 62-78.
- Van der Wal, D., Chopra, P., Drury, M.R. and Fitz Gerald, J., 1993. Relationships between dynamically recrystallized grain size and deformation conditions in experimentally deformed olivine rocks. *Geophysical Research Letters*, 20(14): 1479-1482.
- Van Swygenhoven, H. and Derlet, P.M., 2001. Grain-boundary sliding in nanocrystalline fcc metals. *Physical Review B*, 64(22): 224105.
- Van Wees, J.D., and F. Beekman, *Lithosphere rheology during intraplate basin extension and inversion: Inferences from automated modeling of four basins in western Europe*, *Tectonophysics*, 320 (3-4), 219-242, 2000.
- Vissers, R.L.M., Drury, M.R., Strating, E.H.H., Spiers, C.J. and van der Wal, D., 1995. Mantle shear zones and their effect on lithosphere strength during continental breakup. *Tectonophysics*, 249(3-4): 155-171.
- Von Neumann, J., 1952. Discussion to 'Grain shapes and other metallurgical applications of topology' by C.S. Smith. In: Brick, R.M. (Editor), *Metal Interfaces*. ASM, Cleveland, Ohio, pp. 108-110.
- Walker, A.N., Rutter, E.H., Brodie, K.H., 1990. Experimental study of grain-size sensitive flow of synthetic, hot-pressed calcite rocks. In: Knipe, R.J., Rutter, E.H. (Eds.), *Deformation mechanisms, rheology and tectonics*. Geological Society Special Publications. Geological Society of London, London, United Kingdom, pp. 259-284.
- Wang, J.N., 1994. The effect of grain size distribution on the rheological behavior of polycrystalline materials. *Journal of Structural Geology*, 16(7): 961-970.
- Wang, Y., Houseman, G.A., Lin, G., Guo, F., Wang, Y.-J., Fan, W.-M. and Chang, X., 2005. Mesozoic lithospheric deformation in the North China block: Numerical simulation of evolution from orogenic belt to extensional basin system. *Tectonophysics*, 405(1-4): 47-63.
- Watson, E.B., 1991. Diffusion in fluid-bearing and slightly-melted rocks: experimental and numerical approaches illustrated by iron transport in dunite. *Contributions to Mineralogy and Petrology*, 107(4): 417-434.

- Weaire, D., Kermode, J.P., 1983. Computer simulation of a two-dimensional froth I. Method and motivation. *Philosophical Magazine B* 48 (No.3), 245-259.
- Wenk, H.R., Bennet, K., Canova, G.R. and Molinari, A., 1991. Modeling plastic deformation of peridotite with the self-consistent theory. *Journal of Geophysical Research*, 96: 8337-8349.
- White, S.H., 1976. The effects of strain on microstructures, fabrics and deformation mechanisms in quartzites. *Philosophical Transactions of the Royal Society of London A*, 238: 69-86.
- White, S.H., 1979. Difficulties associated with paleo-stress estimates. *Bulletin de Minéralogie*, 102: 210-215.
- White, S.H., Burrows, S.E., Carreras, J., Shaw, N.D. and Humphreys, F.J., 1980. On mylonites in ductile shear zones. *Journal of Structural Geology*, 2: 175-187.
- Wilkinson, D.S. and Caceres, C.H., 1984. On the mechanism of strain-enhanced grain growth during superplastic deformation. *Acta Metallurgica*, 32(9): 1335-1345.
- Wirth, R., 1996. Thin amorphous films (1-2 nm) at olivine grain boundaries in mantle xenoliths from San carlos, Arizona. *Contributions of Mineralogy and Petrology*, 124: 44-54.
- Yamasaki, T., 2004. Localized rheological weakening by grain-size reduction during lithospheric extension. *Tectonophysics* 386 (3-4), 117-145.
- Yoshii, T., Kono, Y. and Ito, K., 1976. Thickening of the oceanic lithosphere.
- Yund, R.A., 1997. Rates of grain boundary diffusion through enstatite and forsterite reaction rims. *Contributions to Mineralogy and Petrology*, 126(3): 224-236.
- Zhang, S. and Karato, S.-I., 1995. Lattice preferred orientation of olivine aggregates deformed in simple shear. *Nature*, 375: 774-777.
- Zhang, S., Karato, S.-i., Fitz Gerald, J., Faul, U.H. and Zhou, Y., 2000. Simple shear deformation of olivine aggregates. *Tectonophysics*, 316(1-2): 133-152.
- Zhao, Y.H., Ginsberg, S.B. and Kohlstedt, D.L., 2004. Solubility of hydrogen in olivine; dependence on temperature and iron content. *Contributions to Mineralogy and Petrology*, 147(2): 155-161.
- Zhilyaev, A.P., Kim, B.-K., Szpunar, J.A., Baro, M.D., Langdon, T.G., 2005. The microstructural characteristics of ultrafine-grained nickel. *Materials Science and Engineering A* 391 (1-2), 377-389.
- Zhong, S., Zuber, M.T., Moresi, L. and Gurnis, M., 2000. Role of temperature-dependent viscosity and surface plates in spherical shell models of mantle convection. *Journal of Geophysical Research*, 105(B5): 11063-11082.
- Ziegler, P.A. and Cloetingh, S., 2004. Dynamic processes controlling evolution of rifted basins. *Earth-Science Reviews*, 64(1-2): 1-50.

## Papers and abstracts

- Kellermann Slotemaker, A., De Bresser, J.H.P., Spiers, C.J. and Drury, M.R., submitted.  
Deformation induced grain growth in forsterite aggregates. *Physics of the Earth and Planetary Interiors* (chapter 3).
- Kellermann Slotemaker, A. and De Bresser, J.H.P., in press. On the role of cellular defects in dynamic grain growth - 2D microstructural modeling. *Tectonophysics* (chapter 4).
- Kellermann Slotemaker, A. and De Bresser, J.H.P., 2006a. Dynamic grain growth in laboratory experiments, microstructural modelling and naturally deformed rocks. *Geophysical Research Abstracts*, 8 (chapter 3, 4 & 5).
- Kellermann Slotemaker, A., and J.H.P. De Bresser, 2006b. Dynamic grain growth in laboratory experiments, microstructural modelling and naturally deformed rocks, *Nederlands Aardwetenschappelijk Congres NAC 8*, Veldhoven (chapter 3, 4 & 5).
- Kellermann Slotemaker, A., and J.H.P. De Bresser, 2005a. On the role of cellular defects in dynamic grain growth: 2D microstructural modeling. *Int. Conference on Deformation Mechanisms, Rheology and Tectonics*. ETH Zürich, Switzerland (chapter 4).
- Kellermann Slotemaker, A., De Bresser, J.H.P. and Spiers, C.J., 2005b. Strength of rocks affected by deformation enhanced grain growth. *EOS Transactions of the American Geophysical Union*, 86(52) (chapter 3, 4 & 5).
- Kellermann Slotemaker, A., De Bresser, J.H.P., Spiers, C.J. and Drury, M.R., 2004a. Dynamic grain growth in forsterite aggregates experimentally deformed to high strain. *EOS Transactions of the American Geophysical Union*, 85(47) (chapter 3 & 4).
- Kellermann Slotemaker, A., De Bresser, J.H.P., Spiers, C.J. and Drury, M.R., 2004b. Microstructural evolution of synthetic forsterite aggregates deformed to high strain. *Material Science Forum*, 467-470(Part 1): 579-584 (chapter 3).
- Kellermann Slotemaker, A., J.H.P. De Bresser, C.J. Spiers, 2004c. Dynamic grain growth in synthetic forsterite aggregates deformed to high strain, *Nederlands Aardwetenschappelijk Congres NAC 7*, Veldhoven.
- Kellermann Slotemaker, A., J.H.P. de Bresser, C.J. Spiers, and R.D. McDonnell, April 2003. High strain mechanical and microstructural evolution of synthetic forsterite aggregates. *Int. Conference on Deformation Mechanisms, Rheology and Tectonics*. Saint Malo, France.



## Samenvatting

De dynamica van de buitenste schil van de aarde wordt grotendeels gecontroleerd door het vaste stof vloeigedrag (reologie) van materialen die domineren in de bovenmantel van de aarde, in het bijzonder het mineraal olivijn. Een procesmatige beschrijving van de reologie van olivijn is essentieel voor numerieke modellering van geodynamische processen in de bovenmantel en voor de interpretatie van het reologische belang van deformatie structuren in ontsloten bovenmantel gesteente. In de laatste decennia is mantelconvectie onderzocht met behulp van individuele en samengestelde vloeiwetten, die *korrelgrootteafhankelijke* (KGO) dislocatiekruip en/of *korrelgrootteafhankelijke* (KGA) diffusiekruip omvatten. In het algemeen zijn vloeiwetten voor KGO en KGA kruip gekalibreerd op basis van compressie experimenten tot relatief kleine verkortingen, ofwel ‘natural strain’  $\epsilon < 0.2$ . In de afgelopen jaren is het echter duidelijk geworden dat dergelijke kalibraties van vloeiwetten niet representatief zijn voor ware constante (steady state) kruip, omdat de microstructuur zich blijft ontwikkelen en nog geen stabiele configuratie heeft bereikt bij dergelijke kleine verkortingen. Recentelijk is door middel van enkele deformatie experimenten tot hoge vervorming aangetoond dat significante sterkte toename of afname kan plaatsvinden bij vervormingen tot ver boven een ‘natural strain’  $\epsilon = 0.2$ . Bovenal is het ook duidelijk geworden dat een beschrijving van de reologie van materialen rekening dient te houden met het feit dat normaliter een gesteente een distributie in korrelgrootte vertoont, in plaats van de veel gebruikte aanname dat één gemiddelde korrelgrootte representatief is voor een polikristallijn materiaal.

Verschillende rekristallisatie processen controleren microstructurele evolutie tijdens transitieve hoge vervorming. Dit zijn processen op korrelschaal zoals korrelgrens-migratie en nieuwe korrelformatie ofwel ‘nucleatie’. Verschillende theoretische en fenomenologische modellen proberen het bestaan te verklaren van een relatie tussen vloeisterkte en dynamisch gerekristalliseerde korrelgrootte. Echter, slechts in enkele pogingen is geprobeerd om de evolutie van de microstructuur naar een evenwichtsconfiguratie te incorporeren. Bovendien is er tot voor kort op dit gebied maar weinig experimenteel werk verricht, met name wat betreft microstructurele evolutie in het KGA kruip regiem. Daarom is de incorporatie van microstructurele evolutie in de beschrijving van de reologie van olivijn gesteentes een belangrijk punt van innovatie.

Het doel van dit proefschrift is het definiëren van een verbeterde beschrijving van het vaste stof vloeigedrag van Aardse materialen in het algemeen, en van olivijn in het bijzonder, waarbij rekening wordt gehouden met de effecten van microstructurele evolutie tot hoge vervormingen. Dit doel is bereikt door zowel het uitvoeren van nieuwe lab experimenten op polikristallijn olivijn materiaal onder condities slechts beperkt toegepast in voorgaande experimenten, als door middel van een theoretische behandeling en numerieke modellering van microstructurele evolutie gedurende deformatie.

In hoofdstuk 1 wordt een kort overzicht gegeven van olivijn reologie en problemen worden uitgelicht betreffende de beschrijving van de reologie van olivijn wanneer gebruik wordt gemaakt van de ‘kleine-verkortings’ vloeiwetten. Het blijkt dat in het geval van fijnkorrelige materialen het effect van korrelgroei en dynamische rekristallisatie nog niet adequaat is onderzocht. Experimentele gegevens aangaande hoge vervorming van olivijn in het KGA kruip regiem zijn schaars en in het algemeen bestaat er geen toereikend microfysisch model dat de effecten van korrelgroei en dynamische rekristallisatie koppelt aan transitieve en constante reologie. Hiermee is de basis gezet voor de huidige studie.

In hoofdstuk 2 is een model voor dynamische rekristallisatie ontwikkeld door relaties af te leiden die a) de nucleatiesnelheid van nieuw gerekristalliseerde korrels door de operatie van dislocatie kruip en geassocieerde subkorrel rotatie beschrijven en b) de groei- of

krimpsnelheid van korrels beschrijven. Hierbij wordt uitgegaan van materialen met een distributie in korrelgrootte van radius  $r$ . Door de resultaten voor korrelnucleatie en korrelgroei/-krimp als functie van  $r$  te combineren, is de evolutie van de complete korrelgrootte distributie bepaald als functie van de tijd. De complexiteit van het probleem vraagt om een numerieke oplossing. Er is gekozen voor een eenvoudige ‘finite difference’ benadering en deze is toegepast op het mineraal olivijn. Hierbij is uitgegaan van deformatie onder laboratorium condities, zodat een eerste inzicht wordt verkregen in de evolutie van korrelgroottedistributie en vloeisterkte in dit materiaal. Het nieuwe model laat zien dat de evolutie van de korrelgroottedistributie gedurende dynamische rekristallisatie zeer complex kan zijn en onderstreept dat de analyse van één gemiddelde korrelgrootte in onderzoek van dynamische recrystallisatie en korrelgroei waarschijnlijk niet volstaat in het beschrijven van transitieve en constante kruip bij hoge vervormingen.

Hoofdstuk 3 beschrijft de resultaten van statische opwarmingsexperimenten en axiale compressietesten op fijnkorrelige ( $\sim 1 \mu\text{m}$ ) synthetische forsteriet in aanwezigheid van 10 volume% enstatiet en  $\sim 0.5$  gewichts% water. Cilindrische monsters zijn axiaal verkort tot 15, 30 en 45%, onder condities waar KGA kruip en oppervlakte-energie gecontroleerde korrelgroei domineren. De gebruikte temperatuur en alzijdige druk zijn respectievelijk 600 MPa en  $950^\circ\text{C}$ . De korrelgroei tijdens statische condities blijkt sterk beperkt te worden door geblokkeerde korrelgrenzen, veroorzaakt door de aanwezigheid van extra fasen (enstatiet en porositeit). Deformatie-experimenten vertonen een continue toename in vloeisterkte (ofwel ‘hardening’) bij toenemende verkorting. In één experiment is de verkorting tijdelijk 2-maal stop gezet. Voor en na een dergelijke interruptie is geen verschil in vloeisterkte geobserveerd. Het gevonden gedrag voor sterkte versus deformatiesnelheid suggereert dat deformatie plaatsvindt door een korrelgrootte afhankelijk proces. Gedeformeerde monsters laten een toename in korrelgrootte tot 2-maal de startwaarde zien, bij een toename in deformatie. Wij relateren de toename in vloeisterkte aan de toenemende korrelgrootte, welke zelf gerelateerd is aan de deformatie. Het lijkt het meest voor de hand liggend om de geobserveerde korrelgroei te verklaren met een model voor dynamische korrelgroei toegespitst op een toename in cellulaire defect fractie (dat is: the fractie van niet-hexagonale korrels in 2D).

Hoofdstuk 4 test vervolgens de hypothese dat topologische veranderingen veroorzaakt door deformatie, een verklaring kunnen vormen voor de dynamische korrelgroei, zoals gevonden in hoofdstuk 3. Een set van numerieke simulaties is uitgevoerd waarin oppervlakte-energie gecontroleerde korrelgrensmigratie is gecombineerd met eenvoudige geometrisch homogene deformatie of KGA deformatie van korrelaggregaten met een distributie in korrelgrootte. Hierbij is gebruik gemaakt van het 2D-microstructureel modelleer pakket ELLE. De simulaties laten zien dat extra verwisseling van aan elkaar grenzende korrels, een toename in defectfractie en extra korrelgroei plaatsvindt in vergelijking tot statische (normale) korrelgroei. Een toename in defectfractie is ook gevonden in een geselecteerde set natuurlijke mylonieten, die tevens met toenemende temperatuur een toename in korrelgrootte en KGA kruip laten zien. Analyse van defectfractie blijkt dus een betrouwbare microstructurele methode om te bepalen of een materiaal normale statische korrelgroei heeft ondergaan (defect fraction  $\sim 0.7$ ), of dynamische korrelgroei (defect fraction  $\sim 0.8$ ).

Hoofdstuk 5 handelt over een gelijksoortige experimentele studie als gepresenteerd in hoofdstuk 3, aangaande fijnkorrelig ( $\sim 1 \mu\text{m}$ ) synthetisch olivijn materiaal. Anders dan in hoofdstuk 3 bevat het forsteriet materiaal hier een kleine hoeveelheid ijzer, ofwel  $\text{fo}_{90}$ . De vergelijking van de resultaten met bestaande data voor puur magnesium forsteriet, ofwel  $\text{fo}_{100}$ , maakt het mogelijk het effect van ijzer te onderzoeken op 1) het vloeigedrag gedurende KGA kruip, en 2) de microstructurele evolutie gedurende KGA kruip. De synthetische monsters bevatten naast een hoeveelheid ijzer ook  $\sim 0.3$  gewichts% water en 5 volume% enstatiet. Experimenten zijn uitgevoerd bij temperaturen in de range  $850\text{-}1000^\circ\text{C}$  en een alzijdige druk

van 600 MPa. In vergelijking tot data voor  $f_{0100}$  onder verder identieke condities, blijkt de toevoeging van ijzer voor  $f_{090}$  geen significant verschil in reologie op te leveren. Met betrekking tot de microstructurele evolutie is wederom een extra korrelgroei component waargenomen gedurende deformatie. Dit verklaart de continue toename in vloeisterkte met toenemende deformatie. Analyse toont aan dat deze extra korrelgroei component kan worden gerelateerd aan een verandering in de fractie van non-hexagonale korrels, zoals ook geconcludeerd is voor  $f_{0100}$ . De berekende dynamische korrelgroeisnelheid is in overeenstemming met bestaande data voor metalen en keramieken. Correlatie van experimentele resultaten aan theoretische modellen voor dynamische korrelgroei resulteren in een eerste orde schatting van de variatie in diverse model-parameters. Deze parameterwaarden kunnen gebruikt worden om dynamische korrelgroei van olivijn op te nemen in geodynamische modellen.

Als laatste worden in hoofdstuk 6 de belangrijkste conclusies van de studie samengevat en worden enkele aanbevelingen/suggesties gedaan voor toekomstig onderzoek naar dynamische rekristallisatie en korrelgroei in olivijn gesteenten.

## Korte samenvatting voor de leek

De buitenste schil van de aarde bestaat uit een gedeelte dat we de ‘aardkorst’ noemen, waarin vooral gesteenten bestaande uit de mineralen kwarts en veldspaat voorkomen, en een dieper gelegen deel dat we de ‘bovenmantel’ noemen. Het voornaamste mineraal in deze bovenmantel is olivijn. Het vaste stof vloeigedrag (ofwel reologie) van olivijn bepaald in hoge mate het karakter van vele grootschalige geologische/geodynamische processen in de aardkorst en mantel.

Om deze processen beter te begrijpen, worden modellen opgesteld en wordt veldonderzoek gedaan naar gesteenten. Dergelijke model- en veldstudies kunnen echter alleen goed uitgevoerd worden als gedegen kennis beschikbaar is over de reologie van olivijn-gesteenten. Een belangrijk aspect is de geleidelijke verandering van de microstructuur van gesteenten tijdens langzame geologische processen. Met microstructuur wordt bedoeld de grootte, vorm en verdeling van korrels, maar ook de interne structuur van de korrels in gesteente. Doel van dit onderzoek is om met behulp van laboratorium-experimenten en een theoretische behandeling van mogelijk relevante processen een stap voorwaarts te maken wat betreft het begrip van vaste stof vloeigedrag van olivijn, in het bijzonder wanneer dit materiaal in hoge mate wordt vervormd zoals in de bovenmantel.

Het project is opgebouwd uit vier delen: 1) uitvoeren van experimenten op diverse olivijn materialen, met aandacht voor de rol van ijzer in olivijn, 2) microscopisch onderzoek van de behandelde monsters, 3) computer modellering van microstructuren om de resultaten van de experimenten beter te begrijpen, en 4) theoretische analyse van de diverse processen die een rol spelen bij de ontwikkeling van de microstructuren in relatie tot het vloeigedrag van olivijn. De experimenten zijn uitgevoerd op olivijn materialen die in het lab gemaakt zijn. Door zelf olivijn-aggregaten te maken, kan de samenstelling en korrelstructuur goed gecontroleerd worden. De korrelgroottes van olivijn in de synthetische gesteenten zijn ongeveer 0.001 mm. De experimenten zijn uitgevoerd bij drukken tot 6000 atmosfeer en temperaturen variërend van 850 tot 1000°C. Microstructuren zijn vooral bestudeerd met behulp van de Scanning Elektronen Microscoop en de daaruit verkregen foto's zijn kwantitatief geanalyseerd met behulp van beeldverwerkingsoftware. De onder 4) genoemde theoretische analyse is gebaseerd op de fysische processen die op microschaal kunnen optreden in gesteentes. Hun samenhang is met behulp van wiskundige vergelijkingen beschreven en samengevat in een computermodel.

De resultaten van de gecombineerde experimentele, computermodelmatige en theoretische benadering laten zien dat groei van korrels tijdens vervorming ('dynamic grain growth') en vervanging van oude door nieuwe korrels ('dynamic recrystallization') beide een belangrijke rol spelen tijdens de evolutie van olivijn microstructuren. De activiteit van deze processen heeft bovendien invloed op het vloeigedrag; het gemak waarmee het vaste gesteente van vorm verandert tijdens grootschalige geologische processen is afhankelijk van wat er gebeurt met de microstructuur. Op zichzelf was dit al bekend, de resultaten van dit project maken het echter mogelijk de invloed van de diverse processen te kwantificeren. Daardoor wordt de weg vrij gemaakt voor het opstellen van verbeterde numerieke modellen van grootschalige geologische/geodynamische processen, modellen waarin de evolutie van korrelgroottes en korrelgrootte-verdelingen een prominente rol kan spelen.

## Dankwoord

Minstens net zo belangrijk als de wetenschappelijke resultaten in dit proefschrift is een uitgebreid dankwoord aan alle personen die direct of indirect hun bijdrage hebben geleverd. Dit proefschrift was nooit voltooid zonder de medewerking en ondersteuning van vele collega's, familie, vrienden, verschillende geldschieters en andere belangstellenden.

In de eerste plaats zijn mijn twee begeleiders Hans de Bresser en Chris Spiers mede verantwoordelijk voor zowel de start als de succesvolle afronding van dit project. Ik besloot vol enthousiasme (en goede moed) aan deze promotie te beginnen, omdat tijdens en na mijn afstudeerproject de honger naar experimenteren, microstructuren en deformatie mechanismen nog lang niet was gestild. Al gauw kwam ik erachter dat ik met mijn afstudeerproject veel geluk heb gehad. De totstandkoming van dit proefschrift is wat minder soepeltjes verlopen. We hebben zeker een aardige serie technische tegenslagen en vertragingen gekend. We zullen maar zeggen dat dit eigenlijk gewoon thuis hoort in een fatsoenlijk promotie onderzoek, niet? Het is in ieder geval eerder regel dan uitzondering en ik heb er zeker veel van geleerd. Hans en Chris, naast het feit dat jullie beider rollen cruciaal zijn geweest om samen met mij steeds de juiste koers te bepalen, heb ik ook op persoonlijk vlak zeer genoten van onze samenwerking in de afgelopen jaren. Vooral het 'buffelen' op het scherpst van de snede om een deadline te halen (Hans) of het eindeloos sleutelen aan modellen om bijna krankzinnig van te worden (Chris) zijn gek genoeg na afloop de perioden waar je met enige weemoed aan terug denkt. Allebei zeer bedankt!

Evenveel waardering heb ik voor de plezierige contacten en samenwerking met de andere leden van de HPT vakgroep. Colin Peach bedankt voor al je hulp in het lab en consulting betreffende elektronica- en computer problemen. Peter van Krieken, vele uurtjes hebben we samen doorgebracht bij het 10 kbar apparaat of in het hoeklab om weer een nieuwe lading monsters te fabriceren. Jouw inspanningen en kennis van het reilen en zeilen bij het HPT-lab zijn onmisbaar. Hetzelfde geldt voor Gert Kastelein. De lijst is eindeloos van kleine en grote technische problemen die we zijn tegengekomen: falende druk-seals, pompen, monster set-ups, gouden jackets enz. enz. Gert, dankzij jouw praktische vernuft en soms onnavolgbare snelheid weet je toch bijna altijd op tijd een oplossing te vinden, veel dank daarvoor. Ook Tony van der Gon en Eimert de Graaff worden zeer bedankt voor hulp in de 'shop' en het lab. Magda Martens dank voor het verwerken van de administratieve rompslomp, die ik zo nu en dan heb veroorzaakt. Ook je nuchtere kijk op al die wetenschappelijke druktemakerij werkt meestal zeer verfrissend, zeker tijdens de 'laatste loodjes' fase. Rob McDonnell wil ik bedanken voor zijn belangrijke bijdrage aan enkele experimentele data gepresenteerd in dit proefschrift (hoofdstuk 3). André bedank ik voor het meer dan 4 jaar met mij uithouden als directe kamergenoot, het prettige gezelschap tijdens excursies en congressen en zo af en toe een drank & begeleiderklaag-sessie in een of andere Utrechtse uitgaansgelegenheid. Ik ben blij dat je na al die jaren mij ook tot het eind toe wil bijstaan als paranymph.

Gill Pennock en Herman van Roermund wil ik in het bijzonder bedanken voor het mij weg wijsmaken in de wondere wereld van de elektronen microscopie. Ook de hulp en discussies op dit gebied met Martyn Drury, Saskia ten Grotenhuis, en Siska Valeke hebben mij een grote dienst bewezen. Stephan Carpentier bedank ik voor zijn fortran raadgevingen. De hulp van Mark Jessell, Paul Bons en Lynn Evans was onmisbaar tijdens opzetten van ELLE op mijn eigen computer. Jan ter Heege heeft een dubbelfunctie vervuld. Jan, zeer bedankt voor zowel de nuttige discussies over wetenschap en specifiek de materie van dit onderzoek als zeker niet onbelangrijk de fiets-, ski- en drank partijen in Nederland, Duitsland, Frankrijk en Oostenrijk. Ook de volgende personen wil ik bedanken voor de prettige

werksfeer en collegialiteit op het IvA; Jan-Willem, Dirk, Bart, Bernard, Kike, Menno, Edith, Emilia, Suzanne, Reinier, Siese, Douwe, Ans, Mimi, Ronald en Roy.

Aan de éne kant heb ik heb het promoveren ervaren als de flexibelste baan ter wereld; je werkt wanneer je wilt, je kan met enig overleg zo 4 weken op vakantie en krijgt daarnaast zoveel vakantie dagen dat je nog niet eens de helft op krijgt. Aan de andere kant zijn er denk ik ook niet zo heel veel banen waarbij de werkdruk zo exponentieel toeneemt naar het einde van je contract toe (en daar overheen). In de perioden van ontspanning zijn er heel wat mensen geweest, die mij in ieder geval voor even hebben kunnen afleiden van al dat gepromoveer. Ik bedank Jaar '95 voor de (verjaars)feestjes, borrels, reunies, etentjes enz. Ik noem speciaal Joris, Jelle, Noor, Onno, Heiko, Mieke, Douwe, Rob, André, Maarten, Ferry, Stijn, Paulien, Ivo, Stephanie en Tessa. Ik bedank Jaar '94 voor de (halve) marathons, de feestjes, de BBQ's en Peukies in Den Haag, Leiden en Utrecht. Ik noem speciaal Guido, Michiel, Mark, Walter, Ruurd, Bart, Femke en Sam. Ik bedank ook Jaar '2000 voor de avondjes JdW en borrels, de 'oude lullen' Martijn en Jolt, mijn PhD-lotgenoten in Ozzieland en Duitsland, Ivo en Juul, de verschillende UGV-besturen, Kampong 17 en alle gezelschappen waarmee geskied is in Frankrijk, Zwitserland of Oostenrijk.

Onno Houtzager vormt samen met André mijn paronymphen duo. Onno, met jou erbij moet dat wel goed gaan. Na al onze avonturen, vakanties, feesten, en wat allemaal nog meer ken jij mij als één van de besten. Onze vriendschap betekend veel voor mij en ik hoop dat we nog veel leuke dingen mogen meemaken.

Naast deze prachtige vriendenclub ben ik ook gezegend met een fantastische en hechte familie. Op volgorde van leeftijd noem ik hier eerst vol trots mijn lieve lieve Omie. Omie, 'we go way back' en jijzelf nog veel verder (soms haast niet te bevatten) en ik hoop de komende tijd wat vaker langs te komen voor een praatje op de flat, daar steek ik altijd weer wat van op! Dan komen natuurlijk mijn ouders; lieve pap en mam ik ben jullie ontzettend dankbaar voor alles wat jullie voor mij hebben gedaan. De basis van alles wat ik ben en doe ligt bij jullie. Het is heerlijk dat ik dat nu eens zwart op wit kan zetten en in 150-voud kan uitdelen. Jullie verdienen het allerbeste en niks minder. Dan zijn er mijn broers Floris, Reinout en Vincent en de dames Quan en Noor. Floris, jij liet mij de eerste stappen in de linux-wereld zetten en dat leidde uiteindelijk tot een succesvolle publicatie, dat lijkt me geen onbelangrijke bijdrage, dank daarvoor. Ook de film avondjes thuis in Heeswijk waardeer ik zeer. Ik wens jou en Quan veel geluk in jullie nieuwe 'casa' in Heesch. Reinout, of moet ik zeggen de grootste 'pik' in A'dam, je bent een topgozer en dat meen ik. Het is heerlijk om af en toe in Utrecht de boel de boel te laten en lekker met jou op pad te gaan in het bruisende Amsterdamse (nacht)leven. Ik weet zeker dat jij en Floris het helemaal gaan maken in respectievelijk de tandheelkunde en IT-wereld. Dan aangekomen bij de jongste van het stel, kan ik niet in woorden uitdrukken hoe jammer ik het vind dat ik jou niet in persoon een boekje kan overhandigen. Vincent, juist omdat je er niet meer bent is het mij een groot genoegen om je hier en publiek te bedanken, ten eerste voor het simpele feit dat je mijn broer bent ten tweede voor de prachtige tijd die je samen met ons hebt gehad. Het ga je goed!

Dan blijft er eigenlijk nog maar één persoon over: Moniek, mijn lieve vriendinnetje, bijna 4 jaar geleden was je er opeens en sindsdien niet meer van mijn podium weg te denken. Dat spreekt boekdelen, want ik ben zeker niet de makkelijkste en ik denk dat je van te voren niet helemaal de nadelen realiseerde een AIO als vriendje. Lieve Moniek, dank voor al je geduld, belangstelling, steun, hulp en liefde. Ik sta geloof ik nog tot in lengte van dagen bij je in het krijt, maar dat is geen probleem want je bent geweldig!

# Curriculum Vitae

## Arthur Kellermann Slotemaker

29 March 1977, Dutch

Topaaslaan 34-1, 3523 AW, Utrecht, the Netherlands

Tel: +31 614166876

E-mail: arthur@slotemaker.net

### Education

---

2002 – present	<b>PhD Geology</b> (Assistent in Opleiding, AIO). <u>description:</u> Research position at Utrecht University on large strain transient and steady state flow behaviour of olivine rocks. Duties: perform mechanical tests on olivine material at high pressure/temperature. Quantitative SEM & image-analysis. Theoretical and numerical modeling. Publish in peer-reviewed journals. Fieldwork teaching to 2 <sup>nd</sup> year BSc students in Pyrenees, Spain.
1996 – 2001	<b>MSc Geology</b> , Utrecht University (the Netherlands). Specialization: Experimental rock deformation; Thesis on the rheology and microstructure of phyllosilicate-bearing fault gouge under conditions favouring pressure solution.
1995 – 1996	<b>Propaedeutics Geology</b> (BSc equivalent), Utrecht University.
1989 – 1995	<b>Gymnasium</b> , Heeswijk-Dinther

### Computer skills

---

Operating systems: MS Windows (experienced), and Linux (basic)  
Software: MS Office, Matlab, Elle, Adobe Acrobat, Photoshop and Illustrator  
Programming: Fortran, C++

### Technical skills

---

Operate Instron mechanical testing machines for high temperature-pressure tests;  
Sample (rock/ceramic/polycrystalline material) preparation and jacketing;  
Microscale imaging using SEM, FS-imaging, and EBSD-analysis.

### Extracurricular Activities

---

1998 – 1999	<b>Treasurer</b> & member of the board of the Utrecht Earth Science Student Society (UGV); organizing and financial responsible for lots of different activities.
1997 – 1998	<b>Member</b> of the UGV, UBV & MBV Mebiose Gala-committee, organizing a traditional party for the three different student societies (500 guests).

### Languages

---

Fluency in: Dutch, English  
Partial Fluency in: German, French

### Other Interests

---

Travelling, skiing, tennis, sailing, soccer